

Lecture Notes in Mechanical Engineering

Meghanshu Vashista

Gaurav Manik

Om Prakash Verma

Bhuvnesh Bhardwaj *Editors*

# Recent Innovations in Mechanical Engineering


Select Proceedings of ICRITDME 2020



Springer


# Lecture Notes in Mechanical Engineering

## Series Editors

Francisco Cavas-Martínez , Departamento de Estructuras, Construcción y Expresión Gráfica Universidad Politécnica de Cartagena, Cartagena, Murcia, Spain

Fakher Chaari, National School of Engineers, University of Sfax, Sfax, Tunisia

Francesca di Mare, Institute of Energy Technology, Ruhr-Universität Bochum, Bochum, Nordrhein-Westfalen, Germany

Francesco Gherardini , Dipartimento di Ingegneria “Enzo Ferrari”, Università di Modena e Reggio Emilia, Modena, Italy

Mohamed Haddar, National School of Engineers of Sfax (ENIS), Sfax, Tunisia

Vitalii Ivanov, Department of Manufacturing Engineering, Machines and Tools, Sumy State University, Sumy, Ukraine

Young W. Kwon, Department of Manufacturing Engineering and Aerospace Engineering, Graduate School of Engineering and Applied Science, Monterey, CA, USA

Justyna Trojanowska, Poznan University of Technology, Poznan, Poland

**Lecture Notes in Mechanical Engineering (LNME)** publishes the latest developments in Mechanical Engineering—quickly, informally and with high quality. Original research reported in proceedings and post-proceedings represents the core of LNME. Volumes published in LNME embrace all aspects, subfields and new challenges of mechanical engineering. Topics in the series include:

- Engineering Design
- Machinery and Machine Elements
- Mechanical Structures and Stress Analysis
- Automotive Engineering
- Engine Technology
- Aerospace Technology and Astronautics
- Nanotechnology and Microengineering
- Control, Robotics, Mechatronics
- MEMS
- Theoretical and Applied Mechanics
- Dynamical Systems, Control
- Fluid Mechanics
- Engineering Thermodynamics, Heat and Mass Transfer
- Manufacturing
- Precision Engineering, Instrumentation, Measurement
- Materials Engineering
- Tribology and Surface Technology

To submit a proposal or request further information, please contact the Springer Editor of your location:

**China:** Ms. Ella Zhang at [ella.zhang@springer.com](mailto:ella.zhang@springer.com)

**India:** Priya Vyas at [priya.vyas@springer.com](mailto:priya.vyas@springer.com)

**Rest of Asia, Australia, New Zealand:** Swati Meherishi at [swati.meherishi@springer.com](mailto:swati.meherishi@springer.com)

**All other countries:** Dr. Leontina Di Cecco at [Leontina.dicecco@springer.com](mailto:Leontina.dicecco@springer.com)

To submit a proposal for a monograph, please check our Springer Tracts in Mechanical Engineering at <https://link.springer.com/bookseries/11693> or contact [Leontina.dicecco@springer.com](mailto:Leontina.dicecco@springer.com)

**Indexed by SCOPUS. All books published in the series are submitted for consideration in Web of Science.**

More information about this series at <https://link.springer.com/bookseries/11236>

Meghanshu Vashista · Gaurav Manik ·  
Om Prakash Verma · Bhuvnesh Bhardwaj  
Editors

# Recent Innovations in Mechanical Engineering

Select Proceedings of ICRITDME 2020

 Springer

*Editors*

Meghanshu Vashista  
Department of Mechanical Engineering  
Indian Institute of Technology (Banaras  
Hindu University)  
Varanasi, Uttar Pradesh, India

Gaurav Manik  
Department of Polymer and Process  
Engineering  
Indian Institute of Technology Roorkee  
Roorkee, Uttar Pradesh, India

Om Prakash Verma  
Department of Instrumentation and Control  
Engineering  
Dr. B. R. Ambedkar National Institute  
of Technology Jalandhar  
Jalandhar, Punjab, India

Bhuvnesh Bhardwaj  
Jaipur Engineering College and Research  
Centre  
Jaipur, India

ISSN 2195-4356

ISSN 2195-4364 (electronic)

Lecture Notes in Mechanical Engineering

ISBN 978-981-16-9235-2

ISBN 978-981-16-9236-9 (eBook)

<https://doi.org/10.1007/978-981-16-9236-9>

© The Editor(s) (if applicable) and The Author(s), under exclusive license to Springer Nature Singapore Pte Ltd. 2022

This work is subject to copyright. All rights are solely and exclusively licensed by the Publisher, whether the whole or part of the material is concerned, specifically the rights of translation, reprinting, reuse of illustrations, recitation, broadcasting, reproduction on microfilms or in any other physical way, and transmission or information storage and retrieval, electronic adaptation, computer software, or by similar or dissimilar methodology now known or hereafter developed.

The use of general descriptive names, registered names, trademarks, service marks, etc. in this publication does not imply, even in the absence of a specific statement, that such names are exempt from the relevant protective laws and regulations and therefore free for general use.

The publisher, the authors and the editors are safe to assume that the advice and information in this book are believed to be true and accurate at the date of publication. Neither the publisher nor the authors or the editors give a warranty, expressed or implied, with respect to the material contained herein or for any errors or omissions that may have been made. The publisher remains neutral with regard to jurisdictional claims in published maps and institutional affiliations.

This Springer imprint is published by the registered company Springer Nature Singapore Pte Ltd. The registered company address is: 152 Beach Road, #21-01/04 Gateway East, Singapore 189721, Singapore

# Preface

The 3rd International Conference on **Recent Innovations & Technological Development in Mechanical Engineering—2020** (ICRITDME-2020) was held at Jaipur Engineering College and Research Centre, Jaipur, Rajasthan, India, on 27–28 August 2020. The primary aim of this international conference is to create a general awareness, skill enhancement and high-quality standards in the field of mechanical engineering. Further, our main objective is to foster the expertise of eminent experts/industrialists belonging to premier institutes/organizations with researchers, academicians and field engineers to sit together on a congenial platform to share their valuable views addressing recent development in mechanical engineering. This conference focuses on a range of issues related to renewable energy, green manufacturing, lean manufacturing, nonconventional machining, materials, surface engineering, nanotechnology, agile and additive manufacturing, ergonomics, sustainable manufacturing, thermal energy, etc.

We sincerely hope that ICRITDME-2020 will be a forum for excellent discussions that will put forward new ideas and promote collaborative researches. We are sure that the proceedings will serve as an important research source of references and the knowledge, which will lead to not only scientific and engineering progress but also other new products and processes.

We would like to express our gratitude to all the participants, for their contributions to the conference. We also thank the authors for submitting research papers and the reviewers for their excellent work in reviewing the research papers as well as their invaluable input and advice. Thanks to the members of the technical committee for providing valuable suggestions in the course of preparation of this conference. We will be failing in our duty if we do not thank the organizing committee.

We place on record our sincere gratitude to the chairperson of each and every conference session, for smoothly conducting the oral presentation of the research papers and coordinating the discussions among the enthusiastic participants. The discussions and deliberations during the sessions are sure to be cherished by

the participants. The keynote lectures were well attended and appreciated by the conference participants. Our heartfelt thanks to them too.

August 2020

Team ICRITDME-2020

# Contents

<b>Enhancing the Performance of a Burner by Changing Design: A Review</b> .....	1
Lakshy Zaveri and M. P. Singh	
<b>Correlation of Acoustic Emission Parameters with Surface Roughness in End Milling of AISI 4140 Steel</b> .....	19
Nikhil V. Khatekar, Raju S. Pawade, Rishi Pareek, and Shivkumar R. Gaikwad	
<b>A Numerical Study of Free Vibration Behaviour of Shear Deformable Functionally Graded Beam</b> .....	31
Maitreya Limkar, Nimitya Phalke, and Kanishk Sharma	
<b>Controlling of Manipulator for Performing Advance Metal Welding</b> ....	41
Aditi Saxena, Jitendra Kumar, Kamal Sharma, and Debanik Roy	
<b>An EEG Based Approach for the Detection of Mental Stress Level: An Application of BCI</b> .....	49
Perna Singh, Rajesh Singla, and Anshika Kesari	
<b>Smart Classroom Surveillance System Using YOLOv3 Algorithm</b> .....	59
Saurav Kumar, Drishti Yadav, Himanshu Gupta, and Om Prakash Verma	
<b>EEG Based Study of Pictorial Advertisement Impact on Customers' Market Preferences</b> .....	71
Anshika Kesari, Rajesh Singla, and Perna Singh	
<b>Techniques Used in Phonocardiography: A Review</b> .....	79
Nikita Jatia and Karan Veer	
<b>Modal Study on Isotropic Spherical Cap and Functionally Graded Spherical Panel Using COMSOL</b> .....	91
Pankaj Sharma, Ashish Khinchi, and Rahul Singh	



<b>Enhancement of Mechanical Properties of Fly Ash Reinforced Epoxy Composite</b> .....	101
Chandramani Goswami, Ratnesh Sharma, Shiv Ranjan Kumar, Ajay Singh, and Anand Prakash	
<b>Performance Analysis of Wavelet Filters for Heart Rate Variability Analysis</b> .....	107
Sarla and Dilbag Singh	
<b>Effect of Stroke Rotation on Discomfort for Assembly Tasks</b> .....	117
Farheen Bano, Zulquernain Mallick, Abid Ali Khan, and Nabila Elnahas	
<b>Development of Improving Model for the Surface Finish of Ball Bearing (Deep Groove) by Optimizing Cutting Parameter</b> .....	131
Shraddha Arya, Manish Bhargava, and M. P. Singh	
<b>Recent Applications, Developments and Challenges in Waterjet Technology</b> .....	141
Paramjit Thakur, D. N. Raut, and Fauzia Siddiqui	
<b>Modeling and Simulation in Waterjet Technology</b> .....	157
Paramjit Thakur, D. N. Raut, and Fauzia Siddiqui	
<b>Elastic–Plastic Stability Analysis of Perforated FGM Plate</b> .....	173
Daaman Sharma, Nimeesh Rathi, and Kanishk Sharma	
<b>Optimization of Heat Transfer Rate, Efficiency and Effectiveness for Thermal Performances of Stepped Rectangular Fin</b> .....	181
Shyam Babu, Devendra Kumar Vishwakarma, and Sumit Sharma	
<b>Heat Transfer Enhancement of Parallel and Counter Flow Heat Exchangers with Varying Size and Fins Number</b> .....	191
Sumit Sharma, Manish Dadheech, Devendra Vishwakarma, Kamal Kishore Khatri, Marek Jaszczur, and Deepak Sharma	
<b>Friction Welding Process of AA7075 Aluminium Alloy to Mild Steel</b> ....	209
Jitendra Gupta, Bhuvnesh Bhardwaj, and Varun Sharma	
<b>Effect of Tool Tilt Angle on the Mechanical and Metallurgical Properties of Aluminium Alloy 6061-T6 Welded by Friction Stir Welding Process</b> .....	221
Gaurav Kumar, Varun Sharma, Rakesh Kumar, Ankit Thakur, Navdeep Minhas, and Om Prakash Verma	
<b>Physiological Evaluation of Normal and Inclined Walking in Unorganized Sector Workers</b> .....	231
Ram Charan Bairwa, Rahul Jain, M. L. Meena, and K. B. Rana	
<b>Analyzing the Effects of Industrial Protective Glove’s Material on Hand Grip Strength</b> .....	237
Lalit Kumar Sharma, Manoj Kumar Sain, and M. L. Meena	

<b>A Comprehensive Study of Image Segmentation Techniques</b> .....	247
Vivek Singh Sisodiya and Rohit Agrawal	
<b>Autoencoder: Issues, Challenges and Future Prospect</b> .....	257
Anega Maheshwari, Priyanka Mitra, and Bhavna Sharma	

## About the Editors

**Dr. Meghanshu Vashista** is an Associate Professor in the Department of Mechanical Engineering at the Indian Institute of Technology (Banaras Hindu University), India. He was awarded prestigious BOYSCAST fellowship from Government of India to carry out advance research in School of Mechanical Engineering at Newcastle University (UK). Department of Science and Technology (India) also funded him a project under esteemed fast track scheme for young scientist. He holds a Master degree in Welding Engineering from University of Roorkee (India) and a Ph.D. degree from Indian Institute of Technology Kharagpur (India). He has published more than 80 papers in reputed journals and conference proceedings. Dr. Vashista is a member of editorial board in various reputed international journals. His area of interest is grinding and machining.

**Dr. Gaurav Manik** is currently serving as Associate Professor in the Department of Polymer and Process Engineering at IIT Roorkee. He holds a Ph.D. (IITB), M.Tech. (IITK) and B.Tech. (HBTI) in chemical engineering. Prior to joining IITR, he has served extensively in industry (3M, Indo Gulf Fertilizers and Chemicals; Classic Stripes) and academia (BITS Pilani, BIET Jhansi). His research interests include molecular modeling and simulations of polymers, chemical process modeling and simulation, development of novel and industrially relevant polymer composites, coatings, sealants and adhesives. He has 60 research publications in international peer-reviewed SCI journals, patent applications, conferences and book chapters. He has significantly valued 21 publications in journal of repute such as *Energy*, *Composites B: Engineering, Polymer*, to name a few and holds six granted patents/patent applications of industrial commercial relevance, four book chapters, and 30 conference publications. He has executed five sponsored research projects and supervised one post-doctoral, one Ph.D., nine M.Tech. candidates and 20 B.Tech. projects. He has been awarded with the prestigious APAC Tech Forum Contribution Award at 3M, and secondment as visiting faculty sanctioned by the President of India for teaching at international platform at Asian Institute of Technology, Thailand.

**Dr. Om Prakash Verma** is presently working as an Assistant Professor in the Department of Instrumentation and Control Engineering, Dr. B. R. Ambedkar National Institute of Technology Jalandhar. He holds a Ph.D. from IIT Roorkee; M.Tech. from Dr. B. R. Ambedkar National Institute of Technology Jalandhar and B.Tech. from Dr. B. R. Ambedkar University. Prior to joining IITR, he has served extensively in academia (Graphic Era University, Dehradun; Banstahli Vidyapith, Rajasthan and KIIT Bhubaneswar). Dr. Verma research interests are in the areas of process dynamics, modelling, simulation, control and optimization, nonlinear and adaptive control and application of soft computing and machine learning. He has a credit of publishing more than 15 research articles with highest impact factor 10.55 in *Renewable & Sustainable Energy Reviews*. He has published more than 10 book chapters and more than five conference proceedings. He is editor of several books. He is Life Time Member of Instrument Society of India, Bangalore, and reviewer of many reputed peer-reviewed journals including *Energy Journal*, Elsevier; *Pattern Recognition Letter*, Elsevier; *International Journal of Computers & Technology*; *International Journal of Industrial Engineering: Theory, Applications and Practice*; *Journal of Medical and Biological Engineering*, Springer; *International Journal of System Assurance Engineering and Management*, Springer; *International Journal of Electrical and Computer Engineering*. He is Editorial Review Board Member on Mechanical and Mechatronics Engineering, World Academy of Science, Engineering and Technology, USA. He also has credit to organize an International conference SoCTA 2018 in department of ICE partially funded by CSIR New Delhi and MIR Lab, USA. Dr. Verma recently has received ISRO Projects.

**Dr. Bhuvnesh Bhardwaj** is currently working as an Associate Professor in the Department of Mechanical engineering, Jaipur Engineering College and Research Centre, Jaipur. He obtained his B.E. (Mechanical Engineering) from Government Engineering College Ajmer and M.Tech. (Manufacturing System Engineering) and Ph.D. from Sant Longowal Institute of Engineering & Technology, Sangrur, Punjab. He has more than 15 years of teaching experience and has taught a broad spectrum of courses related to mechanical engineering. His major areas of research include Conventional & non conventional Machining, composites, Wear and friction and Material Characteristics. Also he has published a patent on “Apparatus and method for cleaning inner surface of hollow object”. He has published more than 40 papers in reputed international journals.

# Enhancing the Performance of a Burner by Changing Design: A Review



Lakshy Zaveri and M. P. Singh

**Abstract** The most important issue in the present scenario of the world is the availability and use of energy. In developing countries, the energy used for cooking is a major proportion of the total energy consumption. India with a consumption of 22.5 million tons is the world's second-largest consumer of LPG. About 89.9% households in India uses LPG that is 25.95 crore registered customers out of which 25.68 crore are domestic customers. A total of 21.86 crore customers are active domestic customers as on January 2018. The Ministry of Petroleum and Natural Gas reported that a growth of 34% is expected in the LPG consumption, leading to 30.3 million tons by 2025. In the present work, various works dealt with research in increasing thermal and conversional efficiency of stoves using different material burners of different shapes and different burner heads are studied. Various parameters affecting thermal and conversional efficiency of a burner are determined.

**Keywords** Conversional efficiency · Thermal efficiency · Covering · Sealed burners · Swirling effect · Premixed air burners

## 1 Introduction

In the time when globalization is on its peak and industries are growing day by day, there is very high demand of energy. The most important issue in the present scenario of the world is the availability and use of energy. The fast consumption of fossil fuels causes pollution at high rate and increases the chances of unavailability of fuel in near future. There is a very high demand of fossil fuels, and at the same time, the fuels are depleting at a rapid rate. There must be some steps taken toward the conservation of the fuels. In order to meet the increasing energy demand, the use of the sources must be optimized. We are at the verge of extinction of non-renewable sources and still exploiting them at a very high rate. The loss of energy due to inefficient methods is

---

L. Zaveri · M. P. Singh (✉)

Department of Mechanical Engineering, Jaipur Engineering College and Research Centre, Jaipur, India

e-mail: [mpsingh.me@jecrc.ac.in](mailto:mpsingh.me@jecrc.ac.in)

not at all acceptable. Researchers are recommending the use of alternative fuel and use of renewable sources of energy.

To prevent the loss of energy in the existing devices, new methods need to be formulated. A relatively higher proportion of liquefied petroleum gas (LPG) is consumed in domestic sector as compared to the industrial sector. So, the method to enhance the thermal and combustion efficiency of the domestic gas burner has a very wide scope. The idea to enhance the efficiency of the methods and process being practiced is also helpful in order to get optimal results and enhance the sustainable growth.

The swirl effect imparts a tangential component to the flow of the gasses in addition to axial and radial components. The holes in the burner are drilled with an angle inclined with respect to the radial component of the burner. Swirl effect is very significant and has widespread applications. It increases the residence time of the fuel and also increases the time of interaction between the flames and the vessel placed on the top of the stove. The swirl effect provides more stability to the propagation of flame and affects the efficiency of the burner. The swirl motion of flames also creates more intake of secondary air into the combustion area which increases completeness of combustion and decreases the harmful emissions. The covering of the gap between the stove and vessel prevents loss of heat due to radiation. The covering is made of a thermally non-conducting material. The covering does not allow heat to get liberated into the surrounding by means of conductions or radiation and enhances the efficiency of the system. The round shape burner does not have concentration of flames in the center of the vessel; hence, 'X' shape burner is introduced. The 'X' shape will provide flames concentrated towards the center of the vessel and prevent heat loss due to radiation from the outer periphery. The addition of a compressed air input to the burner will provide proper combustion. The compressed air when supplied to the burner will result into complete combustion of the fuel gasses. Complete combustion means higher efficiency of the system, and it will also reduce the production of harmful pollutants that occur due to incomplete combustion or when the fuel is left unburned. The efficiency of the burner has high environmental as well as economic impact as a result of which it is of prime concern.

## 2 Comparison of Different Case Studies

Khan and Saxena [1] focused on the design and different material of the burner heads used and effects on the performance on LPG cooking stoves. Burners of different materials show different efficiencies. Thermal efficiency of a brass burner is more as compared to that of cast iron burners (Fig. 1).

The different designed burner heads are also used for investigation and calculations of the thermal efficiency. The efficiency of cooking gas stoves increased when regular burners were replaced by the flat face and flower shaped burners. Thermal efficiency of a flat face brass burner was found to be 58% in specific conditions (Fig. 2).

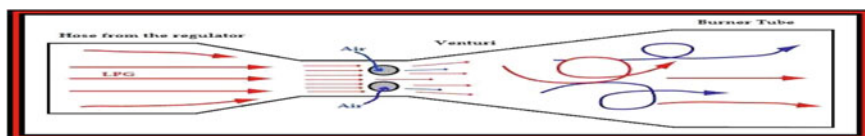


Fig. 1 Mixing of LPG and air

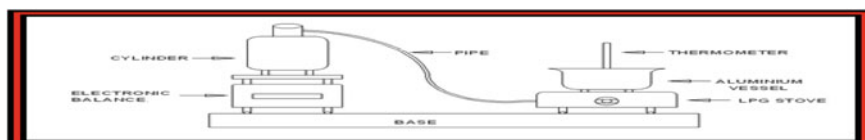


Fig. 2 Line diagram of experimental setup



Fig. 3 Variation of thermal efficiency (%) of LPG stove using different burner heads

Efficiency of a regular cast iron shaped gas stove burner was calculated to be 48%. Using new designed flat face and flower shaped burner improves the efficiency of gas stove. Thermal efficiency of a flower shaped burner was found to be 50% (Fig. 3).

The efficiency of a regular brass burner was 4% more than that of regular cast iron burners. The idea of just changing the burner heads was a great initiative and safe. It is easy to implement and establish in all the households using LPG stoves to decrease the consumption of LPG and conserving the fuel to a great extent.

**1.1 Ashraf Kotb and Hany Saad [2]** studied the effect of swirling flow on flame stability limits and the effect of swirling effect on flame shape. The co- and counter swirl burners have thermal efficiency higher than the base burner under all operating conditions. Also the base burner has output normal to the burner tip, while the co-swirl burner produces a flame that seems to be rotating by an angle relative to the burner tip (Fig. 4).

The counter swirl burner produces complete clean combustion with long flame and looks like it has only half number of outputs due to the mixed combination of two opposite jets. Also the swirl burner shows less emission of CO than the base burner. The co-swirl burner can achieve improved thermal efficiency, and it can also reduce the emission of pollutants with wide operating range (Fig. 5).

**1.2 David S. Bhatt and Irfan A. Mulla [3]** studied the effect of swirl on residence time. Due to the swirling motion, the time available for the diffusion increases since

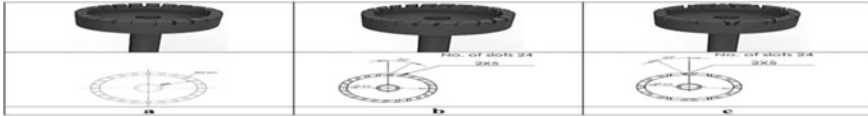


**Fig. 4** Burners design, **a** no swirl burner ( $\theta = 0^\circ$ ), **b** co-swirl burner ( $\theta = 30^\circ$ ), **c** counter swirl burner ( $\theta = 30^\circ$ )



**Fig. 5** Flame shape, **a** no swirl burner ( $\theta = 0^\circ$ ), **b** co-swirl burner ( $\theta = 30^\circ$ ), **c** counter swirl burner ( $\theta = 30^\circ$ ). For interpretation of the references to color in this figure, the reader is referred to the Web version of this article

the path traveled by flame is increased. This provides more time for the chemical reaction to get completed.

The swirl effect also affects the heat transfer. Due to swirling, the flame rotates on the surface of the target, hence increasing the contact time, shear stress which in turn increases the heat transfer efficiency. On imparting, the swirl effect before combustion produces a homogenous mixture and the homogenous mixture results into the complete combustion of the fuel. David S. Bhatt and Irfan A. Mulla also stated that decreasing the heat capacity of the pan support also has a positive influence on the efficiency of the gas burner. The swirl has two effects on the efficiency of the domestic gas burner. It increases the efficiency of the burner by increasing the residence time and providing suction of the secondary gasses to enhance complete combustion, but the secondary gasses at ambient temperature reduce the temperature of the hot gases in the flame. Hence, there exists an optimality of the swirl angle. The optimal swirl angle must provide a balance between the conditions to provide high burner efficiency (Fig. 6).

**1.3 Agung Sugeng Widodo [7]** studied the distance between the pan or the cooker and how it will affect the thermal efficiency of a conventional gas burner. According to the author, efficiency is defined as the fraction of heat input from combustion process which is converted to desire output. The gap between the pan and the gas burner changes the efficiency of the gas burner as it is changed in any positive or negative side. An extra shield covering is used made up of ceramics

**Fig. 6** Swirl burner details

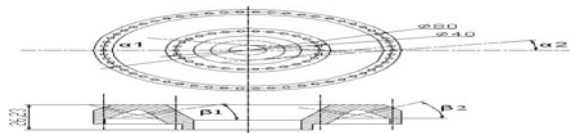
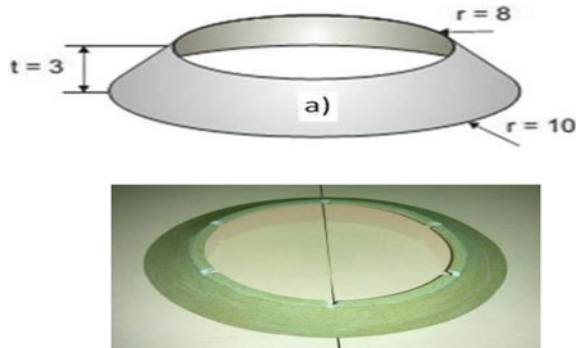




**Fig. 7** a Schematic of stove cover, b ceramic cover



which varies from 1 to 7 mm with 1 mm thickness. Both the factors affects the efficiency of a gas burner. Maximum thermal efficiency is achieved when the gap or the distance between them was 4 mm for regular flow rate. The thermal efficiency calculated at 4 mm gap is about 46.6% by which optimal condition was attained. Optimum conditions are achieved because convection and radiation heat losses were canceled due to the ceramic covering which increases the heat transfer more in form of convection to the pan directly, by which the efficiency is reached at the top level and heat dissipation reduces with great amount. Heat losses will be very low (Fig. 7).

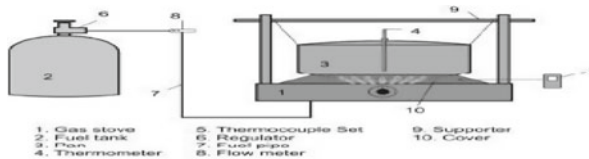


**Figure-1.** Illustration of instalation.

**1.4 Henar Olmedo Gomez, Miguel Casta ~ nos Calleja, Luis Aldea Fern\_andez, Aleksandra Kiedrzy\_nska, Robert Lewtak [9]** worked on the new designs of the gas burners with many different materials. Along with that, new type of alternative feed stocks and integrated monitoring and control systems is permanently attached to the new type of gas furnaces. All these modification are essential to acquire that particular efficiency (Fig. 8).

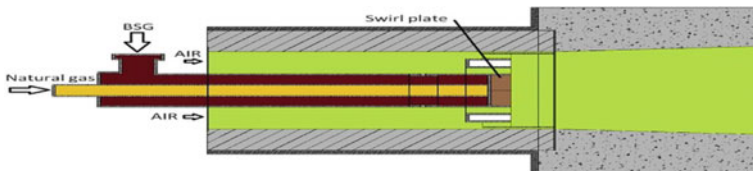


**Fig. 8** Burner with proposed modifications

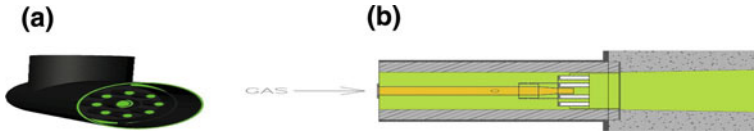
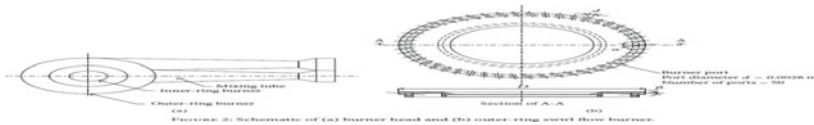


Fig. 9 Cutting plane of the unmodified burner, a 3D view, b 2D view

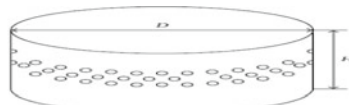
The main objective is to reduce the use of fossil fuels which will be soon to diminish. Addition of an extra secondary fuel or alternative fuel is introduced for co-firing to substitute the natural gas to decrease the usage of fossil fuel. The new design is simulated in CFD for an addition of co-firing and calculations for the new design dimensions. This simulation can be used for increasing the thermal efficiency and reducing the pollutant count (Fig. 9).

**1.5 Shuhn-ShyurngHou and Ching-Hung Chou [6]** worked on investigation of emission of CO, thermal efficiency through the different parameters such as swirl flow, loading height, and semi-confined [sealed burners] combustion flame. Their research shows that the thermal efficiency is increased, with increase in loading height and with the same time, the emission of CO is decreased. For a particular height of about 2–3 cm, high thermal efficiency can be achieved at the inclination angle of 15 degree.

As the loading height increases to about 4 cm, thermal efficiency increases with increase in inclination angle. To attain a high increase in thermal efficiency a shield type of covering is used by which approximately 4–5% of efficiency is increased resulting decrease in CO emission for any type of burners.



As swirl angle is increased from 0 degree to 56 degree, 2% hike in the efficiency of the gas stove burners was found.



Diameter of circular shield ( $D$ ): 0.32 m  
 Thickness of circular shield ( $t$ ): 0.0008 m  
 Height of circular shield ( $H$ ): 0.11 m  
 Number of round holes ( $N$ ): 1.212  
 Diameter of round hole ( $D_h$ ): 0.00125 m  
 Figure 4: Schematic diagram of the circular shield.

**1.6 Jagruti R. Surange, Navneet K. Patil, Akhilesh V. Rajput [10]** in their research, the steps used were for the determination of efficiency of cook stoves. This was determined by using the data of various papers, experiments, and researches. The data was used to calculate the heat gained and the efficiency. They also conducted an

experiment in which they calculated the heat gained by the water which was placed on burner for heating and also the total amount of the fuel that was used in the process of heating the water. In this experiment, they had also included the heat gained by the container in which the water was kept.

The conclusions of this review were that the efficiency of a burner is not same or constant. The efficiency of the burner depends on the environment and the conditions in which it is kept and used. Also it was determined that the efficiency of the burner does depend on the type and the quality of the fuel used. The efficiency of the burner does varies, but in controlled environment, a higher value of efficiency (more than the normal or average) can be achieved. When we use the burner in daily use, due to improper conditions, this value of efficiency is always lower. The energy content of the fuel also determines the efficiency, and preheating the fuel can be very helpful in increasing the efficiency.

**1.7 Bibhuti Bhusan Samantaray, P. Pradhan, Dillip K. Sahoo, P. C. Mishra [5]** presented the experimental analysis of different metallic porous medium cooking burners and calculate its thermal efficiency and pollutant emission. All the experiments were done under same atmospheric conditions for the better results.

Different characterized burners are used for experiment that were.

- (a) Flat type
- (b) Semi-swirl type
- (c) Full-swirl type.

The featured parameters which were taken under considerations are pore size, array of pores, no. of arrays, and no. of pores (Table 1).

More laminar effect is seen in swirl typed burners, and flame seems to be diffused in case conventional open burners. Full-swirl burners gives the maximum thermal efficiency of 64.1%, on the other hand, semi-swirl burners can attain the efficiency of 60.8% and flat burners of 50.2% by this experiment.

**1.8 B. Repic a, A. Eric, D. Djurovic, A. Marinkovic, G. Zivkovic [4]** performed an experiment on different shaped swirl flow burners using pulverized fuel combustion. The main parameters are fuel and burner characteristics for the proper calculations. Different swirl burners model used for investigation are as follows (a) tangential, (b) axial-blade type 1, (c) with movable blocks, and (d) axial-blade type 2.

**Table 1** Geometric characteristics of flat, semi-swirl, and full-swirl burners

SI	Burner type	OD (mm)	Thickness (mm)	No. of pores	Pores size (mm)	Material
1	Swirl	110	5.8	$15 \times 5 = 75$	3.5	Cast iron
2	Semi-swirl	75	5.4	482	3.5–6.5	Cast iron
3	Flat (AL)	75	5.5	$60 + 30 + 30 = 120$	1.5	Aluminum
4	Flat (CI)	75.58	5.4	$60 + 24 + 30 = 120$	1.93	Cast iron

Basic specifications are considered for the selection of best swirl burner, such as thermal efficiency, low heat loss, appropriate flow of fuel for proper consumption, and energy lost. Hydraulic resistance is used for calculating the evaluated cost of the swirl devices used in the burner. It also gives an idea of energy lost during swirling effect. This paper studied has a method and calculations to determine the hydraulic resistance for different swirl burners models used in laboratory (Fig. 10).

**1.9 Krishna Prasad A.** [8] experimental work deals with the new design of the conventional gas burner and fabricating it. It also gives an idea on flow of the producer gas for domestic purpose. The main focus of designing new burner is based on specifications such as simple, low cost, efficient, and safe.

Necessary modifications are kept in mind to attain stable and concentrated flame and performance of the burner.

Premixed types of gas burner are better than that of diffusion type of gas burners. It is calculated that the efficiency is increased by 5% for premixed type of gas burners with comparison to diffusion type burners. An addition mixing chamber is introduced in premixed type gas burners. For calculation of the thermal efficiency, heat loss and heat generated boiling water test is performed. Thermal stresses produced in the burner were low because of uniform distribution of temperature which can be observed in temperature profile (Fig. 11).

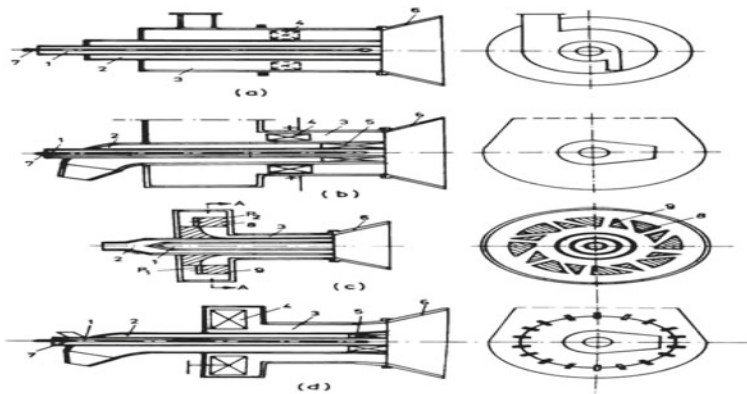


**Fig. 10** Swirl burner models: **a** tangential, **b** axial-blade type 1, **c** with movable blocks, **d** axial-blade type 2. 1-central air, 2-primary air, 3-secondary air, 4,5-blade vane, 6-diffuser, 7-gas burner, 8,9-stationary and movable blocks, P1, P2-movable and stationary plate

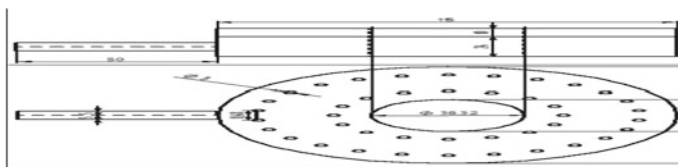
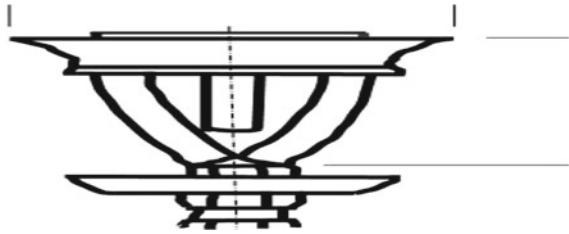


**Fig. 11** Producer gas burner dimensions

**Fig. 12** A typical brass burner without sudden expansion



**1.10 Emmanuel O. B. Ogedengbe and Frank D. Ajibade [12]** designed a new type of burner which includes a preheating chamber for proper, steady, and safe flow of liquefied petroleum gas or liquid fuel used in domestic gas stoves (Fig. 12).

A new technique is introduced which is known as “sudden expansion.” The positive aspect of “sudden expansion” is to reduce back-flow, leakage by seals, mechanical wear, and pressure loss results in improper combustion. Novel feeding technique is used in case of liquid fuel for the setup. The new designed burners are calibrated on unique height between 46 and 60 mm to completely eliminate the back-flow.

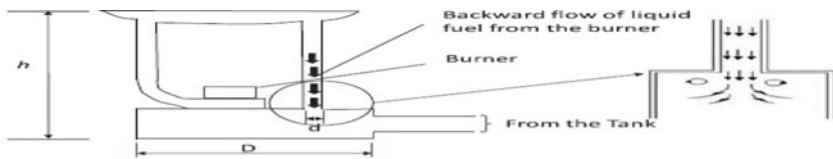


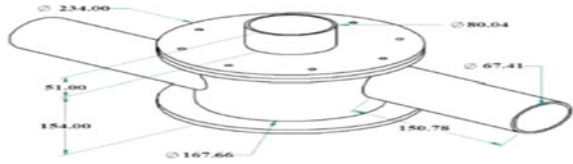
**Figure 2.** Schematic of the Proposed Burner, Showing the Sudden Expansion Section.

**1.11 V. K. Pantangi, Subhash C. Mishra, P. Muthukumar, Rajesh Reddy [11]** they worked on the performance of a porous radiant burner. They carried out certain tests on the porous radiant burner using LPG as a fuel. A modified burner was used with two layers or films or porous medium. There was a preheating zone created which was made up by the help of alumina balls, and the combustion zone was made up of silicon carbide. The data collected from the experiment showed the burner performance, its thermal efficiency, and emission rates for the defined diameter of burner used. For getting the data, the diameter of the burner was varied along with the equivalence ratio and the thermal load.

After the experiment, it was found that the surface temperature of the burner was uniform. It was also noted that when the thermal weight was high, the reaction zone shifted downward for the axial temperature. Also a desirable feature was found that when the thermal weight was increased, the radial temperature was found more stable or we can say uniform. The maximum efficiency for this burner during the experiment was found to be 68%, which is 3% higher than the maximum efficiency of a conventional burner.

**1.12 Ali SafaAlsaegah, Fares AmerHatem, Agustin Valera-Medina [20]** introduced swirl combustors and operates them under the low air–fuel mixtures to attain low emission of pollutants such as  $\text{NO}_x$ , which regulates the power generation from

**Fig. 13** Schematic of the burner



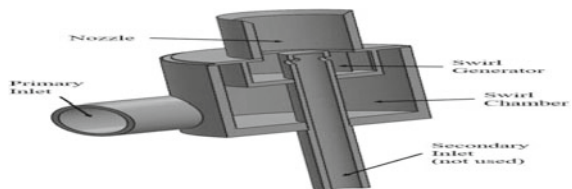
specific amount of fuel. This swirl combustor helps to increase the thermal efficiency (Fig. 13).

There are many loopholes to attain the required efficiency and to restrict the emission of pollutants by modifying the combustors. Many parameters affect the combustion of the fuel while using combustors, such as extinction, low reaction rates, heat dissipation, unstable flames, and improper mixing. Both numerical and experimental approaches are used for calculations and hydrodynamics of the design of the combustor for the turbine to get stabilized flames with taken in consideration. CFD simulations are implemented on the design of tangential swirl burner including diffusive air injection at different three- dimensional positions. Isothermal field flow characteristics, such as turbulence and downstream nozzle flow of the burner. Size, intensity, and position of the central recirculation zone are changed to diffusive air injection. It also reduces the fluctuations in the flame.

**1.13 Victor Castaneda, Agustin Valera-Medina [21]** studied the effects of Coanda phenomenon. Tendency of a fluid to stay attached to the corresponding walls is known as Coanda effect. Discovery of Coanda phenomenon helped in many engineering fields such as aerodynamics and heat transfer and in medical sector also. In this paper, author added this effects in the heating and combustion appliances. Taking flame stability as a main objective introduction of generic swirl burners is used to manage the flow rate and air–fuel mixture (Fig. 14).

Difference between the Coanda jet fuel flow and open jet fuel flow was examined under flame behavior. An additional gas is used for proper combustion at atmospheric pressure which is methane. Flow meters are used to regulate the flow of the gases. Coanda jet injection provides Coanda flames which helps in breaking down of coherent structures of the fuels. It helps in reducing the size of the novel at higher temperature.

**Fig. 14** Swirl burner



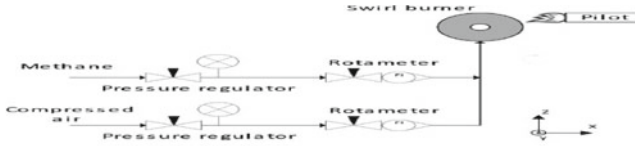


Fig. 2. Experimental setup

**1.14 Sangjukta Devi, Niranjan Sahoo, P. Muthukumar [19]** presented the modified behavior of the porous radiant burners in terms of its combustible properties and which are used in industries. These burners are applicable for the bio-medical solid waste disposal system used for industrial purpose. Double-layer porous media technology is used for the porous radiant burners for different fire rates. Combustion and preheat zones are induced in the layers which is made up of silicon carbide and alumina. The new burners are investigated on same geometric parameters and working on combustion efficiencies and emission characteristic. The results of porous radiant burner were compared with the results of that of conventional burners for a proper conclusion. The combustion efficiencies had a hike and approx. decreasing CO and NO<sub>x</sub> by a great amount for the biogas combustion in porous radiant burners (Fig. 15).

**1.15 N. K. Mishra, P. Muthukumar, Subhash C. Mishra [16]** they used a porous radiant burner which was based on two-layer pmc, a combustion zone, and a preheating zone. The combustion zone was 90% porous by the help of highly porous silicon carbide mixture, whereas the preheating zone was 40% porous and was made by ceramic. The fuel used was LPG. There was a radiation shield attached with the burner along with an adjustable stand. For the data collection, different heat input were taken in the range of 5–10 kW on the thermal efficiency and the emission levels.

After the experiments, it was found that the thermal efficiency was in the range of 30–40% for different thermal loads for a conventional burner. On the other hand, it was seen that the efficiency of porous radiant burner was found in the range of 40–50%. It was also seen that the efficiency of the porous radiant burner gradually decreased on higher power loads. It was noted that at the power load of 5 kW, the maximum thermal efficiency of porous radiant burner was 50% which was 25% more than the conventional burner.

**1.16 Alex Lekov, Andy Sturges, Gabrielle Wong-Parodi [17]** discuss various ways that affect cooking appliances and its efficiencies. They studied about the:

1. Pressure regulated in a gas supply system and its effect on emission of different pollutants by changing of pressure.



Fig. 15 Experimental setup of biogas-operated PRB. Schematic of fuel–air system and burner head

**Fig. 16** Burner design illustrating primary and secondary air flows

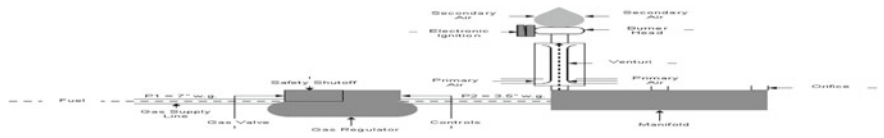
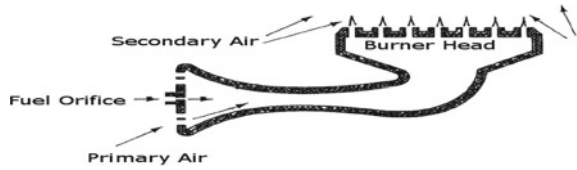


**Fig. 17** Gas appliance burner system layout

2. Improper fuel–air mixture which may cause in increase of CO emission which requires more air (oxygen) for complete combustion (Fig. 16).
3. Ignition temperatures affect the length of the flame and flame lifting and soot formation.
4. New burner heads can decrease the pollutants emission.
5. Introduction of heat exchangers for the betterment of the combustion at proper ignition temperature and stabilizing the flame (Fig. 17).

**1.17 Panya Aroonjarattham** [18] studied about the KB-5 type of burners which are basically used in Thailand. KB-5 is a high-pressurized gas stove burner. The main focus of this research is to study the four significant parameters that are:

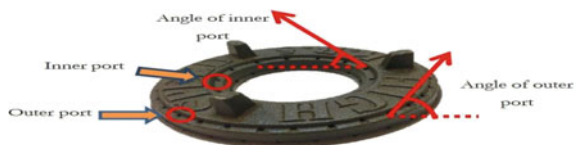
- (a) Angle of inner ports,
- (b) Number of inner ports,
- (c) Angle of outer ports,
- (d) Number of outer ports.

The thermal efficiency was compared with the specification of the standard industrial stoves in households using LPG as the fuel (Fig. 18).

Conclusion:

- (a) By increasing the angle of the outer port, the thermal efficiency is increased by approximately 13%.
- (b) By increasing the number of outer ports, it increases the efficiency by 5%.
- (c) By increasing the angle of the inner port, it does not affect the thermal efficiency of the burner.

**Fig. 18** Parameters of burner heads





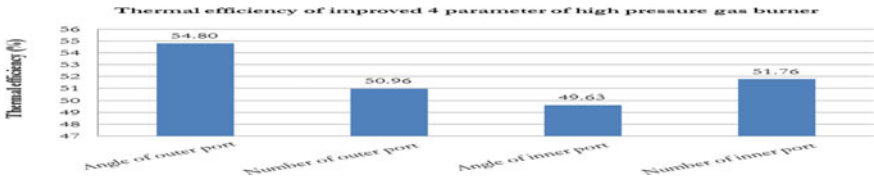


Fig. 19 Thermal efficiency of high-pressure gas burner improved four parameters

- (d) By increasing the number of inner ports, the thermal efficiency is increased by 7% (Fig. 19).

1.18 DarpanDahiya, Rohit Singh Lather and Pramod Bhatia [15] discussed various studies on the improvement of the efficiencies and emission of pollutants for gas stoves burner using LPG as a fuel. The studied was done on the basis of parameters like performance, efficiencies, and emission rates. Biogas variant is also taken as a consideration for the study. The different design of the burners is one of the basic factor of the study and was strongly emphasized it (Fig. 20).

Preheating is a good innovative idea to increase the efficiency of gas burners. Porous media burner gives high thermal efficiency of the gas burner and reduces the emission of CO and NO<sub>x</sub>. Design and material used are factors to increase the efficiency and control emission rates (Fig. 21).

Fig. 20 Commercial burners used for performance 20

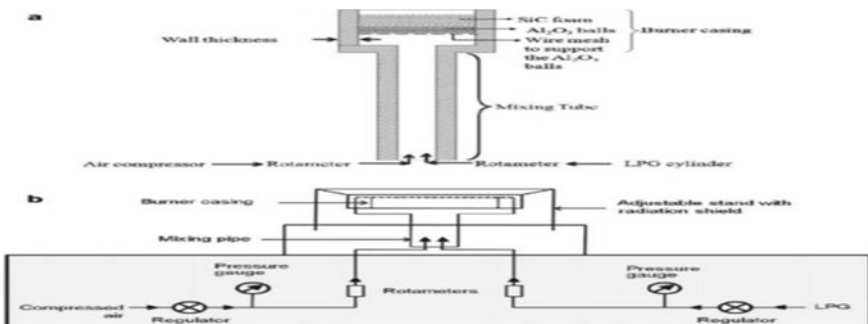


Fig. 21 Schematics of the PRB and the experimental setup 19

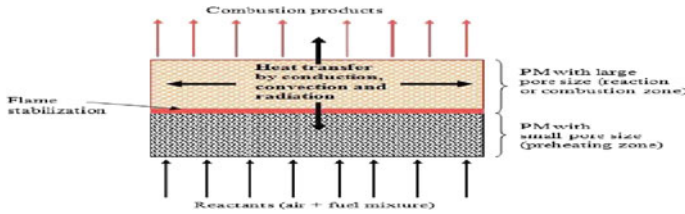


Fig. 22 Schematic diagram of two-layer porous burner

**1.19 Vijay Kumar, Amandeep, Keshwer Eqbal Khan [14]** presented the latest design modification of the LPG gas burners. They also studied about the introduction of porous radiant burners and show its advantages and positive aspects after replacing old conventional burners (Fig. 22).

For higher thermal efficiency and eco-friendly burners, the porous radiant burners are the most suitable type of burner to attain required thermal energy. Type of fuel, material used, geometry, size, and catalytic combustions are also the factors which can enhance the efficiency and decrease the emission of the LPG stove burners (Fig. 23).

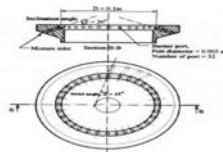


Figure 3. Details of the swirling central flow ring burner (SRB)

**1.20 S. Jugjai, S. Tia, W. Trewetaskorn [13]** presented a new swirl burner which produces a swirling central flame technique by which the thermal efficiency of the open conventional gas burner is increased. Thermal inertia of the pan is reduced for the improvement of the efficiency. Porous medium waste heat is used to preheat the secondary air which is entering the combustion chamber from the technique is used for the recovering of the waste heat which is dissipated in the form of radiations. That bottom of the burner replacing the conventional burner by the swirl burner increases the thermal efficiency by 15%, because of the swirl effect produced. Thermal heat energy also increased in case of swirling central flame technique resulting high temperature flame. Porous support is also added for specific height and heat transfer.

Fig. 23 Flat flame burner developed

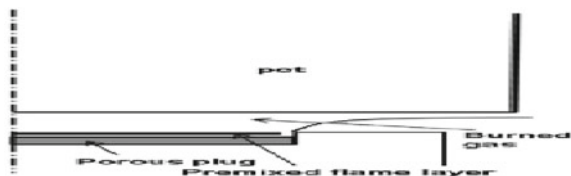




Figure 4. Conventional support (CS).



Figure 5. Light-weight conventional support (LCS).



Figure 6. New support (NS).

**1.21 Fredrik A., Silversand, Catator AB [22]** They used a catalytic wire mesh for their experimental research. They placed the catalytic wire mesh downstream the flames. The reason behind it was to quench the flames if possible, and the main purpose was to attain a mixed type of combustion having both a flame combustion as well as a catalytic combustion. Another approach was also taken into consideration which was to replace the flame port area by the catalytic wire mesh. The second approach could help in attaining a complete catalytic combustion instead of a mixed one. The second approach for a complete catalytic combustion can also be done by using a catalytic coil placed downstream the port area. Due to the catalytic combustion instead of the flame combustion, the emission of  $\text{NO}_x$  and CO would be reduced to zero.

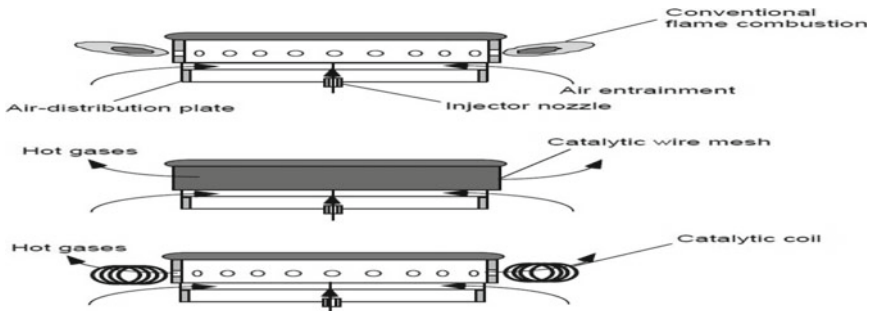


Figure Retrofit installations

The experiment proved that the catalytic combustion is very efficient and can be used to replace the flame combustion easily. The design modifications are very easy and can be done by anyone. The data of experiments proved that the amount of the catalyst used in the combustion was small which makes the modifications and the combustion cost cheap. Also, the mapping to the CO and  $\text{NO}_x$  emission proved that the emission of these gases was very low in catalytic combustion. There is also a tendency that the thermal efficiency of the burner can be increased by replacing the flame combustion used generally by the catalytic combustion.

### 3 Conclusion

Various works related with the enhancement of the performance of a burner were studied thoroughly. There were many methods used such as increasing the number of holes, changing the hole angle, covering the burner surrounding, premixing of fuel and other ways. Other than these, co and counter swirl burners, conventional burners and modified burners were used in various researches but the main purpose of all were found to be similar. All the researches proved that in order to achieve a higher efficiency, the design of the burner must be changed. The conclusions made were that.

- CO swirl, counter swirl, semi-swirl and swirl burner, and the porous radiant burner has higher efficiency than the conventional burner.
- Various modified conventional burner as well as swirl burners shows a higher efficiency by 3–10%.
- A catalyst wire mesh or catalyst coil can be used to gain a full catalytic combustion which will reduce the CO and NO<sub>x</sub> emission as well as enhance the efficiency.
- A pre-heater can be used in order to increase the initial temperature of the fuel which will in turn increase the efficiency of the burner.
- A pre-mixed air–fuel mixture can be used to enhance the efficiency of the burner.
- A covering can be made around the burner to reduce the energy or heat loss to the surrounding, and this will enhance the efficiency the about 3%.
- The gap between the burner and the pan can also be optimized in order to increase the efficiency of the burner.

### References

1. Khan MY, Saxena A (2013) Performance of LPG cooking stove using different design of burner head. *Int J Eng Res Technol* 2(7)
2. Kotb A, Saad H (2018) Case study for co and counter swirling domestic burners. Elsevier, pp 98–104
3. Bhatt DS, Mulla IA (2011) Design and development of burner ring to enhance thermal efficiency of domestic LPG stove and assessment of its performance. In: International conference on recent innovations in technology, RIT Kottayam, pp 385–390
4. Repica B, Eric A, Djurovic D (2012) Experimental determination of swirl burner laboratory models hydraulic resistance, *SciVerse Science Direct*. Elsevier, pp 672–682
5. Samantaray BB, Pradhan P (2015) Comparitive thermal performance and emission analysis of Flat, Semi swirl cooking burners. *Procedia Eng*
6. Hou SS, Chou CH (2013) Parametric study of high efficiency and low emission gas burners. *Hindawi Publication*, pp 932–939
7. Widodo AS (2016) Efficiency of household gas stove by optimizing gap of pan and stove cover. *ARPN J Eng Appl Sci* 11
8. Krishna Prasad A (2016) Experimental study on premixed type producer gas burner. *Int J Innov Eng Res Technol* 3(9):51–61
9. Gomez HO, Calleja MC, Lewtak R (2019) Application of CFD simulation to the evaluation of natural gas replacement by syngas in burners of ceramic sector. Elsevier Ltd. pp 15–27

10. Surange JR, Patil NK, Rajput AV (2014) Performance analysis of burner used in LPG cooking stove: a review. *Int J Innov Res Sci Eng Technol* 3(4)
11. Pantangi VK, Mishra SC, Muthukumar P (2013) Rajesh reddy, study on porous radiant burner for LPG. *Energy* 36
12. Ogedengbe EOB, Ajibade FD (2017) Improved burner efficiency and fuel consumption in domestic cooking appliances. *Energy Policy Res* 4(1):29–35
13. Jugjai S, Tia S, Trewetaskorn W (2001) Thermal efficiency improvement of an LPG gas cooker by a swirling central flame. *Int J Energy Res* 25:657–674
14. Amandeep VK, Khan KE (2016) Porous radiant burner for household cooking purpose: a review. *Int J Adv Eng Technol* VII(IV):07–12
15. Dahiya D, Lather RS, Bhatia P (2016) Improvement of the domestic LPG cooking stoves: a review. *Indian J Sci Technol* 9(S1). <https://doi.org/10.17485/ijst/2016/v9iS1/105856>
16. Mishra NK, Muthukumar P, Mishra SC (2013) Performance tests on medium-scale porous radiant burners for LPG cooking applications. *Int J Emerg Technol Adv Eng* 3(3)
17. Lekov A, Sturges A, Wong-Parodi G (2009) Impacts of imported liquefied natural gas on residential appliance components: literature review. Environ Energy Technologies Division Lawrence Berkeley National Laboratory Berkeley, CA 94720
18. Aroonjarattham P (2016) The parametric studied of high pressure gas burner affect thermal efficiency. *Eng J* 20(3)
19. Devi S, Sahoo N, Muthukumar P (2016) Combustion of biogas in porous radiant burner: low emission combustion. Elsevier Ltd., *Energy Procedia* 158:1116–1121
20. Alsaegah AS, Hatem FA (2017) Agustín Valera-medina, visualisation of turbulent flows in a swirl burner under the effects of axial air jets. Elsevier Ltd. *Energy Procedia* 142:1680–1685
21. Castaneda V, Valera-Medina A (2017) Coanda flames for development of flat burners. *Energy Procedia* 158:1885–1890
22. Silvers FA, Catator AB, Development of a novel catalytic burner for natural gas combustion for gas stove and cooking plate applications. Elsevier *Catalyst Today*

# Correlation of Acoustic Emission Parameters with Surface Roughness in End Milling of AISI 4140 Steel



Nikhil V. Khatekar, Raju S. Pawade, Rishi Pareek,  
and Shivkumar R. Gaikwad

**Abstract** This paper reports correlation of response variables and their effects on machining parameters in end milling of AISI 4140 Steel. In any recent development of precision machining, controlling and monitoring of metal cutting processes is an essential requirement. The recent advancement in intelligent machining industries deals with the effective utilization of cutting tools and different strategies employed to monitor tool condition. During machining, condition monitoring of tool plays an important role to achieve high degree of surface finish. This improves product quality and also helps to minimize machining costs. In this paper, an experimental study is exhibited to examine methodically the acoustic emission (AE) signals for observing and determining the behavior of end milling operation. The logical and scientific results of AE parameters are compared with the roughness parameter  $R_a$ . A surface roughness  $R_a$  value of  $0.517 \mu\text{m}$  is obtained using PVD coated TiAlN carbide insert by end milling of AISI 4140 steel.

**Keywords** AE signals · AISI 4140 steel · PVD · Taguchi orthogonal array ·  $R_a$

## 1 Introduction

Machining comprise is a major part of manufacturing sector. During machining, unwanted material is removed from the workpiece in the form of chips. This utilizes a cutting tool which penetrates into the workpiece imparting good dimensional accuracy and surface finish. A high-speed machine generally serves this purpose [1]. But the tool is subjected to gradual wear and needs to be replaced frequently. This

---

N. V. Khatekar (✉) · S. R. Gaikwad  
PCT's A. P. Shah Institute of Technology, Thane, Maharashtra 400615, India

R. S. Pawade  
Dr. Babasaheb Ambedkar Technological University, Lonere, Maharashtra 402103, India  
e-mail: [rspawade@dbatu.ac.in](mailto:rspawade@dbatu.ac.in)

R. Pareek  
Jaipur Engineering College and Research Centre, Jaipur, Rajasthan 302022, India  
e-mail: [rishipareek.me@jecrc.ac.in](mailto:rishipareek.me@jecrc.ac.in)

increases the product cost and maintenance time due to the premature failure of the tool [2]. The monitoring and controlling of tool condition help to (a) reduce vibrations to the machine tool, (b) prevent damage to the workpiece, (c) improve product quality and reduce machining costs, and (d) predict the problems associated with the tool.

Deshpande et al. [3] studied that surface roughness can be estimated using machining parameters combined with output parameters like cutting force, sound and vibration during turning of Inconel 718. They further applied Artificial Neural Networks (ANN) to predict surface roughness using same set of experimental data for the same material [4]. Experiments were designed using Central Composite Design (CCD) of Response Surface Methodology (RSM) considering three input variables with five levels of each. The variables selected were cutting speed, feed and depth of cut and tungsten carbide uncoated cutting inserts were used for turning operation. Data acquisition (DAQ) was done using piezoelectric dynamometer (Kistler type 9257 B), microphone probe and laser digital vibrometer. It was found that ANN model can be applied favorably to predict surface roughness as compared to multiple regression models.

Lu et al. [5] developed a predicted surface roughness model using RSM in micro-milling of Inconel 718. Imani et al. [6] reported investigation of milling of Inconel 738 using ANN and Genetic Algorithm (GA) to predict and optimize cutting force and surface roughness. The process parameters selected were cutting speed, feed rate, axial depth of cut and coolant considering four levels of two former parameters and two levels of remaining two. It was found that ANN was used successfully to predict cutting force and surface roughness, and GA was utilized favorably to optimize the outputs. Shankar et al. [7] analyzed the prediction of flank wear of tool during keyway milling using Artificial Intelligence (AI) techniques. The workpiece material selected was 7075-T6 Aluminum alloy composite and cutting tool used was three-flute TiN coated cemented carbide with 25 mm diameter. The tool condition was monitored using sound pressure and cutting force and predicted using neural networks. It was reported that ANN model can predict the flank wear of tool with the use of sensors in a precise way.

The spindle power of machine tool was used to predict tool life in milling with neural network technique [8]. It was reported that using ANN, remaining useful life (RUL) of the tool can be predicted precisely.

A backpropagation neural network (BPNN) was applied in micro-milling for spindle vibration to monitor tool wear [9]. A three-axis accelerometer was mounted on a plate attached to the spindle housing to acquire vibration signals during machining. It was found that sharp and blunt micro-tools can be differentiated by vibration of spindle.

Senthil Kumaran et al. [10] developed an experimental setup for online monitoring of single point cutting tool using Acoustic Emission (AE) Technique. The experimental results obtained from AE were used as input to GA. C45 steel of 270 BHN was machined using TiC and TiN coated carbide cutting tool. They studied that AE sensors can be successfully utilized to monitor tool condition.

Sundaram et al. [11] reported the study of flank wear monitoring using AE signals during machining process. The frequency range of acquired signals was from 100 to 2 MHz. A significant effect was observed while monitoring tool condition above 200 kHz.

## 2 Experimental Set up

The three-axis vertical CNC milling machine (HAAS make Model No. TM-2) is used for conducting the experiments. The present investigation is an attempt to methodically examine the AE signals and correlate them with  $R_a$  during machining of AISI 4140 steel. AISI 4140 steel is mainly used to manufacture conveyor parts, axles, crow-bars, gears, spindles, logging parts, shafts, studs, sprockets, pinions, pump shafts, ring gears, rams, etc. From the above review, it has been concluded that monitoring the tool condition is of utmost importance so that its possible failure modes can be diagnosed. The tool has to be replaced before it fails; otherwise, it will affect the product quality. Different sensors were used for monitoring the condition of tool like acoustic emission, force dynamometers, accelerometer, microphone probe and vibrometer. From the above review, an attempt is made with the outcome of comparing the end milling process variables with AE signals obtained from milling of AISI 4140 steel. The workpiece in the form of rectangular slab (120 mm × 100 mm × 18 mm) is selected for end milling operation. The chemical elements of workpiece material are tabulated in the following Table 1.

The cutting tool used is coated carbide end mill cutter of 10 mm diameter, 25 mm cutting length and 75 mm total length consisting of 4 flutes. The coating is of TiAlN by Physical Vapor Deposition (PVD) method. The AE probe is mounted on the workpiece to receive acoustic signals which are measured online and recorded on computer with software. The Mitutoyo SJ-301 stylus type surface roughness tester with resolution 0.01  $\mu\text{m}$  is used for surface roughness measurement (Figs. 1, 2, 3, 4, and 5).

**Table 1** Chemical composition (% by weight) of AISI 4140 steel

Element	Content (%)
Chromium	0.8–1.1
Manganese	0.75–1
Carbon	0.38–0.43
Silicon	0.15–0.3
Molybdenum	0.15–0.25
Sulfur	0.04
Phosphorous	0.035
Iron	Balance





**Fig. 1** AE sensor

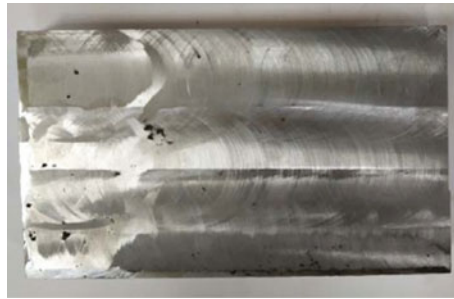


**Fig. 2** AISI 4140 steel workpiece



**Fig. 3** Coated carbide end mill cutter with 4 flutes



Fig. 4 USB AE node

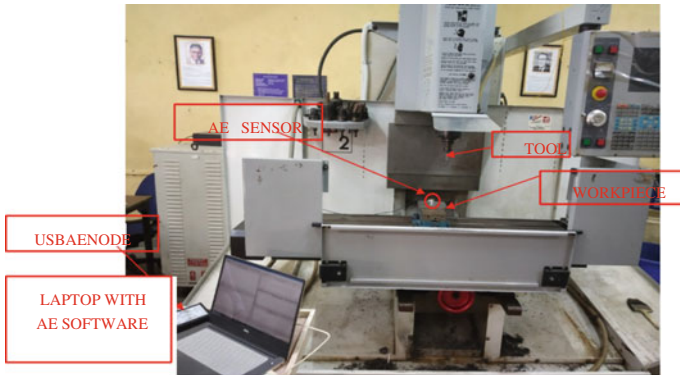


Fig. 5 Schematic of experimental setup

In the present study, experiments based on three levels and three factors using Taguchi L9 Orthogonal Array are designed. The machining parameters such as feed rate, spindle speed and depth of cut are selected as design factors whereas AE parameters like AE absolute energy, AE count, AE RMS and Surface Roughness (Ra) are selected as response variables. The values of machining parameters and surface roughness are shown in Table 2.

### 3 Results and Discussion

The Ra value of surface roughness is measured using SJ 301 Mitutoyo type roughness tester. Table 3 shown below gives the Ra value for each trial according to Taguchi L9 array experimental design.

**Table 2** Taguchi L9 orthogonal array design showing results of surface roughness

L9 orthogonal array						
Experimental run	Control factors					Surface roughness Ra ( $\mu\text{m}$ )
	Spindle speed (rpm)	Cutting speed (m/min)	Feed (mm/tooth)	Feed rate (mm/min)	Depth of Cut (mm)	
1	1019	32	0.03	122.28	0.2	0.853
2	1019	32	0.04	163.04	0.4	0.772
3	1019	32	0.05	203.8	0.6	0.580
4	2038	64	0.03	244.56	0.4	0.517
5	2038	64	0.04	326.08	0.6	0.528
6	2038	64	0.05	407.6	0.2	0.583
7	3057	96	0.03	366.84	0.6	0.530
8	3057	96	0.04	489.12	0.2	0.724
9	3057	96	0.05	611.4	0.4	0.568

**Table 3** Control factors and their levels

Control factors	Spindle speed (rpm)	Feed (mm/tooth)	Depth of cut (mm)
Level 1	1019	0.03	0.2
Level 2	2038	0.04	0.4
Level 3	3057	0.05	0.6

### 3.1 Effect of Machining Parameters on Surface Roughness

Figure 6 shows main effects plot for machining parameters on  $R_a$  value. It can be seen from the main effects plot that  $R_a$  value decreases with increase in cutting speed. The milled workpiece shows lower  $R_a$  value at 64 m/min. But  $R_a$  value increases with further rise in cutting speed. This is because at higher cutting speed, machining vibration increases which ultimately affects the surface finish. Also, increase in feed rate increases the surface roughness. This may be due to the reason that there is a wear at the tip of the flute of cutter initially which affects the surface texture. But further increase in feed may give rise to the built-up edge at the cutting edges of the cutter which again makes the surface smooth to some extent. But increase in depth of cut reduces the surface roughness due to coating provided on the carbide tool tip which reduces the axial thrust. It may be possible that increasing the depth of cut above 0.6 mm can degrade the surface texture as more thickness of the metal will be removed which can increase the wear on the flutes of end mill carbide cutter.

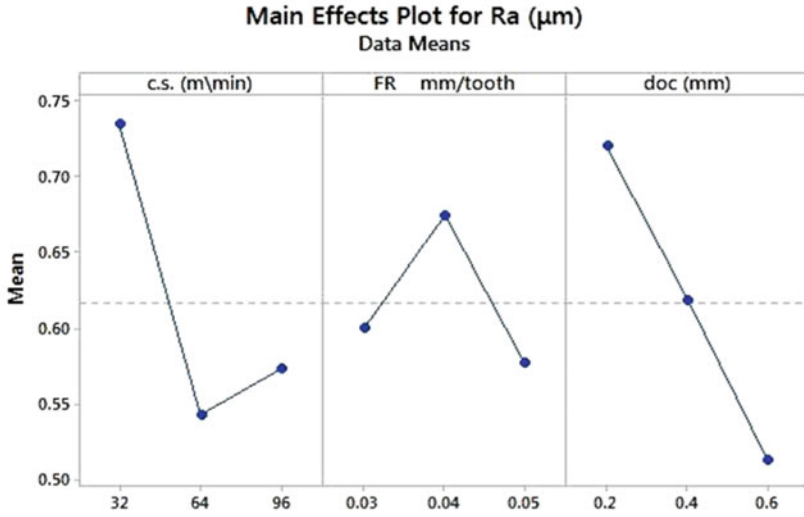


Fig. 6 Main effect plots for surface roughness

### 3.2 Effect of Machining Parameters on AE Characteristics

The number of AE count, AE energy and AE RMS are the parameters of acoustic emission considered for the analysis. Table 4 shows the observed data during the experiments (Fig. 7).

The AE count is a parameter used to record the AE signal. With the increase in cutting speed from 32 to 64 m/min, there is a drastic increase in AE counts which

Table 4 AE characteristics results

Experiment No.	Cutting speed (m/min)	Feed (mm/tooth)	Depth of cut (mm)	AE count	AE Abs energy	AE RMS
1	32	0.03	0.2	5306	3,421,689.5	0.0297
2	32	0.04	0.4	9909.67	5,403,496	0.0544
3	32	0.05	0.6	4059.18	1,721,844	0.0206
4	64	0.03	0.4	11,510.3	89,826,824	0.0941
5	64	0.04	0.6	7719.36	35,585,756	0.0541
6	64	0.05	0.2	10,872.8	36,411,536	0.0595
7	96	0.03	0.6	11,699.1	833,219,328	0.2377
8	96	0.04	0.2	4550.17	77,631,240	0.0731
9	96	0.05	0.4	9245.17	630,584,384	0.3258

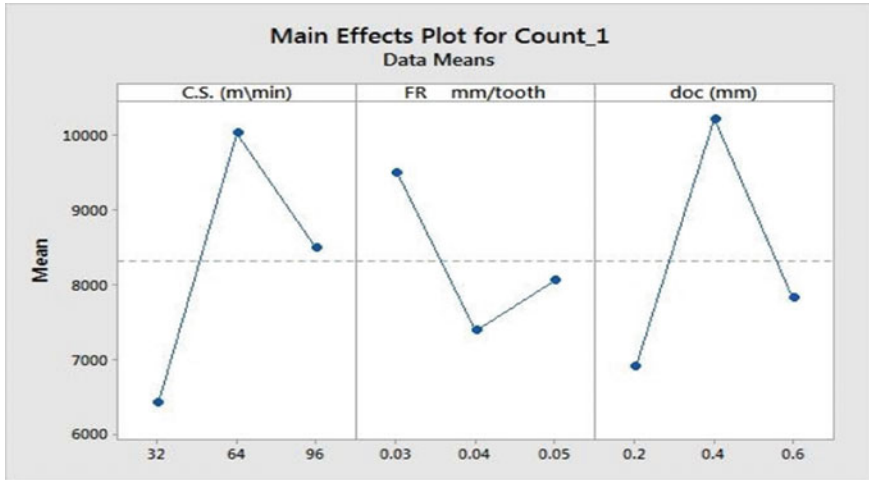


Fig. 7 Main effects plot for AE count

may be due to rapid deformation of the material. However, after 64 m/min there is decrease in AE number of counts by a certain amount. This may be due to less amount of material removed from the workpiece due to hard constituents or impurities and more number of chips gets accumulated near machining area reducing the AE count. As the feed increases from 0.03 to 0.04 mm/tooth, the AE count reduces. But, after that, AE count increases due to rapid deformation of material. From the main effects plot, it can be seen that the number of count increases rapidly when the depth of cut increases from 0.2 to 0.4 mm. This can be due to high volume of deformation of material and due to that greater number of pulses crossing the threshold value increasing the AE count value. After that, as the depth of cut increases the count value starts decreasing (Figs. 8 and 9).

From Fig. 10 it is observed that AE energy released during machining increases for cutting speed ranging from 32 to 96 m/min. The rise in cutting speed tends to deform the workpiece material rapidly due to thermal softening effect. Hence the energy emitted is high with increase in cutting speed. It is also observed that AE energy is reduced by large magnitude with increase in feed from 0.03 to 0.04 mm/tooth. An increase in feed increases the corresponding volume undergoing deformation in the microscopic zone. Thus, the AE energy released due to machining deformation reduces with massive amount of deformation. Therefore, increase in feed causes a drop in AE energy till 0.04 mm/tooth but after 0.04 mm/tooth the AE energy released increases. This may be due to an increase in shear area thereby increasing the release of strain energy during machining. As the depth of cut increases from 0.2 to 0.6 mm, there is rapid increase in amount of AE released. This is because the distortion is extreme at large depth of cut which influence the phenomenon of strain hardening (Fig. 11).

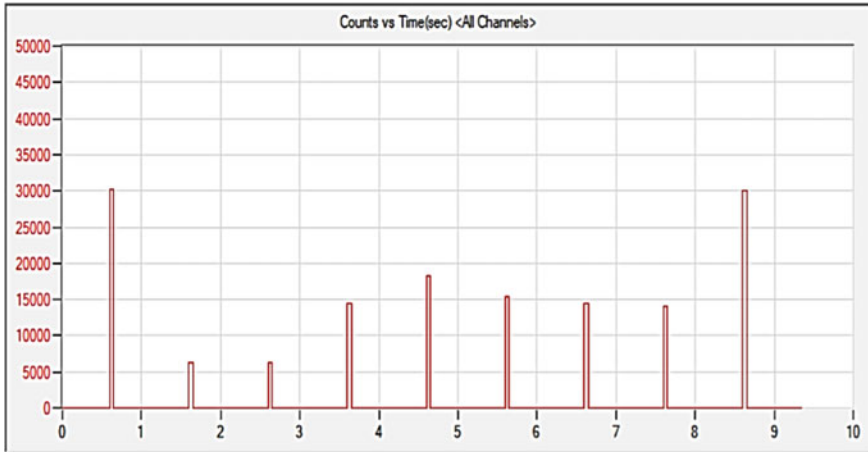


Fig. 8 Actual graph of AE count for experiment run No. 5

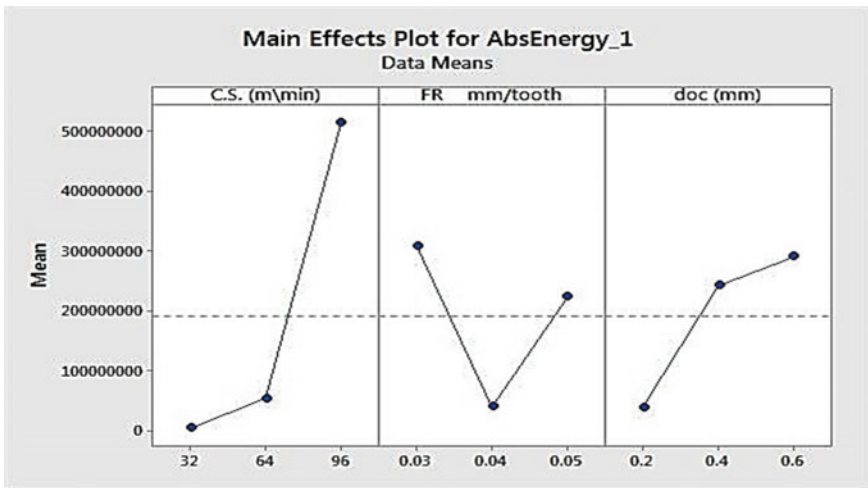


Fig. 9 Main effects plot for AE energy

From Fig. 12 it can be seen that the RMS value is almost proportional to cutting speed, as the cutting speed is increased from 32 to 64 m/min there is small increment in the RMS value but after that RMS value increases drastically, due to enhanced rate of stress development and strain hardening in the workpiece material. Hence, AE RMS has a good sensitivity with cutting speed. Also, it is found from literature that the AE RMS is almost proportionate to the AE Abs energy therefore the plot of cutting speed with AE RMS and AE Abs energy is almost same. It can be seen from the plot that as the feed increases from 0.03 to 0.04 mm/tooth, the RMS value decreases but after 0.04 mm/tooth it starts increasing, which is reverse of the roughness plot with

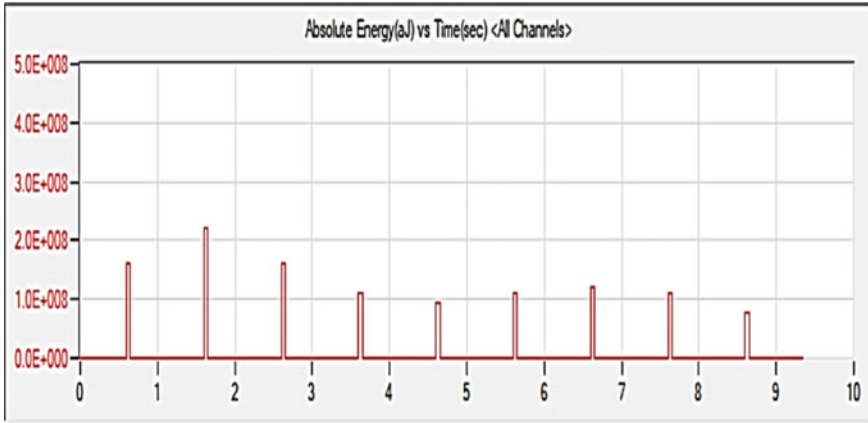


Fig. 10 Actual graph of AE energy for experimental run No. 5

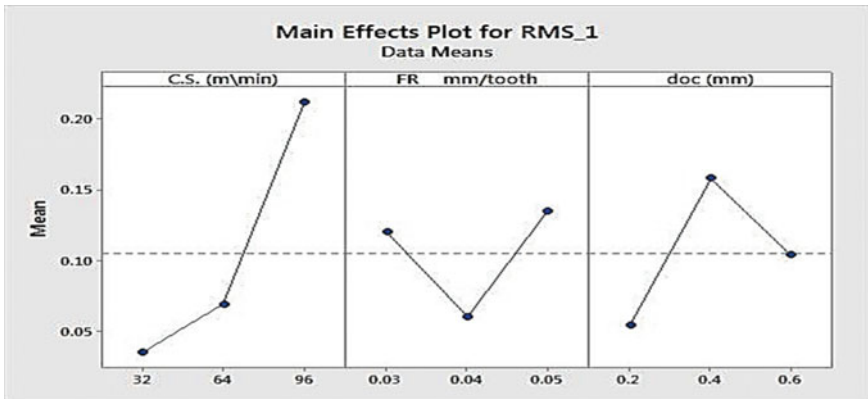


Fig. 11 Main effects plot for AE RMS (voltage)

feed. It is seen from the graph that the RMS values increase with increase in depth of cut from 0.2 to 0.4 mm but after that it starts decreasing.

### 4 Conclusions

The values of minimum surface roughness taken from the main effects plot have been correlated with the AE parameters in the following manner.

- It is concluded that at a cutting speed of 64 m/min, the minimum surface roughness value is 0.543  $\mu\text{m}$  and the value of AE count is 10034, AE Abs energy is 53941372 and for AE RMS is 0.06923.

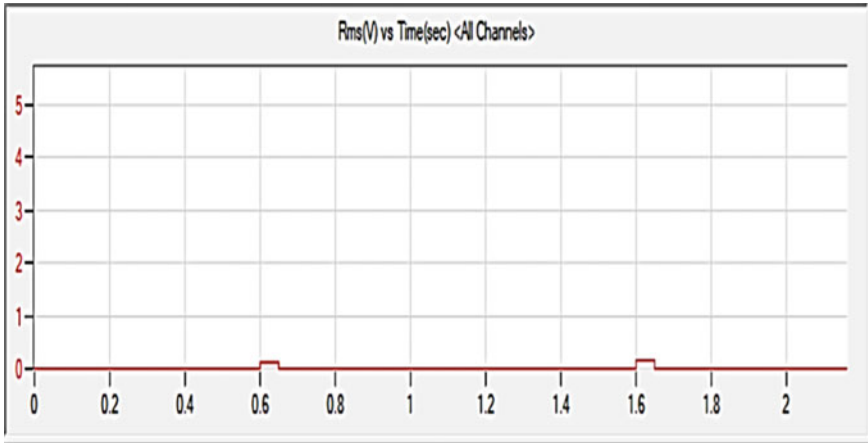


**Fig. 12** Actual graph of AE RMS (voltage) for experimental run No. 5

- At a feed of 0.05 mm/tooth, the minimum surface roughness value is  $0.577 \mu\text{m}$  and the value of AE count, Abs energy, RMS values are 8059, 222,905,921, 0.13530, respectively.
- At a depth of cut of 0.6 mm, the minimum surface roughness value is  $0.517 \mu\text{m}$  and the values of AE count, Abs energy, RMS values are 7826, 290,175,643, 0.10413, respectively.

Thus, it is concluded that surface roughness of machined surface can be monitored online by analyzing AE parameters and the correlation between AE parameters and surface roughness shows that there is significant reduction in surface roughness ( $0.517 \mu\text{m}$ ) with increase in depth of cut.

## References

1. Mohanraj T, Shankar S, Rajasekar R (2020) Tool condition monitoring techniques in milling process—a review. *J Mater Res Technol* 9(1):1032–1042
2. Dimla DE (2000) Sensor signals for tool-wear monitoring in metal cutting operations—a review of methods. *Int J Mach Tools Manuf* 40:1073–1098
3. Deshpande Y, Andhare A, Sahu N (2017) Estimation of surface roughness using cutting parameters, force, sound, and vibration in turning of Inconel 718. *J Braz Soc Mech Sci Eng* 39:5087–5096
4. Deshpande Y, Andhare A, Padole P (2019) Application of ANN to estimate surface roughness using cutting parameters, force, sound and vibration in turning of Inconel 718. *SN Appl Sci* 1:104
5. Lu X, Wang F, Wang X, Lu Y, Si L (2017) A surface roughness prediction model using response surface methodology in micromilling Inconel 718. *Int J Mach Mach Mater* 19(3):230–245
6. Imani L, Henzaki A, Hamzeloo R, Davoodi B (2020) Modeling and optimizing of cutting force and surface roughness in milling process of Inconel 738 using hybrid ANN and GA. *J Eng Manuf* 5:920–932



7. Shankar S, Mohanraj T, Rajasekar R (2019) Prediction of cutting tool wear during milling process using artificial intelligence techniques. *Int J Comput Integr Manuf* 32:174–182
8. Cyril D, Jaydeep K, Chandra N, Anne-Claire J (2016) Tool life predictions in milling using spindle power with the neural network technique. *J Manuf Process* 22:161–168
9. Wan-Hao H, Ming-Chyuan L, Shean-Juinn C (2012) Application of back propagation neural network for spindle vibration-based tool wear monitoring in micro-milling. *Int J Adv Manuf Technol* 61:53–61
10. Senthil Kumaran S, Vetrichelvan G, Sundaram S, Velmurugan P (2014) An investigation of tool wear using acoustic emission and genetic algorithm. *J Vibrat Control* 1–6
11. Sundaram S, Senthil Kumar P, Kumaravel A, Manoharan N (2008) Study of flank wear in single point cutting tool using acoustic emission sensor techniques. *ARNP J Eng Appl Sci* 3:32–36

# A Numerical Study of Free Vibration Behaviour of Shear Deformable Functionally Graded Beam



Maitreya Limkar, Nimitya Phalke, and Kanishk Sharma

**Abstract** A numerical study to analyse the vibration characteristics of the shear deformable graded beam is presented in this paper. The material properties of the beam are assumed to be varied in thickness and/or axial direction in accordance with the power law. The governing differential equations for free vibration analysis of FGM beam are derived using Hamilton's Principle. The finite element formulation is then employed to obtain the numerical solution of derived differential equations. A convergence study is conducted to fix the number of elements for discretization of finite element model of FGM beam. The accuracy of model is verified by comparing the present results with that available in the literature. Parametric studies are conducted to investigate the effect of material properties, boundary conditions and geometrical parameters on the free vibration behaviour of FGM beam. Vibration characteristics of the FGM beam are presented in the form of natural frequencies and corresponding mode shapes. It is found that the vibration response of FGM beam is significantly affected by the material gradation profile.

**Keywords** Vibration · Functionally graded materials · Finite element method · Shear deformable · Mori–Tanaka scheme and power law

## 1 Introduction

In recent years, a new class of composites namely functionally graded materials (FGMs) has gained great attention in many modern engineering applications such as military, aerospace, automotive, biomedical, marine and civil engineering. FGM is advanced class of composites which combines favourable properties of both ceramic and metal by providing smooth and gradual spatial variation of its constituents. Due to its superior properties over composites such as lower transverse shear stresses, high

---

M. Limkar (✉) · N. Phalke · K. Sharma  
JECRC University, Jaipur, Rajasthan, India

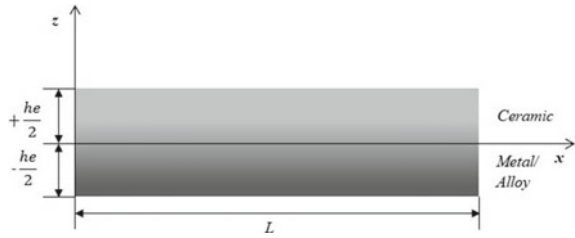
K. Sharma  
e-mail: [kanishk.sharma@jecrcu.edu.in](mailto:kanishk.sharma@jecrcu.edu.in)

resistance to temperature shocks and no interface problems through the layer interfaces, the researchers have extensively examined the static, vibration and buckling responses of these structures.

The literature devoted to predict the structural response of FGMs can be characterized into study of FGM beams, plates and shells. It is also worth to notice that as compared to FGM plate and shell, a smaller number of studies are available on FEM study of continuous FGM beam. The literature on FGM beam can be segregated based on the used beam theories. It is well-known that the classical beam theory, known as Euler–Bernoulli theory, ignores the effects of shear deformation, is oldest beam theory. Studies such as [1–3] investigated the response of FGM beams using classical beam theory. In addition to this researchers [4–11] also used first-order beam theory or Timoshenko theory, which takes shear deformation into account in determining the flexural behaviour. For instance, Aydogdu and Taskin [9] examined the effect of material inhomogeneity on free vibration response of FGM beam using Timoshenko beam theory. The Young's Modulus and density were varied along the thickness of beam while Poisson's ratio was kept constant. Another study by Pradhan and Chakraverty [4] also investigated the effects of constituent volume fractions, slenderness ratios and the beam theories on the natural frequencies on FGM beam. Ziane, Meftah and Belhadj [12] analysed thin and thick functionally graded material box beams under free vibration. Chen, Kitipornchai and Yang [11] investigated the non-linear free vibration behaviour of shear deformable sandwich porous beam by employing Ritz method and von Kármán type non-linear strain–displacement relationships. The effects of porosity coefficient, slenderness ratio was observed in order to improve its vibration behaviour. Sharma [13] developed a generalized beam theory to study the linear-static behaviour of an Aluminium–Zirconia functionally graded beam under thermomechanical loading conditions. Celebi et al. [14] used complementary functions method to convert the problem into initial-value problem for free vibration analysis of FGM beams. Furthermore, functionally graded beams were analysed using shear deformation theories of different orders [5, 11, 15]. Li et al. [16] focused on vibration analysis of a variable thickness beam made of functionally graded materials, which are submerged in water. Babaei et al. [17] examined the effects of large amplitude free vibrations on FGM shallow arches on non-linear elastic foundations.

Present study highlights the effects of various material properties, boundary conditions and geometrical parameters on free vibration behaviour of FGM beam. The primary objective of the present study is to demonstrate an efficient and accurate solution method. Material properties, like Young's Modulus and density, vary in thickness direction according to Mori–Tanaka scheme and power law. Poisson's ratio is kept constant. Hamilton's principle is used to derive the governing differential equations. The numerical solution of the derived differential equations is obtained by employing finite element formulation. Convergence study is conducted and accuracy of model is verified by comparing the results with that in literature. Also, vibration characteristics of the FGM beam are displayed in the form of mode shapes of natural frequencies.

**Fig. 1** Material gradation of FGM beam



**FEM Formulation**

*Material Gradation.* A functionally graded beam with a uniform material distribution on a Cartesian coordinate system is shown in Fig. 1. The beam has a length \$L\$, width \$b\$ and thickness \$h\_e\$. Material properties of the beam are Young’s modulus \$E\$, Poisson’s ratio, shear modulus \$G\$ and mass density \$\rho\$. It is assumed that the effective material properties \$P(z)\$, satisfying all the material properties, vary continuously in the thickness direction (\$z\$) according to the following power law distribution [1, 2]:

$$P(z) = (P_c - P_m)V_c + P_m \tag{1}$$

where \$P\_c\$ and \$P\_m\$ are, respectively, the material properties at the top and bottom surfaces of the FGM beam, \$V\_c\$ is the volume fraction of the top constituent ceramic of the beam defined as:

$$V_c = \left( \frac{z}{h_e} + \frac{1}{2} \right)^n \text{ for } n \geq 0 \tag{2}$$

Following governing equations for shear deformable are obtained using Hamilton’s principle

$$-I_0 \ddot{v} + A_0 v'' + I_1 \ddot{\phi} - A_1 \phi'' = 0 \tag{3}$$

$$-I_0 + A_3 w'' - A_3 \phi' = 0 \tag{4}$$

$$I_1 \ddot{v} - A_1 v'' + A_3 w' - I_2 \ddot{\phi} + A_2 \phi'' - A_3 \phi = 0 \tag{5}$$

wherein \$I\_i\$ (\$i = 0, 1, 2\$) and \$A\_j\$ (\$j = 0, 1, 2, 3\$) are defined as:

$$I_i = \int z^i \rho(z) dA, A_i = \int z^i E(z) dA (i = 0,1,2) A_3 = \int G(z) dA \tag{6}$$

## 2 Convergence Study

A convergence study has been conducted to fix the number of elements in FEA model of FGM beam, and the results of convergence study are presented in Tables 1, 2. For instance, Table 1 shows the variation of the first five natural frequency parameters ( $\lambda = \frac{\omega L^2}{h_e} \sqrt{\frac{\rho_m}{E_m}}$ ) with the corresponding number of elements for FGM beam with simply supported edges (S–S). Similarly, the effect of number of elements on the calculated frequency parameters for functionally graded beam with both edges free (i.e. F–F) is shown in Table 2. It is to be noted that the convergence study is conducted with 20 slenderness ratios (i.e.  $L/h_e = 20$ ) whereas the value of power law exponent is kept unity.

The frequency parameter ( $\lambda$ ) is expressed by normalizing the obtained eigenfrequencies using the following expression:

$$\lambda = \frac{\omega L^2}{h_e} \sqrt{\frac{\rho_m}{E_m}}$$

where

$\omega$  = Natural frequency of beam

$L$  = Length of beam

$h_e$  = Height of beam

$\rho_m$  = Mass Density of metal

**Table 1** Convergence of first five frequency parameters of S–S beam (slenderness ratio = 20; power law exponent = 1)

ndiv	$\lambda_1$	$\lambda_2$	$\lambda_3$	$\lambda_4$	$\lambda_5$
2	1.235	29.661	65.846	231.12	233.03
4	1.156	5.105	10.878	26.915	41.708
8	1.121	4.508	10.255	18.548	26.894
16	1.115	4.414	9.770	17.003	25.918
24	1.113	4.393	9.664	16.678	25.147

**Table 2** Convergence of first five frequency parameters of F–F beam (slenderness ratio = 20; power law exponent = 1)

ndiv	$\lambda_1$	$\lambda_2$	$\lambda_3$	$\lambda_4$	$\lambda_5$
2	11.767	–	–	–	–
4	11.601	32.213	63.909	115.48	378.35
8	6.498	14.540	19.214	24.324	35.440
16	6.456	14.380	19.194	23.832	34.158
24	6.435	14.308	19.184	23.645	33.724

$E_m$  = Young’s Modulus of metal.

By this study, it is found that by increasing the number of discretized elements of either beam, the difference between the consecutive frequencies for any mode decreases considerably. This shows that the results obtained would be of higher accuracy when the number of discretized elements for FG beam is increased. Thus, it can be observed that the difference between frequency parameters becomes minimum as we consider higher values of *ndiv*. Conclusively, the number of discretized elements (*ndiv*) is set as ‘8’ for this complete study.

### 3 Validation Study

To perform the present study, the accuracy of FEM formulation must be validated with the results reported in the relevant literature.

In this section, first five frequency parameters for the free vibration of FGM beam subjected to different sets of boundary conditions are compared. To validate the analysis, results for simply supported (S–S) as well as Fixed (C–C) beam are compared with numerical convergence studies of frequency parameters with the literature published. The results for S–S FGM beam are compared with that reported by Aydogdu and Taskin [9] and presented in Table 3. Table 4 shows the comparison of natural frequencies for C–C FGM beam with Pradhan and Chakraverty [4].

**Table 3** Comparison of natural frequency parameters for S–S Al/Al<sub>2</sub>O<sub>3</sub>FGM beam with Aydogdu and Taskin [9]

Slenderness ratio	Reference of study	<i>n</i> = 0	<i>n</i> = 0.1	<i>n</i> = 1	<i>n</i> = 2	<i>n</i> = ∞
<i>L/h<sub>e</sub></i> = 5	Present study	6.622	6.438	5.095	4.135	2.849
	Aydogdu and Taskin [9]	6.847	6.499	4.821	4.251	2.938
<i>L/h<sub>e</sub></i> = 20	Present study	6.638	6.454	5.107	4.135	2.849
	Aydogdu and Taskin [9]	6.951	6.599	4.907	4.334	2.983

**Table 4** Comparison of natural frequency parameters for F–F Al/Al<sub>2</sub>O<sub>3</sub>FGM beam with Aydogdu and Pradhan and Chakraverty [4]

Slenderness ratio	Reference of study	<i>n</i> = 0	<i>n</i> = 0.1	<i>n</i> = 1	<i>n</i> = 2	<i>n</i> = ∞
<i>L/h<sub>e</sub></i> = 5	Present study	15.048	14.231	13.128	11.579	9.375
	Pradhan and Chakraverty[4]	15.460	14.001	12.450	10.909	9.629
<i>L/h<sub>e</sub></i> = 20	Present study	15.048	14.231	13.128	11.579	9.375
	Pradhan and Chakraverty[4]	15.754	14.268	12.689	11.161	9.864

Material and geometrical parameters for FGM beam are taken from references [9, 10] and mentioned below for ready reference.

$$\begin{aligned} \text{Al} : E_m &= 70 \text{ GPa,} \\ \text{rhom} &= 2702 \text{ kg/m}^3 \\ \text{Al}_2\text{O}_3 : E_c &= 380 \text{ GPa} \\ \text{rhoc} &= 3800 \text{ kg/m}^3 \end{aligned}$$

The Poisson's ratio for both materials is kept constant as 0.3. From Tables 3 and 4, a good agreement between the results of the frequency parameters for different values of the power law exponent can be observed.

## 4 Present Study

In the present study, the first five frequency responses of a functionally graded (FG) beam for three different scenarios are investigated and presented. Functionally graded material of the beam is basically composed of Silicon Carbide at the top of the beam (i.e.  $z = +h/2$ ) and Titanium Aluminide ( $\text{Ti}_{48}\text{Al}_2\text{Cr}_2\text{Nb}$ ) at the bottom of the beam (i.e.  $z = -h/2$ ) with the following properties varying or as per the power law through the thickness of the beam.

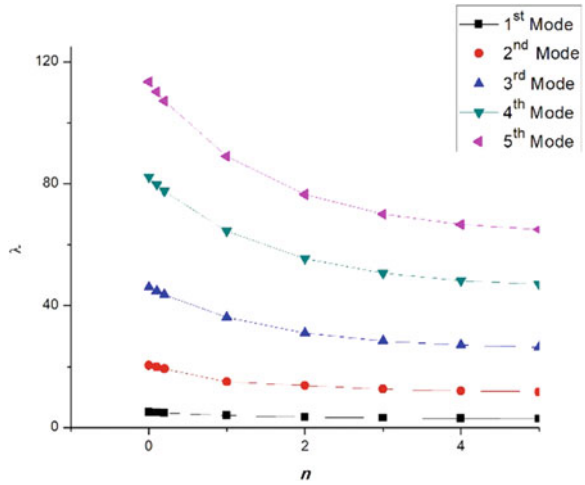
$$\begin{aligned} \text{Silicon Carbide} : E_c &= 410 \text{ GPa} \\ \rho_c &= 3100 \text{ kg/m}^3 \\ \text{Titanium Aluminide} : E_m &= 160 \text{ GPa} \\ \rho_m &= 3600 \text{ kg/m}^3 \end{aligned}$$

For the first study, the behaviour of frequency parameters against various values of power law exponent is observed as shown in Table 5. The value of  $L/h_e$  is set as 20 and boundary condition taken as simply supported. It can be clearly seen that the natural frequency of the FG beam for irrespective of mode shapes decreases with the

**Table 5** Effect of material inhomogeneity on the first five natural frequencies parameters for a TiAl/SiC S-S FG beam with slenderness ratio = 20

Mode	$n = 0$	$n = 0.1$	$n = 0.2$	$n = 1$	$n = 5$	$n = 10$	$n = \infty$
$\lambda_1$	5.115	4.967	4.829	4.013	2.927	2.851	2.849
$\lambda_2$	20.467	19.874	19.323	15.059	11.711	11.409	11.399
$\lambda_3$	46.099	44.762	43.521	36.171	26.378	25.697	25.674
$\lambda_4$	82.171	79.790	77.577	64.476	47.020	45.805	45.765
$\lambda_5$	113.540	110.249	107.191	89.089	64.970	63.290	63.236

**Fig. 2** Variation of frequency parameters for different power law exponents



increase in the value of  $n$ . This behaviour has been portrayed by a 1-D plot graph as shown in Fig. 2.

For the second study, the behaviour of frequency parameters for four different boundary conditions is examined as shown in Table 6. Similar to the previous condition, the value of  $L/h_e$  is set as 20 and the value of power law exponent  $n$  is 1. Out of all four boundary conditions, the value of normalized frequency of C–C beam for any mode shapes is the largest.

For the third study, the behaviour of frequency parameters for different values of slenderness ratio is examined as shown in Table 7. By keeping power law exponent as  $n = 1$  and boundary condition as simply supported beam, the eigen frequencies ( $f$ ) and respective dimensionless frequency parameters ( $\lambda$ ) are evaluated for variable slenderness ratios. Values of eigenfrequencies vary considerably for this part of study.

**Table 6** Effect of boundary conditions on the first five natural frequency parameters of TiAl/SiC FG beam (slenderness ratio = 20; power law exponent = 1)

Frequency parameters	Boundary conditions			
	S–S	C–C	C–F	C–S
$\lambda_1$	4.013	9.099	1.429	6.270
$\lambda_2$	15.059	25.097	8.961	20.328
$\lambda_3$	36.171	49.287	25.107	42.471
$\lambda_4$	64.476	81.789	44.331	72.864
$\lambda_5$	89.089	89.089	49.280	89.089



**Table 7** Effect of slenderness ratio on the first five natural frequency/frequency parameters of TiAl/SiC S-S FG beam WITH power law exponent = 1

Slenderness Ratio	Frequency parameters									
	$\lambda_1$	$f_1$ (Hz)	$\lambda_2$	$f_2$ (Hz)	$\lambda_3$	$f_3$ (Hz)	$\lambda_4$	$f_4$ (Hz)	$\lambda_5$	$f_5$ (Hz)
5	4.0139	818.379	16.059	3274.314	22.272	4540.933	36.171	7374.771	45.404	9257.124
10	4.0140	409.189	16.0599	1637.157	36.1718	3687.385	44.544	4540.933	64.476	6572.769
20	4.0140	204.594	16.0599	818.578	36.1718	1843.692	64.476	3286.384	89.089	4540.933
40	4.0140	102.297	16.0599	409.289	36.1718	921.846	64.476	1643.192	101.278	2581.103
50	4.0139	81.837	16.0599	327.431	36.1718	737.477	64.476	1314.553	101.278	2064.882

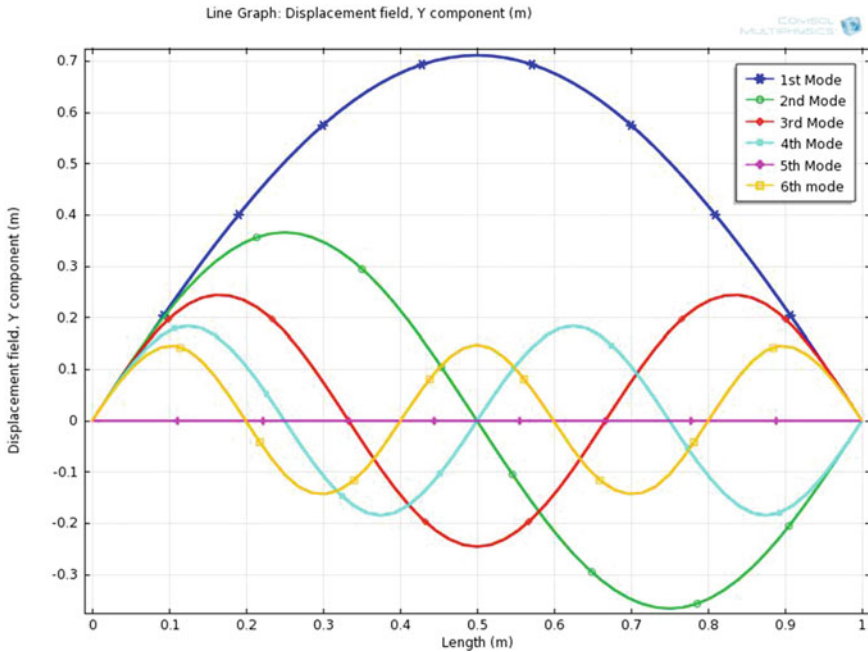


Fig. 3 Variation of displacements for first five-mode shapes

### 5 Conclusion

A finite element formulation for free vibration analysis of FGM beam is carried out in the present study. The accuracy of model is verified by comparing the present results with that available in the literature and various numerical studies are conducted to investigate the effect of material properties, boundary conditions and geometrical parameters on the free vibration behaviour of FGM beam. Based on the present study, following important conclusions can be drawn:

- The behaviour observed in the first study showed the variation in the frequency parameter  $\lambda$  with respect to the power law exponent  $n$  for our parametric considerations. It is observed that with the increase in  $n$ , a subsequent decrease in  $\lambda$  is depicted. We can thus imply that when the volumetric fraction starts leaning more towards metal, then the corresponding natural frequency for the FG beam also increases.
- It is found that out of four boundary conditions the highest natural frequency was attained by the C–C beam whereas the lowest natural frequency was attained by the C–F beam. This indicates that for lowest probability of resonance condition, an FG beam with highest possible natural frequency for any mode should be used, i.e. the C–C FG beam.

- It is observed that the values of eigenfrequency for respective mode shapes were decreasing with increase in  $L/h_e$  ratio. This proves that a thin or slender beam has lower natural frequency compared to that of a thick or rigid beam and more susceptible towards failure.

## References

1. Kvaternik S, Filippi M, Lanc D, Turkalj G, Carrera E (2019) Comparison of classical and refined beam models applied on isotropic and FG thin-walled beams in nonlinear buckling response. *Compos Struct* 229(September):111490
2. Lee JW, Lee JY (2017) Free vibration analysis of functionally graded Bernoulli-Euler beams using an exact transfer matrix expression. *Int J Mech Sci* 122(December 2016):1–17
3. Li SR, Batra RC (2013) Relations between buckling loads of functionally graded timoshenko and homogeneous euler-bernoulli beams. *Compos Struct* 95:5–9
4. Pradhan KK, Chakraverty S (2013) Composites: part B Free vibration of Euler and Timoshenko functionally graded beams by Rayleigh—Ritz method. *Compos PART B* 51:175–184
5. Xie K, Wang Y, Fan X, Fu T (2019) Nonlinear free vibration analysis of functionally graded beams by using different shear deformation theories. *Appl Math Model*
6. Li X (2008) Article in press a unified approach for analyzing static and dynamic behaviors of functionally graded Timoshenko and Euler—Bernoulli beams. 318:1210–1229
7. Ng N (2001) On shear deformable beam theories: the frequency and normal mode equations of the 242:215–245
8. Zohra ZF, Lemya HHA, Abderahman Y, Mustapha M (2017) A publication of IIETA free vibration analysis of functionally graded beams using a higher-order shear deformation theory 4(1):7–12
9. Aydogdu M, Taskin V (2007) Materials and design free vibration analysis of functionally graded beams with simply supported edges 28:1651–1656
10. Wattanasakulpong N, Mao Q (2014) Dynamic response of Timoshenko functionally graded beams with classical and non-classical boundary conditions using Chebyshev collocation method. *Compos Struct* 119:346–354
11. Chen, D., Kitipornchai, S., & Yang, J. (2016). Thin-Walled Structures Nonlinear free vibration of shear deformable sandwich beam with a functionally graded porous core. *Thin-Walled Structures*, 107, 39–48
12. Ziane N, Meftah SA, Belhadj HA, Tounsi A, Bedia EAA (2013) Free vibration analysis of thin and thick-walled FGM box beams. *Int J Mech Sci* 66:273–282
13. Sharma K (2016) Thermal and mechanical analysis of FGM beam using generalized thermal and mechanical analysis of FGM beam using
14. Celebi K, Yarimpabuc D, Tutuncu N (2017) Free vibration analysis of functionally graded beams using. *Arch Appl Mech*
15. Karamanli A (2018) Free vibration analysis of two directional functionally graded beams using a third order shear deformation theory. *Compos Struct* 189(January):127–136
16. Li H, Ke L, Yang J, Kitipornchai S, Wang Y (2019) Free vibration of variable thickness FGM beam submerged in. *Compos Struct* 111582
17. Babaei H, Kiani Y, Eslami MR (2019) Large amplitude free vibration analysis of shear deformable FGM shallow arches on nonlinear elastic foundation. *Thin-Walled Struct* 144(June):106237

# Controlling of Manipulator for Performing Advance Metal Welding



Aditi Saxena, Jitendra Kumar, Kamal Sharma, and Debanik Roy

**Abstract** The regulation of a mechanical manipulator device is a critical step for a simpler and accurate method of welding. In order to ensure accurate metal arc welds, the direction and pace of the deceiver should also be monitored using only a measurement control device using welding parameters such as temperature, swelling speed, and the friction that happens in the gripper, since the number of connections increases their difficulty. This research is performed with assistance of SIMULINK to monitor two-link solid robotic manipulator systems. A mathematical model was developed that serves as an interface and then a Fuzzy-PID regulator is attached whose output acts as a reference into the system. The deceiver has a complex behavioral model. The controlling machine has been further improved using genetic algorithm by simulation results it is found that the Fuzzy PID does have the lowest error value in comparison to the Fuzzy PI, Fuzzy PD, and PID controllers.

**Keywords** Controlling · Robotic welding · Welding parameters · Fuzzy-PID controller · Genetic algorithm · Integral absolute error

## 1 Introduction

Generally, welding may be characterized as a localized coalescent of metals or non-metals (normally known as welding parts) that are mostly heated to a correct depth, pressurized, or pressurizing with or without the use of extra filling metals. The methods of welding are very relevant only for a few applications [1]. Arc welding is among the most common; (i) arc welding refers to a wide variety of welding techniques, using an electrical circuit to combine and merge heat. It is thought to be the largest single community of processes after assembly and machining in the metal manufacturing sector in the global metal manufacturing industry. The very first method of welding from historical standpoint was welding through forge where the slurry is heated and then marked to remove slacken and oxides [2] (Fig. 1).

---

A. Saxena (✉) · J. Kumar · K. Sharma · D. Roy  
IET Department of Electronics and Communication Engineering, GLA University, Mathura  
281406, India

**Fig. 1** Various welding methods

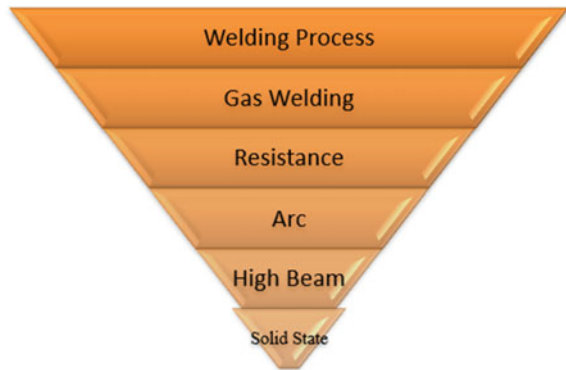


**Fig. 2** Three-link manipulator diagrams



Another option is fusion welding, in which the heat input must be strong enough to dynamically dissolve the dual weld pieces. In this type of welding voltage should be low and current should be high. Developed energy sources can also display data with a variety of output waveform, which can be modified in actual environments based on the input signals. In case of arc soldation management, photographs of the arc, soldering tank, bottom body or ground needle or sold readiness could be necessary where system input is needed. Arc length analysis and electrode adhesive may also provide valuable method detail. Different processing parameters and disruptions also influence arc intensity. In the sensory portion of the electromagnetic range, the sold tank also absorbs radiation. As the strength of the arc itself is much smaller, it is being used to measure the efficiency of the bolt, so it could be found that a substantial deal of potential research opportunities in the field of welding control was also available, especially a visual information control system, since the technical materials are becoming cheaper. In this paper, an application of control system has been displayed that how precisely one can perform welding with the help of control system for this process two-link manipulators system have been used [3] (Fig. 2).

## 2 Controller Structure Designing Through Simulink

Different controllers designed is being shown and discussed here optimization technique that is genetic algorithm is also being introduced and explained here.

**Fig. 3** PID controller diagram



### 2.1 PID Controller Design

On the dynamics of robotic manipulator having two links the structure with a reference wave, a sine wave is being given to check whether the output is tracked with the reference wave or not. Here the gains are being manually tuned so self-tuning is being performed here [4, 5] (Fig. 3).

PID controller is being applied at the input of the plant two PID controllers are being used, respectively, one for first link of the manipulator arm and other for the second link of the manipulator plant. Theta 1 here represents the output of link 1 and out 2 represents the output of link 2. Scope will help to display the result in form of graph.

### 2.2 Optimized PID Controller Design

In this design, we have optimized the controller using Genetic Algorithm (GA). This algorithm is more suitable in comparison to the other existing algorithms. The main purpose of this algorithm is to reduce the value of error as low as possible that integrates the absolute error without adding any sort of weight to the error. In the figure, we can see that the input of PID controllers 1 and 2, respectively, is being connected with Integral Absolute Error. The absolute block is being attached with an integrator this combination gives IAE(Integral Absolute Error) in output. After this genetic Algorithm is being applied for optimization and an optimized result will be obtained [6, 7] (Fig. 4).

**Fig. 4** PID diagram



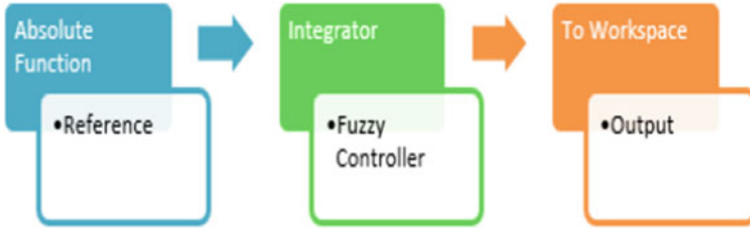


Fig. 5 PD controller structure

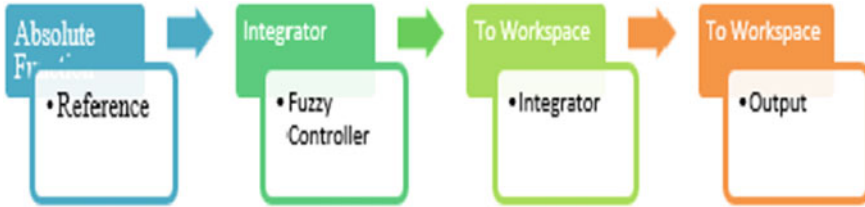


Fig. 6 Fuzzy PI diagram

### 2.3 Fuzzy PD Structure

There are some input and output value in a fuzzy set which are being mapped with the help of membership function. Fuzzy logic controller intakes a value from 0 to 1 as low as possible and can easily deal with non-linearities. A simple PD controller is being attached with fuzzy logic. PD control and IAE are being used here as an objective function for GA optimization [8] (Fig. 5).

### 2.4 Fuzzy PI Control Interface Structured Design

In this design, an integrator has been used that leads to Fuzzy PI control [9], that is then linked with the Fuzzy Logic System and IAE as an objective function (Fig. 6).

### 2.5 PID Fuzzy Control Interface Structured Design

In Input a reference wave is there than a PID controller is being joined consecutively a fuzzy logic controller is being attached with integrator and above all the steps genetic algorithm has been used in all the stages [10] (Fig. 7).



Fig. 7 Optimized Fuzzy-PID controller model diagram

### 3 Results and Discussion

#### 3.1 Fuzzy-PID Structure

In PID controller plant result the figure here represents the perfect tracking of the sine wave which we have given as a reference wave, sine wave is being perfectly tracked by the output of the manipulator [11] arm for the two links so we can say that by applying PID controller the output is able to track the input for welding purpose also Precise tracking is required in order to perform welding at the correct position. Here we can do self-tuning by adjusting the value of the gains (Table 1).

0.04438 the dynamic model description of this plant is being discussed above because of PD controller the stability increased, Maximum Peak Overshoot decreased, settling time decreased but at the same time its disadvantage is that it cannot be used for fast moving process variable like flow, pressure and hence this controller is not fit for [12] advance welding purpose. In fuzzy PI controller error value 0,411,467 PI controller is the most popular controller; it has two tuning parameters to adjust integral action PI controller provides a balance of complexity and capability but it has sluggish response to sudden disturbances and cannot lead to give precise result in advance welding. In Fuzzy PID, after GA optimization is 0.0399573 this is the least value of error that we have obtained so far. Fuzzy controllers are less costly they cover a wide range of operating condition PID controller has fast warm up time accurate set point temperature control which is necessary to keep in mind during welding with the help of this controller we can perform precise welding genetic algorithm (GA) [13, 14]. Genetic Algorithm consist of various steps like Population, Selection, Reproduction, Mutation, Crossover, Stopping criteria, etc.

**Table 1** Controllers error value

Controllers	IAE values
PID without optimization	0.2218
PID using GA	0.0429
Fuzzy PD using GA	0.04438
Fuzzy PI using GA	0.04114
Fuzzy PID using GA	0.03995



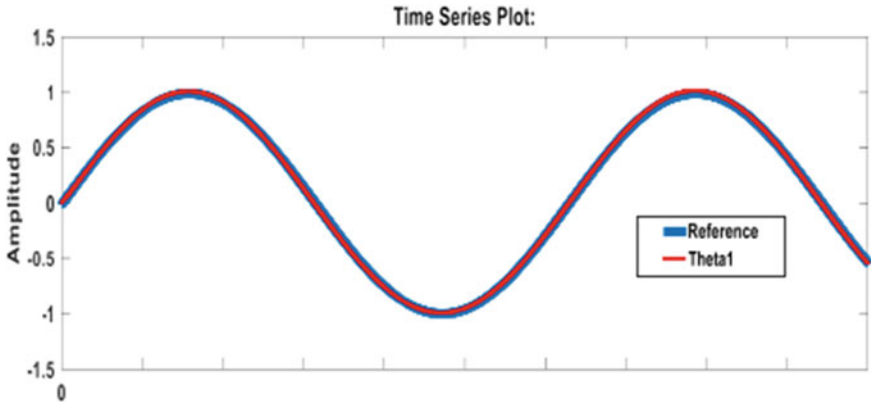


Fig. 8 Model plant results after simulation showing tracking

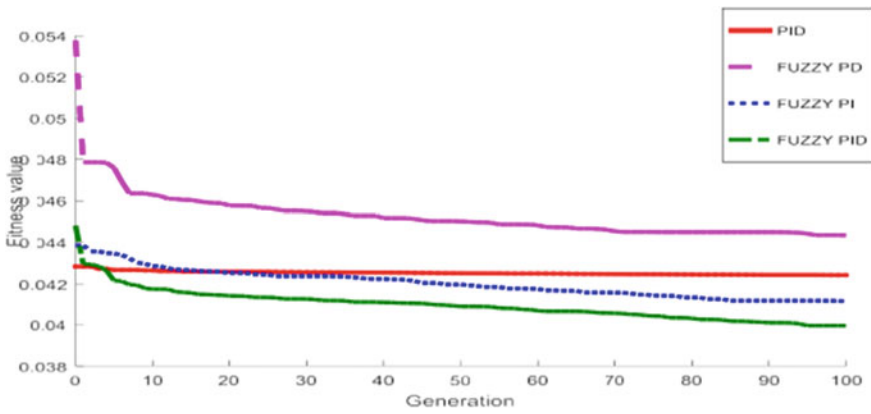


Fig. 9 Different fitness value of controller

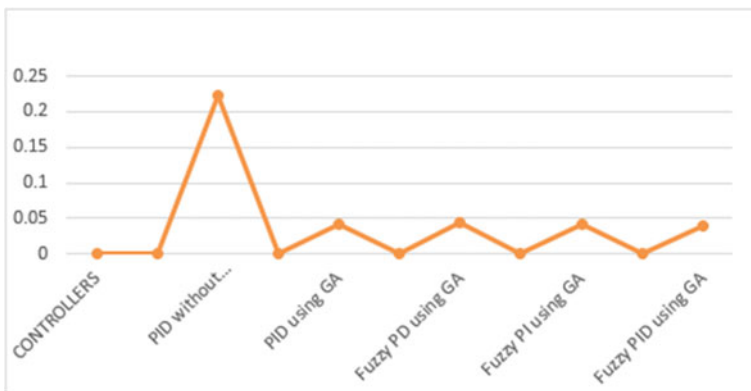


Fig. 10 Graph representing comparison of all the three controllers

[15]. The figure drawn above shows the best fitness value of the various controllers after optimization and as a result found that least value of error is 0.03995. Which means tracking is almost perfect and error rate is even below 1%.

## 4 Conclusion

The stimulated result of a simple PID controller is seen here. We are able to get perfect monitoring of the reference and actual paths, which can assist us in doing precise welding in the correct position. A controller is being developed to manage all non-linearities and overcoming the vibration that occurs at the end effect or during the welding process. It has the properties of providing a short rise time and low overshoot, which helps to do accurate arc welding. This proposed optimized dynamic Fuzzy-PID model can be used to position the robot arm in the pre-defined path and perfect tracking of the path could be done this controller has a potential application in manipulator control for various purposes like arc welding, casting, to bear a payload and further many more.

## References

1. Prajapati VK et al (2020) Experimental studies of regulated metal deposition (RMD™) on ASTM A387 (11) steel: study of parametric influence and welding performance optimization. *J. Brazilian Soc Mech Sci Eng* 42(1):1–21
2. Yu Y et al (2020) Femtosecond laser-induced non-thermal welding for a single Cu nanowire glucose sensor. *Nanoscale Adv* 2(3):1195–1205
3. Toai TT, Duc-Hoang C, Chu AM (2021) Development of a new 6 DOFs welding robotic system for a specialized application. *Further Adv Internet Things Biomed Cyber Phys Syst* 193:135
4. Madesh R et al (2020) Performance characteristics of GMAW process parameters of multi-bead overlap weld claddings. *IOP conference series: materials science and engineering*, vol 988. No. 1. IOP Publishing
5. Mwema FM, Esther TA (2020) Metal-arc welding technologies for additive manufacturing of metals and composites. *Addit Manuf Appl Metals Compos*. IGI Global, 94–105
6. Chaturvedi R et al (2020) Design and analysis of mechanical gripper of aristo-robot for welding
7. Yang S et al (2020) Electrospayed polyamide nanofiltration membrane with intercalated structure for controllable structure manipulation and enhanced separation performance. *J Membr Sci* 602:117971
8. Kafi A, Tünde AK (2020) Arc sensor parameter optimisation for robot welding. *Vehicle and automotive engineering*. Springer, Singapore
9. Vasilev M et al (2021) Feed forward control of welding process parameters through on-line ultrasonic thickness measurement. *J Manuf Process* 64:576–584
10. Fominykh D et al (2020) The task of controlling robotic technological complexes of arc welding in unstable states. In: *International scientific and practical conference in control engineering and decision making*. Springer, Cham
11. Kumar V, Bera TK (2021) Performance of automated machine for different profiles in two-dimensional welding. *Mater Manuf Processes* 36(4):435–447

12. Chkalov RV, Chkalova DG (2020) Laser powder cladding complex: principles of advanced automated control. In: IOP conference series: materials science and engineering, vol 969, No 1. IOP Publishing
13. Vasilev M et al (2021) Non-contact in-process ultrasonic screening of thin fusion welded joints. *J Manuf Process* 64:445–454
14. Alzarok H, Fletcher S, Mian NS (2020) Review for the current performances for machine visions in industrial robotic welding and drilling tasks. *IOSR J Electr Electron Eng* 15.3(1):53–61
15. Balzan A, Aparicio CC, Trabucco D (2020) Robotics in construction: state-of-art of on-site advanced devices. *Int J High-Rise Buil* 9(1):95–104

# An EEG Based Approach for the Detection of Mental Stress Level: An Application of BCI



Prerna Singh, Rajesh Singla, and Anshika Kesari

**Abstract** This paper aims toward detection of pattern in brain waves that are elicited in response to mental stress. For stress level detection, an algorithm based on Electroencephalogram (EEG) has been put forward. To validate the impact of the proposed stress level recognition algorithm, an experimental investigation has been carried out on different subjects. Stroop color-word test, designed on LabVIEW platform, and arithmetic puzzle test (that can be solved mentally) are the two effective stressor that have been utilized to produce different levels of mental stress. The induced stress signals are preprocessed using a software in an eego™ sports ANTNeuro System using 32 electrodes Waveguard™ EEG cap. The Hjorth parameters and various statistical features have been classified using Support Vector Machine (SVM). Additionally, by utilizing the ratio of absolute alpha and beta power along with the other power band features extracted from EEG signals, a mean accuracy of 76.04% is achieved for three-level stress. Moreover, for the analysis of two levels of stress, an average accuracy of 87.5% and 90.625% is obtained by Stroop color-word test and mental arithmetic test, respectively.

**Keywords** EEG · Stress recognition · Stressor · SVM

## 1 Introduction

Stress is basically a human body reaction in return to an audio or visual stimulus resulting in the disturbance of the physical and mental equilibrium which is typically caused by inability to adapt to sudden mental, physical, or emotional challenges/stressors [1]. Positive stress referred as eustress keeps an individual alert for any dangerous or peculiar situation. Distress or simply negative stress exists when

---

P. Singh (✉) · R. Singla · A. Kesari

Department of Instrumentation and Control Engineering, Dr. B. R. Ambedkar National Institute of Technology Jalandhar, Punjab 144011, India

R. Singla

e-mail: [singlar@nitj.ac.in](mailto:singlar@nitj.ac.in)

continuous challenges are faced without any duration of relief or relaxation. Moreover, in the context of health, stress results in several complications as reported in the research work [2].

Based on questionnaire, several techniques have been developed for stress measurement which comprises of Cohens' Perceived Stress Scale (PSS), Hamilton Depression Rating Scale (HDRS), and Stress Response Inventory (SRI). Additionally, by measuring the changes in the physiological signals such as ECG (Electrocardiography) and EEG signal, Plethysmography, Galvanic skin response (GSR), and thermal body condition (temperature of the skin), stress condition can be recognized easily [1]. Among various physiological signals, the research works have mainly focused on EEG based stress recognition [1]. Many techniques can be employed for inducing different levels of stress in laboratory environment as comprehensively reviewed in the research work [3]. Some of these techniques include Stroop color-word test (SCWT) [4], the Trier Social Stress Test (TSST) [5], the cold press or test [6], and the arithmetic puzzle test (solved mentally) [7].

In general, SCWT is employed as a neuropsychological stressor where a list of color words are displayed to the subjects and the color may or may not match with the word being displayed. SCWT has shown its efficiency for human psychophysiological reactivity under stressful circumstances [1].

In addition, for inducing different levels of stress, we can use arithmetic mind tasks, mental puzzles, and various IQ questions; for instance, different stress states can be elicited in an individual by using arithmetic questions of varying difficulty levels [8]. Based on the above discussion, both Stroop color-word test and mental arithmetic test have been utilized for evoking varied stress levels among subjects.

The rest of this paper is organized as under. Section 2 gives a brief description about some of the research works related to comprehensive description on stress experiments along with the classical algorithms of stress recognition based on EEG. After that, the experimental environment along with the proposed stress recognition algorithm based on EEG have been discussed in Sect. 3. The methodology of data acquisition along with signal processing and classification have been discussed in Sect. 4. The result analysis of the EEG data collected from different subjects is carried out in Sect. 5. At last, Sect. 6 provides the conclusions of the present investigation.

## 2 Related Work on Stress and EEG

### 2.1 Literature Survey

In this research work [9], mental stress level of the subject was classified by using the features extracted from EEG data using the Higuchi's fractal dimension, Magnitude Square Coherence Estimation (MSCE), and Gaussian mixtures during an examination of the university. It was concluded that the features that were extracted by MSCE resulted an accuracy above 90% in the classification of individuals among stressed

and non-stressed groups. Moreover, for classifying the different levels of stress like four-level, three-level, and two-level stresses, accuracies of 67.06%, 75.22%, and 85.71% have been reported, respectively [7]. For inducing varied stress levels among individuals, a confined use of SCWT as a stressor has been demonstrated, and for classification purpose different features like fractal dimension, power feature, and statistical features are used [10]. Not only this, a mental stress level detection with respective accuracies of 85% and 80% at two and three levels of difficulty in arithmetic tasks has been depicted in the research work [8]. A combination of extremely complex features to obtain the classification results of stress level has been shown in [7, 9]. The sole purpose of the present study is the interpretation and classification of various mental stress levels from EEG signals using numerous modes of stress.

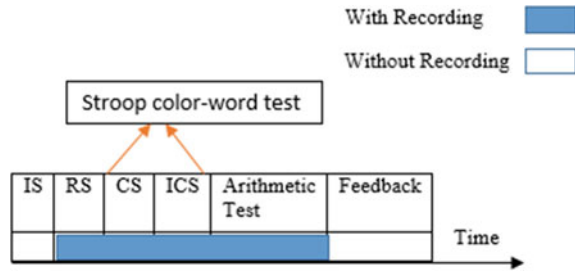
## 2.2 EEG Based Stress Recognition Algorithms

Recognition of human emotions, mental workload, vigilance, etc., have been reported in the literature work [11]. This also helps in the identification of human stress level due to a strong correlation among power in the EEG signal and various levels of psychological stress. For example, an experimental investigation shows the positive correlation of stress with power in the beta band of EEG signal at anterior temporal lobe [12]. The features of power spectrum are frequently employed in the stress recognition using EEG signals [9]. Some features including Gaussian mixtures of EEG spectrogram, fractal dimension, and MSCE have been utilized in stress recognition [9]. Two classifiers, namely SVM and k-NN, have shown the best accuracy of 90% in classification of mental stress of two levels. For evoking different stress states, pictures have been utilized in the research work [13]. Features for logistic regression include signal power from various frequency bands of recorded EEG signals which are classified using k-NN to yield a 73.96% accuracy in the classification of relaxed and stressed states.

## 3 Experimental Procedure

In the present investigation, EEG data from many subjects (without any mental disease and head injury) between the age group of 21–26 years from Dr. B. R. Ambedkar National Institute of Technology Jalandhar (India) were collected. In order to prevent artifacts, during the process of data acquisition while conducting the experiment, subjects were instructed to avoid any movement of head or muscles. Based on the international 10–20 system, an ANTNeuro kit along with 32 electrode Waveguard™ EEG cap had been employed for recording the EEG signals from 17 different channels (AF3, F3, F7, FC5, T7, P4, P7, Pz, P8, O1, O2, T8, FC6, F4, F8, AF4, and CPz as reference) and placed on the scalp. The recorded EEG signals were sampled at 512 Hz within a bandwidth of 0.3–30 Hz. In the present analysis, a Stroop

**Fig. 1** Protocol for collection of EEG data while recording



color-word test on LabVIEW platform has been utilized as the stressor for inducing various stress levels. The protocol for the collection of EEG data has been shown in Fig. 1. The overall experiment based on the Stroop color-word test involves four sections as discussed below.

- **Introductory Section (IS):** This deals with instructing the subjects about the experimental environment where the experimental procedure is explained and the color chart is shown along with the instructions for conducting the test.
- **Resting Section (RS):** This deals with allowing the subjects to remain un-stressed without any movement and with their eyes kept open for a duration of about 2 min. This is done to ensure that the subjects are in the most relaxed state.
- **Congruent Section (CS):** This deals with inducing a state of stress of comparatively lower level using a simple task where the font color of the word exactly matches with the its meaning. Here, the task involves recognition of the font color of words by the subjects.
- **Incongruent Section (ICS):** This deals with inducing a state of high stress which involves dissimilarity in the font color of the words and their meanings. This involves the task of responding to the font color of the words by each subject. It is expected that the subjects are more stressed than in CS.

In this experiment, subject has to go through the Stroop color-word test for 2 min which comprises of both the section CS and ICS as shown in Fig. 2. In addition to the Stroop color-word test, the level of stress using simple arithmetic puzzles is also measured so as to differentiate between three levels of stress i.e., No Stress during RS, Low Stress during arithmetic Puzzles, and High stress during Stroop color-word test. Again, the subject has to solve 6 arithmetic puzzles within a time span of 2 min. Figure 3 shows the schematic diagram of the stimulus designed using two different stressors.

An example of the arithmetic puzzles used in this investigation has been shown in Fig. 4. So, basically the whole experimental procedure is done within a time span of 6–7 min. Each section lasts for 2 min; however, recording of EEG signals is done over the entire duration of experimental analysis. Figure 5 simply depicts the experimental setup used during the experiment. All the subjects are assigned the task of rating their stress levels at the end of each section using a feedback form on the scale of 1–3 where 1 represents no stress, 2 represents low stress, and 3 represents High stress condition.

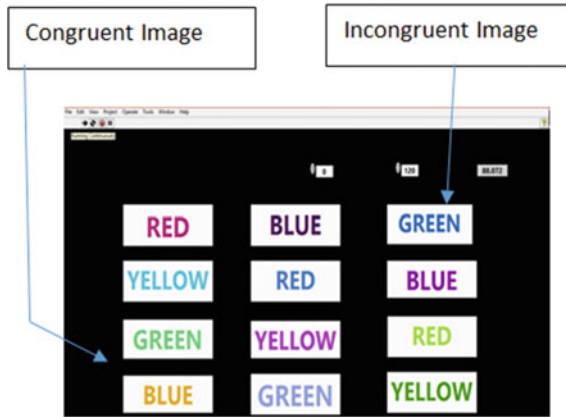


Fig. 2 Picture displaying Stroop color—word test using LabVIEW

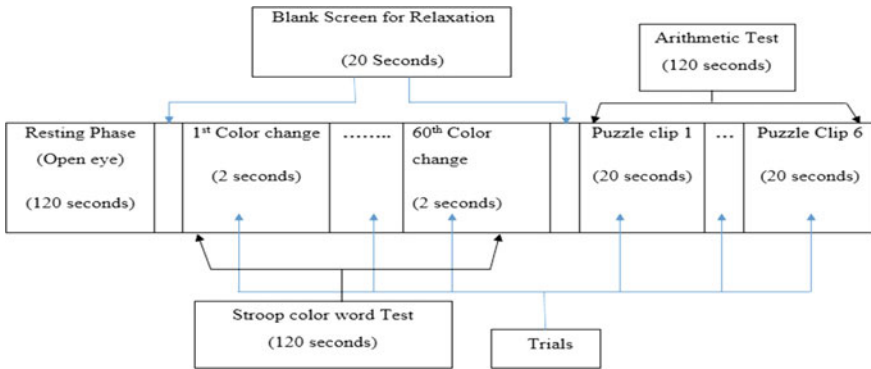


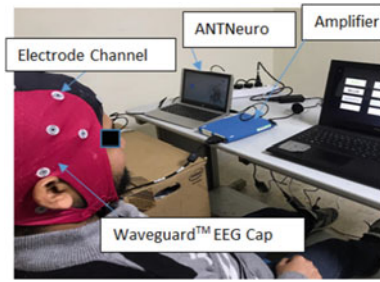
Fig. 3 Schematic diagram of the stimulus

1	1
2	1
3	2
5	1
6	4
???	6

Fig. 4 Example of an arithmetic puzzle used in this work



**Fig. 5** Experimental system used while recording, HMI Laboratory, ICE Dept. NIT Jalandhar



## 4 Stress Recognition Using EEG

Here, the methodology of the proposed method has been briefly discussed. The experimental investigation initiates with data acquisition. After that, a signal processing stage is used which involves extraction of features from the recorded EEG signal. After extraction, the next is the classification phase involving classification of features by Support Vector Machine (SVM) classifier for stress detection.

### 4.1 Signal Processing Phase

This stage consists of band pass filtering, artifact elimination, baseline correction, and time window analysis. In signal processing, the first step is Band pass filtering which is employed to obtain the required frequency bands. Thereafter, for removal of any offset existing in the recorded signal, Baseline correction is carried out on different EEG channels across all the data samples. Using the basic concepts of Fast Fourier Transform (FFT), the discrete signal in time domain is converted to frequency domain followed by the computation of signal power. For different power bands in the EEG signal (theta (4–8 Hz), alpha (8–12 Hz), and beta (12–30 Hz)), the power spectral density (PSD) is computed in order to calculate the absolute power in the specific band. As reported in the research work [7, 9], there is an inter-relation between the stress levels and EEG power spectrum features. Here, the key parameters used are the absolute theta power, alpha power, beta power, and the relative ratio of alpha and beta power.

### 4.2 Feature Extraction

Firstly, by using the EEG signals different features including absolute power, statistical features, and Hjorth parameters are extracted and are labeled with varied stress levels where the labeling was performed through the assessment of the feedback form. After the completion of the recording process, features such as mean and standard

deviation of the normalized signal are then extracted. Following that, the extracted features from the recorded signal are classified. Statistical features, although simple, are extensively used in the EEG Signal classification. The Hjorth parameters are indicators of statistical properties that can be used as a feature as implemented in the research work [14]. It comprises 3 time-domain parameters, i.e., activity, mobility, and complexity. The variance of the signal amplitude corresponds to activity which indicates the average power. Mobility is the proportion of standard deviation of the signal power spectrum and represents the mean frequency. Complexity depicts the resemblance of the signal with pure sine wave and represents change in frequency.

## 5 Results and Analysis

In this study, two different classifiers namely SVM and k-NN have been implemented in the classification step. For accuracy calculation, fivefold cross validation has been utilized. By combining the Hjorth parameters, Statistical features and power features, average classification accuracy of SVM and k-NN classifiers are obtained and shown in Table 1 and 2, respectively.

Also, the mean accuracy obtained for three-level and two-level classification of various subjects has been compared (shown in Figs. 6 and 7, respectively). A pattern has been observed which simply indicates a declination in the classification accuracy with the increase in the number of stress levels. It was observed that the classification of two levels of stress yields a higher accuracy than three levels of stress classification for both SVM and k-NN as shown in Tables 1 and 2.

Moreover, the results clearly indicated that SVM has higher classification accuracy of stress level recognition than that of k-NN for all subjects. Moreover, in terms of

**Table 1** SVM classification results (%)

	3-Level	2-Level
Subject 1	66.67%	93.50%
Subject 2	83.33%	93.75%
Subject 3	75%	93.75%
Subject 4	81.83%	83.75%
Average	76.71%	91.19%

**Table 2** K-NN classification results (%)

	3-Level	2-Level
Subject 1	62.50%	87.50%
Subject 2	79.17%	82.50%
Subject 3	66.67%	75%
Subject 4	77.50%	82.5%
Average	71.46%	81.88%

**Fig. 6** Three-level classification accuracies for stress detection using SVM and K-NN

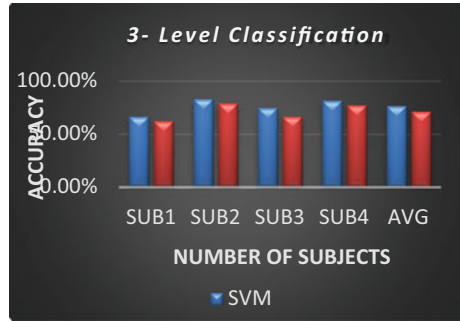
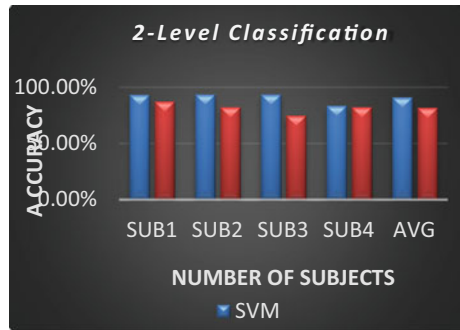


**Fig. 7** Two-level classification accuracies for stress detection using SVM and K-NN



mean accuracy, classification results of SVM are remarkably higher than k-NN (as shown in Figs. 6 and 7).

SVM and k-NN have achieved an average accuracy of 91.19% and 81.88%, respectively, for recognizing two level of stress. Furthermore, the respective average accuracies obtained for recognition of three levels of stress are 76.71% and 71.46%.

## 6 Conclusion

Based on EEG signals, a stress level detection system has been proposed in this study. Both the Stroop color-word test (SCWT) and mental arithmetic (puzzle) test are used as stressors to elicit various stress levels among all the subjects. Separate experiments for Stroop color-word test, mental arithmetic test, and three-level stress test have been performed on different male and female test subjects. The classification results obtained from SCWT, mental arithmetic test, and three-level stress test demonstrate an accuracy of 87.5%, 90.625%, and 76.04%, respectively. Our future work will focus on increasing the number of subjects of different domain for EEG signal acquisition for the further identification of other superior set of EEG features. In order to reduce

the complexity encountered during stress level measurement, our future work will emphasize on performing the data analysis in the real-time mode.

## References

1. Jun G, Smitha KG (2016) EEG based stress level identification. In IEEE international conference on systems, man, and cybernetics (SMC), 2016, pp 3270–3274
2. Patel V, Woodward A, Feigin V, Quah SR, Heggenhougen K (2010) Mental and neurological public health: a global perspective. Academic Press
3. Skoluda N et al (2015) Intra-individual psychological and physiological responses to acute laboratory stressors of different intensity. *Psychoneuroendocrinology*. <https://doi.org/10.1016/j.psyneuen.2014.10.002>
4. Tulen JHM, Moleman P, Van Steenis HG, Boomsma F (1989) Characterization of stress reactions to the Stroop color word test. *Pharmacol Biochem Behav* 32(1):9–15
5. Kirschbaum C, Pirke K-M, Hellhammer DH (1993) The ‘Trier social stress test’—a tool for investigating psychobiological stress responses in a laboratory setting. *Neuropsychobiology* 28(1–2):76–81
6. Schwabe L, Haddad L, Schachinger H (2008) HPA axis activation by a socially evaluated cold-press or test. *Psychoneuroendocrinology* 33(6):890–895
7. Hou X, Liu Y, Sourina O, Tan YRE, Wang L, Mueller-Wittig W (2015) EEG based stress monitoring. In: 2015 IEEE international conference on systems, man, and cybernetics, pp 3110–3115
8. Al-Shargie FM, Tang TB, Badruddin N, Kiguchi M (2015) Mental stress quantification using EEG signals. In: International conference for innovation in biomedical engineering and life sciences, pp 15–19
9. Khosrowabadi R, Quek C, Ang KK, Tung SW, Heijnen M (2011) A brain-computer interface for classifying EEG correlates of chronic mental stress. In The 2011 international joint conference on neural networks, pp 757–762
10. Mueller ST, Piper BJ (2014) The psychology experiment building language (PEBL) and PEBL test battery. *J Neurosci Methods* 222:250–259
11. Liu Y, Sourina O (2014) EEG-based subject-dependent emotion recognition algorithm using fractal dimension. In: IEEE international conference on systems, man, and cybernetics (SMC), 2014, pp 3166–3171
12. Seo S-H, Lee J-T (2010) Stress and EEG (2010) Conver hybrid Inf Technol 1(1):413–424
13. Hosseini SA, Khalilzadeh MA, Naghibi-Sistani MB, Niazmand V (2010) Higher order spectra analysis of EEG signals in emotional stress states. In: Second international conference on information technology and computer science, 2010, pp 60–63
14. Oh S-H, Lee Y-R, Kim H-N (2014) A novel EEG feature extraction method using Hjorth parameter. *Int J Electron Electr Eng* 2(2):106–110

# Smart Classroom Surveillance System Using YOLOv3 Algorithm



Saurav Kumar, Drishti Yadav, Himanshu Gupta, and Om Prakash Verma

**Abstract** One of the major concerns associated with educational institutions is the attendance survey, monitoring, and surveillance. Owing to the labor-intensive nature of manual attendance system involving the management of attendance records, the current focus is on the emergence of an efficient and accurate attendance system. This paper presents a maiden attempt to propose a smart classroom attendance and surveillance system using YOLOv3 algorithm, a novel deep learning approach. An attempt has been made to avoid the unnecessary wastage of time spent during attendance marking and also to avoid fake attendance. Using YOLOv3 algorithm in the DarkNet framework, a realistic dataset of images with around 14 students and faculty members has been used to train the test model. The dataset has been formed by acquiring the realistic images from the Department of Instrumentation and Control Engineering, Dr. B. R. Ambedkar National Institute of Technology Jalandhar, India. The test results demonstrate the efficiency of YOLOv3 algorithm in effective face recognition, thereby endorsing its capability and usage in smart classroom surveillance system. In addition, the performance of YOLOv3 has been compared with YOLOv3-tiny algorithm to validate its robustness and competence in classroom surveillance tasks. The experimental results demonstrate a maximum accuracy of 99% by YOLOv3 algorithm.

**Keywords** Attendance system · Classroom surveillance · Deep learning · YOLOv3 algorithm · YOLOv3-tiny algorithm

## 1 Introduction

The attendance survey and its efficacious monitoring are one of the major concerns existing in the contemporary educational institutions. The assurance of a highly accurate and flawless attendance system is still years away due to the existing drawbacks of manual attendance system. Moreover, the management and monitoring associated

---

S. Kumar · D. Yadav · H. Gupta · O. P. Verma (✉)

Department of Instrumentation and Control Engineering, Dr. B. R. Ambedkar National Institute of Technology Jalandhar, Jalandhar, India

e-mail: [vermaop@nitj.ac.in](mailto:vermaop@nitj.ac.in)

© The Author(s), under exclusive license to Springer Nature Singapore Pte Ltd. 2022

M. Vashista et al. (eds.), *Recent Innovations in Mechanical Engineering*,

Lecture Notes in Mechanical Engineering, [https://doi.org/10.1007/978-981-16-9236-9\\_6](https://doi.org/10.1007/978-981-16-9236-9_6)

with the manual attendance system are tedious, cumbersome, and time-consuming. Also, the issues of fake attendance and proxy in educational institutions call for the improvement in the existing system. Moreover, classroom surveillance assists the higher authorities in investigating and monitoring the cases of unfair means during the examination and gathering evidence of abusing and other banned activities. In addition, the surveillance of classrooms by higher authorities ingests their precious time is extremely arduous and usually, inefficient. Evidently, a proficient and smart classroom surveillance system needs to be proposed to enhance and upgrade the existing scenario of classroom surveillance.

Researchers have shown significant interest toward classroom surveillance through video based on keyframe extraction and student behavior analysis approaches. These are mainly structural similarity index matrix (SSIM)-based approaches which provide moderate accuracy. Moreover, many techniques including deep learning approaches have been investigated in automatic attendance and surveillance systems [1–3]; however, satisfactory accuracy in detection and recognition tasks has not been achieved yet.

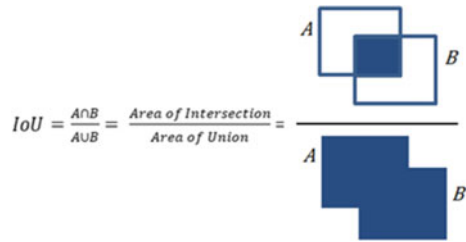
Being motivated by the advancements in deep learning approaches and their performance in object detection and recognition tasks, the performance of YOLOv3 algorithm for classroom surveillance has been evaluated in the present investigation. The main reason behind choosing YOLOv3 [4] is that it is, till date, the best and most popular model for object detection and recognition task. Moreover, the supremacy of YOLOv3 algorithm has been proven by comparing its performance with YOLOv3-tiny algorithm. YOLOv3-tiny [5] is a simplified version of YOLOv3 and has smaller number of convolutional layers, thereby possessing lesser memory and lower computational requirements than YOLOv3. The core idea behind this investigative analysis and exploratory research is to make classroom surveillance effortless so as to allow the authorities to monitor the students and faculties of multiple classrooms from just one place.

The rest of the paper is subdivided into the following sections: Sects. 2 and 3 describe general performance evaluation parameters and methodology used. Section 4 discusses the custom dataset being used and simulation setup utilized in the present investigation. Finally, experimental results and conclusions are presented in Sects. 5 and 6.

## 2 Performance Evaluation Parameters

In the present investigation, the performance of YOLOv3 and YOLOv3-tiny algorithms for object detection and recognition tasks is evaluated on the basis of the following parameters.

**Fig. 1** Illustration of the concept of IoU



### 2.1 Recall

It represents the ability of a detector in finding all ground truth values. It is defined as the ratio of number of objects detected correctly to the number of ground truth objects and expressed by Eq. (1).

$$\text{Recall} = N_{TP} / (N_{TP} + N_{FN}) \tag{1}$$

where  $N_{TP}$  = Number of True Positives,  $N_{FP}$  = Number of False Positives and  $N_{FN}$  = Number of False Negatives.

### 2.2 Intersection Over Union (IoU)

It is used to represent the overlap ratio between intersection and union of predicted and ground truth bounding boxes, expressed by Eq. (2) and illustrated in Fig. 1.

$$IoU = (A \cap B) / (A \cup B) \tag{2}$$

Here,  $A$  and  $B$  represent the area of predicted and ground truth bounding boxes, respectively.

### 2.3 Mean Average Precision (mAP)

The mean of average precision of all classes defined in the model is given by mean average precision (mAP). For  $N$  number of classes, mAP is given by Eq. (3).

$$mAP = (\sum_{i=1}^N [AP]_i) / N \tag{3}$$

where,  $AP_i$  (average precision) represents area under precision–recall curve. Usually, precision is defined as the ratio of number of correctly detected objects to number of total detected objects.

### 2.4 F1 Score

It is another most commonly used performance evaluation parameter and is given by Eq. (4).

$$F(1)\text{score} = (2 \times \text{Precision} \times \text{Recall}) / (\text{Precision} + \text{Recall}) \quad (4)$$

## 3 Methodology

The basic concept of YOLO is illustrated in Fig. 2.

It divides the input image into an  $S \times S$  grid so that each and every grid predicts that object which is centered in that grid. Grid is also liable for the prediction of bounding boxes and their corresponding confidence score. The confidence score represents the likelihood of the existence of an object and its respective confidence to be detected. The confidence and confidence score can be calculated from Eqs. (5) and (6), respectively. When the grid does not contain any object, its respective confidence score will become zero.

$$\text{Confidence} = \text{prob}(\text{object}) \times [\text{IoU}]_{\text{Predicted}}^{\text{Ground truth}} \quad (5)$$

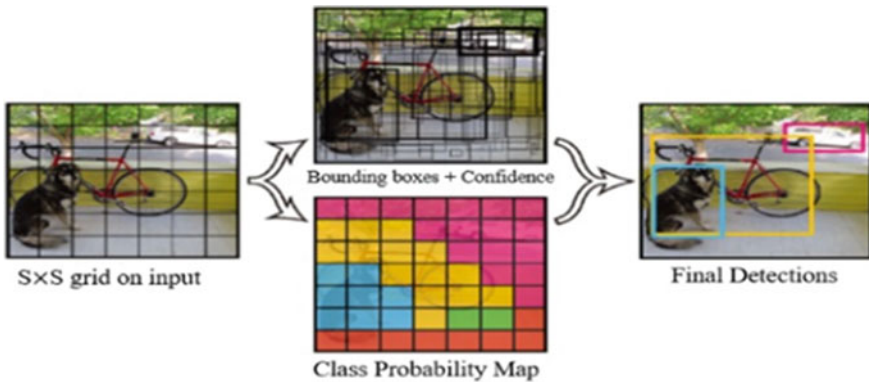


Fig. 2 Basic concept of YOLO



$$\text{Confidencscore} = \text{prob}(\text{Class}_i | \text{object}) \times \text{Confidence} = \frac{\text{prob}(\text{Class}_i) \times \text{IoU}_{\text{Predicted}}}{\text{IoU}_{\text{Ground truth}}} \quad (6)$$

Both YOLOv3-tiny and YOLOv3 belong to You Only Look Once (YOLO) family which is one of the most popular and efficient algorithms used for object detection and recognition tasks. The basic difference between YOLOv3-tiny and YOLOv3 lies in the number of convolutional layers being used. Due to the pipeline architecture of other generally used algorithms (R-CNN family [6, 7] and SSD family [8, 9]), the use of YOLO family in object detection tasks has shown a massive increase. YOLO overcomes the drawbacks of the algorithms with pipeline architecture by converting the detection task into a problem of logical regression. Unlike others, the optimization of detection performance is done by training on the full image instead of converting the image into small blocks and then training the network block by block using a sliding window or region proposal-based approach.

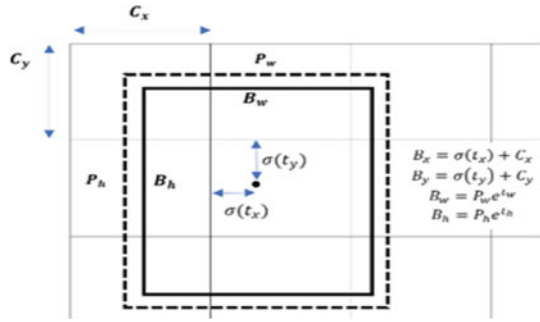
### 3.1 Network Structure

In the context of object detection, YOLOv3 has 106 fully connected convolutional architecture with the residual skip connections and upsampling. Detections at three different scales make YOLOv3 an outstanding performer among all other members of the YOLO family. The detection kernel of YOLOv3 is represented as  $1 \times 1 \times (B \times (4 + 1 + C))$ , where  $B$  is the number of bounding boxes in a grid on the feature map which can be predicted, 4 is for bounding box attributes, 1 is the prediction probability, and  $C$  represents the number of classes. In the present investigation, the model is trained on our self-made dataset, where  $B$  is taken as 3 and  $C$  (number of classes) is taken as 14; so the kernel size becomes  $1 \times 1 \times 57$ .

### 3.2 Selection of Candidate Frames Based on *k*-Means Clustering

Due to multiple downsampling, YOLO is unable to generalize the objects that are relatively new or having unusual aspect ratio. Therefore, it struggles when dealing with small objects especially in groups. To handle such tasks, in the later versions, instead of fixed grids, anchor box mechanism with different aspect ratios as in SSD is adopted. However, usually in SSD and faster R-CNN, the size of this predicted box is set manually which results in slow convergence of network while training and it is greatly affected by local optimization too. Hence, to find the optimal number and anchor box size, *k*-means clustering is used. In both YOLOv3-tiny and YOLOv3, the input image is divided into  $7 \times 7$  grids and predicts four coordinate values for each bounding box. The predicted coordinate values ( $B_x, B_y, B_w, B_h$ ) after offset are

**Fig. 3** Prediction of coordinate values



shown in Fig. 3. These values mainly depend upon the offset value from the upper left corner and the height and width of previous bounding box.

### 3.3 Loss Function

For proper training and accurate detection, YOLO algorithm relies on optimization of loss function which is simply addition of various errors like IoU errors ( $Error_{IoU}$ ), classification errors ( $Error_{cls}$ ), and coordinate errors ( $Error_{coord}$ ). In previous literature, it is formulated as Eq. (7) [10]. To deal with various errors which may diverge the network during training and make system unstable, YOLO sets some predefined weights. For example, to eliminate the problem caused by coordinate error and IoU error, it sets their respective weights to 0.5 and to handle the effect of large and small objects on detection, information items ( $w$  and  $h$ ) of object size are square rooted.

$$Loss = Error_{coord} + Error_{IoU} + Error_{cls} \tag{7}$$

## 4 Dataset and Simulation Setup

### 4.1 Dataset

In the current investigation, every student in the class is considered as a different class of object. Total 576 images were taken from Apple iPhone XR (64 GB) in daylight condition. After preprocessing and filtering, 500 images were considered for excellent recognition and classification. These images were further divided into 14 categories. The training method employed in the present study utilizes unsupervised learning and requires manual labeling of the dataset. To generalize the model and meet

**Table 1** Simulation platform configuration

Name	Related configuration
Operating system	Windows
CPU	Intel(R) Core (TM) i7-9700F CPU @ 3.00 GHz
RAM	8 GB
GPU	MSI Gaming GeForce GTX 1650
GPU acceleration library	CUDA10.0, CUDNN7.4

the classroom scenario, complex background, different postures of students, varying degree of occlusion, and different angles and position of camera were considered.

## 4.2 Simulation Setup

The entire simulation platform configuration used in this paper is shown in Table 1. The simulation environment compiles the entire script in Visual Studio 2017.

The total number of iterations used for both YOLOv3-tiny and YOLOv3 was 8000. The initial learning rate was set to 0.001. However, the learning rate was divided by 10 after 4000 and 5000 iterations. The mini-batch was set to 16 while the subdivisions were set to 16. Weight attenuation coefficient and the momentum coefficient were set to 0.0005 and 0.9, respectively. It took approximately 36 h (10 h for YOLOv3-tiny and 26 h for YOLOv3) to complete the training. During training, the input size of the model was changed 10 times per iteration, so that the final model has a better detection effect for images of different sizes. The above experiment was carried out in the Computer Vision Laboratory in the Department of Instrumentation and Control Engineering at Dr. B. R. Ambedkar. National Institute of Technology Jalandhar, Punjab, India.

## 5 Result and Discussion

During separate training of the test model by YOLOv3 and YOLOv3-tiny algorithms, the performance evaluation parameters (including recall, average IoU, F1-score, and mAP) were observed throughout the training phase at regular intervals of 1000 iterations. These performance evaluation parameters have been tabulated in Table 2. Evidently, the mAP values obtained by YOLOv3 algorithm are significantly higher than that of YOLOv3-tiny throughout the training duration.

After training, the performance of YOLOv3 and YOLOv3-tiny has been validated by investigating the prediction probability and accuracy of detection on four test images as illustrated in Fig. 4. Obviously, YOLOv3 outperforms YOLOv3-tiny in the present context of object detection task involved in classroom surveillance. As

**Table 2** Comparative analysis of YOLOv3-tiny and YOLOv3 Network on the test model during training

Iterations	Recall		Average IoU (%)		F1 -score		mAP (%)	
	YOLOv3-tiny	YOLOv3	YOLOv3-tiny	YOLOv3	YOLOv3-tiny	YOLOv3	YOLOv3-tiny	YOLOv3
1000	0.17	0.66	18.51	59.13	16.92	0.73	17.57	84.86
2000	0.37	0.99	28.28	79.29	30.15	0.99	30.54	99.01
3000	0.38	1.00	53.40	83.54	43.62	1.00	43.75	98.39
4000	0.39	0.99	27.53	82.88	27.96	0.99	28.40	98.98
5000	0.50	1.00	54.28	87.00	47.40	1.00	47.46	99.00
6000	0.53	1.00	52.54	87.30	45.51	1.00	45.60	99.00
7000	0.54	1.00	48.96	87.31	46.29	1.00	47.35	99.00
8000	0.56	1.00	52.47	87.60	47.83	1.00	48.86	99.00

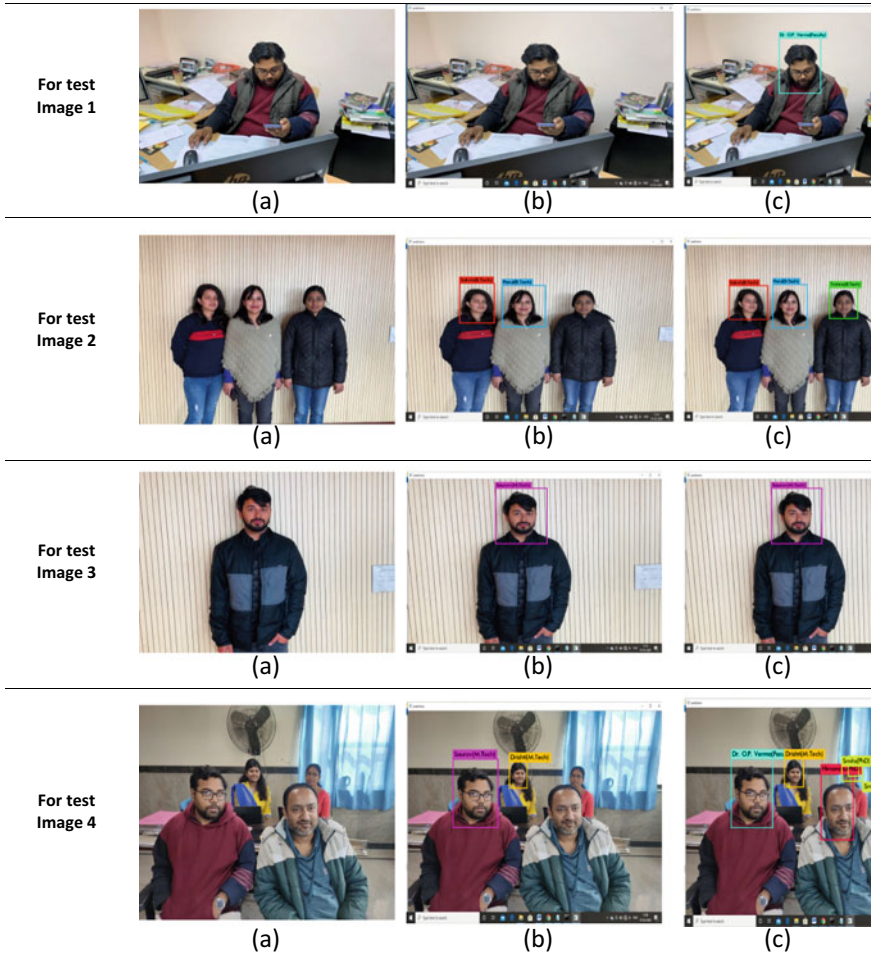


**Fig. 4** Experimental result of object detection for classroom surveillance on various test images: **a** original image, **b** detection by YOLOv3-tiny, **c** detection by YOLOv3

elucidated in Table 3, YOLOv3 provides better results in terms of true predictions and increased prediction probabilities. Maximum accuracy of 99% has been achieved by YOLOv3-algorithm relative to YOLOv3-tiny algorithm with a comparatively low accuracy of 78%.

However, the slow speed of prediction still remains to be a shortcoming of YOLOv3 algorithm which demonstrates the trade-off between prediction probability and speed of prediction.

**Table 3** Quantitative comparison of the experimental results of the test model

Test image	Name	Prediction probability (in %)		Prediction time (in milliseconds)	
		YOLOv3-tiny	YOLOv3	YOLOv3-tiny	YOLOv3
1	Dr. O.P. Verma (Faculty)	No detection	99	52.54	248.65
2	Sakshi (B.Tech)	58	97	54.21	254.25
	Parul (B.Tech)	78	99		
	Trishna (B.Tech)	No detection	86		
3	Saurav (M.Tech)	72	99	52.54	248.65
4	Dr. O.P. Verma (Faculty)	52	97	54.53	246.35
	Himanshu (PhD)	No detection	88		
	Drishiti (M.Tech)	67	99		
	Smita (PhD)	No detection	98		
	Smita (PhD)		False detection		

## 6 Conclusion

This paper attempts to deliver a novel application of deep learning-based YOLOv3 algorithm for detection and recognition tasks involved in smart classroom surveillance system. The training was accomplished on a self-made dataset to provide a realistic solution to classroom surveillance. The quantitative analysis of the experimental results reveals the efficiency of YOLOv3 over YOLOv3-tiny algorithm in terms of improved prediction probability. An exceptionally high prediction probability of 99% has been achieved by YOLOv3 algorithm which is considerably higher than that achieved by YOLOv3-tiny algorithm. The present results endorse the development of an effective and smart classroom surveillance system. Future work will focus on the reduction in prediction time with higher prediction probability.

## References

1. Harikrishnan J, Sudarsan A, Sadashiv A, Remya Ajai AS (2019) Vision-face recognition attendance monitoring system for surveillance using deep learning technology and computer vision. In: Proceedings—international conference on vision towards emerging trends in communication and networking, ViTECoN 2019. <https://doi.org/10.1109/ViTECoN.2019.8899418>
2. Mery D, Mackenney I, Villalobos E (2019) Student attendance system in crowded classrooms

- using a smartphone camera. In: Proceedings—2019 IEEE winter conference on applications of computer vision, WACV 2019, pp 857–866. <https://doi.org/10.1109/WACV.2019.00096>
3. Chowdhury AE, Chowdhury OK, Samrat MA, Rahman MZ, Ahmed T (2020) HFDCM: a low-cost machine learning based class attendance monitoring system 1348–1353. <https://doi.org/10.1109/icicict46008.2019.8993212>
  4. Redmon J, Farhadi A (2018) YOLOv3: an incremental improvement
  5. Nordin P, Lidström F (2019) Object detection using YOLOv3 tiny
  6. Chen C, Liu MY, Tuzel O, Xiao J (2017) R-CNN for small object detection. In: Lecture notes in computer science (including subseries lecture notes in artificial intelligence and lecture notes in bioinformatics), vol 10115, LNCS, pp 214–230. [https://doi.org/10.1007/978-3-319-54193-8\\_14](https://doi.org/10.1007/978-3-319-54193-8_14)
  7. Ren S, He K, Girshick R, Sun J (2015) Faster R-CNN: towards real-time object detection with region proposal networks
  8. Liu W et al (2016) SSD: single shot multibox detector. In: Lecture notes in computer science (including subseries lecture notes in artificial intelligence and lecture notes in bioinformatics), vol 9905 LNCS, pp 21–37. [https://doi.org/10.1007/978-3-319-46448-0\\_2](https://doi.org/10.1007/978-3-319-46448-0_2)
  9. Fu C-Y, Liu W, Ranga A, Tyagi A, Berg AC (2017) DSSD: deconvolutional single shot detector
  10. Tian Y, Yang G, Wang Z, Wang H, Li E, Liang Z (2019) Apple detection during different growth stages in orchards using the improved YOLO-V3 model. *Comput Electron Agric* 157:417–426. <https://doi.org/10.1016/j.compag.2019.01.012>

# EEG Based Study of Pictorial Advertisement Impact on Customers' Market Preferences



Anshika Kesari, Rajesh Singla, and Prerna Singh

**Abstract** Neuromarketing is a way to detect elicited brain activities while customer is engaged toward various products and brands. This paper presents a study regarding customers' engagement with various products and brands available in the market using electroencephalography (EEG). A total of 10 test subjects were presented with a collage of still pictures from the TV commercials, and their brain activity was recorded. Power spectral density (PSD) was obtained from the acquired signals using fast Fourier transform (FFT) technique, and absolute power was obtained. The results showed that test subjects felt change in elicitation in the theta wave and a pattern can be seen in theta band power. This study implies that the variation in theta band power when compared with the Delighted–Terrible (D-T) scale rating changes which signify the same outcome. Hence, the present work would help in effective evaluation of the change in market demands of various products and brands with the help of pictorial advertisement.

**Keywords** EEG · Neuromarketing · D-T scale · Theta band power

## 1 Introduction

Neuromarketing, an integration of neuroscience and marketing, signifies research work in the zone of marketing. It focuses on the study of the behavioral response of consumers to an external stimulus based on marketing. Neuromarketing can be exceptionally useful when it comes to marketing research. The ability to measure physiological consumer responses to everything from a product's packaging to the ad with which you are promoting it is valuable, especially when you follow up with an in-depth interview about why the consumer felt the way they did. This can give

---

A. Kesari (✉) · R. Singla · P. Singh

Department of Instrumentation and Control Engineering, Dr. B. R. Ambedkar National Institute of Technology, Jalandhar, Punjab 144011, India

R. Singla

e-mail: [singlar@nitj.ac.in](mailto:singlar@nitj.ac.in)

© The Author(s), under exclusive license to Springer Nature Singapore Pte Ltd. 2022

M. Vashista et al. (eds.), *Recent Innovations in Mechanical Engineering*,

Lecture Notes in Mechanical Engineering, [https://doi.org/10.1007/978-981-16-9236-9\\_7](https://doi.org/10.1007/978-981-16-9236-9_7)



you incredible insight into how effective your current campaigns are and what you can do to improve them.

The first neuromarketing experiment was conducted at Baylor University of Medicine by Montague, Professor of Neuroscience. The experiment involved scanning brains of a group of individuals in a functional magnetic resonance imaging (fMRI) machine in which the individuals were asked to consume either Pepsi or Coca-Cola without revealing their brands [1, 2]. According to his study, with no knowledge of the brand of the product, the individuals preferred Pepsi over Coca-Cola in contrast to their choice of Coca-Cola over Pepsi with the brand name already revealed to them [3]. A major conclusion of this study was the revelation of activation of some parts of the brain depending on the awareness of the brand of the product that they are consuming. It was demonstrated that a well-known brand (Coca-Cola, in this case) has the potential of activating the frontal cortex. Usually, the frontal lobe corresponds to executive function (EF) of managing attention, controlling short-term memory, thinking, and planning. Several techniques have been presented in the literature for measuring some of the physiological responses to pictorial advertisements.

However, only three non-invasive methods have proven their worth in the measurement and mapping of brain activities including EEG, magneto-encephalography (MEG) and fMRI. The cost of maintenance, insurance, and portability issues restricted the use of an fMRI instrument in other experiments [4]. MEG instrument provides a map of neuron activity in spatiotemporal information. However, the technical complexities involved in device configuration along with higher cost limits its usage among researchers in the field of neuromarketing [5, 6]. To overcome the limitation of the above-mentioned issues, we considered EEG device due to its high-resolution data with lower maintenance and supports cost in comparison with fMRI and MEG instruments.

## 2 Literature Survey

### 2.1 *Link Between EEG Recording, Analysis, and Choice*

Advertisement design involving eye-catchy packing, taglines, colors displayed and luscious shape embrace customers' desire and thus, generate an impact on the customers' choice and shopping practices. One of the recent works in this field include the study conducted by Kumar et al. [7] which combines EEG signals and sentiment analysis of product reviews to achieve a multimodal rating prediction framework for consumer products. Sequentially, 14 categories of products having varieties of colors and textures were displayed and their EEG signals were recorded. Additionally, a framework for prediction of consumer's choice for a product was proposed by Yadava et al. [8] where different products were shown to the users to record their EEG signals. These signals were modeled using Hidden Markov Model (HMM) classifier

for user’s choice prediction. Also, frequency content of brain waves was successfully utilized to investigate the “customers” preferences based on like/dislike [9]. A change in the spectral activity among various parts of the brain (frontal, parietal, and occipital) was demonstrated depending on the preference of the customers. Telpaz et al. [5] revealed that the future preferences of customers can be predicted by using the EEG signals due to the increase in the N200 component at the mid-frontal electrode site for preferred products. Moreover, the preferences for shoe products were successfully predicted by Baldo et al. [10] through EEG data. It was demonstrated that an increase in company profit can be achieved by using the brain scan-based prediction which is more reliable than the self-report-based prediction. In an experiment conducted by Yilmaz et al. on multichannel EEG recording [11], it was found that the most informative channels for discrimination between consumer preferences are revealed by the F7 and T6 channels in the low-frequency band.

### 2.2 Technical Aspects of Rating

For rating purpose in neuromarketing, various Likert scales are present. Andrews and Withey [12] in 1976 proposed the 7-point D-T Scale which takes information from the participants regarding their views and perceptions of life by asking them to provide a response from seven mood adjectives as shown in Fig. 1. Moreover, the suitability of rating scale depending on the customer satisfaction level for marketing studies has been explored [13]. Christina calculated convergent and divergent validity coefficients for the AM Happy Scale [14]. The results were in confirmation with those of multimethod-multitrait analysis of different measures of happiness. These include the D-T Scale and Cantril’s life satisfaction self-anchoring ladder rating. Also, an investigation was performed on the positive and negative effects of happiness [15] along with using the Global Happiness Scale, Affect Balance Scale, and D-T Scale.

The theta band activities were related to the subsequent pleasantness ratings of various products. Hence, for observing the theta band power (TBP) variation in the brain, a setup was made to measure the various changes and elicitations irrespective of others. The subjects were presented collage pictures of 15 items (3 brands, 5 products in each brand). Also, a 7-point Likert scale, where 1 represents “terrible” and 7 represents “delighted” was used regarding participants response to these items in the beginning as well as at the end of the experiment.

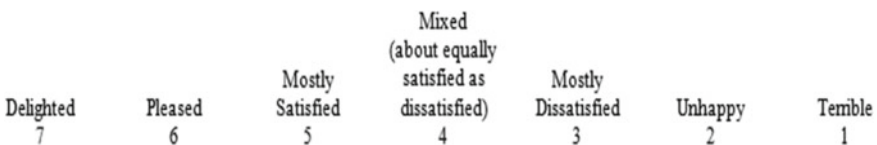


Fig. 1 7-point Delighted–Terrible (D-T) scale

### 3 Methodology

#### 3.1 Experimental Design

In this experiment, 6 male and 4 female students aged between 23 and 26 years from the university actively participated with their due consent. A waveguard EEG cap of 32 channels was used, and EEG recording was performed on 18 channels (Fp1, F3, F7, FC5, T7, P3, P7, O1, Fz, Pz, O2, P8, P4, T8, FC6, F8, F4, Fp2) and Cpz as reference electrode using International 10–20 system standardized by the American Encephalographic Society (see Fig. 2). A sampling frequency of 512 Hz was used during the EEG recording.

At the starting, D-T scale rating sheet was provided to each participant for marking their emotional responses in order to observe their preferences. Secondly, a consent form was signed by the participant, and after that, the instructions regarding the whole experiment were provided to acquire the better results. Thirdly, EEG recording was started and a list of products was displayed which the whole stimulus was going to have and after that the randomized sequence of collaged photographs appeared. As gender, age, and opinions may vary for different subjects, hence various options were provided to reduce biasing. During the presentation of the photograph collage series of 5 products having 3 brands each, none of the frames were lost. The order of appearance of each picture was randomized so that overlapping of elicitations can be prevented. The whole experimental design is shown in Fig. 3.

The experimental paradigm involves 5 blocks, each block having 3 different brands. The participants are allowed to switch to the next photograph according to their choice. Each block has three varieties of single product; hence, in total there are 15 photographs sequencing. A sample of the stimulus is shown in Fig. 4. After completion of the recording task, second D-T scale rating sheet was given for marking the new felt emotions.

**Fig. 2** Experimental setup for data acquisition





Fig. 3 Protocol of the proposed approach used during the entire experimental procedure



Fig. 4 Photo collages of chocolate category with its brands which was shown to the participants during EEG recording in randomized manner

### 3.2 Preprocessing and Feature Extraction

The preprocessing of the raw signals acquired during EEG was done using software, a band-pass filter filtered the frequencies below 0.3 Hz and over 30 Hz. After that artifact correction was applied artifacts like blinks, movements, etc., produced during the experiment with principal component analysis (PCA). Finally, baseline correction was applied which uses the inter-stimulus points and subtracted on the segments.

Prior to feature extraction firstly, the data was normalized followed by windowing of one second of the dataset. Emotions have an impact on different bands of spectral power of EEG signal; thus, PSD was computed on each segment using FFT and for smooth power spectrum periodograms averaging was performed. Each electrode PSD was estimated using 1 s windows with 50% overlapping. The PSD from theta (4 Hz <  $f$  < 8 Hz), alpha (8 Hz <  $f$  < 12 Hz), and beta (12 Hz <  $f$  < 30 Hz) bands were extracted and then converted into absolute power as features.

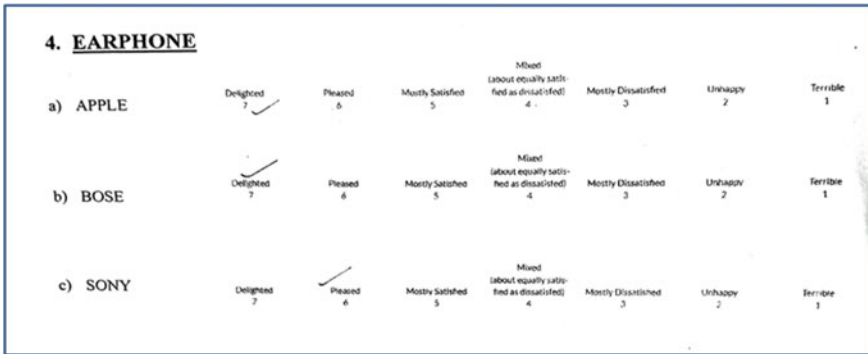


Fig. 5 Subject-assessed D-T scale rating sheet 1

### 4 Results and Discussions

Several studies have shown that EEG activity is linked with some aspect of consumer preferences, and neuromarketing is the one which tries to explore the neuronal basis of preferences of various products among the participants. In this paper, the whole analysis has been done on theta band wave. As the subjects were allowed to switch to the next slide whenever they were done with the previous one; thus, the least time interval taken by all the subjects was of 3 s. Hence, from each product a set of three features, i.e., TBP1, TBP2, TBP3, which represents theta band power obtained by calculating three respective means from the all whole data set of every item. The variation of each has been observed and plotted in bar graphs for all the items. Each participant’s emotional responses were rated by using delighted/terrible rating.

When both EEG analysis and rating sheet were compared the variations came out to be approximately the same, i.e., when the preference of the subject was decreasing disappointment is shown, when it was increasing impressed emotion is appearing and when there is no change felt by the subject then neutral condition was seen. One of the best results of the recorded EEG and peripheral physiological signals of the participants in response to the collaged photograph is shown in Fig. 7, and their respective before and after feedback assessments are shown in Figs. 5 and 6.

### 5 Conclusion

The essence of this paper was to analyze the behavioral changes of consumers when they see the pictorial representation of various products and examining consistency in preferences and liking ratings. This research paper has achieved the proposed objective of finding the change in preference of an item from the whole list and then comparing it with the manual rating done by each participant at each phase of the experiment. The results successfully showed the relation between the EEG analysis

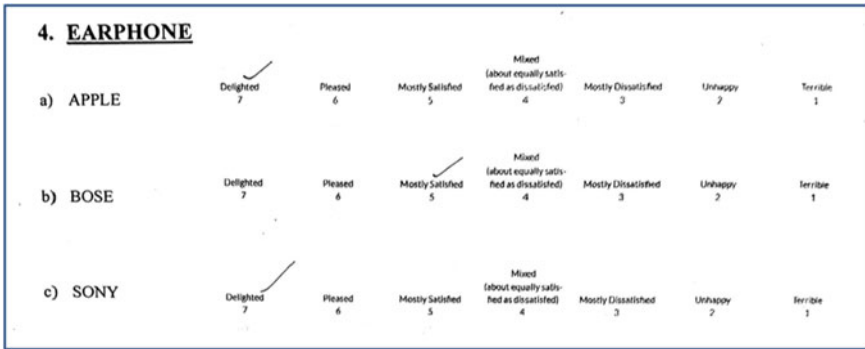


Fig. 6 Subject-assessed D-T scale rating sheet 2

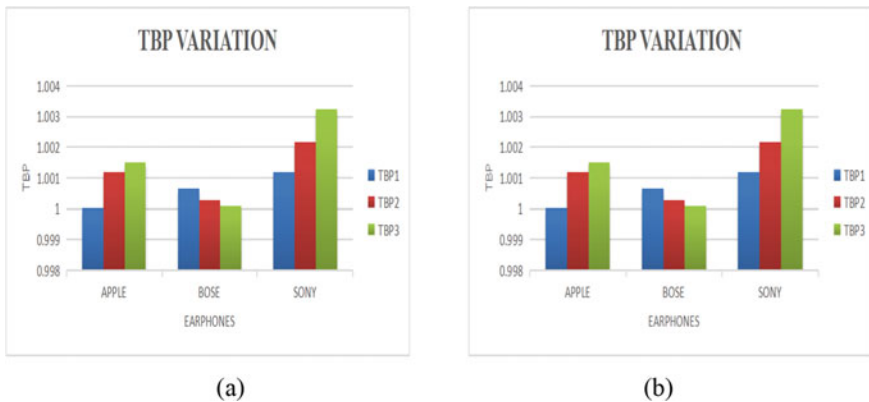


Fig. 7 Statistical representation of theta band power (TBP) variation of single product with 3 brands of a subject across a P7 and b P8 electrodes

and D-T scale. For higher accuracy of the correlation the number of participants should be increased which will lead to better results. In conclusion, neuromarketing is the biggest tool which can be really helpful for the company in improving the creation of the product as well as the style, colors, textures, and techniques they use. In other words, the whole promotional representation of a product should be more interesting, more valuable, and more attractive that mainly affects the costumers’ brain, hence resulting in rapid escalation in market demand of respective product.

**References**

1. Morin C (2011) Neuromarketing: the new science of consumer behavior. Society 48(2):131–135. <https://doi.org/10.1007/s12115-010-9408-1>

2. Vecchiato G et al (2011) On the use of EEG or MEG brain imaging tools in neuromarketing research. *Comput Intell Neurosci* May 2014. <https://doi.org/10.1155/2011/643489>
3. Madan CR (2010) Neuromarketing: the next step in market research? *Eureka* 1(1):34–42. <https://doi.org/10.29173/eureka7786>
4. Berns GS, Moore SE (2012) A neural predictor of cultural popularity. *J Consum Psychol* 22(1):154–160. <https://doi.org/10.1016/j.jcps.2011.05.001>
5. Telpaz A, Webb R, Levy DJ (2015) Using EEG to predict consumers' future choices. *J Mark Res* 52(4):511–529. <https://doi.org/10.1509/jmr.13.0564>
6. Murugappan M, Murugappan S, Balaganapathy B, Gerard C (2014) Wireless EEG signals based Neuromarketing system using Fast Fourier Transform (FFT). In: *Proceedings 2014 IEEE 10th international colloquium on signal processing and its applications CSPA*, pp 25–30. <https://doi.org/10.1109/CSPA.2014.6805714>
7. Kumar S, Yadava M, Roy PP (2019) Fusion of EEG response and sentiment analysis of products review to predict customer satisfaction. *Inf Fusion* 52(Nov 2018):41–52. <https://doi.org/10.1016/j.inffus.2018.11.001>
8. Yadava M, Kumar P, Saini R, Roy PP, Dogr DP (2017) Analysis of EEG signals and its application to neuromarketing. *Multimed Tools Appl* 76(18):19087–19111
9. Khushaba RN, Greenacre L, Kodagoda S, Louviere J, Burke S, Dissanayake G (2012) Choice modeling and the brain: a study on the electroencephalogram (EEG) of preferences. *Expert Syst Appl* 39(16):12378–12388. <https://doi.org/10.1016/j.eswa.2012.04.084>
10. Baldo D, Parikh H, Piu Y, Müller K-M (2015) Brain waves predict success of new fashion products: a practical application for the footwear retailing industry. *J Creat Value* 1(1):61–71. <https://doi.org/10.1177/2394964315569625>
11. Yılmaz B, Korkmaz S, Arslan DB, Güngör E, Asyali MH (2014) Like/dislike analysis using EEG: determination of most discriminative channels and frequencies. *Comput Methods Programs Biomed* 113(2):705–713. <https://doi.org/10.1016/j.cmpb.2013.11.010>
12. Andrews FM, Withey SB (2012) *Social indicators of well-being: Americans' perceptions of life quality*. Springer Science & Business Media
13. Westbrook RA (1980) A rating scale for measuring product/service satisfaction. *J Mark* 44(4):68. <https://doi.org/10.2307/1251232>
14. Moldovan CP (2018) Am happy scale: reliability and validity of a single-item measure of happiness. *Diss Abstr Int Sect B Sci Eng* 79(1-B(E))
15. Kaur H *Gross national happiness index: a nation's pursuit of happiness*

# Techniques Used in Phonocardiography: A Review



Nikita Jatia and Karan Veer

**Abstract** Segmentation of phonocardiogram (PCG) into its significant sound component is the initial phase in the automated diagnosis of cardiac abnormalities. The greater part of the computerized demonstrative calculation that utilized the PCG as a kind of perspective sign to identify side effects of cardiovascular variations from the norm apply time division as a pre-handling venture to separate progressive. In PCG, we identify the first and second heart sounds on recurrence space characteristics. The principal sound emerges from the mitral and tricuspid valve, and the subsequent sound brought about by the closer of aortic and pulmonary valves. For this, we are utilizing here a few methods where we can extricate the PCG signal. We can discover the fetal pulse during pregnancy around eighth week of pregnancy, as PCG is a clinical test to survey fetal prosperity during pregnancy, work, and conveyance. Wavelet transforms a strategy for procedures, as more suitable technique for preparing the FPCG signal. The wavelet technique incorporates the shifting and scaling of signal. This strategy can be utilized for examination of 1-D as well as 2-D data.

**Keywords** Fetal PCG · Wigner distribution · Wavelet transform · Phonocardiography · Auscultation

## 1 Introduction

Auscultation is the standard test performed while assessing the state of the heart framework since it is easy to perform. Auscultation is regularly accomplished utilizing a stethoscope to help the imperfect human ear in recognition of the heart sounds. Graphical recordings of heart sounds are called phonocardiograms, and a microphone gets heart sounds which are then recorded by some devices.

---

N. Jatia (✉) · K. Veer

Department of Instrumentation and Control Engineering, Dr. B R Ambedkar National Institute of Technology, Jalandhar, India



## 1.1 *History of Phonocardiography and Auscultation*

### **Impediments of the Human Ear**

Listening to the human heart (known as auscultation) is an exceptionally old and valuable procedure, which goes back to the times of Hippocrates around 400 BC, for the analysis of heart ailments and conditions (Selig 1993, Luisada 1965). The objective of auscultation is to foresee as far ahead of time as conceivable the advancement of a heart obsessive condition. Significant variables to get the greatest advantage of cardiovascular auscultation as a clinical demonstrative device incorporate the capacity to hear a wide scope of frequencies with sufficient affectability. The normal grown-up hearing reach is around 50–12,000 Hz with the ear performing best and having the best recurrence segregation between 1–2 kHz. The human ear experiences issues segregating between various frequencies of sound similarly as the volume is shifted frequently coming about in difficulties diagnosing heart murmurs and sounds; a solution for this issue is to intensify the low-recurrence sounds since high volume empowers low-recurrence sounds to be heard. Ambient noise may likewise veil cardiovascular sounds bringing about troubles perceiving the genuine heart sounds particularly in emergency clinic rooms or looking at wards which may have up to 70 dBs of encompassing commotion while the main heart sound heard at the zenith is just 20–60 dBs and the volume of the subsequent heart sound at the aortic territory is 30–70 dBs. The third and fourth heart sounds are frequently missed in light of the fact that they have exceptionally low-recurrence content and quite faint. There is also a time delay of 1 s, known as temporal summation, related to hearing the full force of a sound and the human ear cannot separate between time spans littler than 20 ms.

## **2 Why PCG?**

Different developments prompted the PCG being preferred over the stethoscope by 1908. In 1893, K. Hurtle of Breslau portrayed a method of writing heart sounds. He associated the yield of an amplifier through an inductor whose auxiliary curl was associated with the nerve of a frog muscle arrangement which set apart on a smoked drum utilizing an appended layer. The next year the first PCGs like those being used today were recorded by William Einthoven with Gluck in Leyden utilizing Lipmann's slim electrometer which was utilized to record the main ECGs. In 1904, precordial vibrations with optical enhancements (called the Flank fragment case) were recorded by Otto Frank in Munich. 1909, Carl J. Wiggers altered.

Straight to the point's PCG and graphically showed accounts; in any case, the technique experienced confinements in the recurrence reaction of the film which was utilized in the recurrence container. In 1907, Einthoven utilized a string galvanometer to record heart sounds; however, the issue with this technique is that there is a tremendous scope of forces of heart sounds frequently bringing about harm to the string.

For the strategies for circuitous phonocardiography or phonocardiography utilizing a string galvanometer, there was no chance to get of applying electrical filtration so acoustic filtration was utilized. This was practiced by utilizing an air spill in the cylinder associating the chest piece with the Fyank capsule or microphone. In 1942, Maurice Rappaport and Howard Sprague sketched out strategies for utilization of electronic intensification and galvanometers (of an alternate sort) in phonocardiography which turned into the overwhelming method utilized in phonocardiography [1]. They detailed that in the event that low frequencies were sifted extensively, at that point the PCG looked like auscultation.

Until the time that Bell Telephone Laboratories strategy for spectroscopy was utilized to examine heart sounds and murmurs by Geckeler who named it cardiospectrography and by McKusick who called it spectral phonocardiography, all phonocardiography was oscillographic phonocardiography. Created during the 1950s, cardiospectrography or otherworldly phonocardiography had the ability to spread out the recurrence range by utilizing the heterodyne electronic channel which could concentrate on determined recurrence ranges. Huggins created stage separating which permitted heart sounds to be spoken to all the more precisely. With the appearance of the wide bandpass channel, homeless people were presently ready to be shown [2]. An issue existed with building up ordinary qualities for PCGs in light of the fact that the scope of sounds is gigantic extending from faint diastolic murmurs which would be spoken to by an imprint less than 2 mm in length to an enormous checking speaking to a systolic murmur. To address this issue, voltage constraint was presented; so that in the event that one was looking for faint diastolic murmurs, the voltage could be restricted to a little range, in this way making the diastolic murmur more obvious. To make the distinguishing proof of heart sounds simpler, reference signals, for example, the ECG were presented. Frequency moving is additionally now feasible for PCG accounts making sub-perceptible frequencies discernible. Phonocardiography has not advanced as fast as other analytic strategies in view of the absence of principles in hardware and recording areas, helpless comprehension of the heart sound systems, and the multifaceted nature of PCGs, yet signal preparing has supported in the improvement of phonocardiography (Wood and Barry 1995). A significant utilization of sign preparing in the zone of phonocardiography is noise removal.

There are numerous wellsprings of commotion which may contaminate the PCG including thoracic muscular noise (Zhang et al. 1998), peristaltic intestine noise (Zhang et al. 1998), respiratory noise, fetal heart sound noise if the subject is pregnant, noise brought about by contact with the instrumentation and environment noise. The noise present for each situation relies upon the condition of the subject, the instrumentation utilized, and the environment which the PCG was recorded in. Groom et al. (1956) found that the background sound level in emergency clinics and centers was very high being on the request for 60–70 dBs. A sound verification room was developed which decreased commotion levels on the request for 35 dBs. The impact of noise on the auscultatory performance of forty specialists was estimated under stimulated stethoscope assessments [3]. The normal consequences of the gathering showed that similar murmurs heard in the sound verification room must be expanded

multiple times in force to be heard under ordinary commotion conditions in facilities and emergency clinics. Decreasing medical clinic commotion levels to the order of 35 dBs would not be affordable with the exception of on account of a sound-confirmation looking at room which isn't reasonable. Faint heart murmurs, which are all the time of the most significance in diagnosing early coronary illness, might be handily concealed by surrounding commotion. Subsequently, usually discovered degrees of foundation noise genuinely hinder the capacity of the clinical expert to observe heart murmurs through a regular stethoscope. Recording the heart sounds through phonocardiograms and applying noise removal methods may uncover faint heart murmurs which already would have gone undetected.

### 3 The Recording Process

The PCG recording is made by setting the stethoscope ordinarily on the aortic zone. The patient is advised to be still and tranquil, lean forward a piece, and hold their breath if conceivable. The PCG is recorded for around 30–60 s utilizing the chronicle framework portrayed. A jack is connected to the Esclope. The yield of the jack is associated with channel 12 of the A/D converter and sampled at 2500 Hz well over the Nyquist frequency for heart sounds (around 1000 Hz is about the most noteworthy recurrence (Selig 1993)) [4]. Consciousness of the sounds made by the pulses to antiquated occasions. Developing an instrument to record it might go back to Robert Hooke (1635–1703), who expressed “There may likewise be a chance of finding the inside movements and activities of bodies—regardless of whether creature, vegetable, or mineral, by the sound they make.” The soonest known instances of phonocardiography date to the 1800s [5].

Checking and recording hardware for phonocardiography was created through the 1930s and 1940s. Normalization started by 1950, when the primary worldwide meeting was held in Paris. A phonocardiogram framework produced by Beckman Instruments was utilized on at any rate one of the Project Gemini kept an eye on spaceflights (1965–1966) to screen the heartbeat of space explorers on the flight. It was one of numerous Beckman Instruments specific for and utilized by NASA. John Keefer recorded a patent for a phonocardiogram test system in 1970 while he was a worker of the US government. The first patent depiction demonstrates that it is a device which by means of electrical voltage copies the human heart's sounds. Human heart itself is the most significant organ of the body which gives blood to all parts of body using pump-like action. Throughout the siphoning activity, mechanical and electrical exercises are completed bringing about the progression of blood. Figure 1 frameworks a model of all of ECG and PPG signals [6]. Despite ECG and PPG, phonocardiogram (PCG), the record of the sounds and murmurs made by heart during a cardiovascular cycle, can be effectively used to study and screen the activities of heart [7].

Such type of sounds is typically recorded by using a device which is called as phonocardiograph. The mechanical activity of the heart generally produces four

**Fig. 1** Example of ECG and PPG signal [4]

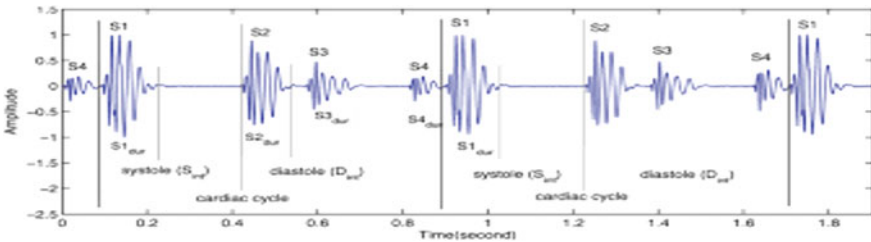
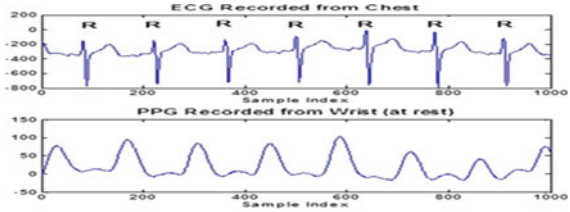


**Fig. 2** An example of PCG signal [4]

different sounds S1, S2, S3, and S4. S1 and S2 can be heard from human ear because other two are just unusual or noisy signal [8].

Cardiac cycle is a continuous or cyclic process as shown in Fig. 2, and the above signal consists of four different sounds such as S1, S2, S3, and S4 [3, 5, 7–10].

## 4 Techniques

The methodologies proposed for customized assessment of PCG signals can be arranged into frequency domain, time domain, and time–frequency domain [11]. In the going with, we talk about the time and frequency domain [2].

### 4.1 Time and Frequency Examination

The broadest procedure for assessment relies upon the time domain. Here, examination is finished on signal itself. Statistics alike mean, mode, median, peak value, and then peak-to-peak value of signal is used throughout the process.

As shown in Fig. 3, P1 and P2 are the peak values, A1 and A2 are peak to peak of the signal, and P1 and P2 are timespans that speak to highlights of S1 and S2. The overall portrayal of signal in time domain is introduced in Eq. 1  $f(t)$  which is displayed by adequacy  $A$ , recurrence  $\omega$ , and stage  $\theta$ . Every one of these boundaries just as various insights got from these boundaries have been utilized as highlights

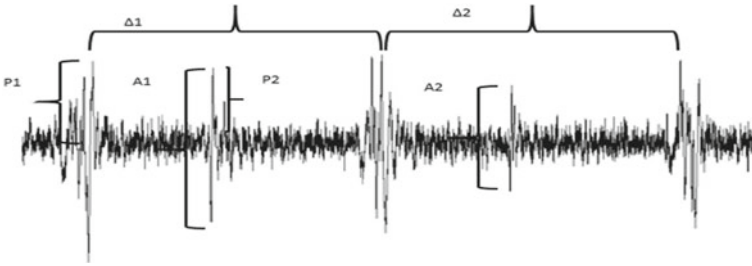


**Fig. 3** Analysis of PCG signal in time domain [4]

for limitation and grouping [10]

$$f(t) = A \sin(\omega * t + \theta) \quad (1)$$

Due to the cyclostationary nature of the PCG signal, a signal cannot be localized in time and frequency because of vulnerability guideline restriction. Therefore, time-recurrence examination of PCG signals is researched in various investigations. Such techniques generally include short time frequency transform (STFT), time–frequency portrayals like Wigner–Ville, wavelet transform, and empirical mode decomposition (EMD) [12, 13].

## 5 Techniques Used for PCG Signal Analysis

### 5.1 Utilizing Wigner Distribution

The Wigner distribution function (WDF) is utilized in signal handling as a change in time–frequency analysis. The WDF was first proposed in quite a while to represent quantum redresses to old-style measurable mechanics in 1932 by Eugene Wigner, and it is of significance in quantum mechanics in stage space (see, by method of correlation: Wigner semi likelihood appropriation, additionally called the Wigner work or the Wigner–Ville conveyance) [14].

Given the common arithmetical structure between position energy and time–frequency conjugate sets, it additionally helpfully serves in signal preparing, as a change in time-recurrence examination, the subject of this article. Contrasted with short time frequency transform, for example, the Gabor transform, the Wigner distribution function can furnish higher clearness in some cases.

## ***5.2 For Interior Point Algorithm***

Interior point calculations for solving LPs are right now picking up prominence over customary simplex techniques. The current work inspects the adequacy of the preconditioned conjugate inclination (PCG) technique for the symmetric positive unequivocal ordinary conditions. What is more, we examine the utilization of a PCG variation for the inconclusive enlarged conditions.

## ***5.3 For Utilizing AI in Content Generation***

PCG strategies are fundamentally as wide and changed as their likely executions. Utilizing models from the reference's own work, this reference presents six pragmatic approaches to actualize AI-driven procedural substance age in games [10]. The strategy clarified will be helpful in the case of building a PCG-based game or to prepare a more created game.

## ***5.4 Using Pattern Recognition Technique***

About the usage of a demonstrative framework as a finder and a classifier; for head illnesses. Example acknowledgment is utilized to give human acknowledgment insight to machine which is required in picture preparing. Example acknowledgment is utilized to remove important highlights from given picture/video tests and is utilized in PC vision for different applications like organic and biomedical imaging.

## ***5.5 For VLSI Format Improvement***

Very enormous scope incorporation (VLSI) is characterized as an innovation that permits the development and interconnection of huge numbers (a huge number of) semiconductors on a solitary coordinated circuit. Incorporated circuit is an assortment of at least one doors created on a solitary silicon chip. The significant target in planning of VLSI incorporated circuits is in general chip region decrease. Hereditary algorithm is an iterative and evolutionary approach that could be applied to VLSI module position issue. In this paper, a genetic algorithm-based methodology is proposed to lessen the chip zone by methods for successful situation of the modules. The modules are set dependent on best-fit position esteems. Significant position limitations are considered so as to deliver successful situation.

## 5.6 Finite Impulse Response Filter

In signal setting up, a constrained inspiration response (FIR) channel is a channel whose drive response (or response to any restricted length input) is of constrained term, since it settles to center in constrained time [15]. This is instead of tremendous drive response (IIR) channels, which may have internal information and may continue responding uncertainly (regularly decaying). The inspiration response (i.e., the yield on account of a Kronecker delta commitment) of a  $N$ th-demand discrete-time FIR channel props up accurately  $N + 1$  models (from first nonzero segment through last nonzero segment) before it by then settles to zero. FIR channels can be discrete time or steady time and mechanized or straightforward. In numerical examination and viable assessment, a discrete wavelet change (DWT) is any wavelet change for which the wavelets are discretely tested. Likewise with other wavelet changes, a key bit of leeway it has over Fourier changes is fleeting goal: it catches both recurrence and area data (area in time).

## 6 Wavelet Transform-Based Analysis

### 6.1 Extraction of Phonocardiogram Signals Utilizing Continuous and Discrete Wavelet Transform:

Prior to beginning the wavelet method, we should know the major of wavelet [4]. What is wavelet? wavelet can be characterized as “A waveform got from heart audio effect with a constrained term and having zero normal worth.” These wavelets are like the sine waves utilized in Fourier series analysis. These sinusoidal waves reach out from  $-\infty$  to  $+\infty$  having a smooth and unsurprising waveform while wavelets are asymmetric and irregular. The wavelet strategy incorporates the shifting and scaling of original signal or mother wavelet. This wavelet method can be utilized for analysis of two-dimensional information as well as one-dimensional [16–19].

#### A. Continuous Wavelet Transform

Fourier series analysis of any signal should be possible with the following condition:

$$F(w) = \int_{-\infty}^{+\infty} f(t)e^{-j\omega t} dt$$

Continuous wavelet transform can be performed with the following condition:

$$C(\text{Scale}, \text{Position}) = \int_{-\infty}^{+\infty} f(t)(\text{Scale}, \text{Position}, t)dt$$

It signifies “Sum for overall time of signal multiplied by scaled and shifted versions of wavelet function is Continuous Wavelet Transform” [19].

### B. Discrete Wavelet Transform

In discrete wavelet transform, the following two segments are utilized.

- Scaling Component
- Wavelet Component.

Suppose  $X(n)$  is sample signal where  $n = 0, 1, 2, \dots, N - 1$  and  $i =$  scaling factor and  $j =$  shifting factor.

Scaling Function:

$$M(\emptyset)(I, j) = \frac{1}{\sqrt{N}} \sum X(n) \cdot \emptyset(n)(i, j)$$

Wavelet Function:

$$M(\alpha)(i, j) = \frac{1}{\sqrt{N}} \sum X(n) \cdot \alpha(n)(i, j)$$

where  $\frac{1}{\sqrt{N}}$  is normalization factor.

Now discrete wavelet transform can be written as

$$X(a, b) = \int_{-\infty}^{+\infty} f(t) \frac{1}{\sqrt{a}} \cdot \left\{ \frac{t - b}{a} \right\} dt$$

## 6.2 Extraction of Phonocardiography Signal Utilizing FIR Filter

For reducing the artifact noise that emerges when taking fetal PCG recording from abdominal area of pregnant woman. For testing, we pick stimulated fPCG database containing 37 records and assessment dependent on SNR determination and Bland–Altman statistics and SD [13].

### Basics of FIR channel

The noise which stays in the band can be eliminated by FIR filter.

1. Filtrations are productive for improving SNR.
2. Noise reduction is referred to as non-recursive channel having multiple posts situated at the beginning which causes a channel delay.

### Results of FIR channel

1. Currently, just two databases that contain clinically gained constant fetal PCG information are accessible.



2. Synthetic databases called simulated fetal PCGs which is open by means of Physio Bank archive [2].

This database represents series of 37 single-channel synthetic abdominal fetal PCGs according to different fetal conditions and recording conditions created utilizing simulation software with length of 8 min [3].

## 7 Application of PCG

### 7.1 *Fetal Phonocardiography*

Fetal heart rate is greater than typical grown-up. Physiological fHR changes during pregnancy around eighth week of pregnancy this heart rate stabilize and extend from 120 to 160 beats for every minute (bpm). Fetal PCG is completely noninvasive, and no energy is sent to the mother's fetus. Signal can be captured by using the sensor on mother's abdominal area without utilizing a gel.

Noninvasive sensor ranges from 0.1 to 200 Hz with an amplifier and an anti-aliasing filter. The fetal ECG offers the opportunities for beat-to-beat fHR estimation since the QRS-complex gives a perfect fiducial point [14].

### 7.2 *Esophageal PCG*

Esophageal phonocardiography (ePCG) has the positive conditions that specific heart sounds are gotten which are close to their origin of sites, while in standard surface phonocardiography (sPCG) debilitating of the vibration occurs in the path to the microphone. The damage of directional sensitivity of an accelerometer-type microphone has been removed by building biaxial microphone; with the guide of an electronic axes rotation, turn, perfect record of heart vibrations in the even plane is practiced. ePCG has its own clinical importance because of diagnosing of the mitral valve regurgitating forward (MR) better than standard PCG, especially in patients who have prosthetic valves in both mitral and aortic gaps where left ventricular angiography cannot perform with no issue. Concerning extent of the recipient in the throat it has been set up that such countless vital vibrational models can be recorded at different heights.

## 8 Suggested Application

- Remote detecting of sub 50 micron removals
- Adult and fetal phonocardiography and phonography

- Remote estimations of consistent materials in airstreams
- Infrasound force estimation
- Biomedical instrumentation
- Low-cost and low force confocal microscopy
- Cell culture estimation.

## 9 Conclusion

The PCG recording is made by setting the stethoscope ordinarily on the aortic zone. The patient is advised to be still and tranquil, lean forward a piece, and hold their breath if conceivable, and the above-mentioned are various techniques used for de-noising the PCG signal. After de-noising, the signal one can easily utilize the filtered signal as in biomedical instrumentation and other suggested applications.

## References

1. Debbal SM, Bereksi-Reguig F (2008) Computerized heart sounds analysis. *Comput Biol Med* 38:263–280
2. Goda MÁ, Hajas P (2016) Morphological determination of pathological PCG signals by time and frequency domain analysis. In: *Computing in cardiology conference (CinC)*, pp 1133–1136
3. Abdollahpur M et al (2016) Cycle selection and neuro-voting system for classifying heart sound recordings. *Comput Cardiol* 43:176–238
4. Shahid I, Imran S, Usman A (2018) Localization and classification of heart beats in phonocardiography signals —a comprehensive review. *J Adv Sig Process* 2018(1):26
5. Abo-Zahhad M et al (2011) A comparative approach between cepstral features for human authentication using heart sounds. *Signal Image Video Process* 10:843–851
6. Abbas AK, Bassam R (2009) Phonocardiography signal processing. *Synthesis Lect Biomed Eng* 4(1):1–194
7. NivithaVarghees V et al (2014) A novel heart sound activity detection framework for automated heart sound analysis. *Biomed Signal Process Control* 13:174–188
8. Deng S-W, Han J-Q (2016) Towards heart sound classification without segmentation via autocorrelation feature and diffusion maps. *Futur Gener Comput Syst* 60:13–21
9. Kao W-C, Wei C-C (2011) Automatic phonocardiography signal analysis for detection heart valve disorders. *Expert Syst Appl* 38(6):6458–6468
10. Yan Z et al (2010) The moment segmentation analysis of heart sound pattern. *Comput Methods Programs Biomed* 98(2):140–150
11. Bertrand O, Bohorquez J, Pernier J (1994) Time-frequency digital filtering based on an invertible wavelet transform: an application to evoked potentials. *IEEE Trans Biomed Eng* 41(1):77–88
12. Manasrakshit SD (2018) An efficient ECG denoising methodology using empirical mode decomposition and adaptive switching mean filter. *Biomed Signal Process Control* 40:140–148
13. Huang N, Shen Z, Long S, Wu M, Shih H, Zheng Q, Yen N, Tung C, Liu H (1998) The empirical mode decomposition and the Hilbert spectrum for nonlinear and non-stationary time series analysis. *Proc R Soc A Math Phys Eng Sci* 454:903–995
14. Salman AH, Ahmadi N, Mengko R, Langi AZ, Mengko TL (2015) Performance comparison of denoising methods for heart sound signal. In: *2015 International symposium on intelligent signal processing and communication systems (ISPACS)*, November 9–12

15. Jaros R et al (2018) Use of a FIR filter for fetal phonocardiography processing. Department of Cybernetics and Biomedical Engineering, Faculty of Electrical Engineering and Computer Science, VSB–Technical University of Czech Republic
16. Jagriti Bhatore, Vinod K Sonkar (2016) An optimized analysis of phonocardiogram signals using discrete wavelet transform. *Int J Softw Hardware Res Eng* 4:27–63
17. Boussaa M et al (2016) Comparison of MFCC and DWT features extractors applied to PCG classification. In: 11th International conference on intelligent systems: theories and applications (SITA). IEEE, New York
18. Jain PK, Tiwari AK (2016) An adaptive method for shrinking of wavelet coefficients for phonocardiogram denoising. Elsevier, New York, pp 1–5
19. Jain PK, Tiwari AK (2017) An adaptive thresholding method for the wavelet based denoising of phonocardiogram signal. *Biomed Signal Process Control* 38:388–399

# Modal Study on Isotropic Spherical Cap and Functionally Graded Spherical Panel Using COMSOL



Pankaj Sharma, Ashish Khinchi, and Rahul Singh

**Abstract** This research article investigates the free vibration behaviour of functionally graded spherical (FGM) panel and isotropic spherical cap. The mechanical parameters are continuously graded along thickness direction according to power law gradation (P-FGM). The natural frequencies and corresponding mode shapes are obtained using FE software COMSOL Multiphysics. The variation of power law indices with natural frequencies under different end support is also reported in detail.

**Keywords** Vibration study · FGM—spherical panel · Isotropic spherical cap · Power law · COMSOL

## 1 Introduction

Functionally graded materials (FGMs) are the microscopically heterogeneous material that facilitates the continuous and directional gradation of material properties [1]. Generally, FGMs have possessed several advantages over composite materials; for example, FGMs can withstand very high operating temperature while composites fail due to debonding or delamination phenomenon [2]. Spherical caps are being significantly used in aerospace and other applications such as roof domes, pressure vessels and submarine. Spherical panels are used in various branches of engineering applications such as hydraulic structures, architectural structures, missiles, airplane, ships and instruments due to lightweight.

---

P. Sharma · R. Singh

Department of Mechanical Engineering, Rajasthan Technical University, Kota, Rajasthan, India  
e-mail: [psharma@rtu.ac.in](mailto:psharma@rtu.ac.in)

R. Singh

e-mail: [rahulsingh18@rtu.ac.in](mailto:rahulsingh18@rtu.ac.in)

A. Khinchi (✉)

Department of Mechanical Engineering, Vedant College of Engineering and Technology, Kota, Rajasthan, India

## 2 Literature Survey

The free vibration characteristics of isotropic and orthotropic spherical caps are studied by Gautham and Ganesan [3]. The governing equations of motion are solved using the finite element technique which is based on higher-order shear deformation method. Wu and Heyliger [4] examined the modal behaviour of asymmetric and axisymmetric piezoelectric sphere-shaped shells. The governing equations are derived using two-dimensional (2-D) first-order shear deformation method under clamped and hinged boundary conditions. Biswal and Mohanty [5] investigated the modal behaviour of multilayer sandwich sphere-shaped shell panels with elastic face layers and viscoelastic material core layers. In this analysis, FSDT was adopted along with Hamilton's principle for derive equation of motion.

Harmonic behaviour of circular and parabolic panel made of FGMs studied by Zhang et al. [6]. The FGM panel is made with the help of ceramic phase and metal phase. The mechanical constants are continuously vary across shell thickness according to rule of mixture. Nonlinear and linear deformation analyses of FGM spherical shell panel under thermo-mechanical load were presented by Kar and Panda [7]. In their work, material properties were varied in accordance with Voigt's micro-mechanical rule and rule of mixture (P-FGM). The nonlinear GE of FG shell panel was derived with the help of vibrational principle. Clamped, simply-supported and free end conditions are used in this research article. The nonlinear free harmonic behaviour of functionally graded sphere-shaped shell panel under nonlinear thermal effect was explained by Kar et al. [8]. The FG material (FGMs) constituents were depends on temperature ( $T$ ) and the thermal conductivity ( $k$ ). The resultant material properties of the FGM were obtained with the help of Voigt micro-mechanical law through rule of mixture (P-FGM). HSDT was adopted by the authors. Pradyumna and Bandyopadhyay [9] carried out the harmonic analysis of curved panel using high-order finite element method (HSDT). Effects of parameter on panel geometry and boundary conditions were also studied. The detail study of FGM structures with and without piezoelectric effect using COMSOL is available in the literature [10–21].

## 3 Finite Element Model

A three-dimensional (3-D) finite model is used for present work as shown in Fig. 1. The fine meshing is used in the present work.

## 4 Material Gradation

The spherical panel is composed of functionally graded materials which are combination of two materials, one is metal phase and other is ceramic phase. The gradation

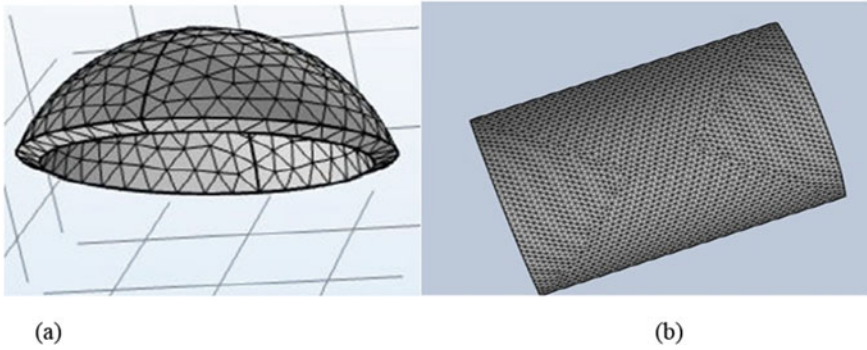


**Fig. 1** Finite element model **a** spherical cap **b** spherical panel

**Table 1** Mechanical constants

Mechanical parameters	Aluminium (Al)	Aluminium Oxide (Al <sub>2</sub> O <sub>3</sub> )
<i>V</i>	0.3	0.3
<i>P</i>	2700 (Kg m <sup>3</sup> )	3800 (Kg m <sup>3</sup> )
<i>E</i>	70 Gpa	380 Gpa

of material constants is such that the composition of ceramic is increased gradually from bottom to top surface while top to bottom composition of metal phase is increased gradually; hence, top surface is pure ceramic while the bottom surface is pure metal. Material gradation followed by rule of mixture (P-FGM) [22] (Table 1).

The material parameters are given as

$$E = (E_c - E_m) + E_m \tag{1}$$

$$\rho = (\rho_c - \rho_m)V_f^p + \rho_m \tag{2}$$

$$V_f = \left( \frac{z}{h} + \frac{1}{2} \right) \tag{3}$$

## 5 Validation Study

To check the authenticity of the work, validation study is carried out. For this purpose, an isotropic spherical cap made of mild steel is considered. In this study, results are obtained for CCCC boundary condition. The parameters used for computations are as follows, *h/R* = 0.1 and 0.05. The non-dimensional fundamental frequency is given

**Table 2** Accuracy of the present work (COMSOL), comparison of frequencies (MHz) under CCCC boundary condition ( $h/R = 0.1$  and  $0.05$ ) with [3]

$h/R$	Mode	Ref. [3]	COMSOL	Error %
0.1	2	0.2319	0.23309	0.51
	3	0.297	0.29821	0.33
	4	0.3628	0.36084	0.54
0.05	(1,1)	0.08418	0.084091	0.10
	(2,1)	0.1011	0.10274	1.6
	(2,2)	0.13788	0.13753	0.25
	(4,1)	0.1307	0.13068	0.015
	(4,2)	0.19681	0.1936	1.63

by  $\Omega$  which is equal to  $\Omega = 2\pi f R \left( \frac{\rho(1-\nu^2)}{E} \right)^{\frac{1}{2}}$  which is used for all the computational purpose. Here,  $E$  is the elastic modulus,  $f$  is the free vibration frequency,  $\rho$  denotes the density and  $\nu$  is Poisson’s ratio. The values of  $E$  and  $\nu$  are taken as  $2.1 \times 10^5$  MPa and 0.3, respectively. Table 2 displays fundamental frequencies (MHz) of isotropic spherical cap under CCCC support condition. It is observed that outcome acquired by COMSOL is exactly matched with data in Ref. [3].

## 6 Parametric Study for Spherical Panel

Free vibration behaviour of spherical panel is taken into account for parametric study. The mechanical characteristics are graded along thickness direction from bottom to top level according to the rule of mixture (P-FGM). Mechanical constants are presented in Table 1. The geometrical parameters are taken as length ( $a$ ), planeform diameter ( $c$ ) and thickness ( $h$ ) as shown in Fig. 2. For several data of power law indices, fundamental natural frequencies are reported under clamped and free end conditions. The fundamental natural frequencies are given in Hz. The fundamental frequencies and corresponding deformed pattern shape are obtained with the help of FEA application software (COMSOL 5.4).

**Fig. 2** Spherical panel



### 6.1 Effect of Power Law Index on Natural Frequencies of FGM Spherical Panels Under (C-C-C-C) End Support

For this study, power law index ( $p$ ) is varied in the range  $p = 1$  to  $p = 6$  (Fig. 3). The dimensions are taken as  $a = 6$  m,  $c = 3$  m and  $h = 0.2$  m. Mechanical constants are given in Table 1. Further, the natural frequencies and corresponding mode shapes for several values of power law indices under C-C-C-C end support are obtained using COMSOL and presented in Table 3 and Fig. 4, respectively.

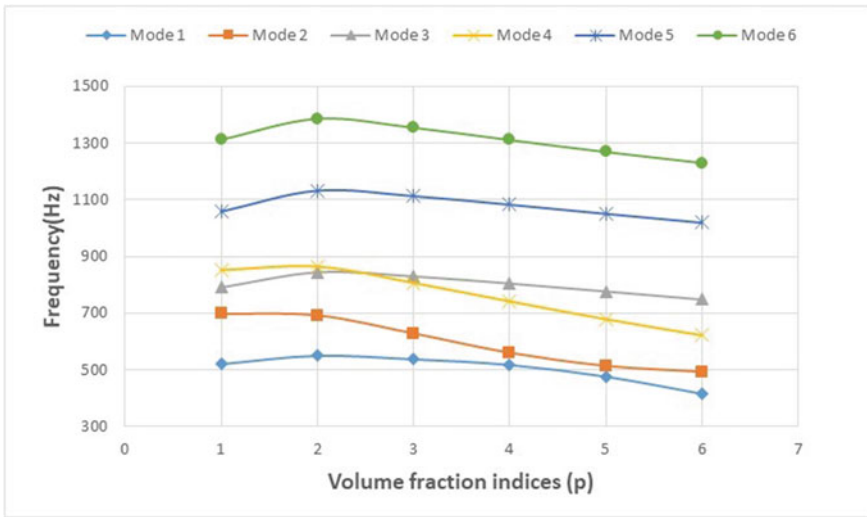


**Fig. 3** Variation of power law indices with natural frequencies for a FGM spherical panel under CCCC end support

**Table 3** Natural frequencies of FGM spherical panel ( $a = 6$  m,  $c = 3$  m and  $h = 0.2$  m) under C-C-C-C end support using power law model

Mode no/power law indices ( $p$ )	$p = 1$	$p = 2$	$p = 3$	$p = 4$	$p = 5$	$p = 6$
Mode 1	520.1	549.65	537.1	517.39	476.17	415.61
Mode 2	698.21	692.4	628.77	560.63	514.53	493.35
Mode 3	790.74	844.16	829.86	804.64	776.72	748.1
Mode 4	852.09	864.52	806.93	741.81	678.74	621.95
Mode 5	1058.4	1132	1112.8	1082.6	1050.3	1018.9
Mode 6	1311.9	1385.6	1353.9	1310.7	1268.4	1230



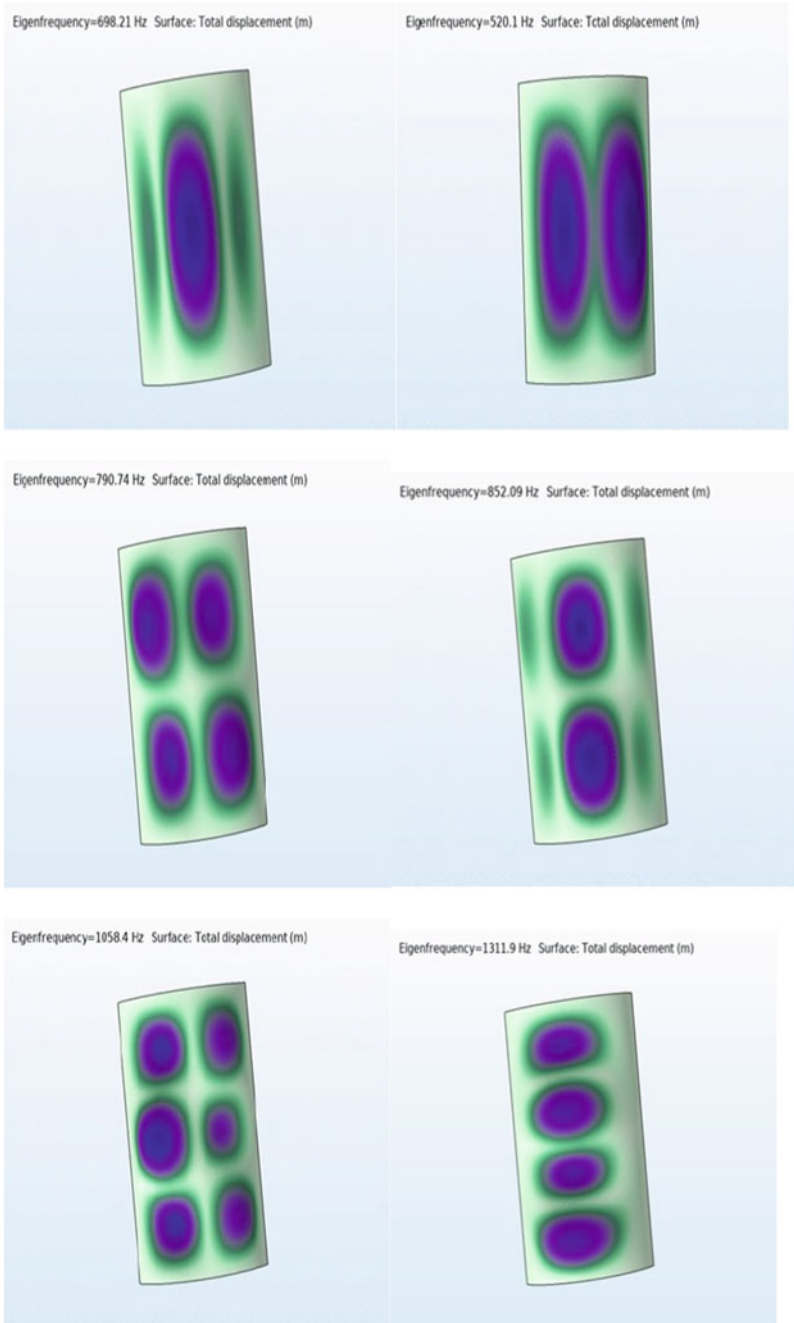
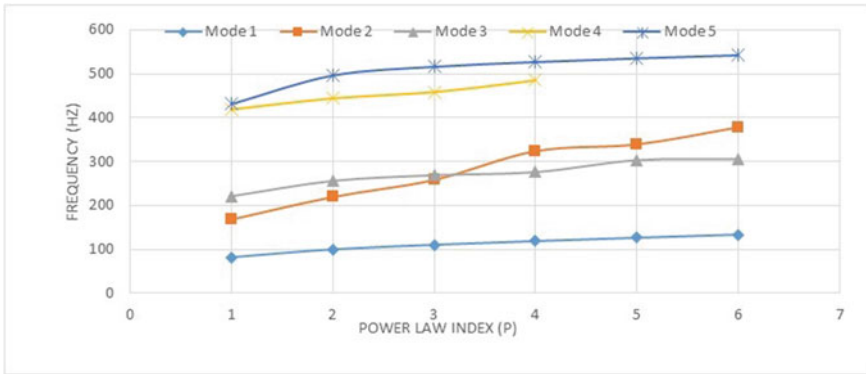


Fig. 4 Mode shape of spherical panel under CCCC end condition



**Fig. 5** Natural frequencies-volume fraction index ( $p$ ) curve for a FG-spherical panel under F-F-F-F boundary condition

**Table 4** Natural frequency of FGM spherical panel when  $a = 6$  m,  $c = 3$  m and  $h = 0.2$  m under FFFF boundary condition under power law

Mode/Power law index ( $p$ )	$p = 1$	$p = 2$	$p = 3$	$p = 4$	$p = 5$	$p = 6$
1	81.927	100.01	110.28	118.69	126.38	133.55
2	167.84	219.22	258.21	323.73	339.27	378.16
3	221.08	255.91	268.81	275.92	303.22	305.75
4	418.79	444.12	458.54	485.12	-	-
5	430.98	496.14	515.97	526.77	535.28	542.38

### 6.2 Effect of Power Law Indices on Natural Frequencies of FGM Spherical Panel Under FFFF Boundary Condition

For this study, power law index ( $p$ ) is varied in the range  $p = 1$  to  $p = 6$  (Fig. 5). The dimensions are taken as  $a = 6$  m,  $c = 3$  m and  $h = 0.2$  m. Mechanical characteristics are shown in Table 1. At power law index ( $p = 5$  and  $p = 6$ ) mode shape is distorted. The fundamental natural frequencies (Hz) for F-F-F-F end support are displayed in Table 4, and corresponding mode shapes are shown in Fig. 6.

## 7 Summary and Conclusions

The natural vibration characteristics of isotropic spherical cap and FGM spherical panel is carried-out in detail. Vibration behaviour of FGM spherical structures are studied, where mechanical constants are graded along thickness direction using rule

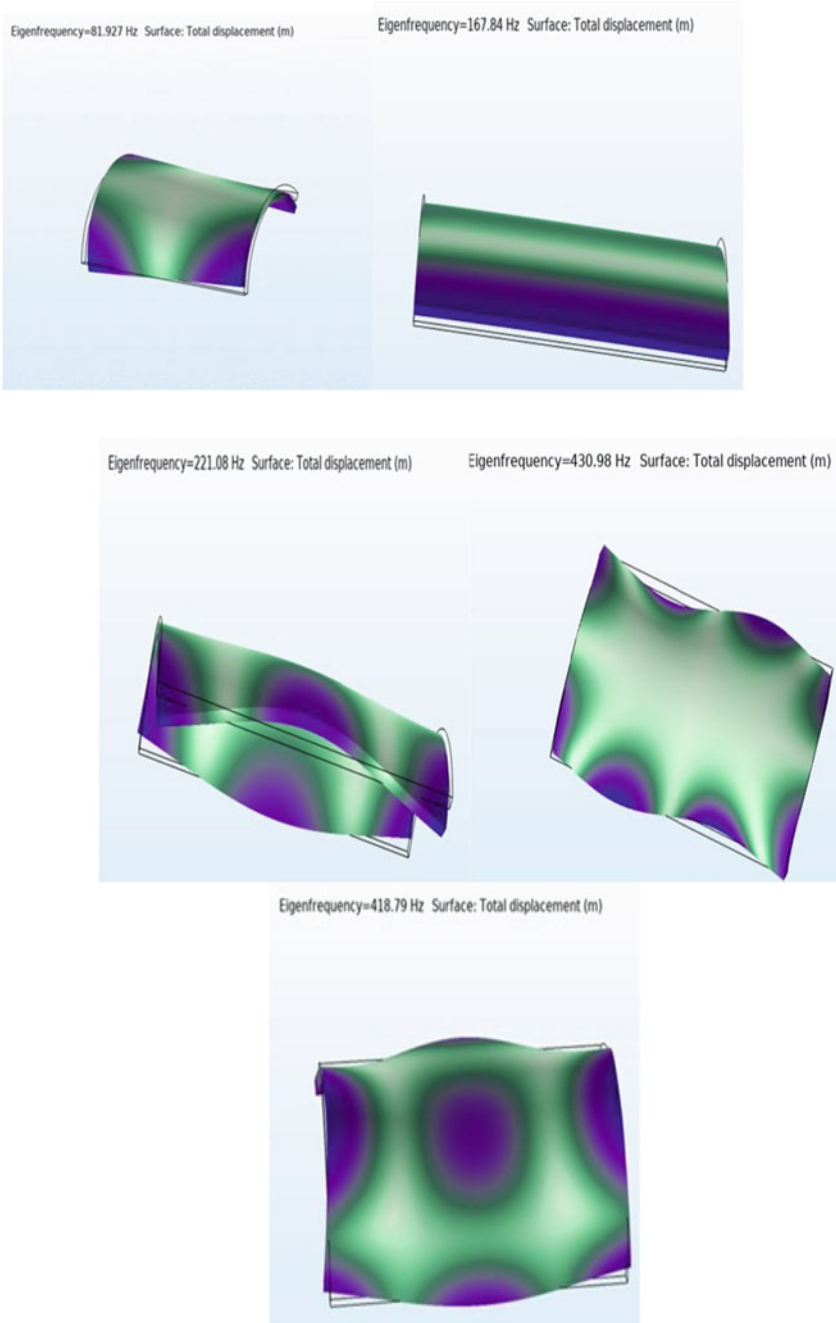


**Fig. 6** Mode shape of spherical panel under FFFF boundary condition

of mixture (P-FGM). The natural frequencies are computed using FEA software COMSOL (version 5.4) for wide range of power law index.

The following observations are made:

- In the spherical panel, with increment in volume fraction index, natural frequencies decline under CCCC end support and increment under F-F-F-F end support.
- It is observed that in CCCC end support the natural frequencies are higher as compared to FFFF end support.

## References

1. Khinchi A, Sharma P (2020) Free vibration analysis of isotropic spherical cap and FG-spherical cap with cut-out using COMSOL. AIP Conf Proc 2220(1):130074. <https://doi.org/10.1063/5.0001299>
2. Sharma P (2019) Vibration analysis of functionally graded piezoelectric actuators. Springer, New York, NY. <https://doi.org/10.1007/978-981-13-3717-8>
3. Gautham BP, Ganesan N (1997) Free vibration characteristics of isotropic and laminated orthotropic spherical caps. J Sound Vib 204(1):17–40. <https://doi.org/10.1006/jsvi.1997.0904>
4. Wu Y-C, Heyliger P (2001) Free vibration of layered piezoelectric spherical caps. J Sound Vib 245(3):527–544. <https://doi.org/10.1006/jsvi.2001.3569>
5. Biswal DK, Mohanty SC (2019) Free vibration study of multilayer sandwich spherical shell panels with viscoelastic core and isotropic/laminated face layers. Compos B Eng 159:72–85. <https://doi.org/10.1016/j.compositesb.2018.09.075>
6. Zhang H, Shi D, Wang Q, Qin B (2017) Free vibration of functionally graded parabolic and circular panels with general boundary conditions. Curved Layered Struct 4(1):52–84. <https://doi.org/10.1515/cls-2017-0006>
7. Kar VR, Panda SK (2016) Geometrical nonlinear free vibration analysis of FGM spherical panel under nonlinear thermal loading with TD and TID properties. J Therm Stresses 39(8):942–959. <https://doi.org/10.1080/01495739.2016.1188623>
8. Kar VR, Panda SK (2015) Nonlinear flexural vibration of shear deformable functionally graded spherical shell panel. Steel Compos Struct 18(3):693–709. <https://doi.org/10.12989/scs.2015.18.3.693>
9. Pradyumna S, Bandyopadhyay JN (2008) Free vibration analysis of functionally graded curved panels using a higher-order finite element formulation. J Sound Vib 318(1–2):176–192. <https://doi.org/10.1016/j.jsv.2008.03.056>
10. Singh R, Sharma P (2019) A review on modal characteristics of FGM structures. AIP Conf Proc 2148(1):030037. <https://doi.org/10.1063/1.5123959>
11. Sharma P, Parashar SK (2016) Exact analytical solution of shear-induced flexural vibration of functionally graded piezoelectric beam. AIP Conf Proc 1728(1):020167. <https://doi.org/10.1063/1.4946218>
12. Sharma P (2020) Vibration analysis of FGP actuator due to longitudinal piezoelectric coupling coefficient. AIP Conf Proc 2220(1):130072. <https://doi.org/10.1063/5.0001180>
13. Parashar SK, Sharma P (2016) Modal analysis of shear-induced flexural vibration of FGPM beam using generalized differential quadrature method. Compos Struct 139:222–232. <https://doi.org/10.1016/j.compstruct.2015.12.012>
14. Sharma P, Parashar SK (2016) Free vibration analysis of shear-induced flexural vibration of FGPM annular plate using generalized differential quadrature method. Compos Struct 155:213–222. <https://doi.org/10.1016/j.compstruct.2016.07.077>

15. Sharma P (2018) Efficacy of harmonic differential quadrature method to vibration analysis of FGPM beam. *Compos Struct* 189:107–116. <https://doi.org/10.1016/j.compstruct.2018.01.059>
16. Singh R, Sharma P (2021) Vibration analysis of an axially functionally graded material non-prismatic beam under axial thermal variation in humid environment. *J Vib Control* 107754632110371. <https://doi.org/10.1177/10775463211037150>
17. Sharma P, Singh R, Hussain M (2020) On modal analysis of axially functionally graded material beam under hygrothermal effect. *Proc Inst Mech Eng Part C: J Mech Eng Sci* 234(5):1085–1101. <https://doi.org/10.1177/0954406219888234>
18. Sharma P, Meena M, Khinchi A (2021) Modal study of bi direction FGM plate. *Mater Today: Proc* 44:1604–1608. <https://doi.org/10.1016/j.matpr.2020.11.814>
19. Sharma P, Khinchi A (2021) On frequency investigation of bi-directional FGM beam under thermal effect. *Mater Today: Proc* 47:6089–6092. <https://doi.org/10.1016/j.matpr.2021.05.022>
20. Sharma P, Khinchi A, Jain A (2021) Free vibration analysis of FGM structures using FEM technique. In: Bag S, Paul CP, Baruah M (eds) *Next generation materials and processing technologies*. Springer proceedings in materials, vol 9. Springer, Singapore. [https://doi.org/10.1007/978-981-16-0182-8\\_31](https://doi.org/10.1007/978-981-16-0182-8_31)
21. Sharma P, Kataria SD, Khinchi A (2021) On modal analysis of bi-direction FGM beam under general end conditions. *Mater Today: Proc* 44:1853–1856. <https://doi.org/10.1016/j.matpr.2020.12.015>
22. Sharma P, Singh R (2019) Investigation on modal behaviour of FGM annular plate under hygrothermal effect. *IOP Conf Ser: Mater Sci Eng* 624(1):012001. <https://doi.org/10.1088/1757-899X/624/1/012001>

# Enhancement of Mechanical Properties of Fly Ash Reinforced Epoxy Composite



Chandramani Goswami, Ratnesh Sharma, Shiv Ranjan Kumar, Ajay Singh, and Anand Prakash

**Abstract** In order to fulfill the increasing demand of electricity, people are dependent upon coal-based thermal power plants. The amount of fly ash waste is also increasing, which leads to air and water pollution, complex problem, and harmful effects on the environment, human health, and agriculture. Therefore, researchers are working on utilizing fly ash in various applications such as automobile and aircrafts fields. In this work, four different epoxy composites were fabricated with different fly ash content from 0 to 15 wt%, and then, the tensile strength and hardness of the fabricated composite were evaluated. The finding of results indicated that for particulate filled composites, the tensile strength and hardness were increased with the addition of fly ash content for most of the composition. However, there was a fall in the tensile strength at the fly ash content of 5 wt%.

**Keywords** Fly ash · Mechanical properties · Epoxy composite · Hardness

## 1 Introduction

Despite India's ambitious plan to increase renewable energy sources, electric power generation is still dependent on thermal power plants that are using coal. The thermal power plants contributed 73% of India's total power, and within the thermal power plant, 90% is based on coal fuel resources. However, one of the major waste byproducts obtained after the combustion of coal in a coal-based thermal plant is fly ash (FA). Coal consists of one or more of harmful and poisonous elements such as As, Pb, B, Cr, Co, Se, Hg, Mo, Tl, Mn, and V. FA includes oxides of silicon, calcium, iron, and aluminum. The amount of fly ash waste is also increasing which leads to air and water pollution, complex problem, and harmful effects on environment, human

---

C. Goswami (✉)

Department of Mechanical Engineering, ACEIT, Jaipur, India

R. Sharma

Department of Mechanical Engineering, Poonima College of Engineering, Jaipur, India

S. R. Kumar · A. Singh · A. Prakash

Department of Mechanical Engineering, JECRC University, Jaipur, India

© The Author(s), under exclusive license to Springer Nature Singapore Pte Ltd. 2022

101

M. Vashista et al. (eds.), *Recent Innovations in Mechanical Engineering*,

Lecture Notes in Mechanical Engineering, [https://doi.org/10.1007/978-981-16-9236-9\\_10](https://doi.org/10.1007/978-981-16-9236-9_10)

health, and agriculture. Therefore, the major problem faced by the researchers is to utilize, recycle, and dispose of FA. Further, utilization of FA will also reduce the space used for disposal of FA. Fly ash has been widely used in many applications, such as mining, construction, manufacturing, and agriculture [1, 2]. FA reduces greenhouse gas emissions; therefore, FA can be a suitable replacement of cement. FA has also been used as an absorbent for the removal of pollutants. Fly ash has been used as a significant ingredient in the composite and alloy materials that have promising applications in manufacturing, automobile, electronic industry, aerospace industry, etc.

It has also been tried to manipulate formulations in different composites. In polymer-based composite, it experimented with other polymers such as high-density polyethylene (HDPE) [3], polypropylene [4], and epoxy [5]. However, the presence of  $-OH$  groups with metal and nonmetal in the form of  $Si-OH$ ,  $Al-OH$  in FA can lead to poor bonding with the polymeric materials. Therefore, the surface of fly ash are modified with the coupling agent to improve the interaction bonding between the resin and fly ash [6]. The addition of fly ash improved the hardness and tensile strength of polyethylene terephthalate composite.

Some researchers have reported that the incorporation of fly ash content led to increase in the tensile strength of  $Al_2O_3$  reinforced LM25 MMC [7–9]. Apart from fly ash content, the size of fly ash particles also plays a vital role in modifying the mechanical properties of the epoxy composite. At larger filler size of fly ash, tensile strength did not vary significantly, but at lower weight fraction, tensile strength improved with the decrease in particle size of fly ash [10]. The hardness of the Al6061 alloy composite was increased with an increase of fly ash [11]. In contrast, it is also reported that hardness was decreased with the addition of fly ash content. On one side, use of fly ash provides one of the possible solution for the disposal of coal waste, and on the other side, it improves mechanical and physical properties of alloy and composite [12]. The better wear resistance fly ash reinforced alloy and composite are obtained at low cost using advanced and precise processes [13].

## 2 Experimental Details

### 2.1 Materials

An araldite epoxy resin and hardener procured from Savita Chemicals Jaipur were used as a matrix. Fly ash was acquired from Kota thermal power plant, Kota, Rajasthan, India. The properties of fly ash are presented in Table 1.

**Table 1** Properties of fly ash

S. no	Samples	Properties
1	Fineness ( $\text{mm}^2/\text{kg}$ )	334
2	Specific gravity	3.1
3	Final setting time (minutes)	440
4	Silica (wt%)	35–60%

**Table 2** Composition of composite with varying fly ash content

S. no.	Samples	Epoxy (g)	Hardener (g)	Fly ash (wt%)
1	P	100	80	0
2	Q	100	80	5
3	R	100	80	10
4	S	100	80	15

## 2.2 Fabrication and Mold Preparation

### 2.2.1 Pattern Preparation

A glass strip-based model was used for casting. The hand layup method was used to fabricate the composite with the help of two glass slab molds of dimension 180 mm  $\times$  90 mm  $\times$  5 mm.

### 2.2.2 Mixing Preparation

Resin and hardener were taken in a container in the composition as presented in Table 2. The materials were uniformly mixed using stirrer to assure that there is no air entrapped inside the solution.

### 2.2.3 Casting of Slabs

The material from the container was transferred to mold cavity. Leveling was done to uniformly fill the cavity. Epoxy-based polymer composites were prepared adding different weight percentages of fly ash (0–15 wt%) in the mixture of resin and hardener proper ratio (100:80). The composite slabs were prepared using hand layup method followed by applying pressure using compression molding technique.

Different weight percentage combinations from 0–15 wt% of fly ash with araldite epoxy were used for making four different samples as given in Table 2.



### 2.2.4 Curing

After the preparation of mold, curing was done and kept the prepared samples for 48 h at room temperature; after 48 h slabs were taken out from the mold and cleaned.

## 2.3 Mechanical Properties Analysis

In calculating the hardness and the tensile strength, ASTM: D256 and ASTM: D638, respectively, were used for sample preparation.

The universal testing machine (UTM) was used to calculating the tensile strength, whereas the hardness test of the specimen was performed on a Vickers hardness tester.

## 3 Results and Discussion

### 3.1 Tensile Strength of Epoxy-Based Fabricated Composite with Different FA Content

The mechanical characterization of epoxy-based composite with varying fly ash content included tensile strength and hardness.

The tensile strength of different polymer matrix samples was analyzed as per the American standard (ASTM: D638). Figure 1 indicated that the tensile strength of composite were 38 MPa, 25 MPa, 33 MPa, and 41 MPa for fly ash content 0 wt%, 5 wt%, 10 wt%, and 15 wt%, respectively. The composite with P sample indicated better tensile strength as compared to other different samples. This increase in tensile strength corresponding to increase in fly ash was attributed to the fact that intermolecular bonding was formed between the epoxy resin and fly ash filler. An increase in fly ash content and better interfacial bonding strength could more effectively transfer the tensile load [10]. Hence, P sample indicated the best combination with epoxy composite for tensile strength attribute.

### 3.2 Hardness of Epoxy-Based Fabricated Composite with Different FA Content

The microhardness of epoxy-based composite with varying fly ash content was depicted in Fig. 2. Figure 2 indicated that the composite's microhardness was 50 Hv, 52 Hv, 54 Hv, and 58 Hv for fly ash content 0–15 wt%. It can be seen from Fig. 2 that hardness was increased with the incorporation of fly ash content. This increase

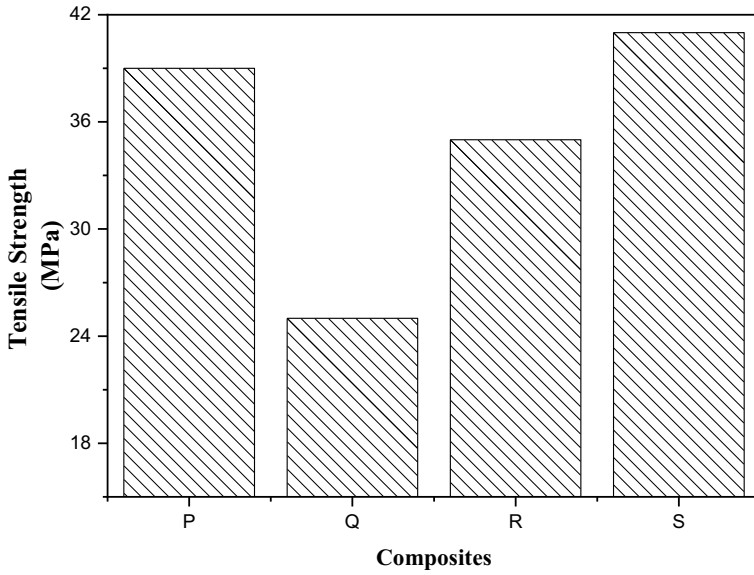


Fig. 1 Tensile strength of composite P, Q, R, and S

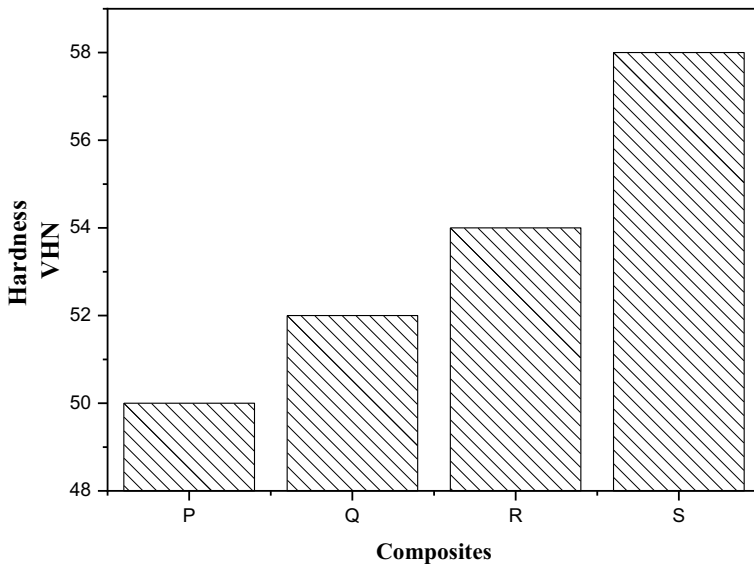


Fig. 2 Hardness of composite with varying fly ash content

in hardness value indicated the wear resistance and resistance against scratch. The increase in hardness was due to presence of inorganic oxide in fly ash.

## 4 Conclusion

Epoxy-based polymer matrix composites with fly ash were fabricated using the hand layup process. The size of fly ash, filler content, and adhesion between epoxy resins and fly ash were the significant factors influencing polymer matrix composite's performance. The addition of fly ash up to 5 wt% initially decreased the tensile strength and further increase in fly ash content increased the composite's tensile strength. However, the hardness of polymer matrix composite was enhanced with the more insertion of fly ash content.

## References

1. Parisara-Envis News Letter (2007) Utility bonanza from dust 2:6
2. Ahmaruzzaman M (2010) A review on the utilization of fly ash. *Prog Energy Combust Sci* 36:327–363
3. Deepthi MV, Sharma M, Sailaja RRN, Anantha P, Sampathkumaran P (2010) Mechanical and thermal characteristics of high density polyethylene–fly ash cenospheres composites. *Mater Des* 31:2051–2060
4. Kulkarni SM (2002) Effects of surface treatments and size of flyash particles on the compressive properties of epoxy based particulate composites. *J Mater Sci* 37:4321–4326
5. Satapathy BK, Das A, Patnaik A (2011) Ductile-to-brittle transition incenosphere-filled polypropylene composites. *J Mater Sci* 46:1963–1974
6. Alkadasi NAN, Hundiwale DG, Kapadi UR (2004) Effect of coupling agent on the mechanical properties of fly ash–filled polybutadiene rubber. *J Appl Polym Sci* 91:1322–1328
7. Patil SR, Motgi BS (2013) A study on mechanical properties of fly ash and alumina reinforced aluminium alloy (LM25) composites. *IOSR J Mech Civil Eng* 7:41–46. <https://doi.org/10.9790/1684-0764146>
8. Mahendra Boopathi M, Arulshri KP, Iyandurai N (2013) Evaluation of mechanical properties of aluminium alloy 2024 reinforced with silicon carbide and fly ash hybrid metal matrix composites. *Am J Appl Sci* 10:219–229. <https://doi.org/10.3844/ajassp.2013.219.229>
9. Sahai RSN, Mahanwar PA (2015) Effect of particle size and concentration of fly ash on mechanical properties of polyphenylene oxide composites. *Int J Chem Environ Biol Sci* 3:64–68
10. Kumar MB, Swamy RP (2011) Evaluation of mechanical properties of Al6061 fly ash and E-glass fiberreinforced hybrid metal matrix composites. *ARPN J Eng Appl Sci* 6:40–41
11. Mahendra KV, Radhakrishna K (2007) Fabrication of Al-4.5% Cu alloy with fly ash MMC and its characterization. *Mater Sci Poland* 25:57–68
12. Guo RQ, Rohatgi PK, Nath D (1996) Compacting characteristics of aluminium-fly ash powder mixtures. *J Mater Sci* 31:5513–5519
13. Golden DM (1994) Solidification processing of metal matrix fly ash particle, composites. *EPRI J* 1:46–49

# Performance Analysis of Wavelet Filters for Heart Rate Variability Analysis



Sarla and Dilbag Singh

**Abstract** Heart rate variability (HRV) analysis yields important insights into the understanding of physiological mechanisms. The HRV analysis is a powerful tool for risk prediction in heart diseases. Most common methods of HRV analysis are fast Fourier transform and autoregressive methods. However, these methods have limitations in the study of long-term nonlinear variations and transient analysis of heart rate variability. Wavelet transform-based HRV analysis overcomes these limitations. This paper identifies the characteristics of wavelet transform in heart rate variability analysis. The number of wavelet filters is suggested in the literature, but every wavelet filter has a specific category of application. To investigate the wavelet filters for heart rate variability analysis, RR tachogram extracted from five minutes of ECG signal recorded from a healthy volunteer. The appropriate wavelet filter should be adaptive to slow and fast variation in the HRV signal. The different wavelet filter performances are assessed, and the observations presented in the results revealed that Db-3 (Daubechies) with six-filter length is the most suitable wavelet filter for HRV analysis.

**Keywords** Heart rate variability · Wavelet transform · Filter · RR interval

## 1 Introduction

There are many mathematical tools which are used for heart rate variability analysis like Fourier transform, autoregressive method and wavelet transform. Discrete Fourier transform is a very popular technique in the frequency domain because it is simple and fast but valid only for stationary signal due to lack of its time resolution [1, 2], while wavelet transforms are used for both stationary and non-stationary kind of signals [3, 4]. Wavelet transform is used for time–frequency domain analysis, and it also works as a filter to take out time-dependent signals [2, 3]. Generally, wavelet

---

Sarla (✉) · D. Singh

Dr. B R Ambedkar National Institute of Technology, Jalandhar, Punjab, India

D. Singh

e-mail: [singhd@nitj.ac.in](mailto:singhd@nitj.ac.in)

decomposes data into distinct frequency component, and after decomposition, every component's resolution is matched to its scale [5, 6].

Heart rate variability (HRV) is a popular tool used for the calculation of cardiac autonomic modulations [7, 8]. Recently studies show that HRV can quickly become one powerful tool for risk prediction in heart disease [9, 10]. HRV provides insight understanding about the relationship between the autonomic nervous system (ANS) and arrhythmia and mechanisms of how ANS influence arrhythmia [11, 12]. The time-varying changes in the heart directly linked with time–frequency estimation HRV which can be easily quantified using time-scale methods, also known as wavelet transform [13, 14]. Wavelet has many shapes, and its aim is to get fit in the shape of the signal that can be analyzed for a good quantitative measurement [15]. Wavelet transform is capable of displaying information such as breakpoints, interference in high derivatives [16]. This work is facilitating a link between the filters used in wavelet transform and power spectral density for the estimation of HRV. From Fig. 1, it observed that there is a discrepancy in the choice of wavelet functions,

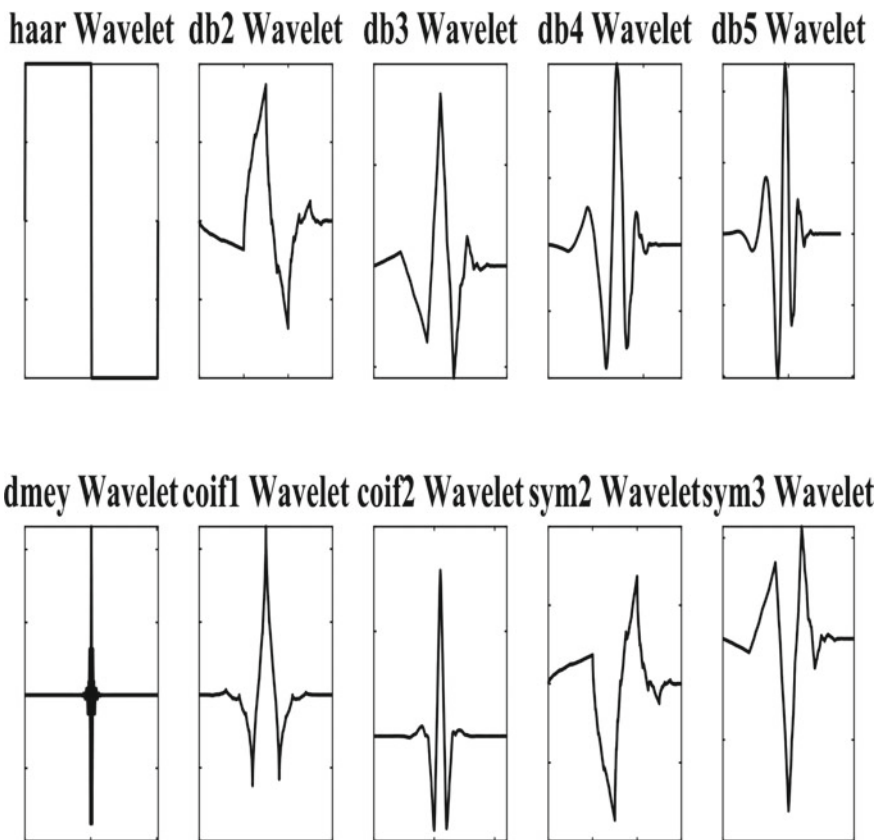


Fig. 1 Selected different wavelet transform

and the selection criteria adopted in their commands are often not reasonable, and performance evaluations are almost absent. Thus, it is required to study this matter of HRV analysis by wavelet. In this paper, the comparison of different types of wavelets is presented with a representation of the instantaneous power of the HRV spectrum.

## 2 Materials and Method

### 2.1 Physiological Recordings

To evaluate wavelet filter performance for HRV analysis, ECG data recorded from a single healthy young volunteer (male, age 23 years) in the supine position in Biomedical Lab in Dr. B R Ambedkar National Institute of Technology, Jalandhar (Punjab) using Biopac® BSL system MP36 and BSL version 3.7.6 Pro.

The acquisition of the ECG signal was performed under dim light conditions and in a noise-free environment. The duration of the ECG recording was 5 min. The subject included for the study possess no history of diabetes mellitus, hypertension, alcohol dependence and other diseases that can affect HRV. Temperature, pulse and blood pressure checked for the possibility of any abnormality. The informed consent form was signed the subject as per institute's Ethical committee guidelines for human subjects.

### 2.2 HRV and Wavelet Transform

Wavelet transform is a mathematical function which is used to divide the data into different frequency components and play an important role in the matching of components resolution with its scale [2, 6]. The large window in wavelet in a signal represents gross features and small window provides detail features. The equation of continuous wavelet transforms for signal  $x(t)$  is–

$$W_a x(b) = \frac{1}{\sqrt{a}} \int_{-\infty}^{\infty} x(t) \Psi^* \left( \frac{t-b}{a} \right) dt, \quad a > 0$$

where 'a' is dilation, 'b' is the translation (both are discretized), '\*' denotes complex conjugate and  $\Psi$  is a wavelet function.

Dyadic wavelet transform of a signal  $x(t)$  is–

$$\text{DyWT}(a, b) = \frac{1}{2^j} \int_{-\infty}^{\infty} x(t) \Psi^* \left( \frac{t-b}{2^j} \right) dt$$

In the discrete-time signal, the dyadic discrete wavelet transform can be a combination of a high-pass filter and low-pass filter. There were seven wavelet scales ( $j = 7$ ) obtained from the wavelet decomposition of signal. During down sampling, the signal is divided into two parts: one is detail signal and other is approximation signal [2, 15]. Detail signal represents the high-pass filter while the approximation signal represents the low-pass filter (Fig. 2). At the moment, the detail coefficient of the filtration collected, while redistributing the approximation into two halves, one is high pass and the other low pass. High-frequency component is obtained from merging the detail signal at scales 5 and 6, while the low-frequency component is obtained from merging the detail signal at scales 3 and 4. The very-low-frequency component obtained from the detail signal at scale 7 (see Fig. 3).

**Fig. 2** Flow chart of wavelet transform-based filter bank evaluation of HRV analysis

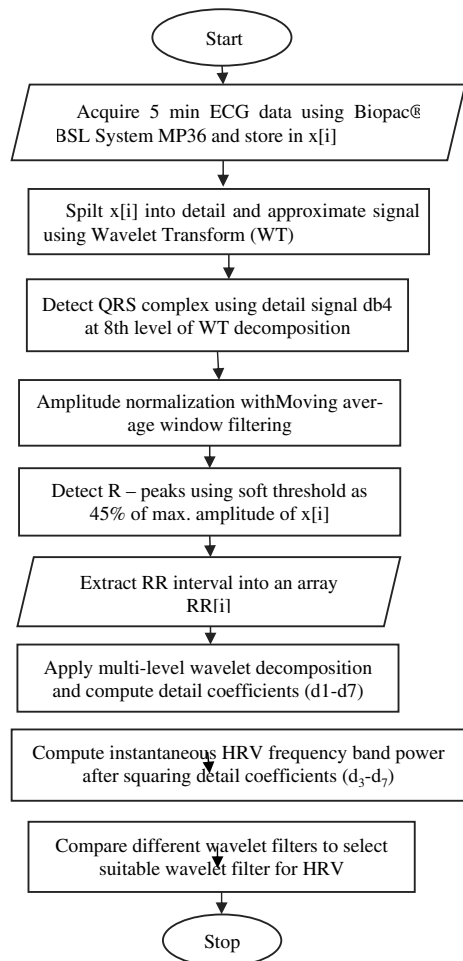


**Fig. 3** Wavelet decomposition of RR tachogram signal to calculate instantaneous HRV frequency bands power [6]: VLF (very low frequency) =  $d_7$  (0.01875 – 0.0375 Hz); LF (low frequency) =  $d_5 + d_6$  (0.0375 – 0.15 Hz); HF (high frequency) =  $d_3 + d_4$  (0.15 – 0.6 Hz)

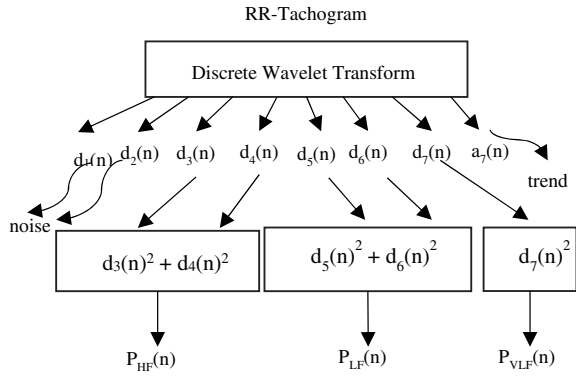
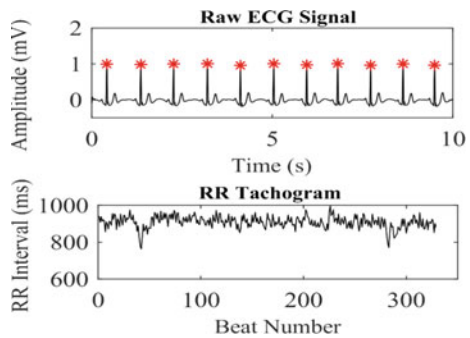


Figure 2 represents the detailed methodology used for this study. In this work, four types of wavelet families are described: Haar Wavelet (HW), Daubechies Wavelet (DW), Discrete Meyer Wavelet and Symmlet Wavelet (SW) [2]. Each wavelet family has different orders of the filter. Daubechies is an orthogonal wavelet that is fully supported [2, 6]. Filter order decides the length of the filter [6]. Higher-order filters provide a higher degree of smoothness in a signal and can be tailored to localize better frequencies, which increases energy compaction. Lower-order filters have a good time localization and save important edge information [6]. Wavelet-based HRV analysis requires a good balance between filter length, degree of smoothness, computational complexity, due to which it prioritizes good localization of time and frequency.

### 3 Results and Discussion

Wavelet transform is a good choice for HRV analysis of ECG because it is orthogonal, smooth and nearly symmetric. In this paper, many standard wavelets were tried but used the one that creates the good performance over a particular application. Figure 4

**Fig. 4** A representative sample of 10 s ECG signal with R peak marked as ‘\*’ sign and corresponding RR tachogram of complete five-minute ECG recording selected for wavelet-based HRV analysis





shows the raw ECG signal and RR tachogram extracted from five minutes of ECG data. The selection of a particular wavelet depends on a particular application. So, the scaling function related to a good wavelet usually resembles that of a given signal. Other important factors like noise sensitivity and errors are to be recognizable. Filter length is one of the factors that affect all decomposition levels of detail coefficient.

The DWT analysis of wavelets such as Db-1 (Haar), Db-2, Db-3, Db-4, Db-5, Dmey, Coif-01, Coif-02, Sym-2 and reporting of results given in Table 1 with Fig. 6 that are representing the instantaneous PSD decomposition of Db-3 wavelet by increasing wavelet order. Instantaneous PSD decompositions are detected to be almost same at VLF, LF and HF levels. Low-order wavelets are needed to identify temporary episodes and higher-order wavelets are a great choice for long-lasting information. Different basis and order distribute the power between different frequency bands. The total PSD is roughly in the same span for all wavelets, and the diffusion of power in the spectral band depending on the wavelet or on order, which also proved from mean and SD values. Figure 5 shows wavelet decomposition of RR tachogram of five-minute ECG signal recorded under resting state in the supine posture, with db3 wavelet filter and  $d_1, d_2, \dots, d_7$  detail signals extracted.

Table 1 shows the comparison of different wavelet filter performance for heart rate variability analysis. In the spectral approximation, the inter-wavelet PSD variance decreases with increasing frequency/scale. Normalized spectral powers continue unobstructed by the order or type of wavelet. Considering the filter length which changes the time-period of all band power after wavelet decomposition and the  $P_{VLF}$  time-period decreased by higher-order filter. There was no signal addition used to ignore the accuracy of results. So, it observed that Haar and symlet-3 are not fitted well in the case of PSD. Figure 6 shows instantaneous PSD for respective HRV frequency bands using wavelet decomposition of RR tachogram of five-minute ECG signal recorded under resting state in the supine posture, with db3 wavelet filter. Now, another concept transient episode detection was focused on many protocols for variable HRV analysis. It can be seen evidently the difference in LF/HF ratio. So, it is obvious that Db-3 wavelet with six-coefficient and minimum filter length represents a good result of variable HRV. So, taking into account the filter length and wavelet coefficients, Db-3 is used in the remaining analysis of HRV.

## 4 Conclusion

This study discussed the comparison of different wavelets and wavelet orders for HRV analysis. Wavelet transform is found to be a tool to analysis transient variation of heart rate variability. The wavelet transform shows spectral changes for specific interval, and it was noted from the observations that db3 as mother wavelet for HRV analysis due to clear changes in LF/HF ratio with lowest filter coefficients, i.e. six. Thus, db3 wavelet filter proposed best fit for heart rate variability analysis.

**Table 1** Comparison of different wavelet filter performance for heart rate variability analysis

Wavelet	$P_{d3}$	$P_{d4}$	$P_{d5}$	$P_{d6}$	$P_{d7} = P_{VLF}$	$P_{LF}$	$P_{HF}$	$P_{Total}$	$P_{nLF}$	$P_{nHF}$	$P_{LF}/P_{HF}$
db1	3657.22	3470.87	7632.52	9594.37	18,973.51	6562.17	5425.40	30,961.08	54.74	45.26	1.21
db2	5209.68	4681.89	4566.17	12,695.22	2835.33	7781.99	7678.31	18,295.63	50.34	49.66	1.01
<b>db3</b>	4084.72	3536.58	3577.17	11,416.62	10,901.14	6408.67	6008.12	23,317.93	51.61	48.39	<b>1.07</b>
db4	4255.62	3794.83	4342.67	6910.13	9224.81	5884.64	6349.32	21,458.77	48.10	51.90	0.93
db5	5080.87	3316.91	4193.36	9418.20	9797.20	7589.13	6960.45	24,346.78	52.16	47.84	1.09
dmey	4247.45	3799.28	4343.53	6936.92	9225.19	5887.02	6343.61	21,455.82	48.13	51.87	0.93
coif1	4254.61	3122.22	3016.40	11,918.78	11,303.25	6600.97	5952.66	23,856.88	52.58	47.42	1.11
coif2	3831.75	3571.34	3264.91	7006.49	4797.11	5344.49	5905.43	16,047.03	47.51	52.49	0.91
sym2	5209.68	4681.89	4566.17	12,695.22	2835.33	7781.99	7678.31	18,295.63	50.34	49.66	1.01
sym3	4084.72	3536.58	3577.17	11,416.62	10,901.14	6408.67	6008.12	23,317.93	51.61	48.39	1.07
sym4	4118.55	3198.14	3584.67	8941.82	14,046.97	6189.46	5883.04	26,119.46	51.27	48.73	1.05

**Bold** indicates db3 behaves as a mother wavelet due to clear changes in LF/RF ratio with lowest filter coefficient

$P_{dj}$  = Mean power of the detail signal at  $j$ th decomposition level

$P_{LF}$  = Mean power of the low-frequency component (0.0375 – 0.15 Hz).

$P_{HF}$  = Mean power of the high-frequency component (0.15 – 0.6 Hz)

$P_{nLF}$  = Normalized low-frequency power,  $P_{LF}/(P_{Total} - P_{VLF})$

$P_{nHF}$  = Normalized low-frequency power,  $P_{HF}/(P_{Total} - P_{VLF})$

$P_{Total} = P_{VLF} + P_{LF} + P_{HF}$

$P_{VLF}$  = Mean power of the very-low-frequency component (0.01875–0.0375 Hz); LF (low frequency) =  $d5 + d6$  (0.0375–0.15 Hz); HF (high frequency) =  $d3 + d4$  (0.15–0.6 Hz)

$P_{LF}/P_{HF}$  = The ratio between the power of LF and HF component

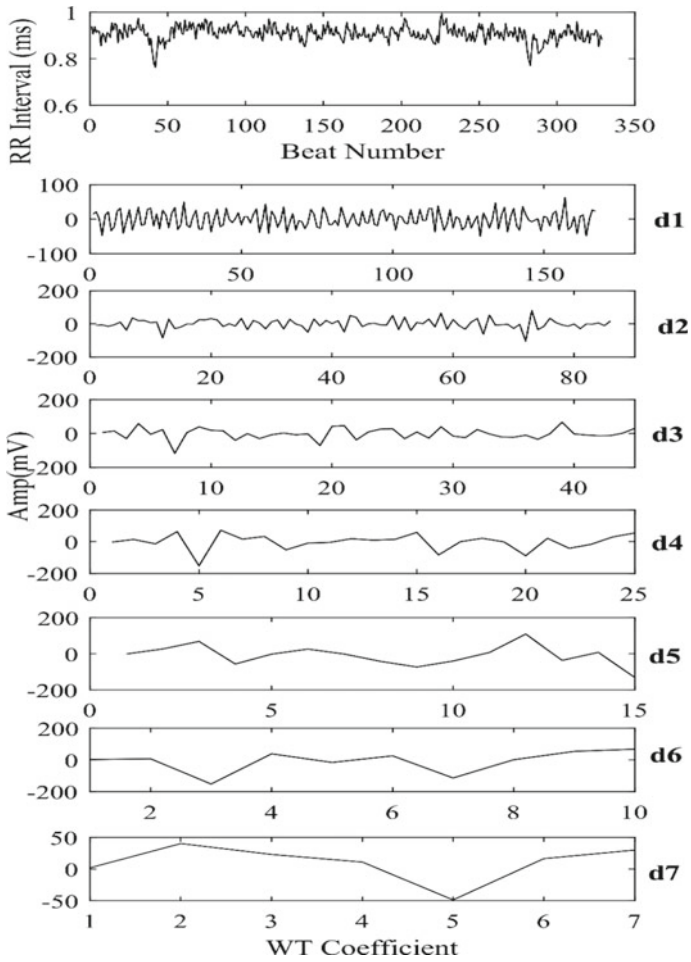


**Fig. 5** Wavelet decomposition of RR tachogram of five-minute ECG signal recorded under resting state in the supine posture, with db3 wavelet filter. Where  $d1, d2, \dots, d7$  indicate detail signals extracted from wavelet decomposition of RR tachogram

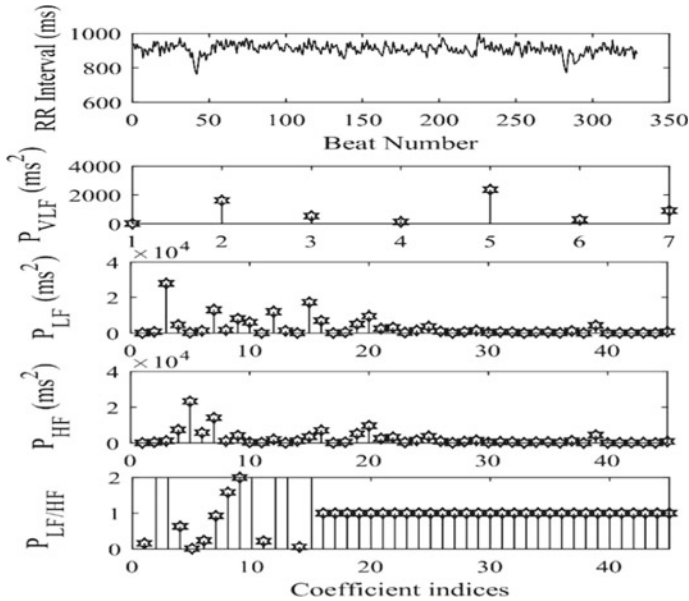


**Fig. 6** Wavelet decomposition of RR tachogram of five-minute ECG signal recorded under resting state in the supine posture, with db3 wavelet filter where  $P_{VLF}$ ,  $P_{LF}$  and  $P_{HF}$  indicates instantaneous PSD for respective HRV frequency bands: VLF (very low frequency) = 0.01875 – 0.0375 Hz; LF (low frequency) = 0.0375 – 0.15 Hz; HF (high frequency) = 0.15 – 0.6 Hz

**Acknowledgements** The authors gratefully acknowledge the support and facilities provided by the Department of Instrumentation and Control Engineering, Dr. B R Ambedkar National Institute of Technology, Jalandhar (Punjab).

## References

1. Dokur Z, Olmez T, Yazgan E (1999) Comparison of discrete wavelet and Fourier transforms for ECG beat classification. *Electron Lett* 35:1502–1504
2. Daubechies I (1992) Ten lectures on wavelets. Siam
3. Mallet Y, Coomans D, Kautsky J, De Vel O (1997) Classification using adaptive wavelets for feature extraction. *IEEE Trans Pattern Anal Mach Intell* 19:1058–1066
4. Sik HH, Gao J, Fan J et al (2017) Using wavelet entropy to demonstrate how mindfulness practice increases coordination between irregular cerebral and cardiac activities. *J Vis Exp* 2017:1–10. <https://doi.org/10.3791/55455>
5. Ajit RMR, Bopardikar S (2002) Wavelet transforms, introduction to theory and applications
6. Singh D, Kumar V, Chawla MPS (2006) Wavelet filter evaluation for HRV signal processing. In: 2006 IET 3rd international conference on advances in medical, signal and information processing-MEDSIP 2006. IET, pp 1–4
7. Gamero LG, Vila J, Palacios F (2002) Wavelet transform analysis of heart rate variability during myocardial ischaemia. *Med Biol Eng Comput* 40:72–78

8. Camm AJ, Malik M, Bigger JT et al (1996) Heart rate variability: standards of measurement, physiological interpretation and clinical use. Task Force of the European Society of Cardiology and the North American Society of Pacing and Electrophysiology
9. Mercy Cleetus HM, Singh D (2014) Multifractal application on electrocardiogram. *J Med Eng Technol* 38:55–61
10. Stein PK, Domitrovich PP, Huikuri HV et al (2005) Traditional and nonlinear heart rate variability are each independently associated with mortality after myocardial infarction. *J Cardiovasc Electrophysiol* 16:13–20
11. Santos CY, Machan JT, Wu W-C, Snyder PJ (2017) Autonomic cardiac function in preclinical Alzheimer's disease. *J Alzheimer's Dis* 59:1057–1065
12. Takatani T, Takahashi Y, Yoshida R et al (2018) Relationship between frequency spectrum of heart rate variability and autonomic nervous activities during sleep in newborns. *Brain Dev* 40:165–171
13. Germán-Salló Z, Germán-Salló M (2016) Non-linear methods in HRV analysis. *Procedia Technol* 22:645–651
14. Singh D, Saini BS, Kumar V, Deepak KK (2006) Time-evolution of cardiovascular variability during autonomic function tests in physiological investigations. In: Annual international conference of the IEEE engineering in medicine and biology society, vol 1, pp 1772–1775. <https://doi.org/10.1109/IEMBS.2006.259322>
15. Thakor NV, Gramatikov B, Sherman D (2006) Wavelet (time-scale) analysis in biomedical signal processing. In: Medical devices and systems. CRC Press, pp 113–138
16. Saxena SC, Kumar V, Hamde ST (2002) QRS detection using new wavelets. *J Med Eng Technol* 26:7–15

# Effect of Stroke Rotation on Discomfort for Assembly Tasks



Farheen Bano, Zulquernain Mallick, Abid Ali Khan, and Nabila Elnahas

**Abstract** This study was performed to investigate the effects of stroke rotation on human performance in terms of discomfort and productivity (duration required to perform given task). Two types of assembly tasks of the plumbing work were considered in this study: socket and threaded pipe assembly and nut and bolt assembly. Twelve right-handed participants volunteered in this study. The participant assembled 50 assemblies of each type for three levels of stroke rotation (30°, 45° and 60°) separately in two sets. The results of MANOVA performed on the recorded data showed that stroke rotation was highly significant on discomfort ( $p < 0.001$ ) and duration ( $p < 0.001$ ) for both given tasks. It was noticed that stroke rotation of 60° was very much comfortable with lowest discomfort and highest productivity. Although it was difficult to control during real-life situations, but may be possible in those tasks which are repetitive and productivity is important to be considered.

**Keywords** Stroke rotation · Discomfort · Productivity · Assembly task

## 1 Introduction

Work-related musculoskeletal disorders (WMSDs) are globally concerned and distributed among both developed and developing industrial countries [1]. WMSDs are considered a serious social problem as they might lead to reduced productivity, medical expenses and in severe cases, wage compensation. Repetitive wrist movement was reported as one of the important factors responsible for the increased discomfort and the risk of injury [2]. A vital concern for ergonomists is to identify

---

F. Bano (✉) · N. Elnahas

Department of Industrial Engineering, King Abdul Aziz University, Jeddah, Saudi Arabia  
e-mail: [fbano@kau.edu.sa](mailto:fbano@kau.edu.sa)

Z. Mallick

Department of Mechanical Engineering, Aligarh Muslim University, Aligarh, India

A. A. Khan

Department of Mechanical Engineering, King Khalid University, Abha, Saudi Arabia

important levels of the factors causing discomfort, and to improve working conditions. However, the improvement is not accepted without the enhanced productivity for efficient and effective human use [3].

Discomfort assessment of physical exertion is considered as the most economical and widely acceptable method by researchers. There are many other ways to predict the risk of injuries such as: biomechanical analysis, electromyography (EMG) and motion analysis [4]. However, these are not simple to perform and do not give the overall assessment of the feeling of the workers. There is a strong evidence for relationship between perceived discomfort and risk of musculoskeletal disorders [5]. Many researchers used discomfort assessment to evaluate the stress in various types of tasks: screwing [6], torqueing [7, 8], gripping and flexion [9].

For an industrial hand tool assembly task, Gooyers and Stevenson [10] investigated the influence of work rate on task demands (muscular effort, posture, etc.) for manual speed fastening work in the simulated environment. The results suggested that an increase in work rate may affect fastening operators with the increased risk of musculoskeletal injuries (MSI), particularly for the work completed at shoulder height. For another simulated assembly task (for electronics assembly work), the interactions of risk factors and the suitability of hand activity level (HAL) and threshold limit values (TVLs) were studied [11]. It was found that both force ( $p < 0.05$ ) and repetition ( $p < 0.05$ ) significantly affected discomfort. In a light assembly work (a computer typing task), Fernandez et al. [12] measured the effect of the arm support system on the level of pain and discomfort felt by volunteers. ErgoRest articulated arm support was found as preferred option for light assembly work.

With the increase quantum of plumbing work, especially due to a lot of construction requirements of developing and developed countries, the reported cases of discomfort are increasing. On the survey of the plumbing work, it was found the absenteeism is a very common phenomenon of the workers involved in plumbing work. Therefore, on observation of the plumbing task, it was found that discomfort may be the reason for absenteeism. In the present study, a couple of small tasks out of many tasks of plumbing were chosen to be considered as example to find out some sort of correlation between task and development of discomfort. The chosen tasks for the investigation involves more of forearm rotation. Therefore, the study of the previous work is significant; that is, highlighting the forearm rotation vs. discomfort score. In the literature, it was found that there is an association between forearm rotation and upper extremity disorder [7, 13, 14]. Khan et al. [9] also investigated the combined effect of forearm rotation on discomfort score for repetitive wrist flexion tasks and found that forearm rotation was highly significant on discomfort. Various other studies also investigated the effect of forearm rotation on discomfort for torqueing tasks [8, 14, 15], and for gripping task [16] and found the significance of postural factors on discomfort.

In the present study, those tasks were considered, which were requiring the forearm rotation at a specific frequency of rotation only. The primary aim of the study was validation of the previous studies of Bano et al. [17–19] to investigate the different levels of stroke rotation on the discomfort for screwing tasks [20], torqueing task [19] and gripping tasks [17]. In line with the previous investigations, it was decided to

validate the findings after applying the results of these studies in some tasks requiring stroke rotations. Therefore, two types of the assembly tasks of the plumbing work were considered as examples: socket and threaded pipe assembly, and nut and bolt assembly. Hence, the objective of the present study was to evaluate the effect of stroke rotation during assembly tasks on human performance in terms of discomfort and required time duration (as sign of productivity). The null hypothesis for the experimental evaluation was assumed as follows:

there was no main or interaction effect of stroke rotation on discomfort and time duration during assembly task.

## 2 Methodology

### 2.1 Experimental Design

Twelve right-handed male college students volunteered in this study with the written consent. Every participant performed two assembly tasks (socket and threaded pipes; nut and bolt) for 50 assemblies of each. The participant assembled at three levels of stroke rotation (30°, 45° and 60°). The independent variable was the stroke rotation for the dependent variables: perceived discomfort score and duration to complete the given task (as a parameter of productivity). One-way multivariate analyses of variances (MANOVA) was applied for the analyses. Each participant had to perform all treatments in a randomized order.

#### Stroke Rotation

Stroke rotation was measured as a function of the amount of rotation of the forearm relative to its neutral position during a complete stroke of tightening of the socket on a threaded pipe, identical to forearm rotation referred in previous studies. As in simulated screwing tasks [20], the participants performed a repetitive screwing with a stroke of 30°, 60° and 90° in the supine direction. In other gripping experiments with torque forces [17, 18], a stroke rotation of 30°, 45° and 60° was considered. These were consistent with the three levels of rotation angles of the forearm (75% prone range of motion (ROM), neutral and 75% supine ROM) in line with the study of O'Sullivan and Gallwey [8]. While in the torquing task Mukhopadhyay et al. [7, 15, 21] considered three levels of rotation of the forearm angles, namely 60% prone ROM, neutral and 60% supine ROM. Consistent with the studies above, the present study examined three levels of stroke rotation at 30°, 45° and 60° from the neutral position in supine. The reason ROM was not considered is because the rotation of the lines is different from the ROM; the task is mandatory in terms of rotation, because the task is not designed based on ROM of the worker rather based on angles.

#### Perceived Discomfort Score

To record the perceived discomfort score for the given experimental task, a code was written in LABVIEW 8.6 to help the participant feed the discomfort on a 10



point 100 mm long Visual Analogue Scale [15, 22]. Participants were explained that perceived discomfort was nothing but the cumulative feeling of discomfort, i.e. numbness, warmth, cramping, pulling, soreness, fatigue aching, tenderness, pressing or pain [13, 23] in the hand arm system, involved in assembly tasks. Participants were asked to enter the level of discomfort perceived in the hand arm system after completing the task in each experimental condition.

### **Time to Complete the Task**

Bano et al. [20] considered number of screws tightened during the given span of time considered as productivity parameter for the screwing task. While, Dempsey et al. [24] defined productivity as the number of revolutions per minute at which screws were turned and reported the strong interactive effect of workplace orientation on working height on productivity for the screwing task. In addition, Finneran and O'Sullivan [25] defined productivity as a duty cycle time inversely proportional to the self-timing cycle time. They concluded that reducing exposure to force and awkward posture could improve productivity in repetitive work. Therefore, in this experiment, the time required for completing the task was considered a dependent variable as a measure of productivity during assembling.

## **2.2 Experimental Set up**

For the experimental investigation, the simulated assembly task was performed in the laboratory. The experimental environment consisted of a work surface, a seat, a support, two boxes with threaded pipes and sockets separately. The working surface/seat height ratio was 1.72 (82.2/45.4 cm), as demonstrated in the previous research, which described in graphs that productivity was greater than 1.72 compared to two other work surface/seat height ratios (1.62 and 1.82) [26]. The box with threaded pipes or nuts was placed on the left side and the box with bushings or bolts on the right side of the work surface. The workstation was designed according to ergonomic principles to reduce the risk of WMSDs and increase productivity.

After designing the workstation, it was decided to place the bins with threaded pipes at 39.4 cm from the participant's left shoulder and that the bin with sockets/bolts was placed at the same distance from the right shoulder. A support was placed 19 cm away from the left tray to support the threaded pipe/nuts. Bins for the installation of threaded pipes/nuts and bushings/bolts have been designed in the laboratory. Their dimensions depend, respectively, on the size and number of threaded pipes/nuts and hoses/socket bolts. The slope of the bins has been considered so that the threaded pipes slide automatically one by one. As a result, the size of the bin for threaded pipes/nuts was 36.4 cm × 23.4 cm and had a slope of 15° on which 50 threaded pipes/nuts were arranged in three rows. Another bin of size 31.6 cm × 28.6 cm and a slope of 27° was used, on which 50 bushings/bolts distributed in 5 rows were placed. The details of the configuration of the setup are shown in Fig. 1 (base and threaded tube) and Fig. 2 (nut and bolt).

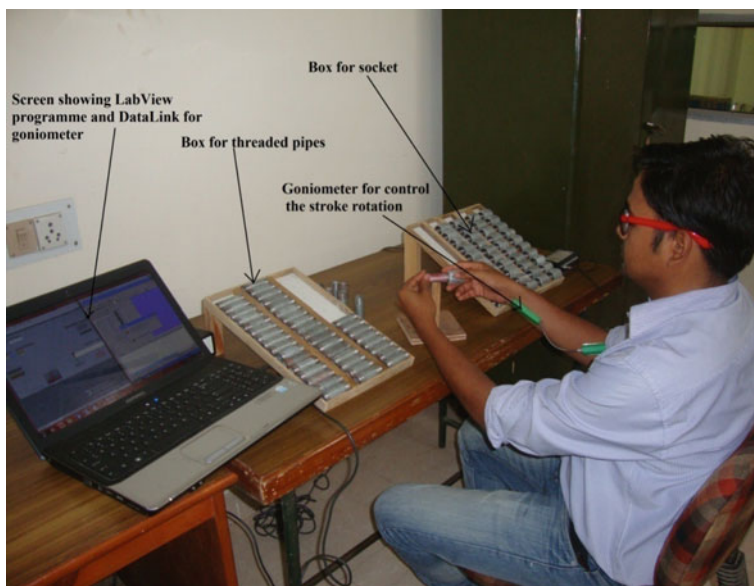


**Fig. 1** Experimental setup for assembling the socket and threaded pipe

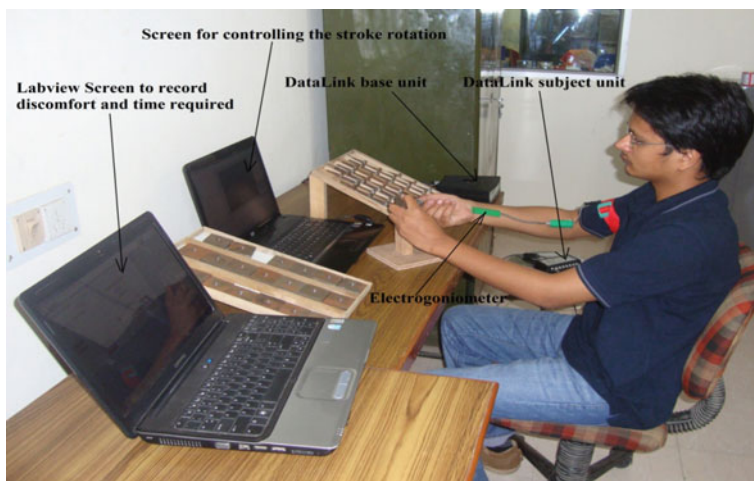


**Fig. 2** Experimental setup for assembling the nut and bolt

### 3 Procedure

To begin the experiment, the participants were informed about the experimental procedure and the risks involved. They were asked to give their prior consent to

the experiment. The electrogoniometer (model Q150 from Biometrics Ltd, UK) was attached to the forearm of the participant to control and monitor the rotation of the stroke using the DATAlink data acquisition system (M/s Biometrics Ltd, UK) interfaced with a PC to obtain the angular deflection form signal on the screen. After the preliminary adjustment, the participants were asked to sit on the chair with their backs supported (Fig. 1). The following steps were explained to the participant for completion of the task.

1. Pick the socket from right hand and threaded pipe from left hand.
2. Leave the threaded pipe on the bracket and place the socket on the mouth of the threaded pipe.
3. Rotated the right forearm from  $0^\circ$  to the assigned stroke rotation (Displayed in random order on the screen, e.g.  $30^\circ$ ), again forearm to neutral, repeat this rotation of the forearm to complete the assembly of the socket and the threaded pipe.
4. Place the assembly in the box placed in the back of the setup.

The experimenter had to record the duration of assembling 50 numbers of each socket and threaded pipe assembly. The participant was asked to mention the discomfort due to the task (Fig. 3) at the end of each experimental exercise. 10 min of rest was provided between the following 50 nut and bolt assemblies. The same steps were also followed for 50 nut and bolt assemblies, and the configuration of the setup was presented in Fig. 2 for all treatments.

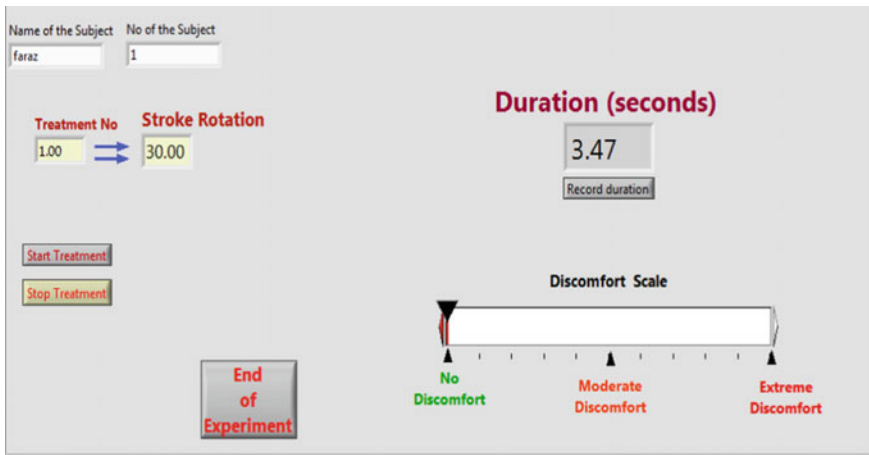


**Fig. 3** Screen shot of LabVIEWvi for recording discomfort and duration

## 4 Results

On the recorded data, statistical analyses were performed using SPSS. The multi-variate analysis of variance (MANOVA) was executed for discomfort and duration for the socket and threaded pipe assembly task, and nut and bolt assembly task.

### Socket and threaded pipe Assembly

The data of perceived discomfort rating and duration for assembling 50 pieces of socket and threaded pipes of every participant for all treatments were summarized in Table 1. It was noticed from the table that perceived discomfort lies in the range of 1.37–8.18. The lowest discomfort score was recorded at 60° stroke rotation and highest discomfort was at 30° stroke rotation for almost all the participants. It was also illustrated that the time taken to complete 50 assemblies of socket and threaded pipes was more at 30° than the other two stroke rotations (45° and 60°); but shortest duration was recorded at 60° stroke rotation.

The mean discomfort score and mean duration with standard deviations for all participants at three levels of stroke rotation for socket and threaded pipe assembly was presented in Table 2.

**Table 1** Data of discomfort and duration for different stroke rotation of each participant for socket and threaded pipe assembly

Participant	Stroke rotation	Discomfort	Duration (sec)	Participant	Stroke rotation	Discomfort	Duration (s)
1	30°	7.94	1131.23	7	30°	5.27	1025.24
1	45°	6.03	582.59	7	45°	4.57	953.26
1	60°	5.97	570.41	7	60°	3.57	752.46
2	30°	6.75	940.75	8	30°	6.26	823.15
2	45°	6.27	832.66	8	45°	5.99	690.13
2	60°	4.69	788.76	8	60°	4.75	599.26
3	30°	6.99	707.62	9	30°	6.25	945.57
3	45°	6.03	571.11	9	45°	5.46	875.36
3	60°	5.61	506.39	9	60°	3.59	789.26
4	30°	8.18	697.57	10	30°	7.26	856.36
4	45°	7.43	685.91	10	45°	5.36	753.70
4	60°	5.79	670.71	10	60°	4.37	685.59
5	30°	3.59	1170.30	11	30°	6.26	863.76
5	45°	2.51	993.87	11	45°	5.99	810.26
5	60°	1.37	880.67	11	60°	3.26	796.27
6	30°	7.88	987.41	12	30°	5.36	945.66
6	45°	6.9	806.86	12	45°	3.27	869.69
6	60°	3.91	599.34	12	60°	2.58	801.26

**Table 2** Mean discomfort score and mean duration with standard deviations for socket and threaded pipe assembly

Stroke rotation	Discomfort		Duration (s)	
	Mean	SD	Mean	SD
30°	6.50	1.32	924.55	146.34
45°	5.48	1.42	785.45	133.89
60°	4.12	1.36	703.36	115.31

The graphical representation of mean discomfort score with standard deviation of all participants at three levels of stroke rotations was shown in Fig. 4. It is illustrated that the discomfort was decreasing as the stroke rotation increases from 30° to 60° and the minimum discomfort was found at 60°. It was noticed that the slightly higher variation of discomfort score was at 45° and the least variation was found at 30°.

Figure 5 illustrated that the duration required for assembly of 50 pieces of socket and threaded pipes was minimum for 60° than the other two stroke rotations. The variation in the duration recorded by the participants was small for all levels of stroke rotation, and it was also noticed that the variation is least at 60° stroke rotation. Less duration means that fast assembling was performed by the participants, which means that high productivity was obtained at 60° stroke rotation.

Further, data was analysed in SPSS, and the results of multivariate analysis of variance (MANOVA) were presented in Table 3. It was noticed that stroke rotation

**Fig. 4** Profile of mean discomfort score versus stroke rotation for socket and threaded pipes at 95% CI

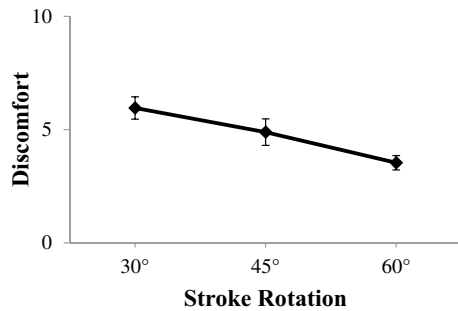


**Fig. 5** Profile of duration versus stroke rotation for nut and bolt assembly

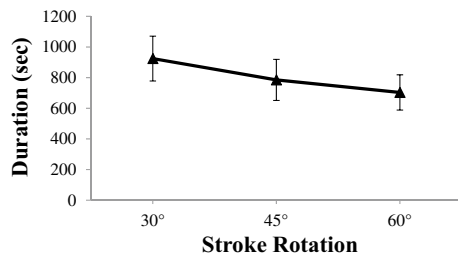


**Table 3** MANOVA results of stroke rotation for discomfort and duration for socket and threaded pipe assembly

Source	Dependent variable	Type III sum of squares	Degree of freedom	Mean square	F-value	Sig. (p-value)
Stroke rotation	Discomfort	34.11	2	17.057	9.101	0.001
	Duration	300,041.38	2	150,020.690	8.551	0.001
Error	Discomfort	61.85	33	1.874		
	Duration	578,983.08	33	17,544.942		
Total	Discomfort	1132.96	36			
	Duration	24,176,292.25	36			
Corrected total	Discomfort	95.96	35			
	Duration	879,024.46	35			

was statistically significant on discomfort ( $p = 0.001$ ) as well as duration ( $p = 0.001$ ) for assembling the 50 sockets and threaded pipes.

**Nut and Bolt Assembly**

The data of perceived discomfort rating and duration for assembling 50 nuts and bolts of each participant for all treatments were summarized in Table 4.

It was noticed from the above table that perceived discomfort score lies in the range of 3.07–6.72. The lowest discomfort score was recorded at 60° stroke rotation and the highest discomfort was at 30° stroke rotation for almost all the participants. It was also illustrated that the duration required for 50 assemblies of nut and bolt lies in between 1127 s and 1691.18 s. It was also noticed that the duration required for the given task was more at 30° than at the other two stroke rotations (45° and 60°), but shortest duration was recorded at 60° stroke rotation.

The graphical representation of perceived discomfort data for 50 nut and bolt assembly was shown in Fig. 6. It was illustrated that discomfort decreases with increase in stroke rotation and least discomfort was found at 60°. It was also illustrated that the variation of discomfort data was very small at all stroke rotations and smallest at 60° than the other two levels of stroke rotations.

In Fig. 7, the mean duration required for assembling 50 nuts and bolts was decreased as stroke rotation increased from 30° to 60°. It was noticed from the figure that the minimum duration required for the given task was at 60° stroke rotation; minimum duration means that the given number of assemblies were completed in less time so productive work was found at stroke rotation 60°. Also, very small variations in data of mean duration was shown.

The mean discomfort score and mean duration with standard deviations for all participants at three levels of stroke rotation for nut and bolt assembly was presented in Table 5.

The MANOVA results of discomfort and duration for nut and bolt assembly was presented in Table 6. It showed that stroke rotation was highly significant on

**Table 4** Data of discomfort and duration for different stroke rotation of each participant for nut and bolt assembly

Participant	Stroke rotation	Discomfort	Duration (s)	Participant	Stroke rotation	Discomfort	Duration (s)
1	30°	5.19	1580.95	7	30°	6.21	1545.75
1	45°	4.79	1326.73	7	45°	4.69	1386.75
1	60°	3.07	1207.65	7	60°	3.32	1187.65
2	30°	5.61	1691.18	8	30°	5.76	1591.08
2	45°	4.03	1580.28	8	45°	4.71	1480.85
2	60°	3.12	1361.75	8	60°	3.86	1325.75
3	30°	6.45	1657.26	9	30°	6.72	1557.86
3	45°	5.23	1345.25	9	45°	5.87	1475.51
3	60°	3.86	1127.81	9	60°	3.31	1207.81
4	30°	6.12	1480.95	10	30°	5.49	1601.95
4	45°	4.59	1366.73	10	45°	4.79	1472.73
4	60°	4.07	1225.65	10	60°	3.37	1207.65
5	30°	5.86	1591.24	11	30°	5.34	1691.08
5	45°	4.43	1475.28	11	45°	4.28	1480.28
5	60°	3.72	1301.76	11	60°	3.76	1241.75
6	30°	6.15	1557.67	12	30°	6.56	1557.46
6	45°	5.38	1385.27	12	45°	5.87	1424.25
6	60°	3.48	1177.84	12	60°	3.49	1147.81

**Fig. 6** Profile of mean discomfort score versus stroke rotation for nut and bolt assembly

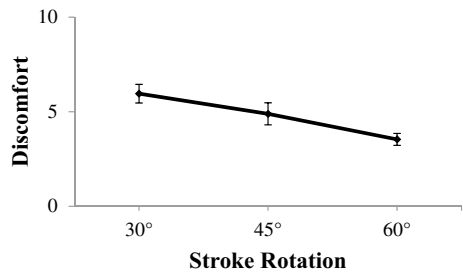


**Fig. 7** Profile of mean duration versus stroke rotation for nut and bolt assembly

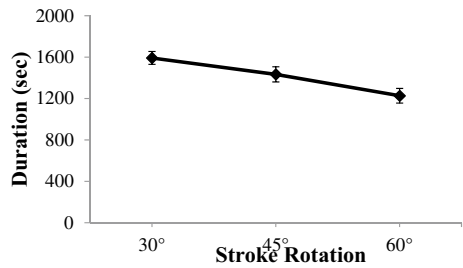


**Table 5** Mean discomfort score and mean duration with standard deviations for nut and bolt assembly

Stroke rotation	Discomfort		Duration (min)	
	Mean	SD	Mean	SD
30°	5.96	0.49	1592.03	61.88
45°	4.89	0.59	1433.33	73.40
60°	3.54	0.32	1226.74	70.65

**Table 6** MANOVA results for nut and bolt assembly

Source	Dependent variable	Type III sum of squares	Degree of freedom	Mean square	F-value	Sig. (p-value)
Stroke rotation	Discomfort	35.278	2	17.639	77.052	<0.001
	Duration	805,193.245	2	402,596.623	85.001	<0.001
Error	Discomfort	7.554	33	0.229		
	Duration	156,300.846	33	4736.389		
Total	Discomfort	869.874	36			
	Duration	73,282,701.961	36			
Corrected total	Discomfort	40.989	35			
	Duration	961,494.092	35			

discomfort ( $p < 0.001$ ) as well as duration ( $<0.001$ ) required for assembly of 50 nut and bolt.

## 5 Discussion

The results showed that stroke rotation was significant on discomfort and duration for both types of assemblies; “Socket and Thread Pipes” and “Nuts and Bolts”. It was also noted that the lowest discomfort and the most productive task were observed at 60° rotation with respect to all other levels of rotation. This may be due to fewer repetitions or almost full rotation of the forearm at a 60° rotation. On the other hand, the frequency of the forearm rotation was high because of the low angle of stroke rotation (30°). Due to the high frequency, discomfort was high and productivity was low. It was also observed in studies [17, 18] that the rotation of the stroke was significant for the discomfort and that the least discomfort was observed at a 60° stroke rotation in combined torqueing with gripping exertions. In other studies by Bano et al. [20, 27], it was revealed that the lowest discomfort and high productivity were found at 60° stroke rotation.

Although, there were similar results found for different kinds of task. In a study for torqueing task, O’Sullivan and Gallwey [8] found that both direction and the angle of



forearm rotation had significant effect on maximum torques applied. In another study, it was reported that both forearm rotation angle and twisting directions significantly affected discomfort for an intermittent pronation torque exertions [14]. Moreover, in isometric pronation torque Mukhopadhyay et al. [7, 15, 21] revealed that discomfort was significantly increased due to the increase in forearm rotation angle in pronation task. In addition, for flexion task, Khan et al. [13, 28] reported that forearm angle significantly affected discomfort.

## 6 Conclusions

The stroke rotation was significant on discomfort during repetitive tasks which involved gripping with torqueing activity. It was observed that stroke rotation 60° was very much comfortable with lowest discomfort and high productivity at this posture/workstation. Results obtained were restricted to predict discomfort for males only in two types of tasks chosen in the study. This research was performed at different levels of stroke rotation, but other wrist deviations were not considered with gripping exertions may be taken for further analysis. Wrist was also supposed to be in neutral position but very difficult and elbow flexed at 90° without upper arm adduction, which is very unlikely in industrial tasks. Therefore, further investigations may be addition to knowledge in this regard.

**Acknowledgements** The authors would like to acknowledge and thanks to the mechanical department, AMU, Aligarh, UP, India, who provide us all the laboratory facilities for conducting the experiment.

## References

1. Choobineh A, Sani GP, Rohani MS (2009) Perceived demands and musculoskeletal symptoms among employees of an Iranian petrochemical industry. *Int J Ind Ergon* 39:766–770
2. O'Sullivan L, Clancy P (2007) Guideline threshold limit values (TLVs) for discomfort in repetitive assembly work. *Hum Factors Ergon Manuf* 17:423–434
3. Kong Y-K, Kim DM, Lee KS, Jung MC (2012) Comparison of comfort, discomfort and continuum ratings of force levels and hand regions during gripping exertions. *Appl Ergon* 43:283–289
4. Lin CL, Wang MJ, Drury CG, Chen YS (2010) Evaluation of perceived discomfort in repetitive arm reaching and holding tasks. *Int J Ind Ergon* 40:90–96
5. Dul J, Douwes M, Smitt P (1994) Ergonomics guidelines for the prevention of discomfort of static postures based on endurance data. *Ergonomics* 37:807–815
6. Ciriello VM, Webster BS, Dempsey PG (2002) Maximal acceptable torques of highly repetitive screw driving, ulnar deviation and handgrip tasks for 7-hour workdays. *AIHA J* 63:594–604
7. Mukhopadhyay P, O'Sullivan L, Gallwey T (2009) Upper limb discomfort profile due to intermittent isometric pronation torque at different postural combinations of the shoulder-arm system. *Ergonomics* 52(5):584–600

8. O'Sullivan LW, Gallwey TJ (2002) Upper-limb surface electromyography at maximum supination and pronation torques: the effect of elbow and forearm angle. *J Electromyography Kinesiol* 12:275–285
9. Khan AA, O'Sullivan L, Gallwey TJ (2010) Effect of discomfort of frequency of wrist exertions combined with wrist articulations and forearm rotation. *Int J Ind Ergon* 40:492–503
10. Gooyers CE, Stevenson JM (2012) The impact of an increase in work rate on task demands for a simulated industrial hand tool assembly task. *Int J Ind Ergon* 42:80–89
11. Chung MK, Lee I, Kee D, Kim SH (2002) A postural workload evaluation system based on a macro-postural classification. *Human Factor Ergon Manufac*:267–277
12. Fernandez JE, Agarwal R, Landwehr HR, Poonawala MF, Garcia DT (1999) The effects of arm supports during light assembly and computer work tasks. *Int J Ind Ergon*:493–502
13. Khan AA, O'Sullivan LW, Gallwey TJ (2009a) Effects of combined wrist deviation and forearm rotation on discomfort score. *Ergonomics* 52(3):345–361
14. O'Sullivan LW, Gallwey TJ (2005) Forearm torque strengths and discomfort profiles in pronation and supination. *Ergonomics* 48:703–721
15. Mukhopadhyay P, O'Sullivan L, Gallwey T (2007a) Estimating upper limb discomfort level due to intermittent isometric pronation torque with various combinations of elbow angles, forearm rotation angles, force and frequency with upper arm at 90° abduction. *Int J Ind Ergon* 37:313–325
16. Farooq M, Khan AA (2012) Effect of shoulder rotation, upper arm rotation and elbow flexion in a repetitive gripping task. *Work* 41:1–16
17. Bano F, Mallick Z, Khan AA (2013a) The effect of stroke rotation and frequency of exertion on discomfort in gripping task. In: *Proceedings of the international conference on automation and mechanical systems*, 21–22 March, Faridabad, pp 152–158
18. Bano F, Mallick Z, Khan A (2013b) The effect of self pace cycle time for combinations of grip force and stroke rotation. In: *e-Proceedings of the 2nd international conference on emerging trends in engineering and technology*, 12–13 April, Moradabad, India
19. Bano F, Mallick Z, Khan AA (2015) Optimization of the levels of grip force, stroke rotation, frequency and grip span for a torqueing task. *Int J Occup Safety Ergon* 21(1):94–104
20. Bano F, Mallick Z, Khan A (2012) Effect of grip, stroke rotation and handle size on discomfort for screwing task. *Int J Hum Factors Ergon* 1(4):390–407
21. Mukhopadhyay P, O'Sullivan LW, Gallwey TJ (2007) Effects of upper arm articulations on shoulder-arm discomfort profile in a pronation task. *Occup Ergon* 7:169–181
22. Carey E, Gallwey T (2005) Wrist discomfort levels for combined movements at constant force and repetition rate. *Ergonomics* 48:171–186
23. Lin M, Radwin R, Snook S (1997) A single metric for quantifying biomechanical stress in repetitive motions and exertions. *Ergonomics* 40:543–558
24. Dempsey P, McGorry RW, O'Brien NV (2004) The effects of work height, workpiece orientation, gender, and screwdriver type on productivity and wrist deviation. *Int J Ind Ergon* 33:339–346
25. Finneran A, O'Sullivan L (2010) Force, posture and repetition induced discomfort as a mediator in self-paced cycle time. *Int J Ind Ergon* 40(3):257–266
26. Muzammil M, Ahmad S, Khan A, Hasan F (2011) Design of a workstation and its evaluation under the influence of noise and illumination for an assembly task. *Work* 39:3–14
27. Bano F, Mallick Z, Khan A (2013c) EMG investigations regarding handle size, grip force and stroke rotation in screw driving. *Int J Ergon* 4(1):1–14
28. Khan AA, O'Sullivan L, Gallwey TJ (2009b) Effects of combined wrist flexion/extension and forearm rotation and two levels of relative force on discomfort. *Ergonomics* 52(10):1265–1275

# Development of Improving Model for the Surface Finish of Ball Bearing (Deep Groove) by Optimizing Cutting Parameter



Shraddha Arya, Manish Bhargava, and M. P. Singh

**Abstract** Deep groove ball bearing is extensively used to support rotational shafts in engines, in order to improve the surface finish, use of design of experiment (DOE) to investigate the most significant responsive factor, which is contributing in improving surface finish. Based on the results, design of experiment is conducted and tries to optimize the most significant responsive factor. For performing design of experiment, first selecting six variable factors in grinding and four variable factors in honing process were obtained through brainstorming. To improve surface finish of inner and outer track of deep groove ball bearing, hereby, the various experiments were to be conducted independently to know the effect of various process parameters on surface finish of deep groove ball bearing.

**Keywords** Deep groove ball bearing · Design of experiments (DOE) · Grinding · Honing

## 1 Introduction

The main persistence of this study is to describe the model preparation for the improvement of the surface finish of deep groove ball bearing by using the methodology of design of experiment, ANOVA (tool), and MINITAB (software). Ball bearings are used as multifaceted part, self-retaining bearing with solid outer rings, inner rings, balls, and cage assemblies.

They are of a simple design, robust in nature, easy to maintain. Due to raceway geometry and the use of balls, deep groove ball bearing can support the axial forces in both direction and radial force. Use of design of experiment (DOE) is to investigate

---

S. Arya (✉)  
Jagannath University, Jaipur, India

M. Bhargava  
NIT Agartala, Agartala, India

M. P. Singh  
JECRC, Jaipur, India

most significant responsive factor which is contributing in improving surface texture by using fishbone diagram [1, 2].

Nowadays, poor surface texture has become a sizable problem especially for automobile industry; so to eliminate this problem and to identify the major optimum solution, DOE tool and MINITAB software are used.

## 2 Research Methodology

The purpose of product or process development is to improve the performance characteristics of the product or process relative to the customer needs and expectations. The purpose of experimentation should be understood how to reduce and control variation of a product and optimizes the cutting parameters to improve the surface finish of ball bearing subsequently [2].

The approach of design of experiment is based on the orthogonal arrays to conduct small, fractional experiments up to larger, full factorial experiments. Note down all the initial conditions in which machine is running and collecting the necessary quality results execute the experiments as per run order [3]. For every experiment, record quality parameters are surface finish, surface roughness, and roundness Talyrond and profile (Fig. 1).

After taking sample pieces, the machine will restore on initial conditions until the next experiment is executed. Final judgment will be taken after doing honing and then check grinding burns [4]. Various experiments were to be conducted independently to know the effect of various process parameters on surface finish as per Table 1.

This is based on the results of the above experiments, if required, process parameters were affecting surface texture to be optimized. The following tables show the experiment done on 64 random bearings for comparison between the various parameters and its response.

**Fig. 1** Design of experiment process and stages



**Table 1** Process parameters for surface finish

Area	Experiments planned for followings process parameters
Grinding	Work RPM (process RPM setting)
	Grinding feed rate (fine)
	Dress compensation (draft compensation)
	Dress feed rate
	Grinding feed rate (rough2)
	Spark out time
Honing	Work head RPM (fast)
	Work head RPM (slow)
	Osc. frequency (fast-low)
	Honing time (fast–slow)

### 3 Design of Experiments for 6205 for Grinding Process

Design of experiment has to be done for 6205 ball bearing for inner race grinding process on random bearings with six different variables on two response factors, i.e., Ra and Talyrond (Table 2).

After conducting all 64 experiments, collecting the results of all the experiments analyzes the data by ANOVA table and interprets the results which then standardize the processing condition if required. It is the procedure of splitting the variance of the observation into the variance caused by the variable and the variance caused by noise [5]. It helps to check if the linear relation between  $y$  and  $x$  is significant [4, 6]. Table 3 shows the Ra response for inner race of ball bearing response on the following.

The analysis of ANOVA outcomes is as follows:

1. All the above critical values ( $P$ ) are more than 0.05.
2. Critical value ( $P$ ) should be less than 0.05 for significant factor selection.
3. On the basis of above results, we can come to conclusion that none of the sources affects the surface roughness (Ra) value at this level.

Hence, machining conditions are already at optimum level for surface texture and no scope of further improvement.

Table 4 shows the Talyrond for inner race of ball bearing response on the following.

The analysis of ANOVA outcomes is as follows:

1. Two out of six critical values ( $P$ ) are less than 0.05.
2. Critical value ( $P$ ) should be less than 0.05 for significant factor selection.
3. After analyzing, the above-given results, we can come to conclusion that two factors work RPM and grinding feed rate (fine) which affects the roundness (Talyrond) value.

However, not all these sources affect the surface finish of the product.

**Table 2** Design matrix and data collection—inner race

Std order	Run order	Variable parameter						Response	
		Work RPM	Grinding feed rate (fine)	Dress compensation	Dress feed rate	Grinding feed rate (R-2)	Spark out time	Ra Avg	Talyrond Avg
60	1	914	0.01	0.02	0.01	0.043	1.5	0.4642	1
34	2	914	0.008	0.02	0.008	0.04	1.5	0.4504	0.82
52	3	914	0.01	0.02	0.008	0.043	1.5	0.4637	0.83
42	4	914	0.008	0.02	0.01	0.04	1.5	0.4889	0.73
16	5	914	0.01	0.03	0.01	0.04	1	0.4214	0.87
8	6	914	0.01	0.03	0.008	0.04	1	0.4361	0.77
1	7	710	0.008	0.02	0.008	0.04	1	0.4332	0.67
2	8	914	0.008	0.02	0.008	0.04	1	0.3567	0.6
15	9	710	0.01	0.03	0.01	0.04	1	0.3549	0.83
9	10	710	0.008	0.02	0.01	0.04	1	0.3795	0.97
27	11	710	0.01	0.02	0.01	0.043	1	0.3812	0.82
61	12	710	0.008	0.03	0.01	0.043	1.5	0.3921	0.68
57	13	710	0.008	0.02	0.01	0.043	1.5	0.3843	0.4

**Table 3** ANOVA table for Ra response

Analysis of variance for Ra Avg., using adjusted SS for tests							
S. no	Source	DF	Seq SS	Adj SS	Adj MS	F	P
1	Work RPM	1	0	0	0	0	1
2	Grinding feed rate (fine)	1	0.0067	0.007	0.0067	1.6	0.22
3	Dress compensation	1	0.0057	0.006	0.0057	1.3	0.25
4	Dress feed rate	1	0.0016	0.002	0.0016	0.4	0.54
5	Grinding feed rate (rough-2)	1	0.0001	1E-04	0.0001	0	0.86
6	Spark out time	1	0.0002	2E-04	0.0002	0.1	0.8
7	Error	57	0.245	0.245	0.0043		
8	Total	63	0.259				

**Table 4** ANOVA table for roundness (Talyrond) response

Analysis of variance for Talyrond Avg., using adjusted SS for tests							
S. no	Source	DF	Seq SS	Adj SS	Adj MS	F	P
1	Work RPM	1	0.3828	0.383	0.3828	8.2	0.01
2	Grinding feed rate (fine)	1	0.318	0.318	0.318	6.8	0.01
3	Dress compensation	1	0.0073	0.007	0.0073	0.2	0.7
4	Dress feed rate	1	0.0005	5E-04	0.0005	0	0.92
5	Grinding feed rate (rough-2)	1	0.0005	5E-04	0.0005	0	0.92
6	Spark out time	1	0.0343	0.034	0.0343	0.7	0.4
7	Error	57	2.67	2.67	0.0468		
8	Total	63	3.414				

Design of experiment has to be done for 6205 ball bearing for inner race grinding process on random bearings with six different variables on two response factors, i.e., Ra and Talyrond.

## 4 Design of Experiments for 6205 for Honing Process

Design of experiment has to be done for 6205 ball bearing for inner race honing process on random bearings with four different variables on two response factors, i.e., Ra and Talyrond. Same is done as grinding process (Tables 5 and 6).

Table 7 shows the results of four different variables in the two respective response and their response after analysis for honing process.

Table 8 shows the results of ANOVA table for surface finish of the tested bearings, where the p value is more than 0.05 for all parameters.

The analysis of ANOVA outcomes is as follows:

**Table 5** Table variable factors, fixed factors, and other factors of honing process

Variables factors				
Factor	Name	Low level	High level	Units
A	Work head RPM (fast)	2000	3000	RPM
B	Work head RPM (slow)	1500	2500	RPM
C	Osc. frequency (fast-low)	450–150	600–200	CPM
D	Honing time (fast–slow)	10–2	13–2	Sec
Fixed factors				
Factor	Name	Value		Unit
1	Honing stone (rough)	WA3000RH28–30-SANWA		–
2	Honing stone (finish)	19R6000RH(-)22-IZUHO		–
3	Rough stone pressure	0.20–0.24		MPa
4	Finish stone pressure	0.24–0.28		MPa
5	Clamp pressure	0.25–0.35		MPa
6	M/c idle time	2.5		s
7	Main line air pressure	0.4		MPa
8	Oscillation angle	30–40		deg
Other fixed factor (environmental)				
S. no	Environmental factor		Value	
1	Tooling condition		Constant	
2	Coolant condition			
3	Environment temperature			
4	Operator skill			
5	Gauge's			
6	Machine			
7	Input material			
8	Inspection method/machine			

**Table 6** Response test result

Response	Name	Std
1	Surface roughness (Ra)	0.04 max
2	Roundness (Talyrond)	2.0

1. All the above critical values ( $P$ ) are more than 0.05.
2. Critical value ( $P$ ) should be less than 0.05 for significant factor selection.
3. On the basis of the above results, we can come to conclusion that none of the sources affects the surface roughness (Ra) value at this level.

Hence, machining conditions are already at optimum level/optimized for surface texture and no scope of further improvement [7, 8].



**Table 7** Results (response) of experiments

Std order	Run order	Variable parameter				Response	
		Work head RPM-fast	Work head RPM-slow	Osc. frequency fast-low	Honing time sec. fast-slow	Surface finish (Ra) $\mu\text{m}$ (Avg.)	Roundness (Talyrond) $\mu\text{m}$ (Avg.)
4	1	3000	2500	450 ~ 150	10 ~ 2	0.0201	0.5
1	2	2000	1500	450 ~ 150	10 ~ 2	0.0203	0.87
16	3	3000	2500	600 ~ 200	13 ~ 2	0.019	0.82
3	4	2000	2500	450 ~ 150	10 ~ 2	0.0303	0.78
12	5	3000	2500	450 ~ 150	13 ~ 2	0.0201	0.52
13	6	2000	1500	600 ~ 200	13 ~ 2	0.0217	0.88
14	7	3000	1500	600 ~ 200	13 ~ 2	0.0181	0.65
7	8	2000	2500	600 ~ 200	10 ~ 2	0.0239	0.78
8	9	3000	2500	600 ~ 200	10 ~ 2	0.0243	0.58
10	10	3000	1500	450 ~ 150	13 ~ 2	0.0265	0.58
5	11	2000	1500	600 ~ 200	10 ~ 2	0.0263	0.72
2	12	3000	1500	450 ~ 150	10 ~ 2	0.0159	0.78
15	13	2000	2500	600 ~ 200	13 ~ 2	0.0177	0.78
11	14	2000	2500	450 ~ 150	13 ~ 2	0.0184	0.75
6	15	3000	1500	600 ~ 200	10 ~ 2	0.02	0.82
9	16	2000	1500	450 ~ 150	13 ~ 2	0.0251	0.8

**Table 8** ANOVA table for surface finish (Ra) response

Analysis of variance for surface finish, using adjusted SS for tests

S. no	Source	DF	Seq SS	Adj SS	Adj MS	F	P
1	Work head RPM (fast)	1	0.0000237	0.0000237	0.000023	1.4	0.27
2	Work head RPM (slow)	1	0	0	0	0	0.99
3	Osc. frequency (fast-low)	1	0.0000019	0.0000019	0.0000019	0.1	0.75
4	Honing time (fast-slow)	1	0.0000131	0.0000131	0.0000131	0.8	0.41
5	Error	11	0.0001391	0.0001391	0.0000176		
6	Total	15	0.0002318				

Table 9 shows the results of ANOVA table for roundness of the tested bearings, where the *p* value of work RPM (fast) is less than 0.05.

Hereby, the analysis of ANOVA outcomes is as follows:

1. One out of four critical values (*P*) is less than 0.05.
2. Critical value (*P*) should be less than 0.05 for significant factor selection.
3. After analyzing the above experiments' results, conclusion is that one factor work head RPM (fast) affects the roundness (Talyrond) value.

**Table 9** ANOVA table for roundness (Talyrond) response

Analysis of variance for Talyrond Avg., using adjusted SS for tests							
S. no	Source	DF	Seq SS	Adj SS	Adj MS	F	P
1	Work head RPM (fast)	1	0.077934	0.077934	0.077934	7.8	0.02
2	Work head RPM (slow)	1	0.021267	0.021267	0.021267	2.1	0.17
3	Osc. frequency (fast-low)	1	0.012656	0.012656	0.012656	1.3	0.28
4	Honing time (fast-slow)	1	0.000156	0.000156	0.000156	0	0.9
5	Error	11	0.109635	0.109635	0.009967		
6	Total	15	0.221649				

However, work head RPM (fast) is not affecting on the surface texture of the product.

## 5 Mathematical Modeling Done by Regression Analysis

Regression analysis is usually used to evaluate the relationship between any two or more dependent variables on independent variables, which shows the effect of that variables on main factor. Regression analysis has been done with response of ball bearing with different variables for inner race ball bearing [1, 9].

Regression Analysis: Ra Avg. versus work RPM, grinding feed rate, dress compensation, dress feed rate, and grinding feed rate-2. The regression equation is

$$\begin{aligned} \text{"Ra Avg.} &= 0.00895 + 0.000012 \text{ Work RPM} - 0.000004 \text{ Grinding Feed rate(Fine)} \\ &- 0.000000 \text{ Dress compensation} - 0.0064 \text{ Dress feed rate} \\ &- 0.0001 \text{ Grinding Feed rate}(R-2)\text{"} \end{aligned} \quad (1)$$

Regression Analysis: Talyrond Avg. versus work RPM, grinding feed rate, dress compensation, dress feed rate, and grinding feed rate-2. The regression equation is

$$\begin{aligned} \text{"Talyrond} &= 0.0409 + 0.000036 \text{ Work RPM} + 0.000006 \text{ Grinding Feed rate(Fine)} \\ &- 0.000000 \text{ Dress compensation} - 0.0080 \text{ Dress feed rate} \\ &- 0.0125 \text{ Grinding Feed rate}(R-2)\text{"} \end{aligned} \quad (2)$$

## 6 First Section Results & Conclusion of Experimental Data for Grinding & Honing Process

In order to improve surface finish, 64 experiments on grinding M/c & 16 experiments on honing M/c for both inner and outer races have to be done (total 80 experiments for each). In each experiments, we have taken three sample pieces for all quality checks and analyzed the results on both machines [3].

After analyzing the data, results show that:

1. The two factors work RPM and grinding feed rate (fine) affect the roundness (Talyrond) value in inner race grinding process.
2. The one factor work head RPM (fast) affects the roundness (Talyrond) value in inner race honing process.
3. The two factors work RPM and dress feed rate affect the Talyrond value in outer race grinding.
4. All the machining conditions are already at optimum level and do not affect the surface texture of the product.

## 7 Results with Graphical Representation

In order to improve surface finish, 64 experiments have to be done on grinding machine and 16 experiments on honing machine for both inner and outer races (total 80 experiments for each process).

In each experiments, we have taken three sample pieces for all quality checks and analyzed the results on both machines. After analyzing the results, for surface roundness concluded that one factor work head RPM (fast) affects the roundness (Talyrond) value but work head RPM (fast) is not affecting on the surface texture of the product.

Two factors work RPM and dress feed rate affect the Talyrond value.

All the machining conditions are already at optimum level and do not affect the surface texture of the product.

## References

1. Yu G, Su M, Xia W, Wu R, Wang Q (2017) Vibration characteristics of deep groove ball bearing based on 4-DOF mathematical model. Proc Eng 174:808–814 (Elsevier)
2. Li S, Zhang G, Chen B, Shen Y (2017) Structure design and performance analysis of high-speed miniature ball bearing. In: 4th international conference on mechanics and mechatronics research ICMR 2017
3. Karolina Anna J, Glovnea R, Bongaerts J (2017) Quantitative measurements of film thickness in a radially loaded deep-groove ball bearing. Tribol Int. ISSN 0301-679X

4. Wu J-m, Zhang J-l, Wang Y, Shi M-l (2017) The effects of commonly used deep groove ball bearing parameters of the printing and packaging equipment on the performance. *Packaging Eng*
5. Satheesh S, Mohan Kumar VVK, Haldar A (2017) Static analysis of rolling bearing using finite element analysis. *Int J Res* 4(14)
6. Kataria Mahendra B, Pandya H, Mehta JP, Kundaliya DD (2017) Fatigue analysis of deep groove ball bearing cage to increase its life using ANSYS. *Int J Emerg Technol Innov Res (Int Open Access J & UGC ISSN Approved)* 4(7):2349–5162
7. Ball bearings—global market outlook (2017–2023). *Statistics Market Research Consulting Product Code*, Sept 1 2017
8. Mišković Z, Mitrović R, Maksimović V, Milivojević A (2017) Analysis and prediction of vibrations of ball bearings contaminated by open pit coal mine debris particles. *Tehnički vjesnik* 1941–1950, June 2017. ISSN 1330-3651 ISSN 1848-6339
9. Yadav HK, Pandya DH, Harsh SP (2017) Nonlinear vibration signature analysis of a rotor supported ball bearings. *Int J Nonlinear Dyn Control* 1(1). Print ISSN: 2050-6902, Online ISSN: 2050-6910

# Recent Applications, Developments and Challenges in Waterjet Technology



Paramjit Thakur, D. N. Raut, and Fauzia Siddiqui

**Abstract** Waterjet technology can cut soft, brittle, fibrous and difficult to cut materials without producing any heat-affected zone. This paper presents a vast review on recent applications, developments and challenges in waterjet technology. The new applications of waterjet technology, namely 3D machining, tool making, hydroentangling, comminution, etc., are elaborated in this paper. In order to increase the performance characteristics and for new application areas, many developments and modifications in AWJ machining process has taken place. And, some of the recent developments are ice waterjet machining, assisted processes, micro machining and submerged waterjet machining. Finally, the review is completed by discussing the challenges in existing waterjet technology for further improvement of the process. The problems like grit embedment, backflow of AWJ, etc., are very well elaborated in this work.

**Keywords** Waterjet · Developments · Grit embedment · Challenges

## 1 Introduction

The waterjet machining process was firstly commercialized in early 1980s in automotive and aerospace industries. Further, the contribution of researchers led the application of WJ in other areas too. The application of WJ machining in various areas is explained in section. The waterjet technology is used to machine variety of materials including difficult to cut materials, glass, ceramics and composites [1]. This process leads no heat affected zone as the heat developed during the cutting process is carried away by the water. Hence, the temperature-sensitive materials like shape memory alloys can be easily cut by WJ. Also, this process leads very less stress concentration on the cut surface which makes this process unique [2]. The small increase in temperature in the cutting process and the production of little flying dust

---

P. Thakur (✉) · D. N. Raut  
Veermata Jijabai Technological Institute, Mumbai, India

F. Siddiqui  
JECRC, Jaipur, India

makes this process safe from fire hazards and pollution. This process can be made easily available due to availability of water which can be recycled after cutting and the use of most commonly available abrasives like garnet and silica. This process gives very less cutting force as compared to the other non-traditional machining processes and very less setup time is required in clamping the workpiece. Hence, the waterjet technology is a versatile machining process which is gaining importance nowadays.

This paper presents a vast review on recent applications, developments and challenges in waterjet technology. The conventional waterjet machining is used for scaling and descaling, food and medical industry and cutting process. However, some new applications have come out in past few years which are mentioned in this paper, namely 3D machining, hydroentangling, comminution and tool making. The recent developments in waterjet have solved the problems like grit embedment to the greater extent, better surface finish, high precision parts, etc. Some of the recent developments discussed in this work are ice waterjet machining, assisted processes, micro machining and submerged waterjet machining. At the end, the challenges in existing waterjet machining are discussed for further development of the process.

## **2 Applications of Pure and Abrasive Waterjet**

The waterjet technology has vast range of applications in many areas. The major application of AWJ/pure WJ process is in cutting industry, descaling and food and medical industry. The other recent applications are in 3D machining, tool making industry, equipment dismantling and microelectronic cutting. The pure waterjet is majorly used in food and medical industry, cleaning and descaling, textile industry (hydroentangling process), comminution industry and mining.

### ***2.1 Material Cutting Industry***

Abrasive waterjet can cut almost every material, and hence, its major application is in material cutting industry. The AWJ is used to cut difficult to cut materials like inconel 718 which has vast applications in aircraft industry [3]. Apart from difficult to cut materials, it is also used in cutting of composite laminates [4], ceramics [5] and glass [6].

### ***2.2 Tool Industry***

The AWJ cutting has started finding its application in tool making industry. Pal and Choudhury [7] fabricated the texturing tool (tools for making square blind holes) for EDM by abrasive waterjet milling process. The micro tools were made on copper

and brass sheets by selecting proper milling strategy, step over and traverse rate. The array of blind holes was made on stainless steel and Ti6Al4V using EDM to check the efficiency of the tools, and the holes were found to be in the range of 10–100  $\mu\text{m}$ .

### 2.3 3D Machining

The AWJ has been used for 3D cutting by accessorizing the conventional 2D AWJ machining with rotary axis of workpiece and tilting the nozzle. The major problem in AWJ 3D machining is that the used abrasives still have enough energy to damage the other parts of the workpiece. And, in order to solve this problem, Liu and Olsen [8] used the sacrificial stainless steel rod inside the tube of titanium to avoid the damage by used abrasives. The authors further showed that the 3D objects can be formed by cutting the workpiece multiple times by changing its orientation.

### 2.4 Cutting of Microelectronic Components

Recently, AWJ is successfully applied for cutting microelectronic components. Hashish [9] used AWJ to cut flash memory card components as illustrated in Fig. 1. The AWJ machine was well equipped with machine vision system and gave 400 finished parts per hour. The efficiency of the system is improved by using the nozzle with vacuum assist and flushing capability. The advantage of AWJ over diamond saw and laser cutting is that it produces the components with no heat-affected zone and mechanical distortion. The author further demonstrated the cutting of micro hard disk arm as illustrated in Fig. 1c.

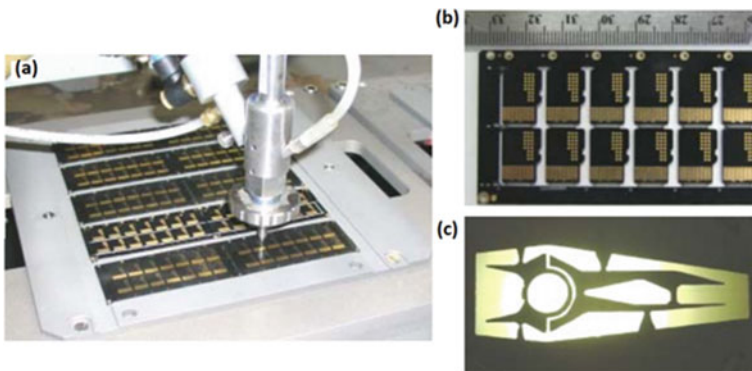


Fig. 1 Cutting of flash memory card components [9]

## 2.5 Textile Industry (Hydroentangling Process)

Apart from cutting of fiber, the series of collimated high pressure pure waterjet is used for hydroentanglement technique to bond the fibers to manufacture nonwoven fabric. The loose fiber in the fiber webs gets entangled due to the impact of high pressure waterjet, and the fibrous structure of high integrity is formed. The efficiency of the system mostly depends on the waterjet pressure [10], waterjet pressure profile [11] and the nozzle geometry. According to Patanaik and Anandjiwala [10], the fiber entanglement increases with the increase in the WJ pressure to the certain extent, and the further increase in WJ pressure has no significant increase in fiber entanglement. Hence, it is very important to find the critical value of the pressure for the best result of hydroentanglement. The waterjet pressure profile is the profile of the variation of water pressure in the series of nozzles. The WJ pressure profile (WPP) affects the fabric thickness, surface quality, bending rigidity and strength. Also, the power consumption can be minimized to the greater extent by the optimal selection of (WPP) [12]. The most important factor affecting the responses in hydroentangling process is the nozzle design which decides the breakup length of the waterjet. The breakup of WJ divides the kinetic energy among the water droplets and reduces the efficiency of hydroentangling to the greater extent. The breakup of the WJ is not desirable as it gives loss in WJ energy. The three basic designs of nozzles for hydroentangling process are cone up, cone down and cylindrical nozzle. Begenir et al. [13] compared the performance of three types of nozzles (cone down nozzle, cone up nozzle and cylindrical nozzle) in terms of breakup length and discharge of the water. The experimental investigation showed that the cone up nozzle led to the shorter breakup length and higher discharger as compared to the other two designs. According to the work done by Anantharamaiah et al. [14], the breakup length of cone down nozzle is higher than that of cone up nozzle due to the formation of constricted WJ. In constricted WJ, the WJ detaches from the wall when it enters the conical part of the nozzle and the absence of the wall friction keeps the WJ collimated to the longer distance.

## 2.6 Comminution Industry

Waterjet technology has found its ways in comminution industry to reduce the size of the particles or disintegrate the material for recycling. The WJ is used in removing the rubberized layer of the old fabric. In this process, the particles of rubber are collected and the fabric is preserved. The WJ is also utilized in disposal of munitions. The conventional technique of disposal is burning and explosion which destroys the components which can be recycled. In this technique, the WJ nozzle is inserted in the hole of grenade and explosives are liberated [15]. Figure 2 illustrates the explosives washed out from the shell by waterjet comminution. The huge tires from regular vehicles and mining vehicles are difficult to dispose in land filling. The continuous



**Fig. 2** Waterjet  
comminution of explosives  
[15]



and pulsating waterjet is successful in separating the wireframe, fabric and rubber particles from waste tires. The production of micronized coal from high pressure waterjet is yet another application of WJ in comminution industry. As compared to the conventional ball mill technique for coal processing, WJ gave less power consumption and more separation efficiency. Also, the high speed waterjet retains the original shape of the coal particles and separates pyrite and other minerals.

## 2.7 Food and Medical Industry

Cutting the food products with pure waterjet removes the problem of contamination of food from abrasives. Pure waterjet has found its place in medical industry for drilling and cutting of bone and flesh, as this technique gives output without any thermal damage. But, controlling the depth of drilling is the major issue in WJ drilling of bones. Hence, Dunnen et al. [16] developed a depth of cut model in drilling of porcine bone. Dunnen et al. [17] worked in the same area of drilling of bone and correlated drilling time, pressure, bone volume fraction and depth of drilling. Apart from drilling of bone, the plain waterjet is used in brain tissue resection as the same was very difficult by the conventional techniques [18]. Also, the resection of the tissues with waterjet is quicker as compared to the general techniques [19].

## 3 Developments in Waterjet Technology

The waterjet machining has emerged as a technology which can machine almost any material. In order to increase the performance characteristics and for new application areas, many developments and modifications in AWJ machining process have taken place. And, some of the recent developments are ice waterjet machining, assisted processes, micro machining and submerged waterjet.

### 3.1 Ice Water Jet Machining

The AWJ machining gave improvement in MRR as compared to conventional plain waterjet machining due to the addition of abrasives in the stream of high pressure waterjet. Around 60% of the operating cost is involved in handling, feeding, purchasing and recycling of abrasives [20]. Also, the use of abrasives in the stream of water jet leads to the contamination of products, if used for food processing and medical applications. These reasons have led to the evolution of ice water jet machining which not only reduces the cost related to the abrasives but also gives no contamination in food cutting or medical applications. McGeough [21] showed no contamination in cutting of meat and bone as the abrasive particles were ice which melt after the cutting process. The ice water jet can be produced by two methods [22] as shown in Fig. 3a, b. In method I, the ice abrasives are formed inside the mixing chamber. Here, the water stream is partially converted into ice abrasives by the supply of cryogenic fluid. In method II, the ice abrasives are formed in a separate chamber with the help of cryogenic fluid. This ice slurry is then transferred to the mixing chamber and mixed with the high pressure water jet and transported to the target surface.

The major problem with method II is the drop in temperature of freezing point due to the heat produced in mixing of ice slurry and high pressure water jet. Although this process gives advantages, it has several drawbacks. The efficiency of this process depends upon the hardness, elastic modulus and flowability of the ice particles. These mechanical properties of ice particles depend upon its temperature. It is very difficult to measure the hardness of the ice particles at a very low temperature. Also, the hardness of ice particles decreases with the increase in temperature. The ice particles generated in the system are very small in diameter and the hardness of the ice abrasive reduces when introduced in the stream of high pressure water jet. Truchot et al. [23] found that the time taken for the ice particles to change its temperature from  $-194$  to  $0$  °C was 0.2 ms when injected in the stream of water jet at  $40$  °C. Hence, it is

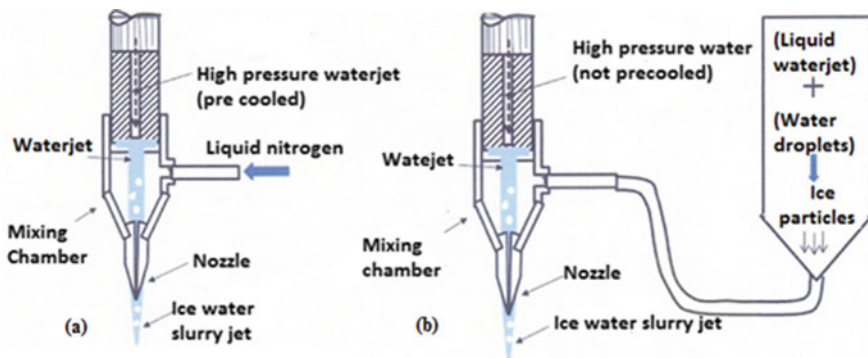


**Fig. 3** Ice abrasive waterjet. **a** Ice is formed in water stream. **b** Ice is formed in a separate chamber [22]

important to cool the WJ stream to a temperature as low as possible before injecting the ice particles. Also, Borkowski [24] showed that the efficiency of the surface treatment depends upon the quality of the ice particles. Further, it was suggested that the ice particles should be of highest quality as the quality of these particles decreases when they are injected in the accelerated water jet stream. Therefore, it is concluded that the efficiency of the system can be increased by reducing the temperature of the ice particles (before injecting in water jet stream) and by precooling the water jet stream before the mixing process. This will maintain the hardness and shape of the ice abrasives at the point of impingement on the target surface.

### 3.2 Assisted AWJ Processes

The performance of AWJ machining can be improved by thermally enhancing the workpiece, cooling the workpiece and by subjecting the workpiece with ultrasonic vibration which are explained below.

- **Thermally enhanced workpiece (TEAWJ)**

Patel and Tandon [25] heated the workpiece before the impingement of AWJ on it, and this process is termed as thermally enhanced AWJ (TEAWJ). To thermally enhance the target material, an oxyacetylene welding torch is used. The target material softens due to the heating process and hence, less amount of cutting force is required for the material removal. The MRR in TEAWJ process was found to be more as compared to that in AWJ process. The major challenge of TEAWJ is the microcracks which are formed on the machined surface. In reference [25], the micro cracks were prominent on the surface of mild steel and no microcracks were found on the surface of Inconel 718 and Ti6Al4V. Further, some compositional defects were found in the material sub layers which can be removed by heat treatment. Hence, the efficiency of this system depends on the temperature to which the workpiece is heated and the type of material used. Although this process reduces the cutting force required for material removal, it can be used only for those materials which do not require superior material properties and desired microstructure.

- **Cryogenic-assisted AWJ (CA-AWJ)**

In this process, the liquid nitrogen is delivered on the cutting front before the impact of AWJ. The cooling effect by liquid nitrogen increases the hardness and reduces the ductility of the material which improves the surface integrity and machinability. Yuvaraj and Pradeep Kumar [26] used cryogenic-assisted AWJ (CAAWJ) for machining of AA5083-H32 aluminum alloy and found no cracks on the target surface. The erosion took place by micro cutting (fine debris) rather than micro chipping. According to the experimental and micro structure analysis, CA-AWJ gave better compressive residual stress and surface integrity as compared to the conventional AWJ in cutting of AA5083-H32 aluminum alloy. The cryogenic waterjet system is cost ineffective, bulky and difficult to maintain.

- **Ultrasonic-assisted–AWJ (UA-AWJ)**

In this process, the workpiece is provided with ultrasonic vibration to enhance the surface quality and material removal rate. Lv et al. [27] applied finite element method to simulate and analyze the influence of impingement angle and abrasive shape on erosion rate in UA-AWJ. The simulation results showed an improvement in erosion rate as compared to the general AWJ process. The major problem with UA-AWJ is that it gives higher surface roughness as compared to general AWJ. Lv et al. [28] compared surface roughness and MRR obtained by AWJ and UA-AWJ in polishing of aluminum nitride. The average depth of indentation obtained by UA-AWJ was more as compared to AWJ and hence, UA-AWJ gave better material removal rate. But, the surface roughness produced by UA-AWJ is slightly higher than AWJ due to the more erosion depth in UA-AWJ process.

### 3.3 Micro Machining with AWJ

The abrasive water jet has great potential for micro machining. Miller [29] used 40  $\mu\text{m}$  diameter abrasive water jet with the abrasives of size ranging from 300 to 50 nm and obtained the hole diameter of 50  $\mu\text{m}$ . Further, Miller [29] compared the beam diameters of laser and water jet. The beam diameter of water jet was found to be less as compared to that of laser but had limited applications in drilling of soft and thin materials like aluminum and copper. Liu [30] demonstrated the AWJ micro machining by developing the fine feature on materials like stainless steel (0.25 mm), titanium (0.25 mm), aluminum (0.25), thick plastic (0.46 mm), alumina (0.64 mm) etc. The finest features developed are spiral slit on stainless steel and miniature butterfly on titanium as shown in Fig. 4a, b. The average size of the slit was found to be 250  $\mu\text{m}$ , and the thinnest rib of the butterfly produced by micro AWJ was 80  $\mu\text{m}$ . This process also gave the high aspect ratio of 80 for thin rib which is very difficult to maintain in other processes. Many researchers have formed micro channels and micro holes in ductile and brittle materials. Pang et al. [31] formed micro channels in glass and found that the material removal predominantly took place by ductile



**Fig. 4** Micro machined. **a** Spiral slit (stainless steel). **b** Miniature butterfly (titanium) [30]

erosion as no surface cracks were found. Also, the wave pattern was seen in the micro channel which occurred due to low kinetic energy of AWJ. At low kinetic energy, the AWJ gets diverged as it impacts the workpiece surface and the secondary jet flow occurs in radial direction which gives wave pattern to the surface of micro channel. Schwartzenruber and Papini [32] used back plate and hybrid  $\mu$ AWJ and AJM to improve the quality of piercing at entry and exit of the hole. Hagbin et al. [33] used micro nozzle (125  $\mu\text{m}$ ) and formed micro channels in Al 6061 T6 and SS 316 L material. The experimental results showed that the geometry of channel and channel depth affects the centerline erosion.

The major challenges in AWJ micro machining are nozzle clogging, fabrication of nozzle for  $\mu$ AWJ and flowability of fine abrasives which are explained below. The major problem associated with AWJ micro machining is clogging of nozzle by abrasives. As the diameter of the nozzle decreases, the vacuum in the mixing tube also decreases. This reduction in vacuum reduces the entrainment of abrasives in water jet stream which leads to frequent clogging of nozzle. The vacuum is minimum in the mixing chamber at the start of AWJ machining; hence, the nozzle clogging is maximum at that time. To solve this problem, an air ejector is used to increase the vacuum in the mixing chamber and avoid the nozzle clogging. The aspect ratio of mixing tube is an important factor for proper mixing and acceleration of entrained abrasives. Till now, the mixing tube with the inner diameter bigger than 200  $\mu\text{m}$  can be fabricated by electro-discharge machining process, but the fabrication of the same for diameter less than 200  $\mu\text{m}$  with optimum aspect ratio is still a problem [34]. In order to avoid the problem of nozzle clogging in  $\mu$ AWJ machining the size of the abrasive should be around one-third of the inner diameter of the mixing tube by thumb rule [34].

But, the flow ability of the particles decreases with the decrease in their size. In addition, the minute particles coagulate due to static electricity and lead to unsteady flow of abrasives in the jet stream. This unsteady flow of abrasives affects the quality of cut in  $\mu$ AWJ.

### ***3.4 Submerged WJ Cutting***

The underwater activities like decommissioning of power plant, cutting of structures, mining activities and cutting of rocks require the use of explosives which are dangerous and hazardous. These disadvantages have led to the development of research in underwater cutting by WJ which is clean, fast and cost-effective process. Some researchers have worked in the area of submerged AWJ machining. Hualin et al. [35] performed the parametric analysis and studied the rock breakage mechanism in underwater breaking of rocks. The maximum volume of rock breakage was found between 12 and 14° of nozzle inclination, and mostly, the mechanism of rock breakage was brittle failure. Haghbin et al. [33] compared unsubmerged and submerged waterjet technology for creating micro channels in metals. They found that the submerged AWJ produced narrower micro channels as compared to

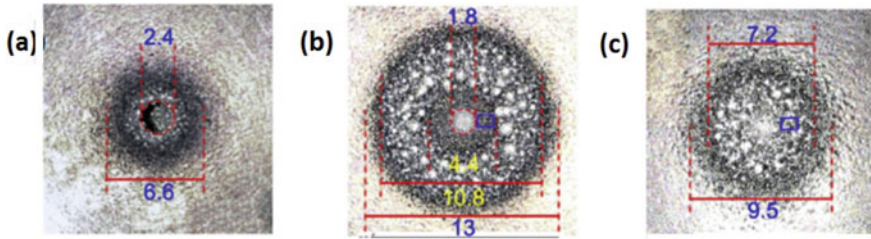


**Fig. 5** Variation of erosion with change in standoff distance. **a** Deep central pit at smaller standoff distance. **b** Ring-shaped erosion at medium standoff distance. **c** Less erosion at larger standoff distance [36]

the unsubmerged AWJ without any change in centerline erosion. The submerged AWJ gave better result due to less divergence of the jet underwater. The underwater WJ machining requires much more investigation to increase its performance characteristics.

The major challenge in submerged WJ cutting is cavitation which increases the material removal rate but decreases the precision of cutting. Peng et al. [36] showed that the standoff distance decides the intensity of the erosion by cavitation. They considered three standoff distances and conducted the erosion test. At the smaller standoff distance, erosion due to the cavitation is less, and the high speed waterjet is the main reason of material removal. The material removal at smaller standoff distance is represented by a central pit in Fig. 5a At the medium standoff distance, the erosion takes place by cavitation, and ring-shaped eroded area is formed as illustrated in Fig. 5b At this stage, the cavitation cloud is fully grown and reaches the target, giving maximum material removal. At the larger standoff distance, very less cavitation bubbles reach at the target surface, giving less erosion without any deep central pit as illustrated in Fig. 5c. Hence, the precision WJ cutting should be done at lower standoff distance, material disintegration should be done at medium standoff distance and operations like waterjet peening can be performed at larger standoff distance.

## 4 Challenges in AWJ

The challenges in existing waterjet machining are grit embedment, backflow of AWJ, high stagnation pressure and error in measurement of abrasive velocity in modeling.

### **4.1 Grit Embedment**

The grit embedment is considered as a serious issue for the fatigue life of the component, especially where the fluctuating stresses are encountered. Generally, in AWJ-CDM process, around 40% of the milled area gets covered with grit, and the problem of grit embedment cannot be solved completely but can be minimized by controlling the WJ milling parameters. Fowler et al. [37] conducted a grit embedment study in AWJ milling of titanium alloy and showed that the best case of the process parameters gave 5% of grit embedment. Shipway et al. [38] found an increase in grit embedment with the increase in impact angle at high traverse rate and even at lowest impact angle, the surface was found to be embedded with 7% grit.

### **4.2 Backflow of AWJ**

The backflow of AWJ is the major concern in drilling of blind holes which increases the diameter of the hole at the inlet due to the kerf formation. The AWJ drilling process removes the material by three types of loads [39]. (i) The direct jet pressure which impacts the surface and responsible for the progression of the hole (ii) the shear load due to the back flow of AWJ. The reversed fluid is the mixture of air and water laden with broken and intact abrasive particles. This backflow of AWJ creates a chaotic and turbulent condition which increases the size of the hole. (iii) The normal pressure is perpendicular to the kerf surface. Guo [39] performed numerical analysis in AWJ drilling and showed that the shear load is the most dominant among all the three loads which affects the displacement field more profoundly.

### **4.3 High Stagnation Pressure**

At the start of the AWJ machining, the formation of the jet leads to the vacuum in the mixing chamber which draws the abrasives from the hopper. Meanwhile, the mixing takes place; the abrasive-less jet impacts the workpiece for the shorter duration. The impact of this abrasive-less jet, having no cutting action, generates high stagnation pressure which damages the material in form of chipping and cracks. Many researchers have provided solutions to reduce the stagnation pressure, and one of them used abrasive cryogenic liquid jet [40]. As the cryogenic jet impacts the target surface, some of the liquid evaporate and reduce the stagnation pressure. However, the complete cryogenic jet system is cost ineffective, bulky and very difficult to maintain. In order to make this system cost effective, Liu and Schubert [34] developed flash AWJ (FAWJ) system which worked on the similar concept of abrasive cryogenic jet. In the developed system, super-heated water is used instead of cryogenic which evaporate to some extent at the time of impact. The authors compared the performance

of AWJ and FAWJ in drilling of composites and ceramics, and FAWJ gave better results as compared to the other. The FAWJ leads negligible stripping of coating as compared to AWJ.

#### ***4.4 Measurement of Particle Velocity***

The performance characteristics of AWJ system, namely surface roughness, depth of cut and surface waviness depend on the kinetic energy of particles in AWJ stream. Due to entrainment of air in abrasive waterjet stream, a three-phase mixture of abrasive, air and water is formed which makes the measurement of particle velocity very difficult. Hence, the measurement or prediction of particle velocity in AWJ stream is a challenging task. Tazibt et al. [41] proposed a three-phase (abrasive, water and air mixture) model of particle velocity without considering the particle distribution. Narayanan et al. [42] proposed a model considering the effect of distribution of abrasive size and breakage of abrasives on energy flux. The model was validated by the vast range of process parameters like geometry of cutting head, abrasive mass flow rate and WJ pressure. The prediction of abrasive velocity by a model generates error due to the assumptions during the modeling phase. Hence, the direct abrasive velocity measuring instruments are used to validate the results given by the various models. Many researchers have used methods like inductive method, laser-based method, optical method, jet impact method and double-disk apparatus method for measurement of abrasive velocity. However, each method has its own drawback which develops difficulty in the proper selection of the method for minimum error.

#### ***4.5 Error in Modeling and Simulation Study Due Assumptions***

The complete literature in modeling of AWJ process showed that most of the authors neglected some important assumptions which generated error in the prediction of results. These assumptions are as follows: distribution of particle size throughout the AWJ, the effect of particle breakage due to collisions, effect of jet structure, the energy distribution at the jet cross section and the change in particle velocity due to the loss of energy. And, incorporating all these assumptions would definitely minimize the error incurred in the prediction. The overall study of the literature in simulation of AWJ process by single particle impact showed that the inaccuracy in the developed models occurred majorly due to the improper definition of energy distribution, avoiding the dynamic loading conditions (velocity and acceleration) of AWJ and neglecting the effect of water impact on the workpiece. And, these inaccuracies can be reduced further by including all the assumption while generating a model. The literature study of erosion by multiple particle impact showed that the



crater wear becomes stable after the impact of few particles. Hence, the simulation models of multiple particle impacts are superior to the simulation models of single particle impact. However, very less work is done in the area of multiple particle impact as compared to the other.

## 5 Conclusion

This work reviewed the recent applications, developments and challenges in waterjet technology. The literature showed some new applications like hydroentangling, comminution, etc. The WJ machining has undergone many recent developments which either increased the performance characteristics or led the new application areas. The recent developments in WJ machining are ice abrasive waterjet cutting, WJ assisted processes, micro machining by WJ and submerged waterjet cutting. The ice abrasives removed the problems of low material removal rate of pure waterjet cutting and contamination of the products by abrasives as the abrasives are made up of ice. However, maintaining the hardness of the ice abrasives is still a challenge. The other developments in AWJ machining are AWJ assisted processes, namely vibration-assisted AWJ, thermally enhanced workpiece and cryogenic-assisted AWJ. All the three assisted processes gave higher material removal rate, but did not give the assurity of expected geometric dimensions. The submerged waterjet cutting is used for underwater decommissioning and dismantling of structures. The cavitation effect improves the efficiency of submerged WJ cutting by giving higher material removal rate. However, cavitation is the major drawback in this area of precision cutting. The general challenges in waterjet technology found in literature are grit embedment, backflow of AWJ, error in measurement of particle velocity and error in modeling and simulation. The problem of grit embedment cannot be solved completely, but it can be minimized by selecting optimum process parameters and by using pure waterjet as the secondary process. The backflow can be controlled by selection of proper pressure. The error in measurement of particle velocity can be minimized by selection of proper measuring instrument, and the error in modeling and simulation can be reduced by involving much assumptions which are left out by many researchers.

## References

1. Naresh BM, Muthukrishnan N (2014) Investigation on surface roughness in abrasive water jet machining by the response surface method. *Mater Manuf Process* 29:1422–1428
2. Natarajan Y, Murugasen PK (2016) Investigation of process parameters influence in AWJ cutting of D2 steel. *Mater Manuf Process* 32:1532–2475

3. Satyanarayana B, Srikar G (2014) Optimization of abrasive water jet machining process parameters using taguchi grey relational analysis. *Int J Mech Prod Eng* 2:82–87
4. Azmir MA, Ahsan AKA (2009) Study of abrasive water jet machining process on glass/epoxy composite laminate. *J Mater Process Technol* 209:6168–6173
5. Liu D, Huang C, Wang J, Zhu H, Yao P, Liu Z (2014) Modeling and optimization of operating parameters for abrasive waterjet turning alumina ceramics using response surface methodology combined with Box–Behnken design. *Ceram Int* 40:7899–7908
6. Aich U, Banerjee S, Bandyopadhyay A (2014) Multi-objective optimisation of abrasive water jet machining responses by simulated annealing and particle swarm. *Int J Mechatron Manuf Syst* 7:38–52
7. Pal VK, Choudhury SK (2016) Fabrication of texturing tool to produce array of square holes for EDM by abrasive water jet machining. *Int J Adv Manuf Technol* 85:2061–2071
8. Liu HT, Olsen JH (2013) Application of abrasive-waterjet For 3D machining. WJTA-IMCA conference and expo
9. Hashish M (2005) Abrasive waterjet cutting of microelectronic components. WJTA American waterjet conference, Houston, Texas
10. Patanaik A, Anandjiwala RD (2010) Hydroentanglement nonwoven filters for air filtration and its performance evaluation. *J Appl Polym Sci* 117:1325–1331
11. Pourmohammadi A, Russel SJ, Hottele S (2003) Effect of water jet pressure profile and initial web geometry on the physical properties of composite hydro entangled fabrics. *Text Res J* 73:503–508
12. Patanaik A, Anandjiwala RD, Boguslavsky L (2009) Development of high efficiency particulate absorbing filter materials. *J Appl Polym Sci* 114:275–280
13. Begenir A, Tafresh HV, Pourdeyhimi B (2004) Effects of nozzle geometry on hydro-entangling water jets: experiments observations. *Text Res J* 74:178–184
14. Anantharamaiah N, Tafreshi HV, Pourdeyhimi B (2006) Numerical simulation of the formation of constricted waterjets in hydroentangling nozzles: effects of nozzle geometry. *Chem Eng Res Des* 84:231–238
15. Borkowski P, Borkowski J, Wozniak D, Szymanowski J, Maranda A, Kostrow R, Milewski E (2007) The basis of high explosives washing out technology from heavy-artillery ammunition. WJTA American waterjet conference, Houston, Texas
16. Dunnen DN, Mulder L, Kerkhoffs GMMJ, Dankelman J, Tuijthof GJM (2013) Waterjet drilling in porcine bone: the effect of the nozzle diameter and bone architecture on the hole dimensions. *J Mech Behav Biomed Mater* 27:84–93
17. Dunnen DN, Dankelman J, Kerkhoffs GM MJ, Tuijthof GJM (2016) How do jet time, pressure and bone volume fraction influence the drilling depth when waterjet drilling in porcine bone. *J Mech Behav Biomed Mater* 62:495–503
18. Ortel J, Gaab MR, Piek J (2003) Water jet resection of brain metastases-first clinical results with 10 patients. *Eur J Surg Oncol* 29(4):407–414
19. Rau HG, Wichmann MW, Schinkel S, Buttler E, Pickelmann S, Schauer R et al (2001) Surgical techniques in hepatic resections: ultrasonic aspirator versus Jet-Cutter. A prospective randomized clinical Trial. *Zentralbl Chir* 126(6):586–590
20. Andersson U, Holmqvist G (2005) Strategies for cost—and time-effective use of abrasive waterjet cutting. WJTA American Waterjet Conference, Houston, Texas: 7B-2
21. McGeoug JA (2016) Cutting of food products by ice-particles in a waterjet. *Procedia CIRP* 42:863–865
22. Gupta K, Avvari M, Mashamba A, Mallaiiah M (2017) Ice jet machining: a sustainable variant of abrasive water jet machining sustainable machining 67–78
23. Truchot P, Mellinger P, Duchamp R (1991) Development of a cryogenic waterjet technique for biomaterial processing applications. In: 6th American waterjet conference, Houston, TX, 24–27 August 1991, pp 473–480. St. Louis, MO: Water Jet Technology Association
24. Borkowski PJ (2001) Physical basis of surface treatment with highpressure cryogenic multiphase liquid jet. *Arch Civ Mech Eng* 1:19–37

25. Patel D, Tandon P (2015) Experimental investigation of thermally enhanced abrasive waterjet machining of hard to machine metals. *CIRP J Manuf Sci Technol* 10:92–101
26. Yuvaraj N, Pradeep Kumar M (2014) Multiresponse optimization of abrasive water jet cutting process parameters using TOPSIS approach. *Mater Manuf Process* 30:882–889
27. Lv Z, Huang C, Zhu H, Wang J, Yao P, Liu Z (2015) FEM analysis on the abrasive erosion process in ultrasonic-assisted abrasive waterjet machining. *Int J Adv Manuf Technol* 78:1641–1649
28. Lv Z, Huang C, Zhu H, Wang J, Wang Y, Yao P (2015) A research on ultrasonic-assisted abrasive waterjet polishing of hard-brittle materials. *Int J Adv Manuf Technol* 78:1361–1369
29. Miller DS (2005) new abrasive water jet system to compete with lasers, Proceeding 2005 WJTA, American waterjet conference, paper 1A-1
30. Liu HT (2010) Waterjet technology for machining fine features pertaining to micro machining. *J Manuf Process* 12:8–18
31. Pang KL, Nguyen T, Fan J, Wang J (2010) Machining of micro-channels on brittle glass using an abrasive slurry jet. *Key Eng Mater* 443:639–644
32. Schwartzentruber J, Papin M (2015) Abrasive waterjet micro-piercing of borosilicate glass. *J Mater Process Technol* 219:143–154
33. Haghbin N, Spelt JK, Papini M (2015) Abrasive waterjet micromachining of channels in metals: comparison between machining in air and submerged in water. *Int J Mach Tools Manuf* 88:108–117
34. Liu HT, Schubert E (2009) Piercing in delicate materials with abrasive waterjets. *Int J Adv Manuf Technol* 42:263–279
35. Haulin L, Gensheng L, Jilei N (2008) Influential factors and mechanism analysis of rock breakage by ultra-high pressure water jet under submerged condition. *Chin J Rock Mech Eng* 27:1243–1250
36. Peng C, Tian S, Li G (2018) Joint experiments of cavitating jet: high speed visualization and erosion test. *Ocean Eng* 149:1–13
37. Fowler G, Shipway GH, Pashby IR (2005) A technical note on grit embedment following abrasive water-jet milling of a titanium alloy. *J Mater Process Technol* 159:356–368
38. Shipway PH, Fowler G, Pashby IR (2005) Characteristics of the surface of a titanium alloy following milling with abrasive waterjets. *Wear* 258:123–132
39. Guo Z (1998) Experimental and numerical analysis of abrasive waterjet drilling of brittle materials, PhD thesis, University of Washington
40. Thongkaew K, Wang J, Yeoh GH (2019) Impact characteristics and stagnation formation on a solid surface by a supersonic abrasive waterjet. *Int J Extreme Manuf* 1:1–19
41. Tazibt A, Parsy F, Abriak N (1996) Theoretical analysis of the particle acceleration process in abrasive water jet cutting. *Comput Mater Sci* 5:243–254
42. Narayanan C, Daniel RB, WeissKurt A, Heiniger C (2013) Modelling of abrasive particle energy in water jet machining. *J Mater Process Technol* 213:2201–2210

# Modeling and Simulation in Waterjet Technology



Paramjit Thakur, D. N. Raut, and Fauzia Siddiqui

**Abstract** Waterjet technology can cut soft, brittle, fibrous and difficult to cut materials without producing any heat-affected zone. This paper presents a vast review on modeling and simulation in pure and abrasive waterjet machining. The modeling in WJ can be divided in volume displacement models, energy conservation models, models developed on the basis of regression and dimensional analysis and fracture mechanics-based models. In simulation of abrasive waterjet machining, water is considered as a medium to accelerate the abrasive particles. The simulation in this area is generally divided into erosion by single particle impact and multi-particle impacts. Finally, the review is completed by discussing the challenges in modeling and simulation.

**Keywords** Modeling · Simulation · Abrasive waterjet · Volume displacement model

## 1 Introduction

The waterjet machining process was firstly commercialized in early 1980s in automotive and aerospace industries. Further, the contribution of researchers led the application of WJ in other areas too. The application of WJ machining in various areas is explained in section. The waterjet technology is used to machine variety of materials including difficult to cut materials, glass, ceramics and composites [1]. This process leads no heat-affected zone as the heat developed during the cutting process is carried away by the water. Hence, the temperature-sensitive materials like shape memory alloys can be easily cut by WJ. Also, and this process leads very less stress concentration on the cut surface which makes this process unique [2]. The small

---

P. Thakur (✉) · D. N. Raut  
Veermata Jijabai Technological Institute, Mumbai, India

D. N. Raut  
e-mail: [dnraut@pe.vjti.ac.in](mailto:dnraut@pe.vjti.ac.in)

F. Siddiqui  
JECRC, Jaipur, India

increase in temperature in the cutting process and the production of little flying dust makes this process safe from fire hazards and pollution. This process can be made easily available due to availability of water which can be recycled after cutting and the use of most commonly available abrasives like garnet and silica. This process gives very less cutting force as compared to the other non-traditional machining processes, and very less setup time is required in clamping the workpiece. Hence, the waterjet technology is a versatile machining process which is gaining importance nowadays.

This paper presents a vast review on modeling and simulation in pure and abrasive waterjet machining. The modeling in WJ can be divided in volume displacement models, energy conservation models, models developed on the basis of regression and dimensional analysis and fracture mechanics-based models. In simulation of abrasive waterjet machining, water is considered as a medium to accelerate the abrasive particles. The simulation in this area is generally divided into erosion by single particle impact and multi-particle impacts. Finally, the review is completed by discussing the challenges in modeling and simulation.

## **2 Modeling of Waterjet Machining**

The modeling in WJ can be divided in volume displacement models, energy conservation models, models developed on the basis of regression and dimensional analysis and fracture mechanics-based models.

### ***2.1 Volume Displacement Models***

The models in this part are developed on the equivalence between the geometrically obtained displacement and the differential volume removal which is physically estimated. The abovementioned assumption is valid only for the steady-state material removal process. The volume displacement models are formed by many authors and are displayed in Table 1.

Please note that the first paragraph of a section or subsection is not indented. The first paragraph that follows a table, figure, equation, etc., does not have an indent, either.

Subsequent paragraphs, however, are indented.

### ***2.2 Energy Conservation Models***

The energy conservation models are based on the equivalence between the kinetic energy of the AWJ and the MRR. The energy of the incoming jet is responsible for

the material removal, and hence, the decrease in WJ energy decreases the MRR. The complete detail about the energy conservation models is illustrated in Table 2.

**Table 1** Volume displacement model

Description	Model
<p>Finnie [3] was the pioneer in developing a model of material removal by single particle erosion. The material removal takes place by plastic deformation. The model was developed in relation to kinetic energy of particle and the flow stress. This model did not give better results for high impact angle which is its drawback. Also this model did not consider the interaction forces between the workpiece and abrasive</p>	$Q_1 = \frac{m_p V_p^2}{\sigma_f K \phi} \cdot f(\alpha)$ $F(\psi) = \sin(2\alpha) - \frac{6}{K} \sin^2 \psi \quad \text{For } \tan(\alpha) < \frac{K}{6}$ $F(\psi) = \frac{K \cos^2 \alpha}{6} \quad \text{For } \tan(\alpha) > \frac{K}{6}$ $K = \frac{F_y}{F_x} \cong 2, \quad \phi \cong 2$
<p>Bitter [4] divided the complete depth of cut by abrasive particles into cutting wear depth at shallow angle and deformation wear depth at large angle. The total material removed is equal to the addition of material removed by individual modes. The deformation wear is the effect of component of particle velocity parallel to the surface, and cutting wear is the effect of component of particle velocity perpendicular to t surface</p>	<p><b>Deformation Wear: <math>Q_d</math></b></p> $\frac{m_p (v \sin \alpha - V_C)^2}{2 \epsilon_d} \quad v \sin \alpha > V_C$ $0 \quad v \sin \alpha < V_C$ <p><b>Cutting Wear: <math>Q_c</math></b></p> $\frac{2 m_p C_3 (v \sin \alpha - V_C)^2}{\sqrt{V}} X \left( v \cos \alpha - \frac{C (v \sin \alpha - V_C)^2}{\sqrt{v \sin \alpha}} \epsilon_d \right)$ $\alpha \leq \alpha_0$ $\frac{m_p (V^2 \cos^2 \alpha - K (v \sin \alpha - V_C)^{3/2})}{2 \epsilon_c} \quad \alpha \geq \alpha_0$ $Q_2 = Q_d + Q_c \quad (C_3 \text{ is empirical constant})$
<p>Depth of cut model for ductile material: Hashish [5] gave depth of cut model for cutting wear (<math>h_c</math>) zone and deformation wear zone (<math>h_d</math>). Both the models are based on Finnie [3] micro-cutting model. Cutting wear (<math>h_c</math>) is the zone, where the particles impact at a relatively shallow angle and the surface is smooth, and deformation wear zone (<math>h_d</math>) is the zone where the particles impact the target at large impact angles. This zone is generally depicted by lower striation zone</p>	$h_c = \frac{c_1 d_{jet}}{2.5} \left( \frac{14 \cdot m_a}{\rho_p v d_{jet}^2} \right)^{0.4} \left( \frac{v_p}{v_{ch}} \right)$ $h_d = \frac{2 c_2 m_a (v_p - v_{ch})^2}{d_{jet} \sigma_f v}$ $h = h_c + h_d$

(continued)

**Table 1** (continued)

Description	Model
Depth of cut model for brittle material: Zeng et al. [6] related the effect of micro-cutting by particles with the macro-material removal rate on the cutting front. This model fits only for brittle material like ceramic, and it does not fit for deep cuts	$h = \frac{m_a m_w^2 p}{2670 (m_a + m_w)^2 d_{Fe} v}$
Physical waviness model: This model is specifically for striation zone when the impact angle is 90° and assumption of idealized geometry by Hashish [7]. The model is made on the assumption that the contact between the jet and the workpiece material is not steady in wear deformation zone. The author considered the circular geometry of the overlapping jet for generating this model	$\frac{2 R_W}{d_{jet}} = 1 - \sqrt{1 - \left(\frac{\pi}{4}\right)^2 \frac{d_{jet}^2 (h-h_c) v}{0.5 m_a v_p^2 / \gamma d}}$
Surface roughness model: Blickwedel et al. [8] approximated the surface roughness by a curvature on the kerf surface	$R_a(h^*) = R_a(0) + C \left(\frac{h^*}{h}\right)^{C_1}$ <p><math>C</math> and <math>C_1</math> are the constants. Also <math>R_a(0)</math> is the roughness near the kerf top</p>

### 2.3 Fracture Mechanics-Based Models

The fracture mechanics-based models for WJ cut surfaces are mostly developed for brittle materials. Many researchers have developed mathematical models based on fracture mechanics concept which is explained in Table 3.

### 2.4 Regression Model and Dimensional Analysis

Many researchers have worked with regression analysis and dimensional analysis in developing the mathematical models in WJ machining process which are displayed in Table 4.

## 3 Simulation in Abrasive Waterjet Machining

In AWJ machining, the erosion occurs due to the impingement of abrasives. In simulation of abrasive waterjet machining, water is considered as a medium to accelerate

**Table 2** Energy conservation models

Description	Model
<p>Chen et al. [9] developed a mathematical model based on the principle of energy conservation (material removal rate is proportional to the kinetic energy of the particles). The author first conducted the visualization study in AWJ cutting of alumina ceramic and found the kerf surface to be divided into three zones (smooth or upper zone, transition or middle zone and lower or deformation wear zone). The author modeled the smooth cutting zone (<math>h_c</math>) and the total depth of cut (<math>h</math>) as the middle zone was found to be around only 15% of the total depth of cut. The experimental analysis showed the strong correlation of depth of cut with the abrasive mass flow rate, pressure and particle velocity. Hence, the developed model consists of only these three variables</p>	$h_c = 0.88 \frac{m_a D_{50}^{0.51}}{V_p^{0.27} P}$ $h = 0.88 \frac{m_a D}{V_p^{0.5} P}$
<p>Wang [10] developed a depth of cut model for polymer matrix composite made up of cotton fiber and resin as matrix. The morphology study of the kerf surface showed that the resin was removed by the combination of cutting, plowing and cracking actions. Also, some amount of resin craters and flakes were found which showed the material removal by intergranular cracking which mostly happens in brittle material. Also, at some places the fiber pull out was found. Hence, the principle of energy conservation is used for the model development as the erosion theory and fracture mechanics methods become inappropriate for such materials. The experimental analysis showed that the abrasive mass flow rate and traverse rate had nonlinear relationship with the depth of cut. Hence, both the parameters were given exponent terms to improve the prediction efficiency of the model. This model gave the standard deviation of 8.17% in prediction of depth of cut</p>	$h = \frac{K P^{1-\alpha_2} m_a^{1-\alpha_1}}{d_{jet}^{0.6} V_p^{1-\alpha_3}}$ <p><math>\alpha_1, \alpha_2, \alpha_3, K</math> need to be calculated by experimentation</p>

(continued)



Table 2 (continued)

Description	Model
<p>Oh and Cho [11] developed a depth of cut model in cutting of rock material. The depth of cut model is developed on the assumption that the erosion of rock takes place by the impact of accelerated particles on the target material, and the energy distribution of the jet follows a normal distribution curve. This model does not take the collision of particles into account. Also, a linear relationship was assumed between standoff distance and jet diffusion. The model correlated the depth of cut with the energy of jet (waterjet pressure, traverse rate, abrasive flow rate and water flow rate), geometry parameter (standoff distance), nozzle system parameters (orifice diameter, focusing tube diameter, etc.) and material properties (properties of rock and abrasives). Once the maximum energy is determined, the cutting depth is obtained according to the values of <math>\alpha_2</math> and <math>\beta_2</math>. The constant <math>\alpha_2</math> depends on the properties of workpiece (hardness, mineral composition and strength) which provide abrasion resistance. As the value of <math>\alpha_2</math> decreases, the abrasion resistance increases; hence, <math>1/\alpha_2</math> is termed as the index of resistance. The constant <math>\beta_2</math> is termed as performance efficiency, and higher the value of <math>\beta_2</math>, better is the depth of cut. This model correlated the large number of parameters as compared to the other models reported in literature; hence, this model can be utilized to estimate the depth of cut for any specified set of waterjet parameters</p>	$\sigma = \frac{\tan \theta \cdot d_s + \frac{d_p}{2}}{2.576}$ <p><b>Maximum kinetic energy (<math>\sigma \leq 0.4</math>)</b></p> $E_{\text{max}} = \frac{m_a d_0 P}{4 \Pi v} \left( \frac{2.576 \cdot C_r C_k}{(\tan \theta \cdot d_s + \frac{d_p}{2}) \cdot (1 + \frac{m_a}{m_w})} \right)^2$ <p><b>Maximum kinetic energy (<math>\sigma \geq 0.4</math>)</b></p> $E_{\text{max}} = \frac{m_a d_0 P}{4 \Pi v} \left( \frac{2.5 \cdot C_r C_k}{(1 + \frac{m_a}{m_w})} \right)^2$ $h = \alpha \left( \frac{E_{\text{max}}}{1 J} \right)^\beta$

the abrasive particles. The simulation in this area is generally divided into erosion by single particle impact and multi-particle impacts.

**Table 3** Fracture mechanics-based model

Description	Model
<p>E1-Domiati and Abdel-Rahman [12] developed two models in cutting of ceramic material on the basis of two assumptions</p> <p>Assumption 1: Surface chipping and the propagation of cracks are led by the plastic deformation process. The parameters considered here are flow stress density, hardness, fracture toughness, etc., and particle properties</p> <p>Assumption 2: Radial crack size is proportional to lateral crack size</p> <p>Both the model predicted almost same results with around 10% error</p>	<p><b>Model 1: (<math>C_1</math> and <math>C_2</math> constants)</b></p> <p><b>Volume removal rate</b></p> $Q = C_1 v^{19/6} r_p^{11/3} \rho_p^{19/12} K_C^{-4/3} H^{-1/4}$ <p><b>Depth of cut</b></p> $h = C_1 g_1(\alpha) \left( \frac{1}{v d_{\text{det}}} \right) m_a v^{19/6} r_p^{2/3} \rho_p^{7/12} K_C^{-4/3} H^{-1/4}$ <p><b>Model 2:</b></p> <p><b>Volume removal rate</b></p> $Q = C_2 v^{22/9} r_p^{11/3} \rho_p^{11/9} K_C^{-4/3} H^{-1/9}$ <p><b>Depth of cut</b></p> $h = C_2 g_2(\alpha) \left( \frac{1}{v d_{\text{det}}} \right) m_a v^{22/9} r_p^{2/3} \rho_p^{2/9} K_C^{-4/3} H^{1/9}$
<p>Zhu et al. [13] generated the material removal model by fracture erosion of brittle material. For this, the author considered experimentation of two brittle materials, namely silicate glass and alumina ceramic. The assumption in this work is that the response of the material is similar to static indentation of sharp indenter</p>	$Q = f_1 \frac{E^{5/4} E_k^{7/6}}{K_2 H^{17/12}} \left( 1 - f_2 \frac{E^{1/4} K_2}{H^{12} E_k^{1/6}} \right)$ <p><math>f_1</math> and <math>f_2</math> are the constants obtained from experimentation</p>
<p>Zeng and Kim [14] studied the erosion mechanism in AWJ cutting of polycrystalline ceramics. The erosion mechanism found in this study was intergranular cracking and plastic deformation. The author used Finnie model for plastic flow contribution and network crack model for contribution of fracture in material removal</p>	<p><b>Volume removed due to fracture:</b> (<math>f_w</math> proportionality constant)</p> $Q_1 = \frac{f_w \sigma_f v^2 (\sin^2 \alpha) \beta R_1 m_p}{3 \gamma E}$ <p><b>Volume removed due to plastic deformation:</b></p> $Q_2 = \frac{m_p v^2}{4 \sigma_f} (\sin 2\alpha - 4(\sin^2 \alpha) + 38.12 v \sin^3 \alpha \sqrt{\frac{\rho_p}{\sigma_f}})$ $\beta = 14.33 - 6.25 \sin 2.8\vartheta$ <p><b>Total volume removed <math>Q = C(Q_1 + Q_2)</math></b></p>

(continued)

**Table 3** (continued)

Description	Model
Zeng and Kim [15] performed AWJ milling of polycrystalline ceramic and developed a model of depth of cut based on fracture mechanics. The erosion mechanism considered in this study was intergranular cracking, and the impact stress waves were linked for intergranular cracking for model generation. Here a new constant erosion resistance was developed which can be calculated easily by experimentation. The constant erosion gives the effect of material properties (grain size, density of target, particle density, elasticity modulus, fracture energy)	<p><b>Volume removed</b> (<math>f_w</math> proportionality constant)</p> $Q = \frac{C f_w R_1 \varepsilon(e) \eta(v) \rho v_p^2 m_p \left(\frac{\rho_p}{\rho}\right)^{\frac{1}{2}} \left(\frac{H_d}{E}\right)^{\frac{3}{2}}}{12\gamma}$ <p><b>Erosion resistance</b></p> $r_e = \frac{12\gamma}{R_1 \varepsilon(e) \eta(v)} \left(\frac{\rho_p}{\rho}\right)^{\frac{1}{2}} \left(\frac{H_d}{E}\right)^{\frac{3}{2}}$

### 3.1 Single Particle Erosion

Many researchers have worked in the domain of erosion by single particle impact, and most of the work is related to the interaction between the particle and the target as illustrated in Fig. 1a. Moreover, many researchers have used different profiles of energy distribution for simulation of material removal process in AWJ machining. Lebar and Junkar [19] simulated the material removal mechanism in single particle erosion at different impact angles using unit event approach. They considered that the uniform distribution of energy at the cross section of the abrasive waterjet and the superimposition of all the unit events gave the eroded surface. Orbanic and Junkar [20] also applied the uniform energy distribution in simulating AWJ process by cellular automata approach. Henning and Westkamper [21] considered Gaussian bell shape as energy distribution in AWJ cross section and simulated the erosion process by phenomenological approach. Here, the wear mechanism was studied by varying the impingement angle and considering the different energy profiles at the cross section of AWJ. Similarly, Chen and Siores [22] used double slope energy distribution for the simulation of AWJ process. The optimum profile of the energy distribution is not yet reported in literature. Also, the dynamic behavior of abrasive waterjet on the impact of the particle is not considered by many researchers which is considered in the work by Junkar et al. [23] and Hassan and Kosmol [24]. Junkar et al. [23] considered the velocity and gravity as the dynamic properties of AWJ in simulation of single particle impact on AISI 304 steel. The crater wear was studied in their work by varying the impact angle which was found to be an influential parameter in the formation of crater wear. Hasan and Kosmol [24] studied the behavior of target material under the dynamic load of AWJ and found that the stresses increase in the workpiece in a short time (the period of impact) and decrease thereafter. The compressive stresses generated in the target material exceed the rupture strength of the material which causes the material to flow.

### 3.2 Multiple Particle Erosion

The material removal in AWJ process takes place by the impingement of abrasives on the target surface. When the particles impinge on the target surface, the initial few particles only provide the plastic deformation in the material, and the erosion occurs by the impact of the subsequent particles [25]. Hence, the simulation of AWJ machining process gives more accurate results by multi-particle erosion

**Table 4** Models by regression and dimensional analysis

Description	Model
<p>Kovacevic et al. [16] developed a regression model of depth of cut in AWJ cutting of concrete. The experimental design used for experimentation was 2<sup>n</sup> factorial design</p>	<p><math>h = C_0 p^{C_1} d_F^{C_4} v^{C_3} m_a^{C_2} S_d^{C_6}</math>  <math>C_0, C_1, C_2, C_3</math> and <math>C_4</math> are the constants</p>
<p>Matsui et al. [17] developed a relationship between the AWJ cutting process parameters and the material properties. Here, the elongation, plastic deformation energy and hardness are used to evaluate the depth of cut for ductile material. However, the fracture toughness is used to evaluate the same for the brittle material. During the experimentation, only the traverse rate was varied, and rest of the process parameters were kept constant. The ductile materials used in this work are stainless steel, mild steel, titanium, etc., and brittle materials used are soda glass, granite, marble, etc. The SEM analysis of the cut surface showed that the different material removal mechanisms are involved in the cutting of ductile and brittle materials. The author also suggested that the model can be further refined by taking micro-cutting phenomenon into consideration</p>	<p><b>Ductile material</b>  <math>h = \frac{10^{4.74}}{(H, \epsilon)^{0.67}}</math>  <b>Brittle material</b>  <math>h = 10^{0.91} \left( \frac{\sigma_T^2}{2 E_M} \right)^{-1.97}</math></p>

(continued)

**Table 4** (continued)

Description	Model
<p>Wang [18] developed a depth of cut model using dimensional analysis technique in cutting of alumina ceramic by AWJ. In this work, the author assumed the kerf width to be constant throughout the depth of cut. Also, the kerf width is assumed to be equal to the diameter of jet exiting the nozzle which means the jet divergence was neglected in this work. Around 104 experiments were conducted for model assessment with the following process variables: traverse rate, water pressure, standoff distance and abrasive mass flow rate. The model predicted the results with 1% average error and the standard deviation of 6.48%</p>	<p><b>Volume removal rate</b></p> $Q = C_1 d_p^3 \alpha^a \left(\frac{H_d}{E}\right)^b \frac{2(k_1 k_d k_m)^2 \rho_p P}{\rho_w \sigma_f}$ <p><b>Depth of cut</b></p> $h = K \frac{15615.20 m_u}{\rho_p d_{jet} v} \left(\frac{P}{\sigma_f}\right)^{0.255} \left(\frac{S_d}{d_p}\right)^{0.933} \left(\frac{S_d m_u}{d_p^3 \rho_p u}\right)^{-0.915} \left(\frac{\rho_p v_p^2}{P}\right)^{-0.014}$ <p><math>a, b, d, K</math> and <math>C_1</math> are the constants</p>

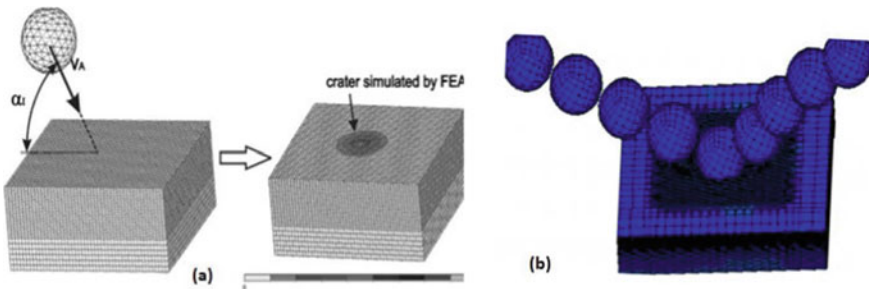


**Fig. 1** Simulation in AWJ machining. **a** Single impact erosion [26]. **b** Multiple impact erosion [27]

which is much more complex than single particle erosion. Maniadaki [25] performed the multi-particle erosion simulation to find the influence of particle velocity and impingement angle on crater circularity. Here, twenty abrasive particles were used for three different values of particle velocity and impingement angle. The crater circularity was found to be stable after the impact of thirteenth particle. El Tobgy et al. [26] developed an elasto-plastic model and simulated AWJ process by impact of three particles on the target surface. The flow stress was based on Johnson cook material model, and the rate of erosion was found to be stable after the impact of three particles. On the similar ways, Kumar and Shukla [27] studied the effect of

particle velocity and impingement angle on erosion rate, depth of crater and crater circularity rate by finite element (FE) simulation as illustrated in Fig. 1b. The new thing in this work was that the author used the size of particle equivalent to that used in practical AWJ machining (100  $\mu\text{m}$ ) which was smaller than that used in most of the works. The elasto-plastic model in FE analysis was found to be stable after the impact of 17th particle.

## **4 Challenges in Modeling and Simulation of AWJ Process**

The major challenges in modeling and simulation of AWJ process are error in modeling study due to the non-involvements of some important assumptions, error in simulation study due to non-involvements of some important assumptions and measurement of particle velocity.

### ***4.1 Error in Modeling Study Due to the Non-Involvements of Some Important Assumptions***

The complete literature in modeling of AWJ process showed that most of the authors neglected some important assumptions which generated error in the prediction of results. These assumptions are as follows: distribution of particle size throughout the AWJ, the effect of particle breakage due to collisions, effect of jet structure, the energy distribution at the jet cross section and the change in particle velocity due to the loss of energy. And, incorporating all these assumptions would definitely minimize the error incurred in the prediction.

### ***4.2 Error in Simulation Study Due to Non-Involvements of Some Important Assumptions***

The overall study of the literature in simulation of AWJ process by single particle impact showed that the inaccuracy in the developed models occurred majorly due to the improper definition of energy distribution, avoiding the dynamic loading conditions (velocity and acceleration) of AWJ and neglecting the effect of water impact on the workpiece. And, these inaccuracies can be reduced further by including all the assumption while generating a model. The literature study of erosion by multiple particle impact showed that the crater wear becomes stable after the impact of few particles. Hence, the simulation models of multiple particle impacts are superior to the simulation models of single particle impact. However, very less work is done in the area of multiple particle impact as compared to the other.

### 4.3 Measurement of Particle Velocity

The performance characteristics of AWJ system, namely surface roughness, depth of cut and surface waviness, depend on the kinetic energy of particles in AWJ stream. Due to entrainment of air in abrasive waterjet stream, a three-phase mixture of abrasive, air and water is formed which makes the measurement of particle velocity very difficult. Hence, the measurement or prediction of particle velocity in AWJ stream is a challenging task. Tazibt et al. [28] proposed a three-phase (abrasive, water and air mixture) model of particle velocity without considering the particle distribution. Narayanan et al. [29] proposed a model considering the effect of distribution of abrasive size and breakage of abrasives on energy flux. The model was validated by the vast range of process parameters like geometry of cutting head, abrasive mass flow rate and WJ pressure. The prediction of abrasive velocity by a model generates error due to the assumptions during the modeling phase. Hence, the direct abrasive velocity measuring instruments are used to validate the results given by the various models. Many researchers have used methods like inductive method, laser-based method, optical method, jet impact method and double disk apparatus method for measurement of abrasive velocity. However, each method has its own drawback which develops difficulty in the proper selection of the method for minimum error.

## 5 Conclusions

The area of modeling of AWJ process consisted of volume displacement models, energy conservation models, models based on regression and dimensional analysis, fracture mechanics-based models and simulation models. The simulation models found in literature dealt with single particle and multi-particle erosion. The multi-particle erosion represents the actual process where the erosion becomes stable after the impacts of multiple particles. However, not much literature is found in the area of multiple particle erosion as compared to the erosion by single particle impact. The major problem in modeling of AWJ is the measurement of particle velocity and non-involvement of some of the important assumptions. There are many devices which are used for the measurement of particle velocity, but they have their own drawbacks. Hence, it is difficult to select a proper particle measuring instrument for minimum error.

## Appendix

### List of Abbreviation

$C_f$	Friction coefficient on kerf wall
$C_k$	Characteristic velocity (m/s)

$C_a$	Amphibole content (%)
$C_b$	Biotite content (%)
$D$	Measurement of roughness (mm)
$D_r$	Direction of rotation of workpiece
$D_m$	Diameter of mixing tube (mm)
$E_{\max}$	Maximum kinetic energy (J)
$E_K$	Kinetic energy (J)
$E$	Modulus of elasticity (GPa)
$E_0$	Percentage elongation (%)
$F_f$	Constant of proportion of wave energy
$G_s$	Maximum grain size (mm)
$G_m$	Mean grain size (mm)
$H_c$	Cutting wear depth (mm)
$H_d$	Deformation wear depth (mm)
$J$	Material thickness (mm)
$J_t$	Type of jet
$K_d$	Function of coefficient of drag
$K_C$	Fracture toughness (MPa)
$K_{CI}$	Critical stress intensity factor
$K_d$	Discharge coefficient for AWJ
$K_m$	Efficiency for momentum transfer
$MRR$	Material removal rate
$M_p$	Mass of the impacting particle
$M_a$	Mass flow rate of abrasives ( $\text{g min}^{-1}$ )
$M_w$	Mass flow rate of water ( $\text{g min}^{-1}$ )
$M$	Total mass of particles impacting on a surface
$Q_p$	Volume due to plastic deformation ( $\text{mm}^3/\text{min}$ )
$R_w$	Surface waviness
$R_a$	Surface roughness ( $\mu\text{m}$ )
$R_f$	Roundness factor of abrasive
$S_f$	Sphericity of abrasive
$V_j$	Velocity of particle (m/s)
$V_p$	Average particle velocity (m/s)
$V_{\text{jet}}$	Velocity of abrasive waterjet (m/s)
$V$	Traverse rate
$W_L$	Stress wave energy
$W_o$	Stress wave energy at impact angle
$W_{ab}$	Water absorption of rock
$W_m$	Minimum kerf width (mm)
$W_t$	Kerf width (mm)
$\xi_D$	Constant of specific erosion energy
$\rho$	Fluid jet density ( $\text{Kg/m}^3$ )
$\epsilon$	Energy per unit volume ( $\text{J/mm}^3$ )
$\gamma$	Fracture energy ( $\text{J/m}^3$ )
$\rho_w$	Density of workpiece ( $\text{Kg/mm}^3$ )



$\rho_b$	Bulk density (Kg/mm <sup>3</sup> )
$\rho_p$	Density of particle (Kg/m <sup>3</sup> )
$\sigma_0$	Flexural strength (MPa)
$\sigma_t$	Tensile stress (MPa)
$\sigma_f$	Flow stress (MPa)
$\sigma_{sp}$	Specific energy of target material
$\varepsilon_c$	Cutting wear factor
$\varepsilon_d$	Deformation wear factor
$\theta$	Jet diffuse angle (°)
$\theta_f$	Kerf angle (°)
$\beta_2$	Performance

## References

1. Naresh BM, Muthukrishnan N (2014) Investigation on surface roughness in abrasive water jet machining by the response surface method. *Mater Manuf Process* 29:1422–1428
2. Natarajan Y, Murugasen PK (2016) Investigation of process parameters influence in AWJ cutting of D2 steel. *Mater Manuf Processes* 32:1532–2475
3. Finnie I (1960) Erosion of surfaces by solid particles. *Wear* 3:87–103
4. Bitter JA (1963) Study of erosion phenomena, part 1. *Wear* 6:161–190
5. Hashish M (1984) A modeling study of metal cutting with abrasive waterjet. *J Eng Technol* 106:88–10
6. Zeng J, Heines R, Kim TJ (1991) Characterization of energy dissipation phenomena in abrasive water jet cutting. In: Labus TJ (ed) 1991 Proceedings of 6th American water jet conference, Water Jet Techn. Ass., St. Louis, vol 225, pp. 163–177
7. Hashish M (1992) On the modeling of surface waviness produced by abrasivewaterjets. *Jet Cutting Technol* 17–34
8. Blickwedel H, Guo NS, Haferkamp H, Louis H (1990) Prediction of abrasive jet cutting performance and quality. In: Proceedings of the 9th international symposium on jet cutting technology, Amsterdam, The Netherlands, pp 164–179
9. Chen L, Siores E, Wong (1996) WCK Kerf characteristics in abrasive waterjet cutting of ceramic materials. *Int J Machine Tools Manuf* 36:1201–1206
10. Wang J (1999) Abrasive waterjet machining of polymer matrix composites—cutting performance, erosive process and predictive models. *Int J Adv Manuf Technol* 15:757–768
11. Oh TM, Cho GC (2016) Rock cutting depth model based on kinetic energy of abrasive waterjet. *Rock Mech Rock Eng* 49:1059–1072
12. E1-Domiaty I, Abdel-Rahman AA (1997) Fracture mechanics-based model of abrasive waterjet cutting for brittle materials. *Int J Adv Manuf Technol* 13:172–181
13. Zhu H, Huang C, Wang J, Zhao G, Li Q (2009) Modeling material removal in fracture erosion for brittle materials by abrasive waterjet. *Adv Mater Res* 76–78:357–362
14. Zeng J, Kim TJ (1996) An erosion model for abrasive waterjet milling of polycrystalline ceramics. *Wear* 199:275–282
15. Zeng J, Kim TJ (1996) An erosion model of polycrystalline ceramics in abrasive waterjet cutting. *Wear* 193:207–217
16. Kovacevic R (1978) Surface texture in abrasive waterjet cutting. *J Manuf Syst* 10:32–40
17. Matsui S, Matsumura H, Ikemoto Y, et al (1991) Prediction equations for depth of cut made by abrasive water jet. In: Labus T J (ed) 1991 Proc. 6th Amer. Water Jet Conf, WJTA, St.Louis.31–41(1991).

18. Wang J (2009) A new model for predicting the depth of cut in abrasive waterjet contouring of alumina ceramics. *J Mater Process Technol* 209:2314–2320
19. Lebar A, Junkar M (2003) Simulation of abrasive waterjet machining based on unit event features. *ProcInstMechEng B J Eng Manuf.* 217(B5):699–703
20. Orbanic H, Junkar M: Cellular automata in mechanical engineering. In: Junkar M, Levy PR, editors. *Proceedings of the sixth international conference on management of innovative technologies*. Piran, Slovenia: LAT, TAVO. 139–47 (2003).
21. Henning A, Westkamper E (2003) Modelling of wear mechanisms at the abrasive waterjet cutting front. In: Summers DA (ed) *Proceedings of the 2003 WJTA American waterjet conference*, WJTA. Paper3-A, Houston, TX, USA
22. Chen FL, Siores E (2003) The effect of cutting jet variation on surface striation formation in AWJ cutting. *J Mater Process Technol* 135:1–5
23. Junkar M, Jurisevic B, Fajdiga M, Grah M (2006) Finite element analysis of single-particle impact in abrasive water jet machining. *Int J Impact Eng* 32:1095–1112
24. Hassan AI, Kosmol J (2000) A finite element model for abrasive waterjet machining. *J Theor Appl Mech* 38:957–968
25. Maniadaki K, Antoniadis A, Bilalis N (2011) Effect of impact angle and velocity in crater circularity in abrasive water jet machining by means of multi-particle impact simulation. *Int J Mach Mach Mater* 10:34–47
26. El Tobgy MS, Ng E, Elbestawi MA (2005) Finite element modeling of erosive wear. *Int J Mach Tools Manuf* 45:1337–1346
27. Kumar N (2012) Shukla M : Finite element analysis of multi-particle impact on erosion in abrasive water jet machining of titanium alloy. *J Comput Appl Math* 236:4600–4610
28. Tazibt A, Parsy F (1996) Abriak N : Theoretical analysis of the particle acceleration process in abrasive water jet cutting. *Comput Mater Sci* 5:243–254
29. Narayanan C, Daniel RB, WeissKurt A (2013) Heiniger C : Modelling of abrasive particle energy in water jet machining. *J Mater Process Technol* 213:2201–2210

# Elastic–Plastic Stability Analysis of Perforated FGM Plate



Daaman Sharma, Nimeesh Rathi, and Kanishk Sharma

**Abstract** Present work examines the elastic–plastic behavior of shear deformable FGM plate using ANSYS. The proportions of the parent materials are varied across the thickness of FGM plate via power law. The results from present formulation are compared with the available literature and various parametric studies are conducted. From the current study, it has been revealed that the plate thickness induces plasticity region prominently, especially, around the cutout regions in the FGM plate. Moreover, the FGM plate with higher ceramic proportion possesses higher buckling and failure load. The cutout size affects the buckling load significantly and plate with larger size of cutout depicted lower buckling strength.

**Keywords** Elastic–plastic FGM · Stability analysis · Functionally graded material (FGM) · Nonlinear finite element analysis · FGM failure

## 1 Introduction

Thin-walled structural elements such as beam, plate, and shell are primarily used in almost all engineering applications due to their innumerable attractive geometrical properties features such as lightweight, high specific strength, and stiffness. Meanwhile, the composite structures have been widely used in various engineering applications due to their higher specific strength and stiffness. Consequently, the application of composite plates has been engendered in aerospace, marine, and automotive structures. Despite the preferable properties offered by composite materials, the abrupt changes in material composition at the interface of the conventional composites provokes higher interfacial stress that can lead to delamination, matrix cracking, and adhesive bond separation failure under critical loading conditions at elevated temperature. As a means to overcome the limitations associated

---

D. Sharma (✉) · N. Rathi · K. Sharma  
JECRC University, Jaipur, India

K. Sharma  
e-mail: [kanishk.sharma@jecrcu.edu.in](mailto:kanishk.sharma@jecrcu.edu.in)

with the traditional composite materials, a new class of composites namely functionally graded materials (FGMs) were proposed by Japanese Scientists in 1984 [1]. In FGMs, the material composition of two or more materials is varied smoothly and continuously in one or more spatial directions according to some mathematical function. The preferable material properties at a particular location of FGM structures can be tailored and achieved by virtue of controlling the volume fractions of constituent materials ascribed by the predefined function. For instance, the required thermal resistance altogether with the desired mechanical strength for thermal barrier structures can be readily obtained by combining and varying the proportions of ceramic and metallic constituents in a predefined manner. FGM offers enormous advantages over traditional materials, particularly under severe operating conditions, such as in heat shields, heat exchangers, biomedical implants, and fusion reactors, and many more [2]. It is found in many investigations that functionally graded structures show much better structural performance as compared to the homogenous isotropic materials under thermo-mechanical loading [3–5]. A comprehensive review comprising the recent advancement in FGM fabrication techniques and research contribution in the field of thermos-elastic static and vibration analysis of FGM structures can be found in the works of [1, 2, 6–8].

In the current analysis, the buckling and post buckling response of shear deformable elastic–plastic FGM plate is examined. Parametric studies are conducted and effects of cutout sizes and material gradation on the response of FGM plate are presented.

## 2 Finite Element Model of Layerwise FGM Plate

The material properties of FGM plate are calculated with the power law, wherein the volume fractions of metal and ceramic are given as follows,

$$V_m(z) = \left( \frac{z}{h} + \frac{1}{2} \right)^n ; V_c(z) = 1 - V_m(z) \quad (1)$$

where  $V_c$  and  $V_m$  are volume fractions of the ceramic and the metallic phases of FGM. The power law exponent  $n$ , controls the material gradation of FGM plate.

The mechanical properties of FGM plate are evaluated at mid of each layer using TTO model [4, 9, 10]. The elastic-plastic response of FGM plate is examined using FEM software ANSYS. The FGM is modeled using ANSYS in which the material properties of FGM plate are calculated using modified rule of mixture called TTO model which is originally developed for two-phase composites. The four-noded shell element with five degree of freedom is used. The considered meshing element is applicable in modeling the elasto-plastic large deformation behavior.

### 3 Problem Definition

The FGM plate with length  $a$ , width  $b$ , and thickness  $h$ , having central cutout with cutout ratio ( $d/b$ ) is analyzed under uni-axial in-plane compression load. The FGM plate is made of TiB and Ti with  $E_c = 375$  GPa,  $E_m = 107$  GPa,  $\nu = 0.24$  (for ceramic and metal both)  $\sigma_{ym} = 400$  MPa and  $H_m = 14$  GPa. The stress–strain transfer ratio is 4.5 GPa as given in Ref. [11].

The FGM plate with simply supported boundary condition on all the edges is depicted in Fig. 1. It is important to mention that the present study is carried out with circular cutout of ratio  $d/b = 0.1$ , wherein  $d$  denotes the diameter of circular cutout at the center of FGM plate with width  $b$ , excluding the study wherein effect appertaining to the cutout size is considered; in which the size of circular cutout is varied by taking different cutout ratios (i.e.,  $d/b = 0.10, 0.15, 0.20, 0.25$  and  $0.30$ ). The model of axially compressed FGM plate carrying a central circular cutout with simply supported boundary conditions is depicted in Fig. 1.

Non-dimensionalized buckling and failure load are used in results in the following form:

In-plane buckling and failure load:  $\frac{N_x b^2}{E_c h^3}$ .

The non-dimensionalized transverse deflection is given by  $\frac{w_{max}}{h}$  where  $E_c$ ,  $h$ ,  $b$ ,  $N_x$  and  $w_{max}$  are the respective values of Young’s modulus, thickness, width, the in-plane compressive load per unit length, whereas the maximum deflection in the transverse direction is  $w_{max}$ .

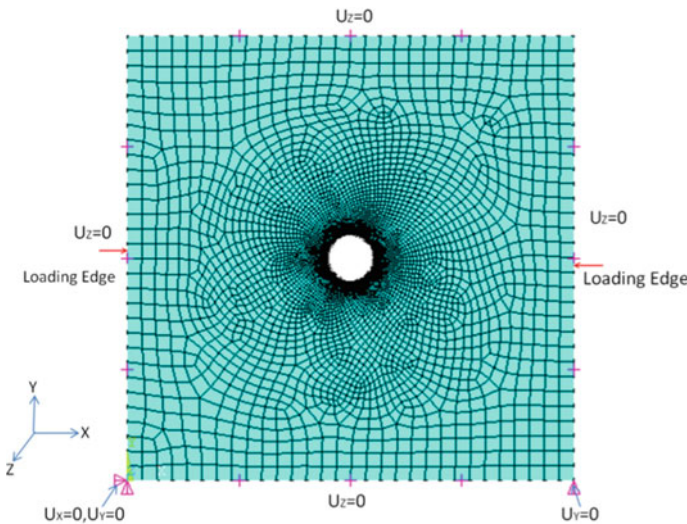


**Fig. 1** Boundary and loading conditions for present study

**Table 1** Convergence analysis for buckling load ( $\lambda = \frac{N_x b^2}{E_c h^3}$ ) and failure load ( $\lambda^* = \frac{N_{fail} b^2}{E_c h^3}$ ) of Ti/TiB FGM square plate with concentric cutout of size 0.1 under uni-axial compression

Size of elements (at outer area, near cutout)	No. of layers					
	10		20		30	
	$\lambda$	$\lambda^*$	$\lambda$	$\lambda^*$	$\lambda$	$\lambda^*$
(1/10,1/40)	1.6831	6.5333	1.6678	4.0000	1.6622	4.0000
(1/20,1/80)	1.6687	3.7333	1.6535	3.7333	1.6481	3.6000
(1/30,1/120)	1.6672	3.7333	1.6521	3.6000	1.6467	3.5733
(1/40,1/160)	1.6614	3.7333	1.6463	3.5733	1.6414	3.5200

## 4 Convergence Study

In the layerwise modeling of FGM plate, a convergence study is required to determine the required layer number which can closely approximate the FGM with continuously varied material composition. Accordingly, a convergence study to decide the required number of layers and elements is conducted for an FGM plate with central circular cutout using 10, 20, and 30 layers and different element size (i.e., as mentioned earlier, the entire plate is meshed uniformly with shell 181 element except at the periphery of cutout, where smaller size of shell 181 element is used).

It should be noted that at the cutout edges, there is a need of more dens meshing due to involved geometrical irregularities; hence, at cutout edges, the meshing elements are four times smaller than other meshing elements. The results of convergence study for element performed with considered for convergence study are (1/5,1/20); (1/10,1/40); (1/20,1/80); (1/40,1/160); and (1/80,1/320) with 10, 20, and 30 layers. Results of convergence study in the non-dimensional form of buckling and ultimate failure load of FGM plate are shown in Table 1. As shown in Table 1, the results converged for the element sizes of (1/30,1/120) with 20 layers.

## 5 Validation

To validate the present FEM model, the present results are compared with the previous literature for a perforated plate made of steel and containing a central cutout of circular shape. The ratio of ultimate buckling load with squash load are compared with the available literature [12], keeping the same material properties and geometry for plate as provided in previous literature [12]. The results of present model are in good accordance with the established work (Table 2).

**Table 2** Comparison of inelastic buckling stress ratios calculated using present model and that reported in the literature [12]

<i>b/h</i>	<i>d/b</i> = 0.1		<i>d/b</i> = 0.2		<i>d/b</i> = 0.3	
	Present	Ref. [9]	Present	Ref. [9]	Present	Ref. [9]
30	0.91	0.91	0.81	0.81	0.72	0.71
40	0.90	0.85	0.81	0.79	0.69	0.67
50	0.75	0.76	0.69	0.72	0.62	0.64

## 6 Numerical Results and Discussion

In the current section, different studies pertaining to the material gradation and cutout size are conducted and results are presented to examine the effects of these parameters on the buckling and post-buckling responses of FGM plate.

The effect of material in-homogeneity is examined by varying the power law exponent in Eq. (1) for FGM plate with slenderness ratio equals to 100 and with centrally located circular cutout of size  $d/b = 0.1$ . The corresponding results are presented in Table 3.

As shown in Table 3, the FGM plate depicted greater buckling strength and failure loads in comparison of metal plate. It is to be noted that the volume fractions of both the ceramic and metal depend upon the power law exponent  $n$ . Higher value of  $n$  corresponds to larger proportion of ceramic phase (TiB) that offered higher buckling load and failure strengths in comparison to metal phase.

Effects pertaining to slenderness ratio (i.e.,  $b/h$ ) on buckling, post-buckling and failure response of FGM (for  $n = 1$ ) plate cutout under uni-axial compression are examined and depicted in Table 4. The various values of thickness of FGM plate are considered while keeping the width constant and respective values of buckling, yielding, and failure loads are tabulated. As observed from Table 4, the thickness of FGM plate prominently affected the dimensional values of critical buckling and failure loads. It can also be noticed from Table 4 that except for FGM plate with slenderness ratio equal to 30, wherein the failure occurs before the start of buckling; for all the other values of slenderness ratio, the FGM fails after the occurrence of buckling. It can be established that thin FGM plate is more prone to the buckling failure, whereas the thick FGM plate would be likely to fail in plastic region due to higher value of compressive stresses well before the buckling.

**Table 3** Effect of material gradation profile on non-dimensional buckling, yielding, and failure loads

$n$	Buckling load	Failure load	Yielding load
0	0.96	2.50	2.02
1	1.66	3.68	1.86
2	1.87	4.13	2.13
3	2.00	8.40	2.40
10	2.49	15.20	2.66

**Table 4** Effect of plate thickness on the buckling and failure loads

$b/h$	Buckling load		Failure load	
	dimensional (kN)	Non-dimensional	dimensional (kN)	Non-dimensional
30	22,490	1.61	14,520	1.04
50	4930	1.64	5480	1.82
100	620	1.66	1380	3.68
200	70	1.67	370	7.94
300	20	1.67	160	11.66

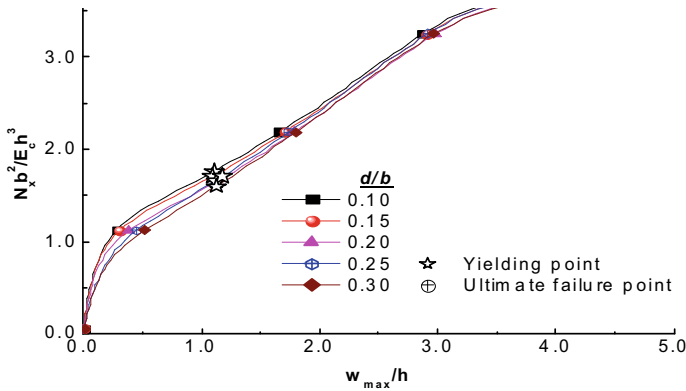


**Fig. 2** Effects of circular cutout size on axial deflection and failure load of FGM plate with circular cutout

Figures 2, 3 depict the effect of cutout size on the nonlinear uni-axial buckling response of FGM plate. It can be observed from the results that the effect of cutout size on buckling and post-buckling loads of FGM plate is insignificant; however, the effect of larger cutout size is to increase the deformation and plastic strain at failure point.

## 7 Conclusion

FEM analysis of FGM plate with cutout is carried out to analyze the elastic–plastic and failure response under in-plane compression. Present model is verified with the available literature, and parametric study is carried out to assess the effect of material and geometrical parameters. Following are the important finding of the present study:



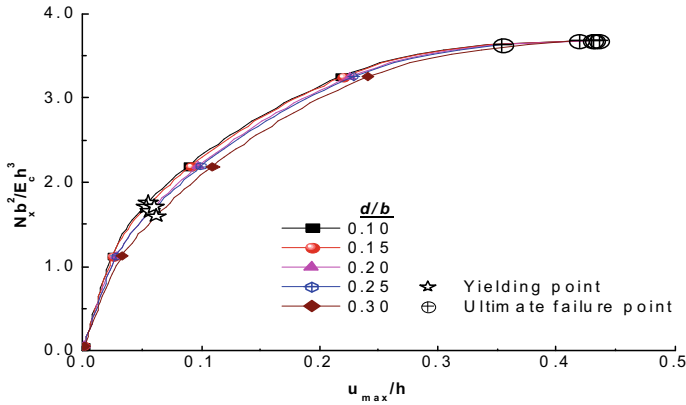


**Fig. 3** Effects of circular cutout size on transverse deflection and failure load of FGM plate with circular cutout

- It is divulged that attributed to its high buckling resistance the FGM plate with higher ceramic proportion possess higher buckling and post-buckling strengths and depicted higher value of transverse deflection corresponding to the failure point.
- It is observed that the presence of large size cutout results in higher value of deflection at the time of failure.

## References

1. Naebe M, Shirvanimoghaddam K (2016) Functionally graded materials: a review of fabrication and properties. *Appl Mater Today* 5:223–245
2. Jha DK, Kant T, Singh RK (2013) A critical review of recent research on functionally graded plates. *Compos Struct* 96:833–849
3. Sharma K, Kumar D (2016) Nonlinear stability and failure analysis of perforated FGM plate. *Indian J Pure Appl Phys* 54(10):665–675
4. Sharma K, Kumar D (2017) Elastoplastic analysis of FGM plate with a central cutout of various shapes under thermomechanical loading. *J Therm Stress*
5. Sharma K, Kumar D (2018) Nonlinear stability analysis of a perforated FGM plate under thermal load. *Mech Adv Mater Struct* 25(2):100–114
6. Xu F, Zhang X, Zhang H (2018) A review on functionally graded structures and materials for energy absorption. *Eng Struct* 171:309–325
7. Markworth AJ, Ramesh KS, Parks WP (1995) Modelling studies applied to functionally graded materials. *J Mater Sci* 30(9):2183–2193
8. Gupta A, Talha M (2015) Recent development in modeling and analysis of functionally graded materials and structures. *Prog Aersp Sci* 79:1–14
9. Sharma and K, Kumar D (2017) Elastoplastic stability and failure analysis of FGM plate with temperature dependent material properties under thermomechanical loading. *Lat Am J Solids Struct*
10. Sharma K, Kumar D (2016) Nonlinear stability and failure analysis of perforated FGM plate. *Indian J Pure Appl Phys* 54(October):665–675

11. Jin ZH, Paulino GH, Dodds RH (2003) Cohesive fracture modeling of elastic-plastic crack growth in functionally graded materials. *Eng Fract Mech* 70(14):1885–1912
12. Shanmugam NE, Thevendran V, Tan YH (1999) Design formula for axially compressed perforated plates. *Thin-Walled Struct* 34:1–20

# Optimization of Heat Transfer Rate, Efficiency and Effectiveness for Thermal Performances of Stepped Rectangular Fin



Shyam Babu, Devendra Kumar Vishwakarma, and Sumit Sharma

**Abstract** In the present experimental assessment, an effort has been made to investigate the effect of fin height, step length ratio and temperature difference on the thermal performance of the single stepped rectangular fin. The optimization of given parameters using Taguchi phenomenon has been done for maximum heat transfer rate, efficiency and effectiveness. Step length ratio was found to be significant parameter. Increased value of step length ratio leads to lower the efficiency of fin and heat transfer.

**Keywords** Stepped rectangular fin · Optimization · Taguchi method · Thermal performance

## 1 Introduction

Heat transfer enhancement can be achieved by various methods. These methods are categorized as active, passive and compound/combined method of heat transfer augmentation [1]. Active methods need external power for enhancing the heat transfer, passive methods use geometrical modifications and combined methods use the combination of more active as well as passive methods [2]. Use of fins is one of the most economical and reliable passive methods of heat transfer enhancement.

Fin is a conductive–convective element used as an extension to the primary surface for the augmentation of heat transfer [3]. Fins found application in various industries such as automobile, refrigeration and air-conditioning, power generation, electrical and electronic devices, heat exchangers [4]. Fins are of various types, namely rectangular fins, parabolic fins, pin fins, radial fins, etc. [5]. Researchers like Hollands and Stedman [6] introduce an alternative design for convectational rectangular fins used

---

S. Babu

Department of Mechanical Engineering, BIET, Jhansi 284001, India

D. K. Vishwakarma

Department of Mechanical Engineering, BITS, Pilani 333031, India

S. Sharma (✉)

Department of Mechanical Engineering, ACEIT, Jaipur 302028, India

in tube and fin absorber plate. The proposed fin reduces the material usage by 20% for a fixed efficiency of 95.65%. It was also reported that if we compensate 0.5% of efficiency, then we can save up to 25% of material. Huang and Shah [7] presented an analysis for calculating rectangular straight fin efficiency under ideal condition of one-dimensional flow, uniform thermal conductivity, uniform thickness, uniform heat transfer coefficient and uniform surrounding temperature and made recommendation for calculating the efficiency of plate type heat exchanger. Adhikari et al. [8] numerically investigated the rectangular fin for optimal heat transfer. The parameters studied for optimization are spacing, height and length of fin. Dynamic  $Q$  algorithm is used to optimization. The results revealed that dynamic  $Q$  algorithm is suited best for the optimization of heat transfer using CFD. Zadhoush et al. [9] presented a combination of analytical and numerical study for optimizing the geometrical arrangement for rectangular fins. Two types of arrangement, namely longitudinal and transverse, are used for the study. The results revealed that an optimum number of fins are six with 34.47 W of heat transfer rate. Aziz [10] performed optimization of stepped rectangular fins having fixed profile area for maximum heat dissipation using Lagrange multiplier. The results obtained from the investigation revealed 9% enhancement in heat transfer rate with 25% less material when compared with straight rectangular fin. Baskaya et al. [11] numerically investigated the free convection for fin spacing, height, length and temperature difference between fin and ambient atmosphere and reported that heat transfer rate depends on all the above parameters and hence considering all parameters together present better optimal solution. Cuce and Cuce [12] investigated the stepped rectangular fins for heat transfer and reported enhancement in heat transfer and increase in efficiency when compared with conventional fin. Dwivedi and Das [13] experimentally investigated the impact of fin height ( $L$ ); fin spacing ( $S$ ) and Rayleigh number ( $Ra$ ) on the convective heat transfer of triangular fins attached to the rectangular plate. Taguchi method is used to optimize the design parameters for maximum heat transfer. It was revealed that Taguchi method is best suited for optimization of design parameter, and the results obtained using Taguchi method are in good agreement with experimental results. Kim and Moon [14] numerically investigated the circular stepped fins for heat transfer augmentation. Kriging metamodeling techniques have been utilized for the optimization of fins parameters. The result shows good agreement between data obtained using Kriging modelling when analysed using RANS analysis. It was found that the thermal performance of stepped circular fin is significantly high when related to straight fins performance.

After thoroughly reviewing the literature, it is found that lot of research work has been available on optimization of stepped rectangular fins for various parameters affecting thermal performance, but no research work is reported on optimizing the input parameters. Hence, the objective of this work to optimize the input variables for thermal performance using the Taguchi method.

## 2 Experimentation

The schematic diagram of experimental set-up used for the test runs is shown in Fig. 1. Test section is made up of wooden box of dimension 30 cm × 30 cm × 8 cm filled with cement, and hollow square cavity of dimension 100 mm × 100 mm × 20 mm is created in the centre in which nichrome heating element is fitted. Nine single-stepped rectangular fins made up of Al 1100 are used for the investigation. These fins are of different combination of total fin height, step length ratio having same fin volume of  $1.5 \times 10^{-5} \text{ m}^3$ . All three fins are made of Al 1100 plate of width 100 mm. Base plate dimensions of cooling fin pattern are same in all pattern (i.e. 100 mm × 100 mm). Dimensions of all nine fins are given in Table 1. The parameters

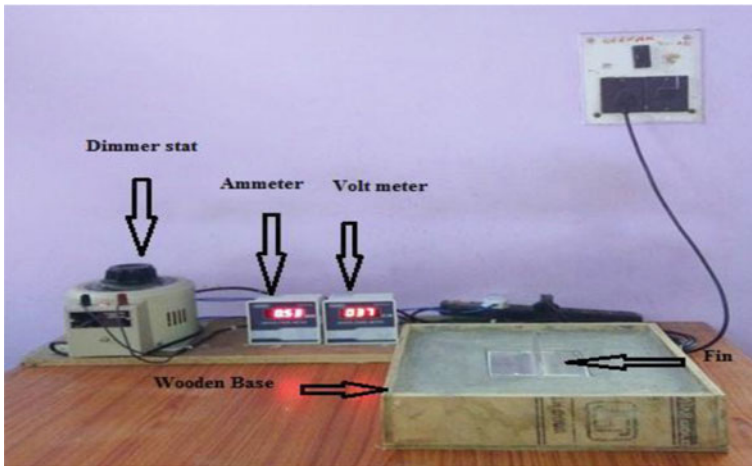


Fig. 1 Pictographic view of experimental set-up

Table 1 Dimensions of rectangular stepped fins

Fin	$L$ (mm)	$L_1$ (mm)	$L_2$ (mm)	$t_1$ (mm)	$t_2$ (mm)	$t_1/t_2$
1	40	16	24	5.35	2.67	2
2	40	20	20	5.00	2.50	2
3	40	24	16	4.68	2.34	2
4	50	20	30	4.28	2.14	2
5	50	25	25	4.00	2.00	2
6	50	30	20	3.75	1.87	2
7	60	24	36	3.57	1.87	2
8	60	30	30	3.33	1.66	2
9	60	36	24	3.12	1.56	2

**Table 2** Control parameters and their level

Parameters	Symbol	Units	Levels		
			1	2	3
Fin height	$L$	mm	40	50	60
Step length ratio	$\lambda$	–	0.4	0.5	0.6
Temperature difference	$\Delta T = (T_b - T_\infty)$	°C	10	20	30

chosen to study are fin height ( $L$ ), step length ratio ( $\lambda$ ) and temperature difference ( $T_b - T_\infty$ ). The control parameters and their level are shown in Table 2.

### 3 Taguchi Method

Taguchi method is a Design of Experiments (DOE) developed by Genichi Taguchi used to find the minimum number of experimental runs required to predict the results within permissible limit. Technique is used for the optimization. The method found application in both static and dynamic problems, and the results obtained using it are in good agreement with experiments. Taguchi revealed eight steps in order to optimize any process. They are as follows—

1. Identification of quality characteristics.
2. Identification of control factors.
3. Designing of orthogonal array.
4. Define data analysis.
5. Conduct the matrix experiments.
6. Analyse the data obtained from matrix experiments.
7. Determine optimum levels of control factors.
8. Perform verification experiments and plan the actions accordingly.

### 4 Design of Experiments

In order to evaluate the effects of input parameter for heat transfer process from fin in terms of thermal performance such as temperature distribution, heat transfer rate, efficiency and effectiveness, a Taguchi method with  $L_9$  orthogonal array was used. In Taguchi method, the array chosen is  $L_9$ , which have 9 rows corresponding to the number of experiments with 3 columns at the three levels as shown in Table 3.

**Table 3** *L9* orthogonal array of experimentation

Experiment No.	<i>L</i>		$\lambda$		$\Delta T$	
	Level	Value	Level	Value	Level	Value
1	1	40	1	0.4	1	10
2	1	40	2	0.5	2	20
3	1	40	3	0.6	3	30
4	2	50	1	0.4	2	20
5	2	50	2	0.5	3	30
6	2	50	3	0.6	1	10
7	3	60	1	0.4	3	30
8	3	60	2	0.5	1	10
9	3	60	3	0.6	2	20

## 5 Result and Discussion

After successfully performing all the tests, decision must be made concerning with parameters that affect the performance of the stepped rectangular fins such as heat transfer rate, efficiency, effectiveness and temperature distribution in natural convection heat transfer. The decisions are made on the basis ANOVA. Table 4 shows the values of various parameters obtained after successful completion of tests.

The effect of fin parameters, viz. fin length, step length ratio, base to ambient temperature difference on response characteristics, viz. heat transfer rate, efficiency and effectiveness, were studied.

**Table 4** Experimental design using *L9* orthogonal array and observed value

S. No.	Factor assignment			<i>Q</i> (W)	$\eta$	$\epsilon_{fin}$
	<i>L</i>	$\lambda$	$\Delta T$			
1.	1	1	1	3.80	0.869	15.99
2.	1	2	2	7.50	0.866	17.1
3.	1	3	3	11.20	0.857	18.2
4.	2	1	2	8.40	0.845	24.56
5.	2	2	3	12.10	0.840	26.25
6.	2	3	1	4.00	0.835	27.96
7.	3	1	3	12.60	0.831	34.97
8.	3	2	1	4.20	0.829	37.43
9.	3	3	2	8.15	0.818	39.86

**Table 5** Analysis of variance for heat transfer rate

Parameters	DOF	Sum of square	Mean square	<i>F</i> -ratio	Percentage (%)
<i>L</i>	2	1.134	0.567	65.84	1.172
$\lambda$	2	0.367	0.184	21.32	0.37
$\Delta T$	2	95.204	47.602	5527.97	98.43
Error	2	0.017	0.009		0.768
Total	8	96.722			100

**Table 6** Analysis of variance for efficiency

Parameters	DOF	Sum of square	Mean square	<i>F</i> -ratio	Percentage (%)
<i>L</i>	2	0.0022160	0.0011080	474.86	90.74
$\Lambda$	2	0.0002167	0.0001083	46.43	8.870
$\Delta T$	2	0.0000047	0.0000023	1.0	0.192
Error	2	0.0000047	0.0000023		0.1975
Total	8	0.0024420			100

### 5.1 Heat Transfer Rate

Table 5 shows the ANOVA and *F*-test for heat transfer rate. It is believed that if *F*-ratio is larger than the given criterion, then it is influencing the population and if this value is less than the given criterion, it has no influence. For the case of heat transfer rate, the *F*-ratios from the computed value are shown in Table 5. It is clear from the values that  $\Delta T$  is the most influencing factor with percentage contribution of more than 98% while other two factors show no significant effect.

### 5.2 Efficiency

Table 6 shows the ANOVA and *F*-test for efficiency. It is clear from the values obtained from *F*-ratio and percentage contribution that most influencing parameter for efficiency is *L*, i.e. Height of fin. It shows that *L* contributes 90% in influencing the efficiency followed by  $\lambda$  while  $\Delta T$  is negligible.

### 5.3 Effectiveness

Table 7 shows analysis of variance for effectiveness. The data obtained from the analysis revealed that fin height is most influencing factor which contributes 96% in



**Table 7** Analysis of variance for effectiveness

Parameters	DOF	Sum of square	Mean square	F-ratio	Percentage (%)
<i>L</i>	2	621.56	310.78	702.90	96.85
$\lambda$	2	18.38	9.19	20.78	2.86
$\Delta T$	2	0.92	0.46	1.04	0.143
Error	2	0.88	0.44		0.1466
Total	8	641.74			100

changing the effectiveness performance of the fin, while other two parameters show no significant contribution.

## 6 Confirmation Tests

A confirmation experiment is performed by conducting a test using a specific combination of the factors and levels as above evaluated. The purpose of the confirmation test is to be validating the conclusions drawn during the analysis phase. The results obtained from the confirmation test for heat transfer rate, efficiency and effectiveness are summarized in Table 9. The optimal setting levels for all the parameters are shown in Table 8.

**Table 8** Optimum setting levels

Parameter	Heat transfer rate and level	Efficiency and level	Effectiveness and level
<i>L</i> : Length of fin (mm)	3	1	3
$\lambda$ : Step length ratio	1	1	3
$\Delta T$ : Temp. difference (°C)	3	1	1

**Table 9** Confirmation experiment results

	Heat transfer rate		Efficiency		Effectiveness	
	Prediction	Experiment	Prediction	Experiment	Prediction	Experiment
Level	<i>L</i> 3, $\lambda$ 1, and $\Delta T$ 3	<i>L</i> 3, $\lambda$ 1, and $\Delta T$ 3	<i>L</i> 1, $\lambda$ 1, and $\Delta T$ 1	<i>L</i> 1, $\lambda$ 1, and $\Delta T$ 1	<i>L</i> 3, $\lambda$ 3, and $\Delta T$ 1	<i>L</i> 3, $\lambda$ 3, and $\Delta T$ 1
Mean value	12.5611	12.100	0.87	0.8457	39.3711	37.60

## 7 Conclusion

In this study, natural convection heat transfer from stepped rectangular fin on a horizontal base has been investigated experimentally and a detailed methodology of the Taguchi optimization design method has been discussed and applied to evaluate optimum design parameter combinations yielding maximum heat transfer, efficiency and effectiveness separately. Following conclusions have been made from the obtained results and analysis—

1.  $L$ ,  $\lambda$  and  $\Delta T$  are the significant parameter for heat transfer, as the value of  $L$  and  $\Delta T$  are increasing, heat transfer rate also increases while decreases with increasing  $\lambda$ .
2. Step length ratio was found to be significant parameter. Increased value of step length ratio leads to lower the efficiency of fin and heat transfer. For these experiments, its optimum value is found to be 0.4.
3. Heat transfer can be increased up to 10.50%, 12.00% and 12.50% if the efficiency is allowed to drop by 4.60%, 2.42% and 3.03% for their respective levels of temperature differences.
4. The optimal sets of process parameter were obtained for various performance characteristics using Taguchi experimental technique are  $L3$ ,  $\lambda1$  and  $\Delta T3$  for maximum heat transfer rate,  $L1$ ,  $\lambda1$  and  $\Delta T1$  for maximum efficiency and  $L3$ ,  $\lambda3$  and  $\Delta T1$  for maximum effectiveness.

## References

1. Rashidi S, Eskandarian M, Mahian O (2019) Combination of nanofluid and inserts for heat transfer enhancement. *J Therm Anal Calorim* 135:437–460
2. Sidik NAC, Muhamad MNAW, Japar WMAA, Rasid ZA (2019) An overview of passive techniques for heat transfer augmentation in microchannel heat sink. *Int Commun Heat Mass* 88:74–83
3. AlEssa AH, Maqableh AM, Ammourah S (2019) Enhancement of natural convection heat transfer from a fin by rectangular perforations with aspect ratio of two. *Int J Phys Sci* 4(10):540–547
4. Yu LT, Chen CK (1999) Optimization of circular fins with variable thermal parameters. *J Franklin I* 336(1):77–95
5. Cengel Y, Ghajar A (2015) *Heat and mass transfer: fundamentals and applications*, 5th edn. McGrawHill
6. Hollands KGT, Stedman BA (1992) Optimization of an absorber plate fin having a step-change in local thickness. *Sol Energy* 49(6):493–495
7. Huang LJ, Shah RK (1992) Assessment of calculating methods for efficiency of straight fins or rectangular profile. *Int J Heat Fluid Fl* 13(3)
8. Adhikari RC, Wood DH, Pahlevani M (2020) Optimizing rectangular fins for natural convection cooling using CFD. *Therm Sci Eng Prog* 17:100484
9. Zadhoush M, Nadooshan AA, Afrand M, Ghafari H (2017) Constructal optimization of longitudinal and latitudinal rectangular fins used for cooling a plate under free convection by the intersection of asymptotes method. *Int J Heat Mass Tran* 112:441–453

10. Aziz A (1994) Optimum design of a rectangular fin with a step change in cross-sectional area. *Int Commun Heat Mass* 21(3):389–401
11. Baskaya S, Sivrioglu M, Ozek M (2000) Parametric study of natural convection heat transfer from horizontal rectangular fin arrays. *Int J Therm Sci* 39:797–805
12. Cuce PM, Cuce E (2014) Optimization of configurations to enhance heat transfer from a longitudinal fin exposed to natural convection and radiation. *Int J Low Carbon Tec* 9:305–310
13. Dwivedi A, Das D (2015) Application of Taguchi philosophy for optimization of design parameters in a rectangular enclosure with triangular fin array. *J Inst Eng India Ser C*. <https://doi.org/10.1007/s40032-015-0186-9>
14. Kim K, Moon M (2009) Optimization of a stepped circular pin-fin array to enhance heat transfer performance. *Heat Mass Transf* 46:63–74

# Heat Transfer Enhancement of Parallel and Counter Flow Heat Exchangers with Varying Size and Fins Number



Sumit Sharma, Manish Dadheech, Devendra Vishwakarma,  
Kamal Kishore Khatri, Marek Jaszczur, and Deepak Sharma

**Abstract** Parallel as well as counter flow heat exchanger plays essential role in industry and become one of the most significant parts of the major industrialized processes involving heat transfer. Heat exchanger is also very important in waste heat recovery process, which is considered as one of the major energy intensive areas, where its role is noteworthy. In the present study, parallel flow heat exchanger (PFHE) and counter flow heat exchanger (CFHE) were numerically analysed and its results were validated experimentally. The number of fins and stature of fins on thermal performance of PFHE were investigated using computational fluid dynamics. It was seen from the results that increasing the height and fins number enhances the heat transfer rate of CFHE. The best results were evaluated for five fins with 12 mm height. It was inferred from the results that fins additions in CFHE can improve the effectiveness of the heat exchangers. By using CFD analysis, heat exchangers can be fully optimized in order to obtain high performance and the heat exchanger sizing can be accurately and efficiently précised using this numerical tool.

**Keywords** Heat exchanger · Counter flow heat exchanger · Parallel flow heat exchanger · Fin height · Heat transfer analysis · CFD

---

S. Sharma (✉) · M. Dadheech

Department of Mechanical Engineering, Arya College of Engineering & IT, Jaipur, Rajasthan 302028, India

D. Sharma

Department of Mechanical Engineering, SKIT, Jaipur, Rajasthan, India

D. Vishwakarma

BITS, Pilani, Rajasthan, India

K. K. Khatri

Department of Mechanical-Mechatronics Engineering, LNMIIT, Jaipur, Rajasthan, India

M. Jaszczur

Faculty of Energy and Fuels, AGH University of Science and Technology, Kraków, Poland

## 1 Introduction

The parallel flow heat exchanger (PFHE) and counter flow heat exchangers (CFHE) are one of the most significant parts of the major industrialized processes involving heat transfer. They have applications in different areas such as power plant, refrigeration and air-conditioning, internal combustion, gas extraction industry and chemical processing industries. However, due to fast growth in digitalization and compact design of devices, the heat generated per unit volume has increased significantly. Subsequently, the expectations are increasing day by day to dissipate significant amount of heat from a confined space in order to surge the safety and increase lifetime of the device. The heat exchangers are classified on the basis of flow arrangements, fins shaping and placing, contact and type of the flow. In recent years, tremendous works have been done with the objective to enhance the rate of heat transfer and the thermal characteristic of heat exchangers through various techniques such as geometrical changes, cooling fluid types and flow behaviours, i.e. single or multiphase flow, and surface morphology of the heat exchangers [8, 16, 18]. Many researches have been carried out to study the performance of fin heat exchangers under diverse conformations. In [1], the authors investigated the performance of tube heat exchanger with fins by using three-dimensionally laminar and turbulent numerical analysis. It was observed that longitudinal and crosswise pitches improved thermal performance of the heat exchanger. In another research study, thermal performance of heat exchanger was experimentally investigated by using different geometrical configuration by Wang et al. [21], and Ereke et al. [5] conducted the numerical investigation of fin heat exchanger comprising elliptical tubes of changing eccentricity to consider the influence of designing factor like the fin height and tubes thickness on heat exchanger performance.

The literatures review carried out by Sinha [19], Lotfi et al. [10] and Dong et al. [3] has shown that performance of fin tube heat exchangers was significantly amplified by using the wavy fins in the place of plate fins heat exchangers. In [11], authors experimentally studied the effect of pricked fins on a performance enhancement of fin tube heat exchanger. The evaluated results revealed that on increasing Reynolds number from 750 to 2300, j-factor significantly increased. Wang et al. [22] concluded from their investigation that internal helical fin tube heat exchanger enhances the thermal performance associated to the plate fins. Hatami et al. [6] explained the optimization of finned tube heat exchangers for diesel engine. They used the response surface methodology RSM optimization technique to optimize the design of heat exchanger for OM314 diesel engine in order to recover waste heat. In this experimental analysis, authors varied fin thickness, length and number of fins. Finally, a construction was optimized for the highest heat transfer rate and the lowest pressure drops. In [9], author investigated the performance of helical baffles heat exchangers and also identified a best helix angle at which energy transfer is maximized. Master et al. [12] conducted studies on the industrial application of a heat exchanger (helically baffled) with 13 integral low finned tubes. Authors concluded that the pressure drops on both the corresponding bare tube surface and shell side is one-half of that baffled bare

tube. Eiamsaard and Promvong [4] experimentally explored the effect of addition of a helical screw-tape through or without core-rod in a double-tube heat exchanger (concentric) on flow characteristics and heat transfer. They stated a surge in normal Nusselt number of the loose-fit, helical tape through and without core-rod.

[17] analysed bared tube and finned tube type heat exchanger and observed that the finned tube heat exchanger obtained higher efficiency than bare tube heat exchanger. Authors observed that fluid velocity and pressure drop at tube side are slightly greater than the conservative tube exchanger, which reduces fouling inside the tubes, whereas lower shell side pressure drop with higher fluid velocity were observed in bare tube exchanger. Zhang et al. [23] performed the CFD simulation of shell-and-tube heat exchangers with continuous baffles and middle-overlapped helical baffles with three helix angles of baffles 30°, 40° and 50°. In study, fluent solver was used for simulation purpose. It was observed that 40° helix angle of baffle gives high heat transfer rate but also high pressure drop. Ozden and Tari [15] investigated numerically the shell and tube heat exchanger. Authors reported an increment in baffle cut value by varying the baffle cut values enhanced by of 36% and 25% for 0.5 and 2 kg/s flow rate, respectively, and baffle spacing between six and twelve. Vats et al. [20] performed the theoretical thermal analysis by analysing temperature distribution and heat dissipation that transferred through the surfaces of an object. Bhutta et al. [2] investigated various turbulence models coupled with SIMPLER, SIMPLE, PISO, SIMPLEC scheme. The simulations result varied in the range from 2 to 10%, depending on scheme. Authors also perform a CFD analysis of finned tube heat exchanger using FLUENT after modelling the heat exchanger and using waste gas by the bus as heat transfer fluid (HTF). Mishra and Paramanik [13] performed numerical and experimental computations to extend the velocity at the mixing pipe and to assess the quantity of air entrained as a function of pipe geometry using Ansys Fluent. Results show that the maximum air entrainment to be at 0.6 m length of the pipe and outside this dimension, the entrainment drops significantly. Mohapatra and Mishra [14] performed investigation of flow characteristics of a tube which is ribbed inside, based on k- $\epsilon$  model. It has been found that the pressure drop and heat transfer are improved by increasing the rib number and rib height, and an optimum angle of rib inclination 45° has minimum pressure drop and maximum heat transfer in triangular-shaped rib. Jalaluddin et al. [7] presented the comparative study between the conventional U-tube and spiral-tube GHEs and also investigates the thermal performance by numerical method using CFD. Results show the reduction in borehole about a half when using spiral-tube GHE in parallel and series configurations and are 64.6 W and 46.9 W per metre borehole depth in turbulent and laminar flows, respectively.

It has been inferred from the literature reviews that various investigations have been carried out in order to enhance the performance of heat exchangers with fins. However, as to the authors' knowledge, there is no detailed research study which considered the impact of fins numbers and fins size on heat exchangers performance, i.e. heat transfer to pressure drop. Hence, the present research work aims to investigate the effect of number of fins and stature of fins on performance of parallel and counter flow heat exchangers. Subsequently, the impact of cumulative mass flow rate on performance of heat exchanger and the Reynolds number has been investigated and

reported. Contours illustrating the change in nature of temperature by varying nature of flow, i.e. flow field and thermal field, parallel and counter flow, number of fins and height of the fins have also been reported in order to clearly and easily understand the physics phenomenon inside of a three-dimensional fin heat exchanger.

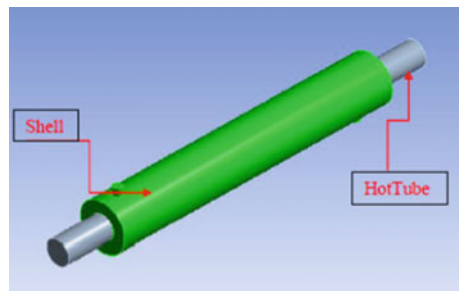
## 2 Experimental Setup

The experimentally analysed heat exchanger is designed to use the waste heat from the diesel engine. The thermal performance of heat exchanger has been evaluated under different mass flow rate, number of fins and fins heights. The experimental setup is shown in Fig. 1. The setup consists of two pipes of different diameters. The inner pipe has diameter 76.2 mm and its length is 1200 mm. The outer pipe has diameter 152.4 mm and its length is 900 mm. As presented in Fig. 2, inner pipe is installed inside the outer pipe, and there are four valves to connect water inlet and outlet to provide parallel or counter flows. On each valves, calibrated ( $\pm 0.5^\circ\text{C}$ ) K-type (chromel–alumel) thermocouple is mounted to show the temperature of water at the inlet and outlet. A heat exchanger flange is connected at one side of the small diameter pipe to the engine exhaust, and the other side is open to atmospheric pressure. For parallel flow configuration, water and exhaust gases from the engine

**Fig. 1** Experimental setup



**Fig. 2** Computational domain of the heat exchange



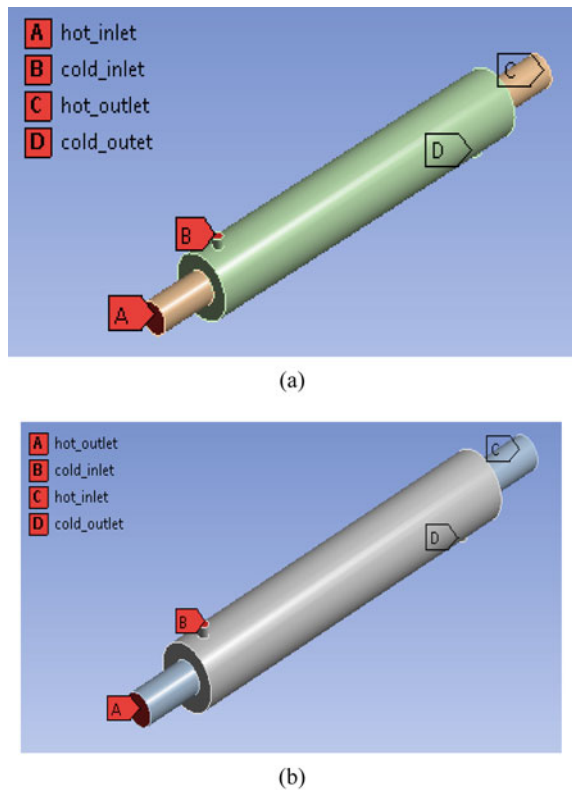
are flowing in the same direction, whereas in counter flow configuration, water and exhaust gases are flowing in the opposite direction. For insulation of heat exchanger, glen dory and plaster of Paris are used.

### 3 Numerical Methodology

The three-dimensional fin tube heat exchanger (parallel and counter flow) has been generated and numerically investigated in this current study. Initially, the PFHE and CFHE with different number of fins have been modelled in the SOLIDWORKS 9.0. Figure 2 shows the domain of the heat exchanger.

The 3-D geometry of heat exchangers were imported to the ANSYS Meshing in order to discretize the domain of heat exchangers. The meshed 3-D heat exchangers model for PFHE and CFHE configuration is used in Fluent solver to solve the governing equations, i.e. turbulence, mass, momentum and energy and to analyse the flow performance and rate of heat transfer. Figure 3a displays the temperature points

**Fig. 3** Temperature junctions of **a** PFHE, **b** CFHE





in parallel flow heat exchanger while the counter flow heat exchangers temperature points are illustrated in Fig. 3b.

CFHEs with different fins numbers such as 2, 3, 4 and 5 are depicted in Fig. 4.

After creating the geometry of the domain is meshed as shown in Fig. 5. Flow domain is divided into computational cells. While performing the meshing, it should

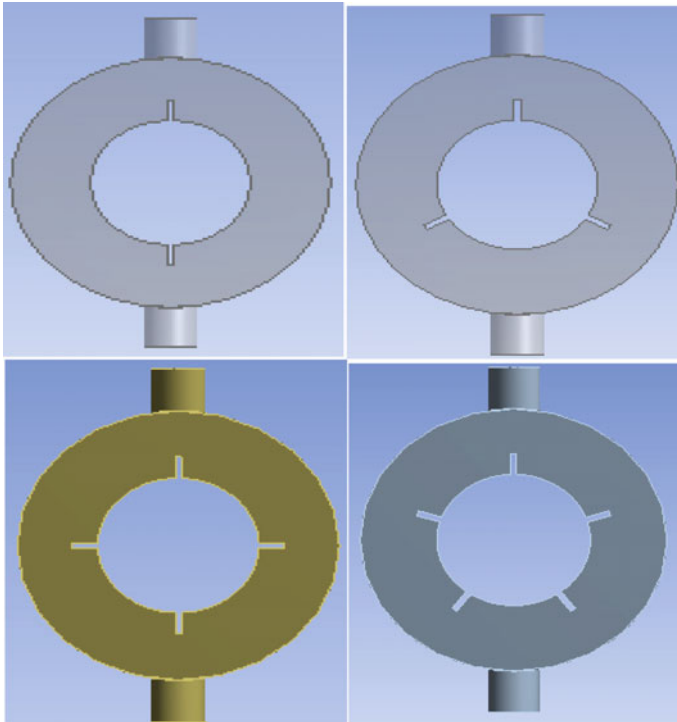
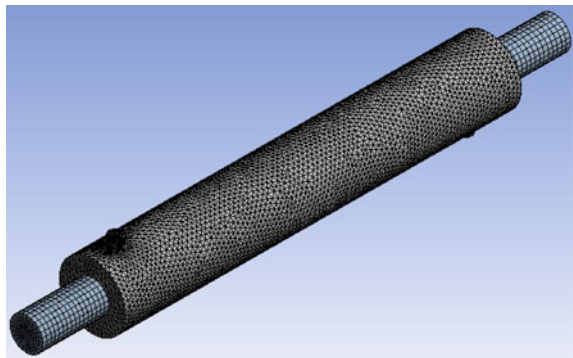


Fig. 4 CFHEs with fins

Fig. 5 Discretize domain



**Table 1** The boundary conditions applied for the model are summarized

Inlet	Mass flow proportion	Temperature
Cold inlet	0.055 kg/s	300 K
Hot fluid	0.04–0.17 kg/s	423 K

**Table 2** Residuals values for convergence

Residuals	Convergence measures
Continuity	1e-05
x-velocity	1e-05
y-velocity	1e-05
z-velocity	1e-05
Energy	1e-06
K	1e-05
Omega	1e-05

be taken care that mesh resolution is adequately large to resolve all flow features. In the present simulation, transient calculation was performed with the pressure-based solver and SST  $k-\omega$  turbulent model. The boundary conditions applied for the model are summarized in Table 1.

The following assumption has been made to perform the numerical simulation of heat exchangers. (i) Air velocity at shell and tubes inlet are assumed constant and has only 'Y and X' direction. Also, the temperature of air at shell and tubes inlet is constant. (ii) The outer surfaces of the shell are assumed to be adiabatic insulated. The shell walls have coupled boundary conditions.

Convergence is a key topic with the usage of CFD software and often measured by the level of residuals, the extent by which neither discretize equations nor error in the solution are not satisfied. Table 2 and Fig. 6 show the convergence criteria of the present work.

## 4 Thermal Performance Analysis of Heat Exchanger

The equations used in present study for the calculation of heat supplied, heat transfer coefficient, Nusselt number, Reynolds number are as follows:

### Heat supplied to circular pipe

$$Q = V * I \quad (1)$$

where  $I$  is current, and  $V$  is voltage given to be the heating coil.

### Energy absorbed by circular pipe

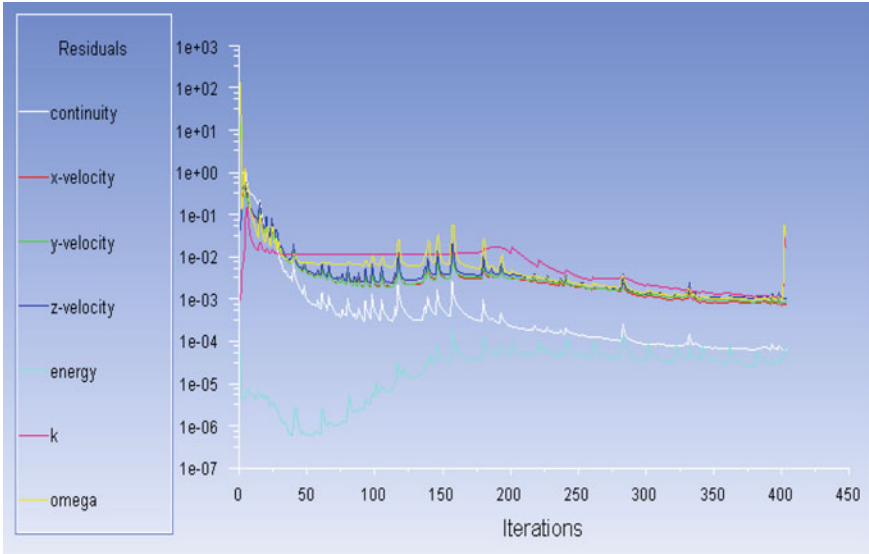


**Fig. 6** Convergence criteria

$$Q = m * C * (T_o - T_i) \quad (2)$$

### Heat transfer coefficient

$$h_{\text{exp}} = \frac{Q}{A_s (T_{\text{plate}} - T_{\text{avg}})} \quad (3)$$

where  $T_{\text{plate}}$  is the average temperature of heater plate wall,  $T_{\text{avg}}$  is the average temperature at an outer part of the pipe.

### Reynolds number

$$\text{Re} = \frac{4\dot{m}}{\pi D \mu} \quad (4)$$

And

$$\text{Re} = \frac{\rho v D}{\mu} \quad (5)$$

### Nusselt number

$$\text{Nu} = \frac{hD}{K} \quad (6)$$

## 5 Results and Discussions

The performance of PFHE and CFHE has been investigated using simulation with different number of fins and varying thickness, so as to optimize and achieved the best design of heat exchanger. In the present study, heat transfer level, Nusselt number and Reynolds number for all designs using varying mass flow rate from 0.04 to 0.17 kg/sec have been investigated. It was observed that use of fins in heat exchangers augmented the rate of heat transfer. Also, this increased the Nusselt number. This was mainly due to the turbulence developed within the domain, and it forced fluid particle to collides by each other and thus, it takes more time to escape from the pipe and finally, maximum heat absorbed. Table 3 shows the various temperatures inside the concentric tube heat exchanger, when parallel flow is passed through it.

It is seen from table that mass flow level has significant effect in augmented temperature at various positions.

Figure 7 shows the heat transfer rate and convective heat transfer rate experimental and numerical values. It was observed from the Figure that as the mass flow rate increased from 0.04 to 0.17 kg/s, both the parameters improved significantly. It is well known that higher mass flow rate allows higher turbulence, which in turn improved the heat transfer rate. It was also observed that the investigational calculated values well matched with the numerical simulation results and it shows that all the boundary parameters and heat transfer analysis done in the numerical simulation are well justified.

The temperature contours of PFHE, where five diverse mass flow rates were used to analyse the temperature distributions inside the heat exchanger is presented in Fig. 8a–e. It obviously seen from the contours that with increased flow rate, temperature augmented significantly. Temperature varies from 302 to 423 K.

Figure 9 shows the experimental value and numerical value of the Reynolds and Nusselt number. Inclusion of fins in heat exchanger enhances the heat transfer rate, and the major objective of the investigation is to observe and quantify the heat transfer rate. Table 4 shows the temperature due to variation in mass flow rate. It was observed that higher temperature gradient occurs in case of CFHE, due to higher heat transfer

**Table 3** Influence of mass flow rate on temperature at various locations of the PFHE

Mass flow rate of hot Fluid (kg/s)	Cold Junction		Hot Junction		$T_{wall}$ (°C)
	$T_{in}$ (°C)	$T_{out}$ (°C)	$T_{in}$ (°C)	$T_{out}$ (°C)	
0.04	27	33.55	150	137.65	137.54
0.07	27	35.2	150	141.94	139.99
0.1	27	35.73	150	143.99	141.45
0.13	27	36.87	150	145.14	142.37
0.17	27	37.66	150	146.05	143.24

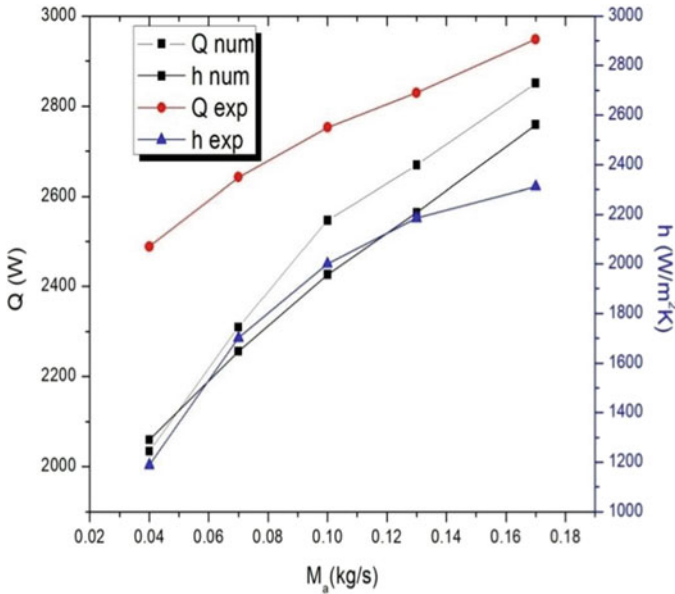


Fig. 7 Influence of mass flow rate on heat transfer performance of PFHE

rate and the obtained results is also in the same order. Figure 10 shows the influence of mass flow rate on heat transfer rate and convective heat transfer in the case of CFHE with different mass flow rate. It was observed from the results that increasing mass flow rate, the performance of heat exchangers also increases. CFHE has given improved results as compared to the PFHE. It was also seen that numerical simulation results are close to the experimental results, and it shows that all the coupling and heat transfer assumptions made during the studies are very accurate.

Figure 11 shows the comparisons between PFHE and CFHE on the basis of dimensionless number. It was seen from the results that CFHE showed higher values of Nu number, due to heat transfer enhancement compared to the PFHE. Figure 12a–e shows the temperature contour of the CFHE with varied mass flow rates. It is clear from the Figure that as compared to PFHE, there was a significant rise in the temperature across various junctions in the heat exchanger due to the actual thermal behaviour and high heat transfer in the CFHE.

The key purpose of this experiment is to relate the enactment of heat exchanger under different number of fins with varying height. The effect of number of fins and height of fins on thermal performance of CFHE is studied using CFD analysis. Table 5 showed the effect of number of fins and height of fins on the outlet temperature for CFHE.

Table 5 contains the data of outlet temperature with a varying number of fins and height of fins. Total four heights were taken in present study from 6.0 to 12.0 mm and numbers of fins were varying from 2 to 5. It is found that the maximum outlet temperature observed for five fins with fin height 12 mm and minimum for two fins

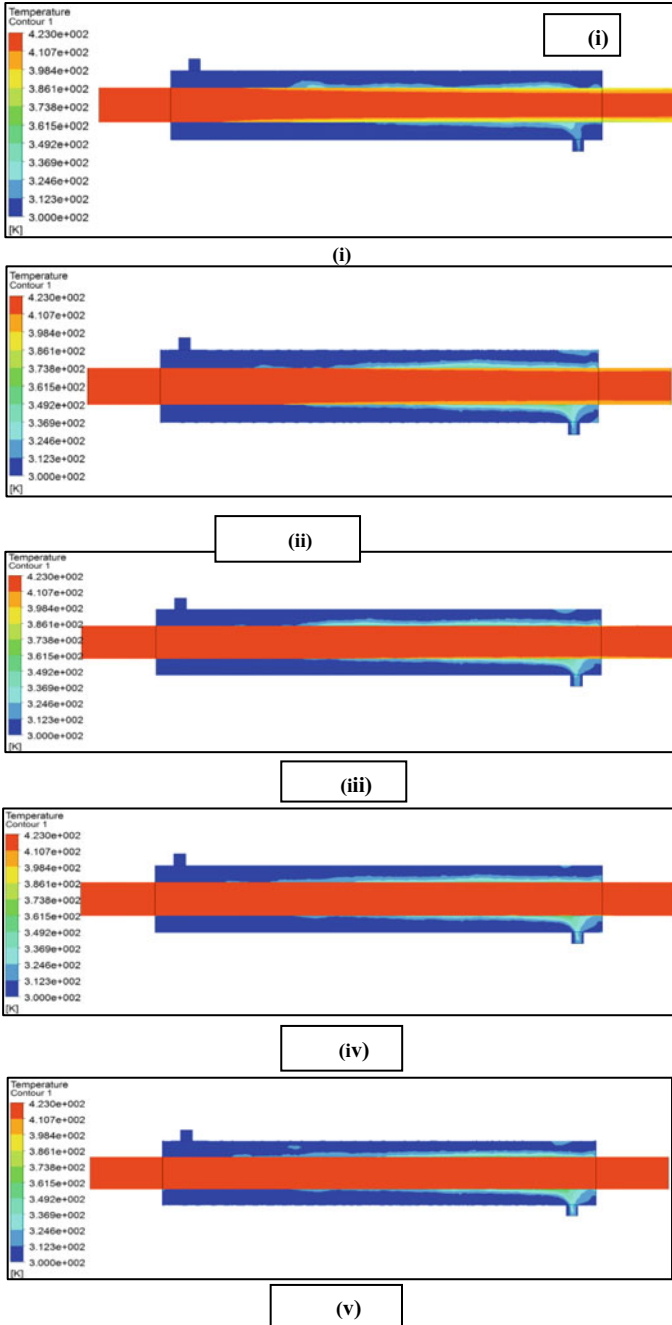
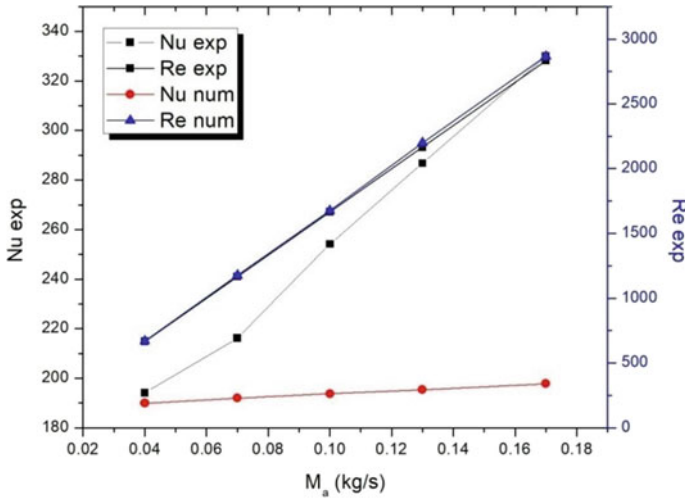


Fig. 8 PFHE, a 0.04 kg/s, b 0.07 kg/s, c 0.10 kg/s, d 0.14 kg/s, e 0.17 kg/s



**Fig. 9** Influence of mass flow rate on Nu, Re in PFHE

**Table 4** Influence of mass flow rate on temperature at various locations of the CFHE

Mass flow rate of hot fluid (Kg/sec)	Cold junction		Hot junction		T <sub>wall</sub> (°C)
	T <sub>in</sub> (°C)	T <sub>out</sub> (°C)	T <sub>in</sub> (°C)	T <sub>out</sub> (°C)	
0.04	27	35.53	150	138.32	138.34
0.07	27	37.12	150	142.53	140.23
0.1	27	35.24	150	144.67	142.89
0.13	27	37.43	150	146.49	143.36
0.17	27	38.41	150	147.44	144.27

with fin height 6 mm as revealed in Fig. 13. Fins are varying from two to five. The high heat transfer rate is obtained in fins inserts as related to the simple heat exchanger. The outlet temperatures for two, three, four and five fins are approximately 47–48 °C, 47–49 °C, 48–51°C and 48–53 °C, respectively. It has been noticed that the heat exchanger using five fins has the maximum value of outlet temperature, and the heat exchanger with one fin has the least value of outlet temperature. Figure 14 showed the temperature contours of five fins based CFHE with varying heights of the fins.

It was observed from the results that with increase in number of fins, the heat transfer rate improved, and it augmented the outlet temperature of the heat exchanger. Fins provide extra extended surface area during the heat flow and hence, the rate of heat transfer improved. It was also noticed that increased height of fin also supports higher heat transfer rate.

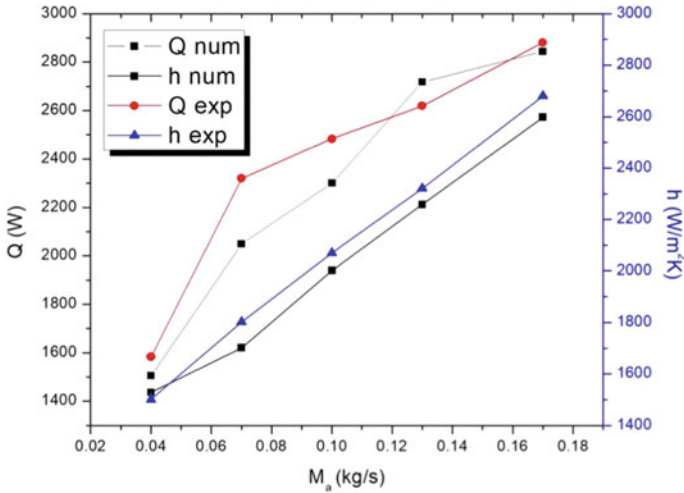
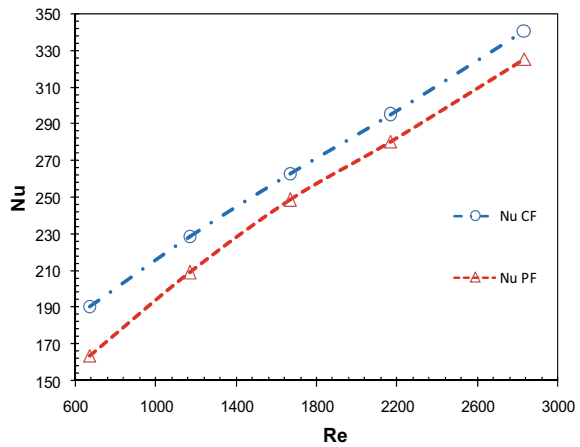


**Fig. 10** Influence of mass flow rate on heat transfer performance of CFHE

**Fig. 11** Comparison of PFHE and CFHE



## 6 Conclusions

The heat transfer behaviour of parallel and counter flow heat exchanger has been experimentally and numerically investigated for possible application in waste heat recovery system. The effect of fins' number and fins' height on heat transfer characteristics of counter flow heat exchangers has been studied. Based on the comparative study of the results, subsequent important outcomes have been described.

- Increased mass flow rate, improved the heat transfer, which in turn give higher output temperature in both the cases of heat exchangers.



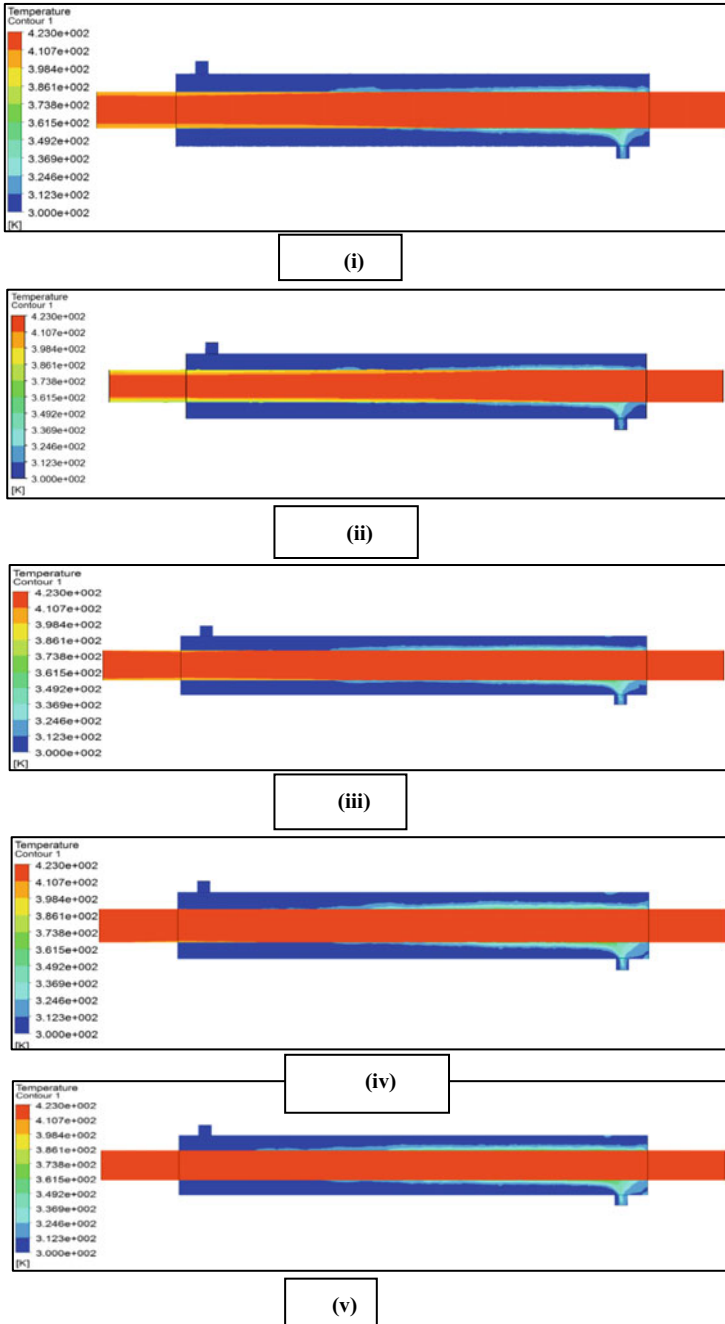
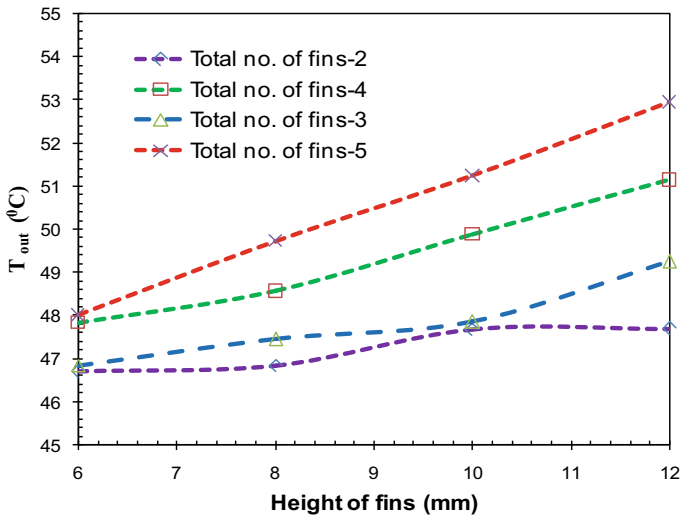


Fig. 12 CFHE, a 0.04 kg/s, b 0.07 kg/s, c 0.10 kg/s, d 0.14 kg/s, e 0.17 kg/s

**Table 5** Influence of number of fins and height of fins on outlet temperature of CFHE

Number of fins	Height of fin (mm)	T <sub>out</sub> (°C)
2	6	47
2	8	47
2	10	48
2	12	48
3	6	47
3	8	47
3	10	48
3	12	49
4	6	48
4	8	49
4	10	50
4	12	51
5	6	48
5	8	50
5	10	51
5	12	53



**Fig. 13** Effect of fins on outlet temperature of CFHE

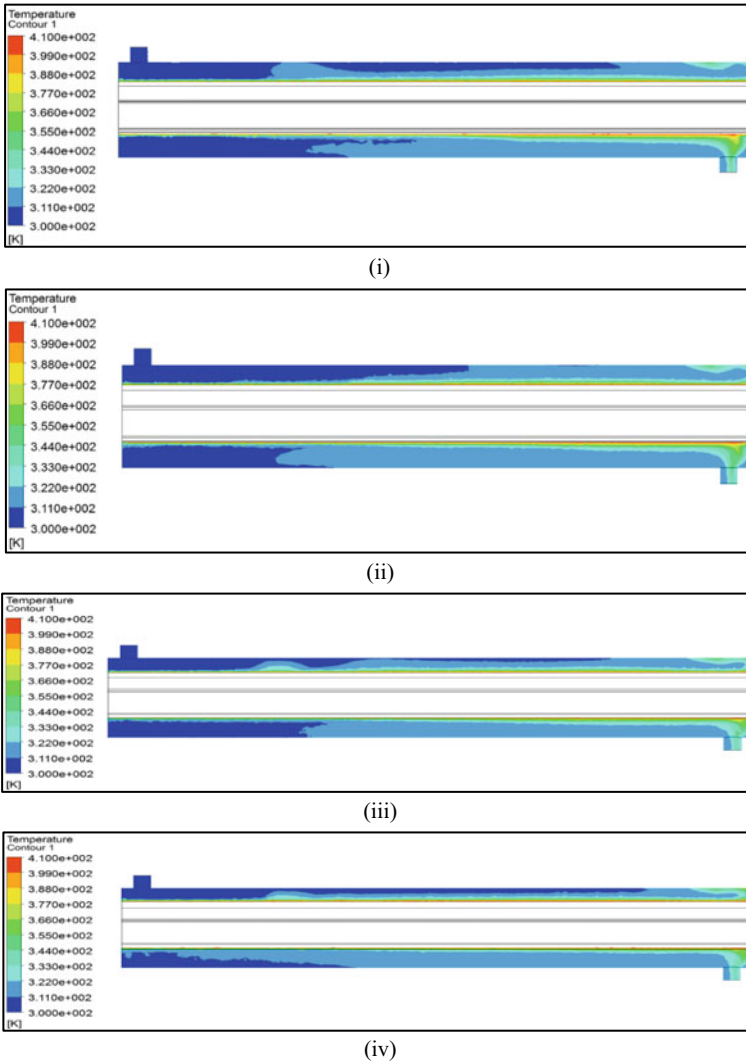


**Fig. 14** Temperature contour of CFHE with fins heights of **a** 6 mm, **b** 8 mm, **c** 10 mm and **d** 12 mm

- The heat transfer rate and convective heat transfer coefficient of CFHE were enhanced by 4% and 12.3%, respectively, as compared to PFHE. Also, the Nu number values were significantly improved in CHHE.
- The experimental values and numerical simulations values were similar, which reveal the accuracy of the CFD simulations.
- The heat transfer enhancement and outer temperature were achieved, when the number of fins were increased and maximum five number of fins inserted in the CFHE.

- With increasing the height of fins, the outer temperature also increased, and the maximum values were observed for 12 mm height fins in the CFHE.
- The optimized results using CFD tool will be helpful in sizing the heat exchanger and designing the high efficient system, incorporating these optimum values.

## References

1. Bhuiyan AA, Amin MR, Islam AS (2013) Three-dimensional performance analysis of plain fin tube heat exchangers in transitional regime. *Appl Therm Eng* 50:445–454
2. Bhutta MMA, Hayat N, Bashir MH, Khan AR, Ahmad KN, Khan S (2012) CFD applications in various heat exchangers design: a review. *Appl Therm Eng* 32:1–12
3. Dong J, Chen J, Zhang W, Hu J (2010) Experimental and numerical investigation of thermal-hydraulic performance in wavy fin-and-flat tube heat exchangers. *Appl Therm Eng* 30:1377–1386
4. Eiamsaard S, Promvong P (2007) Heat transfer characteristics in a tube fitted with helical screw-tape with/without core-rod inserts. *Int Commun Heat Mass Transf* 34:176–185
5. Ereke A, Ozerdem B, Bilir L, Ilken Z (2005) Effect of geometrical parameters on heat transfer and pressure drop characteristics of plate fin and tube heat exchangers. *Appl Therm Eng* 25:2421–2431
6. Hatami M, Jafaryar M, Ganji DD, Gorji-Bandpy M (2014) Optimization of finned-tube heat exchangers for diesel exhaust waste heat recovery using CFD and CCD techniques. *Int Commun Heat Mass Transfer* 57:254–263
7. Jalaluddin TR, Miyara A (2018) Performance of shallow borehole of spiral-tube ground heat exchanger. *J Mech Eng* 15(2):41–52
8. Kandlikar S (2012) History, advances, and challenges in liquid flow and flow boiling heat transfer in micro channels: a critical review. *J Heat Transfer* 134:34001–34015
9. Kral D, Stehlik P, Van Der Ploeg HJ, Master BI (2007) Helical baffles in shell-and-tube heat exchangers, Part I: experimental verification. *Heat Transfer Eng* 17(1):93–101
10. Lotfi B, Sunden B, Wang Q (2016) An investigation of the thermo-hydraulic performance of the smooth wavy fin-and-elliptical tube heat exchangers utilizing new type vortex generators. *Appl Energy* 162:1282–1302
11. Liu X, Yu J, Yan G (2016) A numerical study on the air-side heat transfer of perforated finned-tube heat exchangers with large fin pitches. *Int J Heat Mass Transfer* 100:199–207
12. Master BI, Chunangad KS, Pushpanathan V (2003) Fouling mitigation using helix heat exchangers. In: *Refereed proceedings heat exchanger fouling and cleaning: fundamentals and applications, engineering conferences international*
13. Mishra DP, Paramanik SC (2019) Computation of air entrainment into a mixing pipe: an experimental and numerical analysis. *J Mech Eng* 16(2):11–28
14. Mohapatra K, Mishra DP (2015) Numerical investigation of heat transfer and fluid flow characteristics of an internally ribbed tube. *J Mech Eng (JMehE)* 12(2):85–103
15. Ozden E, Tari I (2010) Shell side CFD analysis of a small shell-and-tube heat exchanger. *Energy Conv Manage* 51:1004–1014
16. Prajapati YK, Bhandari P (2017) Flow boiling instabilities in micro channels and their promising solutions—a review. *Exp Therm Fluid Sci* 88:576–593
17. Rathore SK, Bergale A (2012) Comparative analysis of finned tube and bare tube type shell and tube heat exchanger. *Int J Eng Innovative Technol (IJEIT)* 2(1):1–9
18. Rosa P, Karayiannis TG, Collins MW (2009) Single-phase heat transfer in micro channels: the importance of scaling effects. *Appl Therm Eng* 29:3447–3468
19. Sinha A, Chattopadhyay H, Iyengar AK, Biswas G (2016) Enhancement of heat transfer in a fin-tube heat exchanger using rectangular winglet type vortex generators. *Int J Heat Mass Transf* 101:667–681

20. Vats P, Sharma BC, Sharma S (2014) Heat transfer through journal bearing: a case study. *Int J Res Eng Technol* 03(10), eISSN:2319–1163
21. Wang CC, Chang YJ, Hsieh YC, Lin YT (1996) Sensible heat and friction characteristics of plate fin-and-tube heat exchangers having plane fins. *Int J Refrig* 19:223–230
22. Wang YH, Zhang JL, Ma ZX (2017) Experimental determination of single-phase pressure drop and heat transfer in a horizontal internal helically-finned tube. *Int J Heat Mass Transf* 104:240–246
23. Zhang J, He YL, Tao W (2009) 3D numerical simulation on shell-and-tube heat exchangers with middle-overlapped helical baffles and continuous baffles. *Int J Heat Mass Transfer* 52:5371–5380

# Friction Welding Process of AA7075 Aluminium Alloy to Mild Steel



Jitendra Gupta, Bhuvnesh Bhardwaj, and Varun Sharma

**Abstract** The objective of present research is to examine the effect of friction welding parameters on the impact energy of fabricated weldments during the welding of mild steel with aluminium alloy AA7075. An attempt has also been made to formulate the mathematical relationship between the welding conditions and impact strength. The rotational speed, welding time and workpiece diameter have been considered as welding conditions. The workpiece diameter has been found most significant welding parameter that affects the impact strength of weldments followed by rotational speed and welding time. The  $R^2$  and adjusted  $R^2$  values for the impact strength prediction model have been found as 0.991 and 0.980, respectively, which are very close to each other.

**Keywords** Friction welding · Impact energy · AA7075 · Mild steel

## 1 Introduction

Welding of aluminium alloy using fusion welding is very difficult due to high thermal conductivity, thermal expansion, solidification shrinkage and high solubility of gases in molten aluminium. This leads to formation of oxide layers, cracks, hot tears, discontinuities, porosity in aluminium weldments, formation of brittle inter dendritic structure etc. The formation of brittle weldments decreases the mechanical properties of the weldments [1]. In addition to this, increase in grain growth in base alloy takes place due to high heat generation during the fusion welding. Further, this reduces strength and hardness of weldments. In order to overcome these difficulties, many researches have been carried out in the past. The researchers developed new welding technique called friction welding. Friction welding is a solid state, environmental friendly welding process. It is also called green energy welding. Friction welding

---

J. Gupta (✉) · B. Bhardwaj

Department of Mechanical Engineering, Jaipur Engineering College and Research Centre, Jaipur, India

V. Sharma

Department of Production and Industrial Engineering, NIT Jalandhar, Punjab, India

© The Author(s), under exclusive license to Springer Nature Singapore Pte Ltd. 2022

M. Vashista et al. (eds.), *Recent Innovations in Mechanical Engineering*,

Lecture Notes in Mechanical Engineering, [https://doi.org/10.1007/978-981-16-9236-9\\_19](https://doi.org/10.1007/978-981-16-9236-9_19)

does not require filler material, flux and shielding gases like fusion welding. The friction welding is carried out below recrystallization temperature; therefore, less distortion of the base material and weldments occurs due to absence of melting and solidification. In friction, welding heat for the welding of two materials is generated due to mechanical friction between the moving workpiece and stationary workpiece. Friction welding is widely used for joining the similar and dissimilar metals. In the past, number of researches have been published to study the effect of friction welding conditions on the mechanical properties of the weldments. A brief discussion in this regard has been presented in this section.

Ericsson et al. made a comparison between the fatigue strength of the weldments which obtained using friction stir welding with weld fatigue strength obtained using metal inert gas welding (MIG) and tungsten inert gas welding (TIG) [2]. Reynolds et al. examined the mechanical properties of weldments of 304L stainless steel [3]. Mustafa and Adem optimized friction stir spot welding parameters (tool rotation speed, plunge depth and dwell time) for maximum weld strength during the welding of high-density polypropylene [4]. Zhang et al. used solid mechanics-based 2D finite element for the development of residual stress prediction model for the weldments obtained using friction stir welding [5]. Gharacheh et al. fabricated weldments of AZ31 magnesium alloy using friction stir welding at different ratio of rotation speed to welding speed for the examination of the mechanical properties of weldments [6]. Ren et al. studied the effect of friction stir welding parameters on the tensile and yield strength of weldments of Al–Mg–Si alloy [7]. Sayer et al. examined the microstructure, mechanical properties and low cycle fatigue behaviour of weldments during the friction stir welding of AA6063 aluminium alloy [8]. Sunggon et al. [9] studied the effect of friction stir welding process parameters on the mechanical properties of the weldments of AA6061-T651 alloy. Zadeh et al. [10] used friction stir welding process for the joining of two dissimilar materials and examine the effect of friction stir welding process parameters on the strength of weldments.

Jayaraman et al. [11] examined the effect of friction stir welding parameters on the tensile strength of the weldments of A319 alloy. Rajkumar et al. [12] developed tensile strength prediction model in terms of friction stir welding parameters during the welding of AA7075–T6 alloy. Mohanty et al. [13] employed friction stir welding for the joining of AA1100 aluminium alloys to study the mechanical properties of weldments. Paventhan et al. [14] used friction stir welding for the joining of two dissimilar materials, namely AISI 1040 grade medium carbon steel and AISI 304 austenitic stainless steel for the study of tensile property of the weldments. Rambabu et al. [15] used friction stir welding for the study of the corrosion resistance of the fabricated weldments of AA2219 aluminium alloy. Kurian et al. [16] used friction stir welding for the joining of dissimilar materials, namely aluminium alloy AA6063 and AA5052. Mallieswaran et al. [17] formulated the mathematical relationship between the frictional stir welding parameters and tensile strength of the weldments of aluminium alloys AA1100 with AA6061. Zulu and Mashinini [18] studied the performance of rotary friction weldments of Ti–6Al–4 V alloy rods. The friction and forging pressure, rotational speed, forging time and upset distance have been taken as welding parameters. Eslami et al. [19] fabricated welded joints to examine

the impact of friction stir welding on the mechanical and electrical properties of the weldments. The traverse speed and tool rotation have been considered as welding conditions.

From the review of published literature, it has been concluded that mostly research has been carried out to examine the effect of friction welding conditions on mechanical properties of weldments that obtained using friction welding of similar materials. Fewer efforts have been carried out to examine the mechanical properties of welding joint of dissimilar material.

The aluminium alloy AA 7075 is widely used for highly stressed structural applications like fabrication of aircraft structural parts and it is very difficult to join AA7075 alloy using fusion welding due to the formation of dendritic structure in the fusion zone. On the other hand, mild steel is most commonly used steel because its price. Therefore, the study of the mechanical properties (impact strength) of welded joints of these materials will be quite useful.

## 2 Materials and Methods

In the present work, AA 7075 alloy and mild steel (each having 6 cm lengths) have been used as dissimilar materials for friction welding. The friction welding has been carried out on conventional lathe machine. For the welding on lathe, one piece of sample (aluminium) has been fitted in chuck while another piece (mild steel) has been fixed in tool post under pressure. The pressure has been applied using tail stock.

The impact strength of the fabricated weldments has been measured using Charpy impact test or Charpy v-notch test. The Charpy test on the fabricated samples has been conducted at room temperature on the Charpy impact tester manufacturer by Engineering Models and Equipment, Roorkee. The Charpy test is a standard test for the measurement of amount of energy absorbed by the material before failure under sudden loading. This absorbed energy indicates the toughness of the material.

## 3 Selection of the Friction Welding Parameters and Working Range

In the present work, friction welding experiments have been carried out on the conventional lathe machine. Therefore, only friction welding parameters that can be considered for the present work are rotational speed, friction time and diameter of rod. The working range of the parameters has been evaluated using hit and trial method. For the evaluation of working range, the experiments have been conducted according to Table 1.

From the table, it has been revealed that at the rotational speed 300 rpm, for the rod having diameter 10 mm, the welding occurs at 18 min friction time. Therefore,



**Table 1** Trial experiments for working range

Sample No.	Rotational speed (rpm)	Friction time (min.)	Diameter	Remarks
1	300	4	10	Not welded
2	300	6	10	Not welded
3	300	8	10	Not welded
4	300	10	10	Not welded
5	300	12	10	Not welded
6	300	14	10	Not welded
7	300	16	10	Not welded
8	300	18	10	Welded

minimum limit of rotational speed is taken as 300 rpm and maximum 900 rpm (due to limitation of machine condition) and maximum diameter 10 mm (due to holding problem) and minimum 5 mm and minimum welding time 20 min and maximum 30 min.

## 4 Development of Prediction Model for Impact Strength

In this work, the prediction model of impact strength has been developed using response surface methodology with the help of design expert software. The levels of friction welding parameters and the experimentation plan according to face centred design have been presented in Tables 2 and 3, respectively.

### 4.1 Diagnosis of Assumptions of ANOVA

Analysis of variance test is employed to check the (1) significance of the develop model, (2) significance of the individual model terms and (3) to check the adequacy

**Table 2** Welding conditions and levels of friction welding parameters

Friction welding parameters	Levels		
	Minimum value	Centre value	Maximum value
Rotational speed (RPM)	300	600	900
Welding time (min)	20	25	30
Diameter (mm)	5	7.5	10

**Table 3** Experimentation plan and measured value of mechanical properties

Std	Run	A:Rotational speed (RPM)	B:Welding time (min)	C:Diameter (mm)	Impact strength (J)
1	7	300	20	5	15.79
2	8	900	20	5	11.65
3	10	300	30	5	11.58
4	5	900	30	5	8.93
5	3	300	20	10	11.34
6	14	900	20	10	8.57
7	17	300	30	10	8.80
8	2	900	30	10	8.10
9	18	300	25	7.5	15.79
10	12	900	25	7.5	12.82
11	6	600	20	7.5	15.79
12	1	600	30	7.5	14.48
13	15	600	25	5	19.2
14	9	600	25	10	16.10
15	11	600	25	7.5	17.79
16	4	600	25	7.5	19.16
17	13	600	25	7.5	18.62
18	16	600	25	7.5	17.57

of the lack of fit. In this work, ANOVA is carried out at 95% confidence level. Before applying the ANOVA test on the data, it is necessary to check the assumptions of ANOVA. The ANOVA can be applied on the data only when the data obey the assumptions of ANOVA. The ANOVA is based on the two assumptions (1) normal distribution and (2) constant variance. The first assumption, i.e. assumption of normal distribution can be verified using normal probability plot. If the data follow normal distribution, mostly points should fall on the straight line and near the straight line. The second assumption of ANOVA, i.e. assumption of constant variance can be verified using studentized residuals versus predicted values plot. If the data follow assumption of constant variance, residual versus predicted response plot should not follow some specific pattern. It should be scatter. In this work, normal probability plots for the residuals of impact strength has been presented in Fig. 1, while Fig. 2 shows the residuals versus predicted values plots for impact strength.

From Fig. 1, it has been cleared that most of points are falling on the straight line or near the straight line. That means residuals of impact strength follows the assumption of normal distribution of data. On the other hand, it has been appeared from Fig. 2 that the pattern of the data is scattered and residuals are not following any specific pattern. This indicates that there is no reason to suspect any violation of the second assumption of ANOVA.

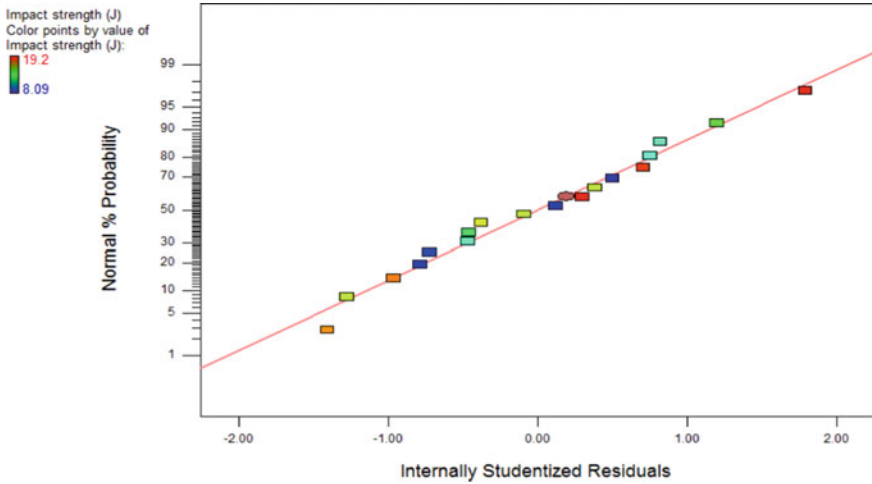


Fig. 1 Normality plot for the residuals of impact strength

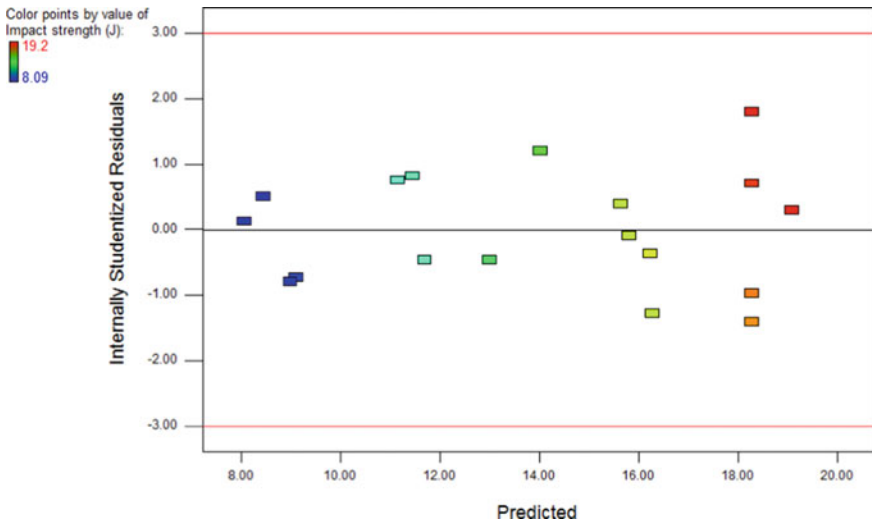


Fig. 2 Plot residuals versus predicted for impact strength

### 4.2 Development of the Prediction Models for Mechanical Properties

In the present work, ANOVA, analysis has been carried out at 95% confidence level for checking the adequacy of model and individual model terms. The ANOVA table for impact strength has been presented in Table 4.

**Table 4** ANOVA for impact strength

Source	Sum of squares	Degree of freedom	Mean square	F-Value	p-value Prob > F
Model	251.00	9	27.89	95.42	<0.0001
A-Rotational speed	17.53	1	17.53	59.98	<0.0001
B-Welding time	12.68	1	12.68	43.38	0.0002
C-Diameter	20.33	1	20.33	69.58	<0.0001
AB	1.58	1	1.58	5.39	0.0488
AC	1.37	1	1.37	4.69	0.0623
BC	1.91	1	1.91	6.54	0.0338
A <sup>2</sup>	42.28	1	42.28	144.66	<0.0001
B <sup>2</sup>	26.38	1	26.38	90.25	<0.0001
C <sup>2</sup>	1.01	1	1.01	3.45	0.1003
Residual	2.34	8	0.29		
Lack of Fit	0.70	5	0.14	0.26	0.9103
Pure Error	1.63	3	0.54		
Cor. Total	253.33	17			
Std. Dev	0.54		R-squared		0.991
Mean	14.00		Adj. R-squared		0.980
C.V. %	3.86		Pred. R-squared		0.966
PRESS	8.53		Adeq. precision		27.363

Table 4 shows that impact strength prediction model, main effect of rotational speed, welding time, diameter, interaction terms of rotational speed friction time, welding time diameter and quadratic terms of rotational speed and welding time have been found significant while lack of fit has been found insignificant. The ordinary  $R^2$ , adjusted  $R^2$  and adequate precision values have been found as 0.991, 0.980 and 27.363, respectively. The impact strength prediction model in terms of parameters is shown in Eq. 1.

$$\begin{aligned}
 \text{Impact strength} = & -54.21 + 0.04 * \text{Rotational speed} \\
 & + 5.54 * \text{Welding time} - 0.41 * \text{Diameter} \\
 & + 2.95833E - 004 * \text{Rotational speed} * \text{Welding time} \\
 & + 5.51667E - 004 * \text{Rotational speed} * \text{Diameter} \\
 & + 0.039 * \text{Welding time} * \text{Diameter} \\
 & - 4.38889E - 005 * \text{Rotational speed}^2 \\
 & - 0.125 * \text{Welding time}^2 - 0.097 * \text{Diameter}^2 \quad (1)
 \end{aligned}$$

## 5 Effect of Parameters on Mechanical Properties

The 3D plots have been plotted to investigate the effect of friction welding parameters (rotational speed, welding time and workpiece diameter) on impact strength of the weldments.

Figures 3 and 4 shows the 3D Plots for impact strength. The 3D plot is useful for the investigation of the simultaneous effect of two parameters on response. Figure 3 shows the 3D plot for impact strength in terms of rotational speed and welding time. The figure has been plotted at fixed value of workpiece diameter (7.5 mm). The curvature of the plot indicates that the variation of impact strength is quadratic with rotational speed and welding time. Also, it has been revealed from the figure that the impact strength initially increases up to a certain values with increase in rotational speed as well as with increase in welding time. Further increase in rotational speed and welding time decreases the impact strength. Also, it has been revealed that maximum impact strength has been achieved at approximate rotational speed 600 rpm and welding time 25 min. Fig. 4 shows the 3 D plot for impact strength in terms of rotational speed and workpiece diameter. The plot has been plotted at constant value of welding time (25 min). From the plot, it has been revealed that impact strength continuously decreases with increase in workpiece diameter. Also, it has been revealed that maximum impact strength have been achieved at approximate workpiece diameter 5 mm.

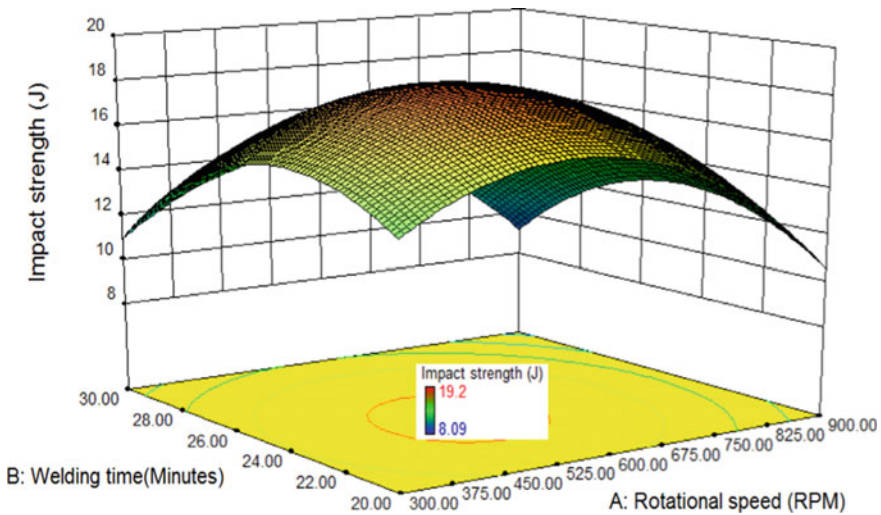


Fig. 3 3D plot of impact strength in terms of rotational speed and welding time

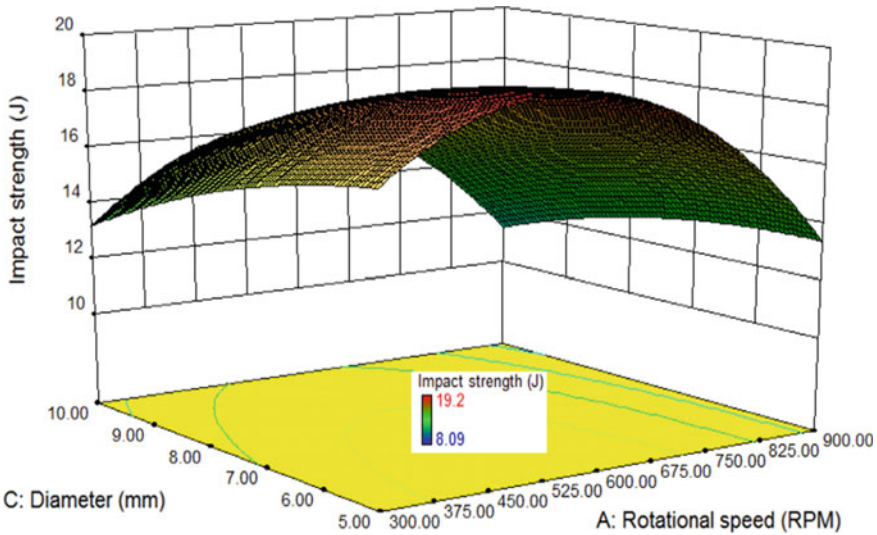


Fig. 4 3D plot of impact strength in terms of rotational speed and workpiece diameter

### 5.1 Justifications of the Results Obtained from the Analysis

In this process, required heat is generated due to friction between the two metal joints. The heat generation for welding increases with increase in rotational speed. The sound bonding between the two metal joints takes place when sufficient heat generated. At the low speed (300 rpm), sufficient axial forging heat due to friction has not been generated for sound bonding between the mild steel and AA7075 alloy joints. The bonding between the joints becomes brittle [20]. Therefore, joints fabricated at low rotational speed exhibited low impact strength. In addition to this, unbounded region around the centre of the weld interface is formed due to less heat generation. The unbounded region shows the insufficient bonding between the metal joint due to less adhesion and inter-diffusion of each element. Only outer region of metal joints has been bonded due to the high temperature as compare to the inner region [21]. This further decreases the impact strength of weldments. The heat generation increases with increase in rotational speed. The 600 rpm rotational speed generated sufficient heat for bonding, results in sound bonding at the interface of AA7075 alloy and mild steel which produce good weld strength. Further increase in rotational speed beyond 600 rpm produces weak weld strength. At the high rotational speed, intermetallic ordered FeAl layers forms at the weld interface due to high heat generation. This intermetallic layer provides a barrier for diffusion [22]. Therefore, weak bonding takes place, resulting in poor weld strength. Same effect has been observed with welding time. In addition to this, weld strength continuously decreases with increase in workpiece diameter. The required heat for friction welding increases with increase in diameter of workpiece. Due to insufficient heat generation according to diameter

of workpiece, weak bonding between the AA7075 alloy and mild steel metal joints takes place. Therefore, poor weld strength obtained with large workpiece diameter.

## 6 Conclusion

The major conclusions drawn from the current study are as:

- The friction welding has been found good welding technique for the joining of dissimilar materials.
- The workpiece diameter has been found most significant welding parameter that affects the impact strength of weldments followed by rotational speed and welding time.
- The variations of impact strength with rotational speed and welding time have been found quadratic.
- The  $R^2$  and adjusted  $R^2$  values for the impact strength prediction model have been found as 0.991 and 0.980, respectively, which are very close to each other.
- The impact strength initially increases up to a certain values with increase in rotational speed and welding time. Further increase in rotational speed and welding time decreases the impact strength. On the other hand, impact strength continuously decreases with increase in workpiece diameter.

## References

1. Su JQ, Nelson TW, Mishra R, Mahoney M (2003) Microstructural investigation of friction stir welded 7050–T651 aluminium. *Acta Mater* 51(3):713–729
2. Ericsson M, Sandstrom R (2003) Influence of welding speed on the fatigue of friction stir welds and comparison with TIG and MIG. *Int J Fatigue* 25:1379–1387
3. Reynolds AP, Tang W, Herold TG, Prask H (2003) Structure, properties and residual stress of 304L stainless steel friction stir welds. *Scripta Mater* 48:1289–1294
4. Mustafa B, Adem K (2004) The influence of stirrer geometry on bonding and mechanical properties in friction stir welding process. *Mater Des* 25:343–347
5. Zhang HW, Zhang Z, Chen JT (2005) The finite element simulation of the friction stir welding process. *Mater Sci Eng A* A403:340–348
6. Gharacheh A, Kokabi AH, Daneshi GH, Shalchi B, Sarrafi R (2006) The influence of the ratio of “rotational speed/traverse speed” ( $\omega/v$ ) on mechanical properties of AZ31 friction stir welds. *Int J Mach Tools Manuf* 46:1983–1987
7. Ren SR, Ma ZY, Chen LQ (2007) Effect of welding parameters on tensile properties and fracture behavior of friction stir welded Al–Mg–Si alloy. *Scripta Mater* 56:69–72
8. Sayer S, Ceyhun V, Tezcan O (2008) The influence of friction stir welding parameters on the mechanical properties and low cycle fatigue in AA6063 (AlmgSi0.5) Alloy. *Kovove Materialia* 46:157–164
9. Sunggon L, Sangshik K, Chang GL, Sungjoon K (2008) Tensile behavior of friction-stir-welded Al 6061-T651. *Metall Mater Trans A* 35a:2829–2835
10. Abdollah-Zadeh A, Saeid T, Saizgari B (2008) Microstructural and mechanical properties of friction stir welded aluminum/copper lap joints. *Alloys Compd* 460:535–538

11. Jayaraman M, Sivasubramanian R, Balasubramanian V (2009) Optimization of process parameters for friction stir welding of cast aluminium alloy A319 by Taguchi method. *J Mater Sci Technol* 25(5):655–664
12. Rajakumar S, Muralidharan C, Balasubramanian V (2010) Optimization of the friction-stir-welding process and tool parameters to attain a maximum tensile strength of AA7075-T-6 aluminium alloy. *Proc Instit Mech Eng Part B J Eng Manuf* 224:1175–1191
13. Mohanty HK, Venkateswarlu D, Mahapatra MM, Pradeep KN, Mandal R (2012) Modeling the effects of tool probe geometries and process parameters on friction stirred aluminium welds. *J Mech Eng Autom* 2(4):74–79
14. Paventhan R, Lakshminarayanan PR, Balasubramanian V (2012) Optimization of friction welding process parameters for joining carbon steel and stainless steel. *J Iron Steel Res Int* 19(1):66–71
15. Rambabu G, Naik DB, Rao CHV, Rao KS, Reddy GM (2015) Optimization of friction stir welding parameters for improved corrosion resistance of AA2219 aluminum alloy joints. *Defence Technol* 11:330–337
16. Kurian A, Sritharan V, Mohan DG (2016) Optimization of process parameters of friction stir welding of dissimilar aluminium alloys (AA6063-AA5052). *Int Res J Eng Technol* 3(12):502–504
17. Mallieswaran K, Padmanabhan R, Balasubramanian V (2017) Friction stir welding parameters optimization for tailored welded blank sheets of AA1100 with AA6061 dissimilar alloy using response surface methodology. *Adv Mater Process Technol*. <https://doi.org/10.1080/2374068X.2017.1410690>
18. Zulu MC, Mashinini PM (2018) Process optimization of rotary friction welding of Ti-6Al-4V alloy rods *IOP Conf Series Mater Sci Eng* 430(2018):1–6
19. Eslami N, Hischer Y, Harms A, Lauterbach D, Bohm S (2019) Optimization of process parameters for friction stir welding of aluminum and copper using the Taguchi method. *Metals* 9(63):1–15
20. Shubhavardhan RN, Surendran S (2012) Friction welding to join stainless steel and aluminum materials, *Int J Metall Mater Sci Eng* 2(3):53–73
21. Fukumoto S, Tsubakino H, Okita K, Aritoshi M, Tomita T (1999) Friction welding process of 5052 aluminium alloy to 304 stainless steel. *Mater Sci Technol* 15:1080–1086
22. Fukumoto S, Tsubakino H, Okita K, Aritoshi M, Tomita T (2000) Amorphization by friction welding between 5052 aluminium alloy and 304 stainless steel. *Scripta Mater* 42:807–812



# Effect of Tool Tilt Angle on the Mechanical and Metallurgical Properties of Aluminium Alloy 6061-T6 Welded by Friction Stir Welding Process



Gaurav Kumar, Varun Sharma, Rakesh Kumar, Ankit Thakur,  
Navdeep Minhas, and Om Prakash Verma

**Abstract** The present study investigates the effect of tool tilt angle on the weldability, mechanical and metallurgical properties of aluminium alloy when welded by friction stir welding process. During this study, 6 mm thick plates of aluminium alloy of grade AA6061-T6 were friction stir welded using heat-treated high strength steel tool material. The scroll tool consists of spiral geometry on the shoulder of 18 mm diameter and threaded tapered pin of 5.8 mm length. The friction stir welded joints of 80 mm weld length were fabricated at 45 mm/min tool travel speed using tool rotational speed of 800 rpm with 0° and 2° tool tilt angle. The weldability of the joints was measured in terms of mechanical and microstructural properties. The experimental results obtained as mechanical properties in terms of tensile strength and micro-hardness revealed a significant improvement by tool tilt angle as compared to without tool tilt angle. Further, the microstructural observations obtained using optical microscopy clearly depict the grain size reduction in stir zone and thermo-mechanically affected zones of welded joints fabricated by tool tilt angle.

**Keywords** Friction stir welding · Scroll tool · Tilt angle · Mechanical properties · Metallurgical characterization

---

G. Kumar (✉) · V. Sharma · R. Kumar · A. Thakur · N. Minhas · O. P. Verma  
National Institute of Technology, Jalandhar, Punjab, India

V. Sharma  
e-mail: [sharmav@nitj.ac.in](mailto:sharmav@nitj.ac.in)

R. Kumar  
e-mail: [sharmark@nitj.ac.in](mailto:sharmark@nitj.ac.in)

A. Thakur  
e-mail: [ankit.ip.18@nitj.ac.in](mailto:ankit.ip.18@nitj.ac.in)

O. P. Verma  
e-mail: [vermaop@nitj.ac.in](mailto:vermaop@nitj.ac.in)

## 1 Introduction

Friction stir welding is a technique of solid-state joining process. The friction stir welding process was developed by The Welding Institute (TWI) at Cambridge, the UK, in 1991. It has been well applied in the aerospace, shipbuilding, automobile industries [1, 2]. This technique is used to join the high strength aluminium alloys, which are tough to join with the fusion welding process. Initially, this process is developed for high strength aluminium alloys, but after the applications found that it is useful for joining many other materials, lightweight materials, as well as high strength and weight ratio alloys [3]. In FSW, a specially designed pin and the shoulder non-consumable tool with rotating action plunged into the two mating surfaces edges of the workpiece that is to be weld and then travelled along the joint line [4]. There is no liquid state of the workpiece material in the FSW technique, and welding takes place below the melting point of the workpiece material [5]. So, the problems that are relevant to the solidification of a fused material are restricted.

Elangovan [6] studied the effect of tool pin shape and rotational speed of tool on mechanical properties of aluminium alloy 6061 welded by friction stir welding process. Five different tool pin profiles such as straight cylindrical, tapered cylindrical, threaded cylindrical, triangular and square are used at five different tools rotational speed ranging from 800 to 1600 RPM to fabricate the weld joints and concluded that the joint welded at 1200 RPM with a square tool pin profile showed excellent mechanical properties. Feng et al. [7] studied the effect of welding speed, fracture mode and tool rotation speed on the tensile strength and microstructure and concluded that the better yield strength and ultimate tensile strength of the weld joints are obtained by increasing trend of welding speed ranging from 200 to 600 mm/min.

Among all the friction stir welding process parameters, the tool tilt angle is a crucial factor for the heat generation and flow of material. Krishna et al. [8] investigated the effect of tool tilt angle on friction stir welds of Aluminium 2014-T6. He studied the influence of varying tool tilt angle from  $0^\circ$  to  $3^\circ$  at an interval of  $0.5^\circ$  and kept all other process parameters constant. He found by his study defects are produced on the workpiece surface and inside the weld because of improper filling of material at lower tilt angles. Mehta et al. [9] studied the influence of tilt angles on the mechanical and metallurgical properties of dissimilar friction stir welding. Different tool tilt angles such as  $0^\circ$ ,  $1^\circ$ ,  $2^\circ$ ,  $3^\circ$  and  $4^\circ$  are taken for investigation considering other process parameters constant and found that the defect-free weld using tilt angles  $2^\circ$ ,  $3^\circ$  and  $4^\circ$  but at lower tool tilt angles such as  $0^\circ$  and  $1^\circ$  defects are formed. In addition, a maximum tensile strength of 117 MPa and macrohardness of 181 VH in stir zone are detected in the welds fabricated at  $4^\circ$ .

The present investigation focused on the effect of the tool tilt angle using scroll tool geometry of shoulder with respect to the mechanical properties.

## 2 Experimental Procedures

AA6061-T6 aluminium alloy is used for the present experimental study. The chemical composition and mechanical properties of the base metal are tabulated in Tables 1 and 2. The specimens of the dimension of 100 mm × 50 mm × 6 mm were prepared from a raw sheet by a power hacksaw. Butt joint configuration was used for the welding of plates. Before joining the plates, surfaces were cleaned using acetone to avoid any obstruction during welding and get good quality weld.

The conical shape threaded tool pin profile was made from tool steel H13 was used. Shoulder diameter of 18 mm and shoulder length of 80 mm were welded sample used. The scroll shoulder is enabled with the end features as shown in Fig. 3. The conical tool consists of right-hand threads of 1 mm pitch with upper diameter 6 mm and bottom diameter 3 mm, pin length of the tool was 5.8 mm, smaller than the base metal thickness, i.e. 6 mm. Tool rotation was considered to be clockwise for all the experiments, and welding is done along the rolling direction of the base plates. The actual FSW tool and schematic diagram shown in Fig. 1a, b, respectively. All the experiments were done on the vertical milling machine (VMC). Firstly, the plates were rigidly clamped on a fixture, which further fixed on the machine bed as shown in Fig. 2. A set of three experiments for each were done by changing the tool tilt angle by 0°, 2° and keeping other process parameters constant. All experimental process parameters were listed in Table 3. The single-pass technique of the FSW process was followed to prepare the weld joints for investigation.

After the welding process, the welded joints were cut by the wire EDM as per the required dimensions of tensile specimens. All tensile samples were prepared according to the American Society for Testing of Materials (ASTME8-04) guidelines [12]. The tensile test was performed on Tinius H50KS Universal Testing Machine. Hardness tests were carried out on the radical Vicker’s Hardness testing machine. The hardness profile was measured across the transverse cross section of the weld joint line. The load condition for measurement hardness was 0.5 kg load with 30 s dwell time in radical Vicker’s hardness tester.

The metallographic samples were prepared separately by a proper standard process from welded specimens. Firstly, the samples were firstly polished by using emery papers of different grades. Final polishing was performed by using diamond paste (1 μm particle size) and alumina powder on velvet in the double-disc polishing

**Table 1** Chemical composition of base metal used for investigation AA 6061-T6 [10]

	Mg	Si	Fe	Cu	Mn	Cr	Zn	Ti	Al
Al 6061-T6	1.0	0.4–0.8	0.70	0.15–0.40	0.15	0.04–0.35	0.25	0.15	Bal

**Table 2** Mechanical properties of base metal used for investigation AA 6061-T6 [11]

Al 6061-T6	Ultimate strength (MPa)	Elongation (%)	Microhardness (HV)
	284	15	105

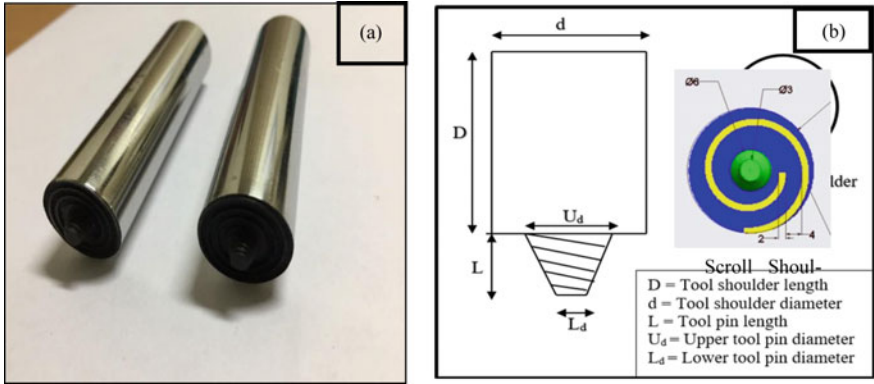


**Fig. 1** a Conical threaded pin FSW tool, b schematic diagram of a left-handed threaded pin profile with scroll shoulder end features

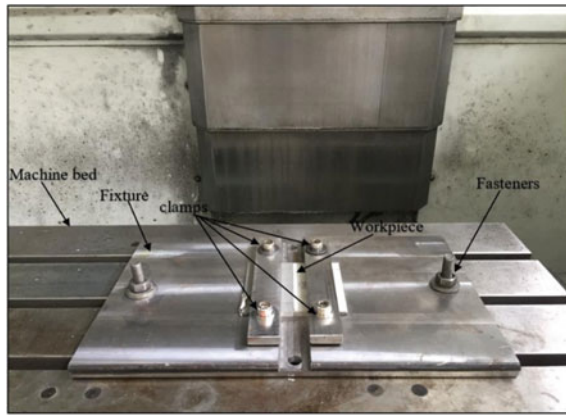


**Fig. 2** Fixture assembly for FSW process on the vertical milling machine bed

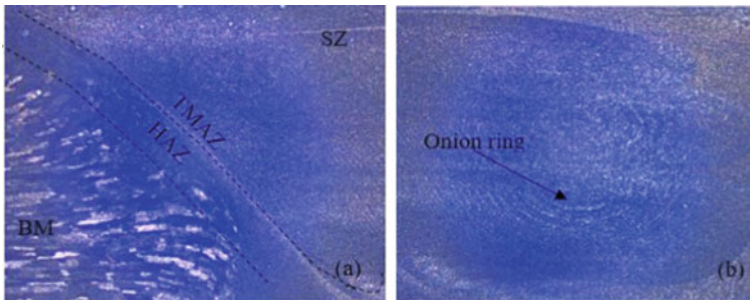


**Fig. 3** Macrostructure of welded sample using 2° tilt angle a advancing side of the welded sample, b joint cross section

**Table 3** Selected process parameters for investigation FSW process

Process parameters	Value
Tool rotational speed (RPM)	800
Welding speed (mm/min)	45
Plunge depth (mm)	5.8
Tool shoulder profile and diameter (mm)	Scroll type and 18
Tool pin profile and pin length (mm)	Conical threaded type and 5.8
Dwell time (s)	3
Tool tilt angle	0°, 2°

machine. Then the polished samples were finally etched by using Keller's reagent (a solution of 2 mL hydrofluoric acid, 5 mL concentrated nitric acid, 3 mL hydrochloric acid and 190 mL distilled water) to reveal the macrostructures and microstructures [5]. After etching, the samples are immediately washed with distilled water and wipe with a cotton cloth wetted with ethanol to obtain the clear presence of all the zones. Weld bead and onion rings formed on samples were visualized clearly after the etching process. For evaluating the microstructures of the samples, an optical microscope was used.

### 3 Results and Discussions

#### 3.1 Microstructural Observations

Figure 3 represents the macrostructure of the friction stir welded AA6061 T6 joint with 2° tilt angles. The possible weld zone of one side of the sample was clearly shown in Fig. 3a. HAZ and TMAZ delimited by the dashed lines. Whereas, at the centre of the joint, the stirred zone or nugget zone is specified. Figure 3b clearly shows the onion ring structure and clears that material is completely mixed in both sides, and there is no defect detected at the weld zones, which indicated that material flow is good using a tilt angle.

The microstructure of the AA 6061-T6 FS-welded joint with and without tilt angle is shown in Fig. 4. The grain size of the TMAZ and HAZ in both cases shows elongated grains due to the stirring and flow of material around the tool pin, whereas the grain size of TMAZ and HAZ compare to NZ is larger due to not enough flow of heat, which results in a lack of dynamic recrystallization. Table 4 shows the grain size of different zones with or without a tilt angle.

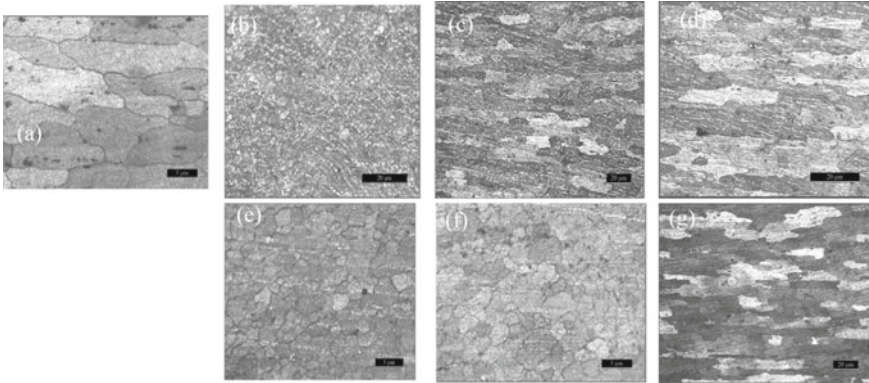


**Fig. 4** Effect of tool tilt angle on the microstructure of AA 6061-T6 FSW joint **a** microstructure of BM **b–d** microstructure of FS-weld joint using 0° tilt angle, NZ, TMAZ and HAZ, respectively. **e–g** Microstructure of the FS-weld using 2° tilt angle NZ, TMAZ and HAZ, respectively

**Table 4** Grain size of the different zone with or without tilt angle

Zones	Grain size (μm)	
	With 0° tilt angle	With 2° tilt angle
BM	15.30	
NZ	2.264667	1.606667
TMAZ	3.452333	1.984333
HAZ	19.27117	22.48767

### 3.2 Tensile Properties

The tensile testing of FSW joint obtained under different tool tilt angles (0° and 2°) and constant travel speed and rotational speed is shown in Fig. 5a. All the testing samples were evaluated under room temperature. The tensile strength of the weld joint

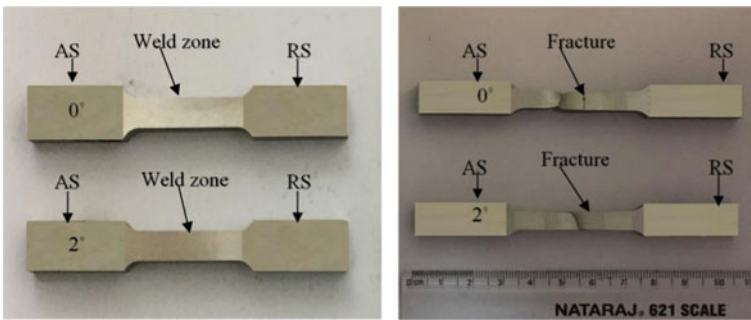


**Fig. 5** Tensile testing **a** tensile samples before testing, **b** fractured tensile samples

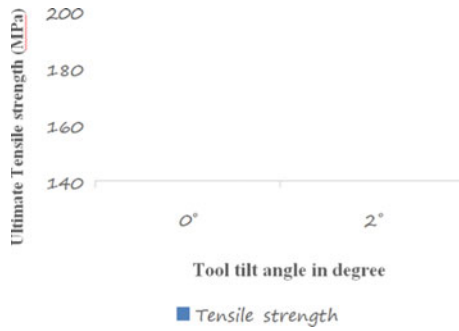


Fig. 6 Ultimate tensile strength of sample welded without tilt and tilt angle

fabricated at 0° tool tilt angle showing show less ultimate tensile strength compared to the joint fabricated at 2° tilt angle. The value noted at 0° was 165 MPa and at 2° noted to 186 MPa as shown in Fig. 6. The joint fracture was noted in the weld or nugget zone with the both tilt angles. However, 0° tilt angle, the crack grown-up towards the advancing side of the joint and in case 2° the crack grown-up towards the retracting side of the joint. The tensile properties and location of the fracture in the weld joint are mainly influenced by the void defects that were present in the weld joint. The fractured tensile samples of the joints are shown in Fig. 5b.

### 3.3 Microhardness

The hardness of the weld joint was measured crosswise the weld on the transverse plane to evaluate the hardness variations with different tool tilt angle, which is shown in Fig. 7. Comparatively, the microhardness of the weld joint with tilt angle shows

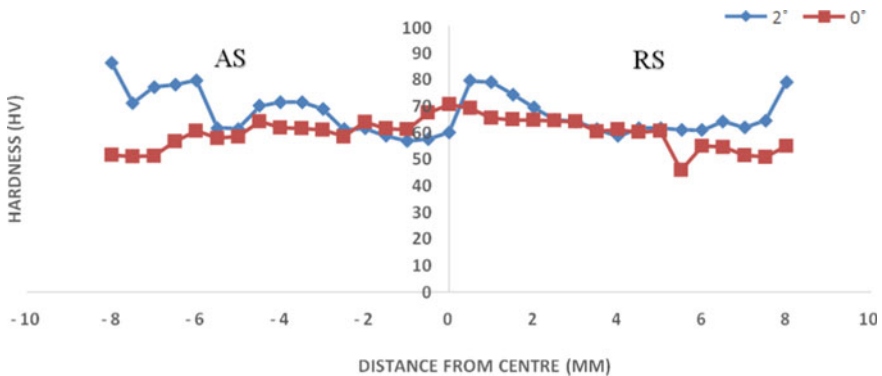


Fig. 7 Variation of microhardness

higher than without tilt and this is attributed due to the material flow in the weld zone is uniform while using a tilt angle. Also, RS of the nugget zone shows the highest hardness throughout the weld, which is approximately noted to be 80 Hv and minimum hardness was noted in HAZ. The lower hardness in the HAZ, when compared to the base material, is due to the occurrence of the over ageing in the HAZ during the welding.

## 4 Conclusions

- Sound defect-free joint of AA 6061-T6 FSW joint using scroll shoulder tool with good mechanical properties could be obtained with a combination of with or without tool tilt angle. The tensile strength could reach up to 65% of that of the base material.
- Grain refinement in the nugget zone comparatively more using tilt angle attributed to be better material flow and heat input. Besides, NZ shows a refined grain structure compared to the TMAZ and HAZ.
- Microhardness of the tilt angle sample shows better results in terms of uniformity and hardness value throughout the weld zones. Further, the highest hardness was noted on the stirred zone retracting side.

## References

1. Prasanna P, Penchalayya Ch, Rao DDA (2013) Effect of tool pin profiles and heat treatment process In: The friction stir welding of Aa 6061 aluminium alloy. *Am J Eng Res* 02(01):7–15
2. Zhang Z, Liu YL, Chen JT (2009) Effect of shoulder size on the temperature rise and the material deformation in friction stir welding. *Int J Adv Manuf Technol* 45(9–10):889–895. <https://doi.org/10.1007/s00170-009-2034-7>
3. Gopi S, Manonmani K (2012) Influence of shoulder profile and shoulder penetration on joint strength; of friction stir welded AA6082 in conventional milling machine. *Eur J Sci Res* 73(1):20–32
4. Ramulu PJ, Narayanan RG, Kailas SV (2013) Forming limit investigation of friction stir welded sheets: influence of shoulder diameter and plunge depth. *Int J Adv Manuf Technol* 69(9–12):2757–2772. <https://doi.org/10.1007/s00170-013-5245-x>
5. Dawood HI, Mohammed KS, Rahmat A, Uday MB (2015) Effect of small tool pin profiles on microstructures and mechanical properties of 6061 aluminum alloy by friction stir welding. *Trans Nonferrous Met Soc China (English Ed.)* 25(9):2856–2865. [https://doi.org/10.1016/S1003-6326\(15\)63911-5](https://doi.org/10.1016/S1003-6326(15)63911-5)
6. Elangovan K, Balasubramanian V, Valliappan M (2008) Effect of tool pin profile and tool rotational speed on mechanical properties of friction stir welded AA6061 aluminium alloy. *Mater Manuf Process* 23(3):251–260. <https://doi.org/10.1080/10426910701860723>
7. Feng AH, Chen DL, Ma ZY (2009) Effect of welding parameters on microstructure and tensile properties of friction stir welded 6061 AL joints. *Mater Sci Forum* 618(619):41–44. <https://doi.org/10.4028/www.scientific.net/MSF.618-619.41>



8. Krishna GG, Reddy PR, Hussain MM (2014) Effect of tool tilt angle on aluminum 2014 friction stir welds. *Glob J Res Eng* 14(7):61–70
9. Mehta KP, Badheka VJ (2016) Effects of tilt angle on the properties of dissimilar friction stir welding copper to aluminum. *Mater Manuf Process* 31(3):255–263. <https://doi.org/10.1080/10426914.2014.994754>
10. Somasekharan AC, Murr LE (2004) Microstructures in friction-stir welded dissimilar magnesium alloys and magnesium alloys to 6061–T6 aluminum alloy. *Mater Charact* 52(1):49–64. <https://doi.org/10.1016/j.matchar.2004.03.005>
11. Ji S, Huang R, Meng X, Zhang L, Huang Y (2017) Enhancing friction stir weldability of 6061–T6 Al and AZ31B Mg alloys assisted by external non-rotational shoulder. *J Mater Eng Perform* 26(5):2359–2367. <https://doi.org/10.1007/s11665-017-2640-8>
12. Sreenivas P, Anil Kumar R, Sreejith PS (2017) Effect of applied axial force on FSW of AA 6082–T6 aluminium alloys. *Int J Mech Eng Technol* 8(1):88–99

# Physiological Evaluation of Normal and Inclined Walking in Unorganized Sector Workers



Ram Charan Bairwa, Rahul Jain, M. L. Meena, and K. B. Rana

**Abstract** The economy of any country is divided into two parts that are organized and unorganized sectors. A significant part of the workforce is employed in informal sectors; hence, unorganized sector workers play a vital role in the Nation's economy. Manual material handling is the prominent activity in the workplace through which a vast amount of finished goods or raw material is handled manually without caring for their physical capacity. Ergonomic is sciences that identify the erroneous working technique and provide a safe and convenient method to perform the task. This research aims to find out the stress in the various muscle of the body during various locomotion conditions. The desired objective is fulfilled by performing an exercise test on sixty male workers of three different age groups of 21–30, 31–40, and  $\geq 41$  years that are involved in the construction and housekeeping sector are chosen to walk on a treadmill with their self-selected speed of 3.6–3.8 km/hr at 0°, 5°, 10°, 15°, 20° walking inclination. The stress in muscles is measured in terms of amplitude by measuring physiological performance like HR and  $VO_2$  uptake. Experimental data are interpreting using SPSS to find out the best results, which reduces fatigue in muscle during different locomotion situations. The study results illustrate that for the age group 21–30 year, 31–40 year, and  $\geq 41$  years worker, the most favorable angle of walking surface is  $<15^\circ$ ,  $\leq 10^\circ$ , and  $\leq 5^\circ$ , respectively.

**Keywords** Ergonomics · Walking · Physiological · Unorganized sector workers

---

R. C. Bairwa · M. L. Meena

Department of Mechanical Engineering, Malaviya National Institute of Technology Jaipur, JLN Marg, Jaipur, Rajasthan, India  
e-mail: [ram.mech@mnit.ac.in](mailto:ram.mech@mnit.ac.in)

M. L. Meena

e-mail: [mlmeena.mech@mnit.ac.in](mailto:mlmeena.mech@mnit.ac.in)

R. Jain (✉) · K. B. Rana

Department of Mechanical Engineering, Rajasthan Technical University, Kota, Rajasthan, India  
e-mail: [rjain.npiu.me@rtu.ac.in](mailto:rjain.npiu.me@rtu.ac.in)

K. B. Rana

e-mail: [kbrana@rtu.ac.in](mailto:kbrana@rtu.ac.in)

## 1 Introduction

The majority of the workforce in India works in the informal sector. The share of the unorganized and organized sectors in net domestic product is 56.7% and 43.3%, respectively [1]. In this age of machinery, many workplace activities are carried manually by workers, which include manual handling of goods, loading, and unloading, pushing and pulling, etc. Carrying heavy and undefined load in awkward postures or for a prolonged period induces physical stress in the body that may injure the bones, joints, muscles, tendons, and ligaments of upper and lower limbs along with neck, upper back, and hip muscles, which causes pain in the body that further affect the human productivity [2]. In the literature, it was said that most of the workplace-related injuries are due to fall, and it is sprains/strains (31%) and fractures (27%) [3, 4]. Both safety and health of workers have a positive impact on human productivity. Therefore, The International Labor Organization (ILO) and Occupational Safety and Health Administration (OSHA) have released guidelines to avoid musculoskeletal disorders even though workers of the unorganized sector do not adhere to these rules due to the lack of training [1, 5]. It became essential to make aware of the workers about the severity of hazards associated with the muscles.

The foot's bipedal movement is achieved by GAIT that is defined as the time interval between two repetitive events of walking. The main biomechanical functions of the foot are: (a) to accommodate the ground irregularities and maintain balance, (b) serve as a shock absorber to support the weight, and (c) transmit propulsive force to move forward [6]. Walking, jogging, and running are the means of moving our body that have a speed of 4.5–5 km/hr, 6.4–8 km/hr, and >8 km/hr, respectively [7]. When the muscles work more, the oxygen demand increases, and the person has to breathe more rapidly [8]. The variation in speed and slope changes may affect the kinetics, kinematics, and body physiology [4]. For safe and convenient locomotion, the following essential factors are to be controlled within a permissible limit to avoid excess fatigue on the body: (a) speed of walking (b) walking surface inclination (c) carrying load (d) method of carrying the load. The physiological stress in the muscles is determined by considering various parameters like mean and peak heart rate HR (bpm) and maximum rate of oxygen consumption ( $\text{VO}_2\text{max}$  in ml/kg/min) [9].

The following research gap has been identified from the literature that various slopes on physiological parameters are to be analyzed. After going through the literature gaps recognized from the literature review, the objective of the work is to evaluate the physiological performance of unorganized sector workers during normal and inclined walking.

## 2 Methods

A total of 60 male workers in three age groups (21–30, 31–40, and  $\geq 41$  years) were chosen to participate in an experiment on the treadmill with a self-selected speed

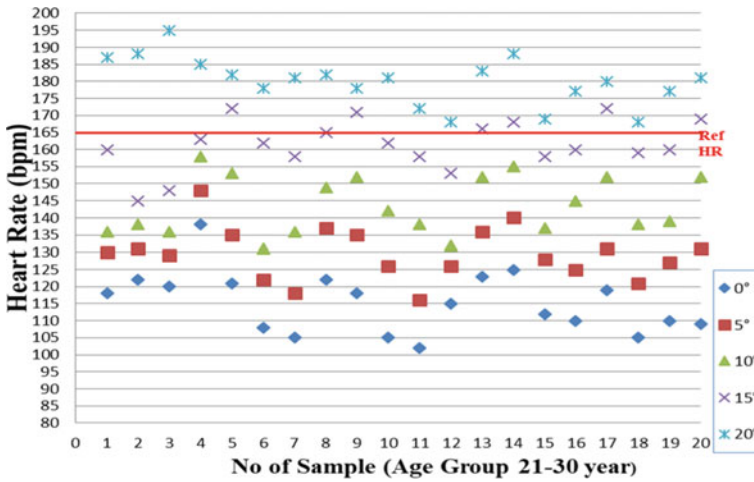


Fig. 1 Scatter plot between HR versus angles of walking for age group 21–30 year

of 3.2–3.8 km/hr for a time of 10 min [7, 9–12]. The HR and VO<sub>2</sub> uptake values are calculated for each worker at 0°, 5°, 10°, 15°, 20° walking slope. Accusure pulse oximeter, stadiometer, and weighing scale were used to measure the various characteristics of participants. VO<sub>2</sub>max is calculated from the formula mentioned below [13].

$$VO_2 \text{ uptake} \left( \frac{\text{kg}}{\text{ml} \times \text{min}} \right) = \frac{HR_{\text{max}}}{HR_{\text{resting}}} \times 15.3 \tag{1}$$

### 3 Results

#### 3.1 Heart Rate Versus Different Angle of Walking

Figures 1, 2, and 3 show the trend of heart rate versus different angles of walking for different age groups.

#### 3.2 VO<sub>2</sub> Uptake Versus Different Angle of Walking

Figures 4, 5, and 6 show VO<sub>2</sub> uptake versus different walking angles for different age groups.

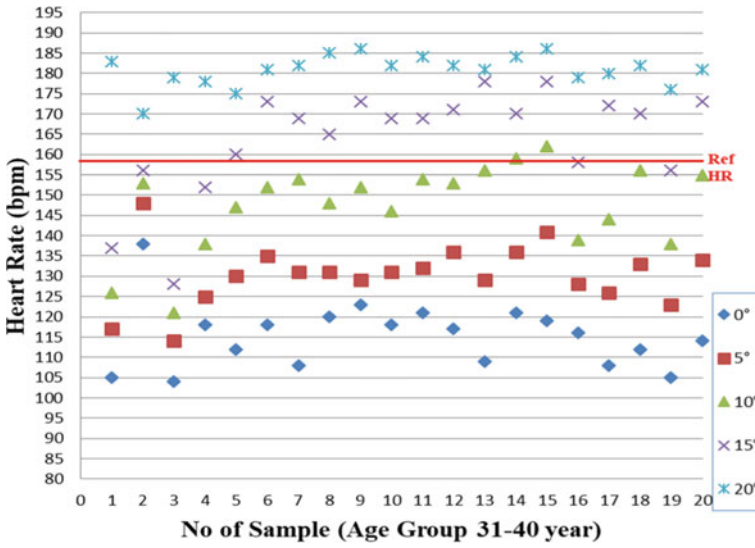


Fig. 2 Scatter plot between HR versus angles of walking for age group 31–40 year

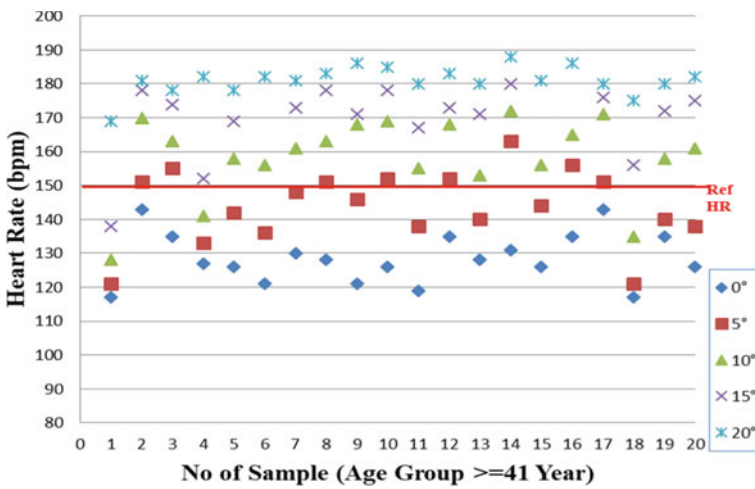


Fig. 3 Scatter plot between HR versus angles of walking for the age group ≥41 year

### 4 Discussion and Conclusions

Previous investigations found that the heart rate above 85% of the targeted heart rate, and the maximum oxygen uptake beyond the defined value of 35–40 ml/kg min may cause the worker’s sore joints and muscles. If the workers do work beyond these

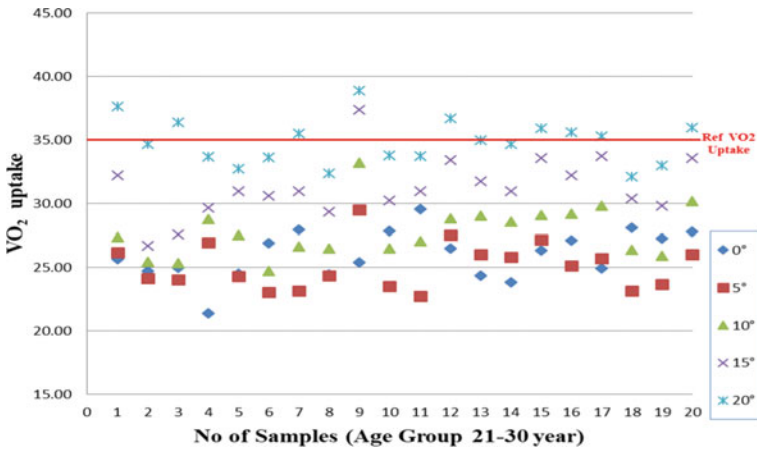


Fig. 4 Scatter plot between  $VO_2$  uptake versus angles of walking for age group 21–30 year

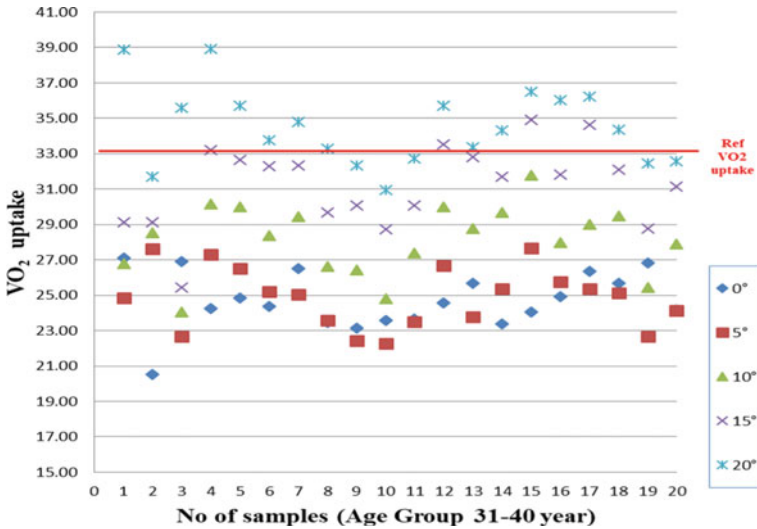


Fig. 5 Scatter plot between  $VO_2$  uptake versus angles of walking for age group 31–40 year

values, then the worker would become unduly fatigued before the 8 h have elapsed, impacting the quality of workers' lives, and human productivity decreases.

Twenty workers from each group were gone through the treadmill experiment, and their HR and  $VO_2$  uptake values are measured for each worker at 0°, 5°, 10°, 15°, 20° walking inclination.

For the age group 21–30 year, 31–40 year, and  $\geq 41$  years worker, the most favorable walking surface angle is  $<15^\circ$ ,  $\leq 10^\circ$ , and  $\leq 5^\circ$ , respectively where the value heart rate, maximum oxygen uptake is within the acceptable limit.

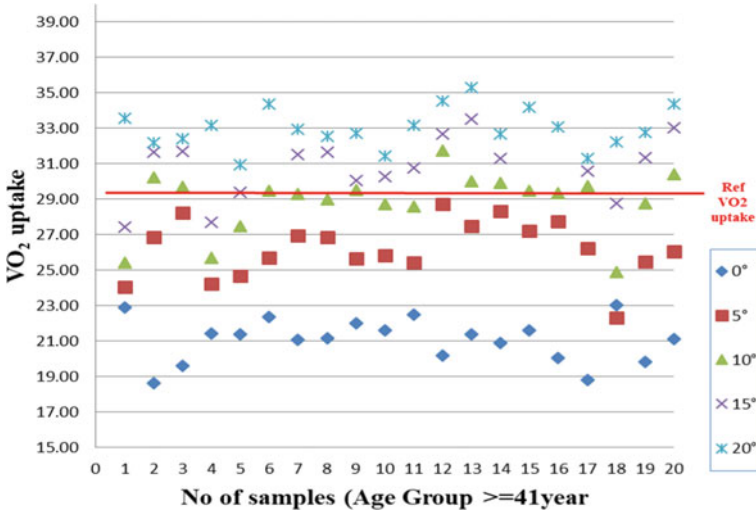


Fig. 6 Scatter plot between VO<sub>2</sub> uptake versus angles of walking for the age group ≥41 year

**References**

1. Mishra S (2018) Social security for unorganised workers in India. *J Social Sci* 53(2):73–80
2. D’souza AP (2013) Unorganized sectors: role of an entrepreneur and challenges in self-employment. *Int J Scien Res Publ* 3(6):1–5
3. Oxley J, O’Hern S, Burt D et al (2018) Falling while walking: a hidden contributor to pedestrian injury. *Accid Anal Prev* 114:77–82
4. Mohammadi R, Phadke C (2016) The impact of incline and speed of treadmill on ankle muscle activity in middle-aged adults. *J Bodywork Movement Therap* 21(2):306–313
5. Jain R, Sain MK, Meena ML et al (2018) Non-powered hand tool improvement research for prevention of work-related problems: a review. *Int J Occup Saf Ergon* 24(3):347–357
6. Anders C, Wagner H, Puta C et al (2007) Trunk muscle activation patterns during walking at different speeds. *J Electromyogr Kinesiol* 17(2):245–252
7. Jeremy V, Gautier Z, Denis T et al (2009) Equivalence of accelerometer data for walking and running: treadmill versus on land. *J Sports Sci* 27(7):669–675
8. Khademi-Kalantari K, Rahimi F, Hosseini SM et al (2017) Lower limb muscular activity during walking at different speeds: over-ground versus treadmill walking; a voluntary response evaluation. *J Bodywork Movement Therap* 21(3):605–611
9. Sharma R, Kamboj K, Bhardwaj J (2019) Gender response and safe carrying load limit for sugar industry workers. *Int J Occup Saf Ergon* 25(1):51–60
10. Mohammadi R, Phadke C (2017) Effects of treadmill incline and speed on peroneus longus muscle activity in persons with chronic. *Gait Posture* 54:221–228
11. Simon SW, Otto HT (2019) Effects of backpack and double pack loads on postural stability. *Ergonomics* 62(4):537–547
12. Hudson S, Cooke C, Davies S et al (2018) A comparison of economy and sagittal plane trunk movements among back-, back/front- and head loading. *Ergonomics* 61(9):1216–1222
13. Gordon M, Goslin B, Graham T et al (2007) Comparison between load carriage and grade walking on a treadmill. *Ergonomics* 26(3):289–298

# Analyzing the Effects of Industrial Protective Glove's Material on Hand Grip Strength



Lalit Kumar Sharma, Manoj Kumar Sain, and M. L. Meena

**Abstract** Hand and forearm muscles contribute significantly in grip force execution during routine and industrial activities. Industrial gloves are used in various small-scale industries for safety purpose. However, the use of hand gloves may lead to the change in grip strength. The present study has been designed to investigate the effect of hand glove's material on hand grip strength of workers employed in various Small and Medium Enterprises (SMEs). During this study, to record the strength of workers' hand grip while performing work using different gloves, a digital hand grip dynamometer was used. Statistical test one-way ANOVA was applied to analyze the collected data. From the analysis of data, it can be concluded that there are significant differences among the grip strength means with various glove's material at the 0.05 level of significance. It is also observed that fabric gloves give best grip strength; however, there are limitations in its use.

**Keywords** ANOVA · Gloves · Hand grip strength · Muscles

## 1 Introduction

India has many small and medium enterprises (SMEs) where the labor do hand work. The labor associated with such enterprise is victim of various musculoskeletal disorders. Researchers identified that ergonomics intervention are not applied widely in SMEs and suggested that with appropriate anthropometric data, designers can design proper equipment and tools for the workers. With the improvements in currently adopted procedures, the quality of manual operations can be improved [1–3]. Grip strength is a major attribute of various operational activities in everyday working

---

L. K. Sharma (✉) · M. L. Meena

Malaviya National Institute of Technology, Jaipur, Rajasthan 302017, India

M. L. Meena

e-mail: [mlmeena.mech@mnit.ac.in](mailto:mlmeena.mech@mnit.ac.in)

M. K. Sain

Swami Keshvanand Institute of Technology, Management and Gramothan, Jaipur, Rajasthan 302017, India



life in which labor perform different manual operations with their hands. Workers perform better with higher grip strength in standing posture [4]. In certain manual operations, labor operates with handheld power tools and exposed to hand vibrations. These vibrations can cause different disorders in hands and arms, so the operator uses gloves to protect their hands from these harmful vibrations. Many of these operations generally take place in open surroundings. Adequate hands and fingers temperatures in the winter can be maintained by body heat (muscles and circulation) and by some added insulation using gloves. The muscle tissues mass is almost insignificant, so production of body heat largely depends on circulation. Hence, ergonomist should consider this issue while designing tools and equipments that are used by labor in everyday working. Hand grip is caused when we bend all our fingers altogether. Thus, hands grip strength may be defined by the total force of contact that we apply to handlebar with our maximum voluntary contraction effort.

## 2 Literature Review

Hamouda et al. [5] revealed significant reduction in the hand grip strength. In his study, no significant evidence of relationship among the glove thickness and the hand grip strength was observed. Taylor et al. [6] found a significant correlation between the environmental air temperature and mean hand skin temperature. This temperature of hand skin affects the thermal exchange of body with the thermal environment. Jaber et al. [7] and Chkeir et al. [8] suggested that ergonomists must think about environmental issue while designing tools used by labor in their everyday work-life. Gripping of hand is a necessary factor of daily operational activities. Concentrated cooling of their hands reduces physical performance and flexibility due to higher viscosity inside the joints [9]. Farmers, medical doctors, industrial and construction site workers and machinists use gloves in their respective workplaces to keep their arms, fingers and hands protected from environment exposures, chemicals and physical harm such as blisters and cuts [10, 11]. Sudhakar et al. [12] found that a fraction of muscle force is usually lost in the interface of hand and glove. Fleming et al. [13] observed that a physical fatigue may occur with the use of different type of gloves and hand and finger grip contraction. The advanced knowledge of information of the expected effects of using gloves on hand grip strength can be helpful for labors, safety professionals and managers in order to make them informed and take right decisions regarding selection of gloves and theirs workplace uses [14]. Many researchers [15–19] identified that hands grip strength depends on several factors. Male workers have greater hands grip strength as compared to female workers, reason being the body composition differences such as high fat mass and low muscle mass in female.

Vikram et al. [20] observed that length of dominant hand and circumference of forearm can help in prediction of grip strength. Fraser et al. [21] and Mohamed et al. [22] identified a significant relationship between hands grip strength and circumference of forearm. Incel et al. [23] stated that hand grip strength was greater in

right-handed workers than left-handed workers. However, some researchers found no significant difference in hands grip strength of the dominant and non-dominant hands [24, 25]. Su et al. [26] identified that 180° flexion shoulders have greater hands grip strength than 0° flexion shoulders. Swanson et al. [27] observed that the operator's grip of hands was stronger when the arms were not supported with compared to when the arms were supported. Watson and Ring [28] revealed that a few psychological factors like depression score was related with decreased hands grip strength.

Ramadan [29] observed that reduction in strength due to greater thickness of glove is more severe compared to thinner gloves, apart from hand skin temperature. Dianat et al. [30] reported that the glove's greater thickness would affect the efficiency of hand, which may lead to discouragement of using gloves by workers. The physical exertion, relative humidity and temperature have considerable effect on hand skin conductance [31]. Skin temperature is directly affected by cold immersion. Maximum voluntary contraction (MVC) and temperature of hand skin have direct impact of gender [32]. In this study, researcher did not investigate hand skin temperature. Goonetilleke and Hoffmanns [33] investigated that the temperature of hands skin could be considered to be near to water bath temperature. Hand glove tends to increase discomfort, muscle activity and wrist posture. Hands grip, touch sensitivity and torque strength of forearm can be decreased with the use of hand glove [34]. Sormunen et al. [35] observed no correlation between cooling of skin and upper extremity muscular strain. Researcher found maximum muscular strain in muscles of wrist extensor. The grip span is the key parameter that should be analyzed during modeling of endurance time of force and work rest cycles [36]. The gloves used in medical have tighter fitting and thinner comparatively. A small change in their properties like thickness, friction and fit can led to huge effect on their performance [37]. Dianat et al. [38] identified that if thickness of a glove is varied selectively over some portions where it is in contact with hand, performance of worker can be improved. This approach is valuable for hand glove used to protect workers hand from environment simultaneously allowing better capabilities of hand performance. This study investigated effects of industrial protective glove's material on hand grip strength of workers.

### 3 Methodology

To analyze the effects of glove's material, hand grip strength of workers was measured without gloves and with different types of gloves (i.e., fabric, nylon and latex). A total of 50 workers aged between 20 and 50 years were randomly chosen from various SMEs of Jaipur. During study, to record the strength of workers' hand grip while performing work using different gloves, a digital hand grip dynamometer was used. Verbal instructions were given to each of the participant. They were given demonstration prior to testing and were encouraged during testing. This was done to get their maximal hands and fingers grip of the dominant hand. The test was conducted in the

sitting position of the participants keeping arms straight outwards and inclined down. Each of the participants held the dynamometer tightly approximately for 3 s and then relaxed for a minute. This test was conducted three times in one minute interval in two successive measurements. The highest recorded score ( $N$ ) then was considered as hand grips strength score of participant. Statistical tests one way ANOVA was applied to analyze the collected data.

## 4 Observations and Results

To analyze the effect of gloves, the participants hands grip strength was measured and then compared. These all measurements were obtained with the participant upper limb horizontal, i.e., at  $0^\circ$  angle of elbow. The observations are shown below in Table 1.

From the analysis of data, it can be seen that the mean grip strength is maximum with bare hands followed by fabric hand gloves. Figure 1 depicts the power report of one way ANOVA. Mean standard deviation and 95% confidence interval values can be seen from the figure.

Figure 2 shows the mean comparison chart and comparison of mean grip strength. Figure shows that the mean grip strength with latex gloves is minimum and has a significant difference from other type of gloves. Hand grip strength with fabric gloves is found to be significantly high compared to hand grip strength with latex gloves. It can be seen that differences between means at significance level 0.05 are there. Red interval that does not overlap indicates means that differ from each other.

## 5 Conclusion

Hands grip strength is key characteristic in physical operation and everyday activities. It is significantly influenced by the use of protective gloves but not documented well. Therefore, the effect of three typical gloves on hand grip strength was examined. This study was conducted using three different types of glove that are used in various SMEs in Jaipur. In this study, it is observed that there are significant differences among the grip strength with different glove's materials (fabric, nylon and latex). It is observed that fabric gloves give best grip strength; however, there are some limitations in its use. From the analysis of data, it is found that the mean grip strength is maximum with bare hands followed by fabric hand gloves. The mean grip strength with latex gloves is observed minimum. Hand grip strength with fabric gloves is found to be significantly high compared to hand grip strength with latex gloves. As various industrial operations need a quite great role of forearm muscle in execution of grip force, the study of MVC could be incorporated with such studies. This may lead ergonomists and designers to work harder in order to get better glove characteristics.

**Table 1** Hand grip strength of workers without and with gloves

S. No	Bare hand	Fabric gloves	Nylon gloves	Latex gloves	S. No	Bare hand	Fabric gloves	Nylon gloves	Latex gloves
1	35	35	33.5	31	26	32	31	30	28
2	37	36	35	32.5	27	37.5	37	36	33.5
3	36.5	35	33.5	33	28	35.5	35	34	31
4	34	34	32	30	29	30	29	25	23.5
5	35	34	33.5	31	30	38	36.5	26	24
6	37	36.5	35	32.5	31	39	37	37	35
7	36	35.5	34	31.5	32	37	36	36	34
8	35	35	33.5	31	33	38.5	37	37	35
9	37	36	36	34	34	40	37.5	37.5	35
10	37	36.5	36	34	35	37	37	36	34
11	36	35	33.5	32	36	37	36	36	34
12	35	35	33.5	31	37	34	33	32	30
13	34	33	33	30	38	36.5	34.5	34	32
14	36.5	36	34	32.5	39	40	39.5	37	35
15	36.5	33	34	32	40	37	36	36	34
16	37	36	36	34	41	30.5	30	29	28
17	30	30.5	26	24.5	42	38.5	30	37	35
18	40	39.5	37	35	43	37	35	35	33
19	37	36	36	34	44	38.5	37	37	35
20	39	37.5	37.5	35	45	35.5	34	34	31
21	38	38	35.5	33	46	37.5	36.5	36.5	35

(continued)

**Table 1** (continued)

S. No	Bare hand	Fabric gloves	Nylon gloves	Latex gloves	S. No	Bare hand	Fabric gloves	Nylon gloves	Latex gloves
22	38	37.5	35.5	33.5	47	40	40	37	35
23	37	35.5	35.5	32.5	48	39	38	37	35
24	41	40.5	38.5	35	49	38.5	38	37	35
25	30	29.5	27.5	26	50	35.5	35.5	33.5	31

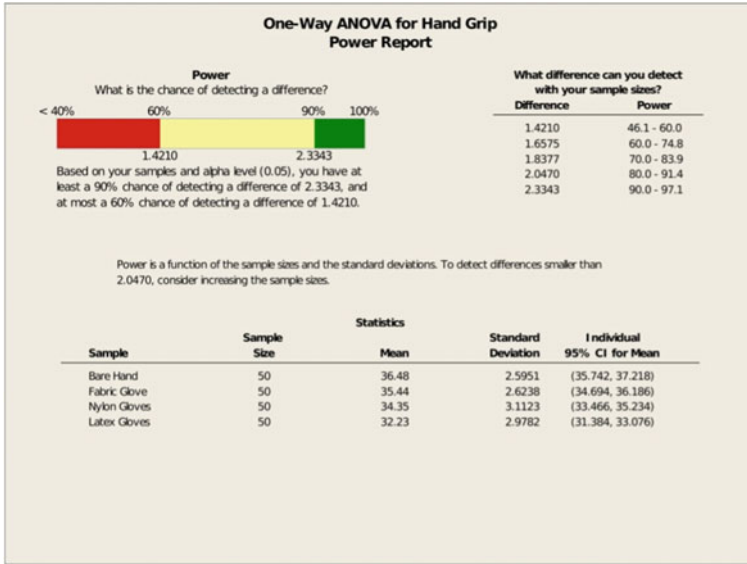


Fig. 1 Summary of power report of one way ANOVA

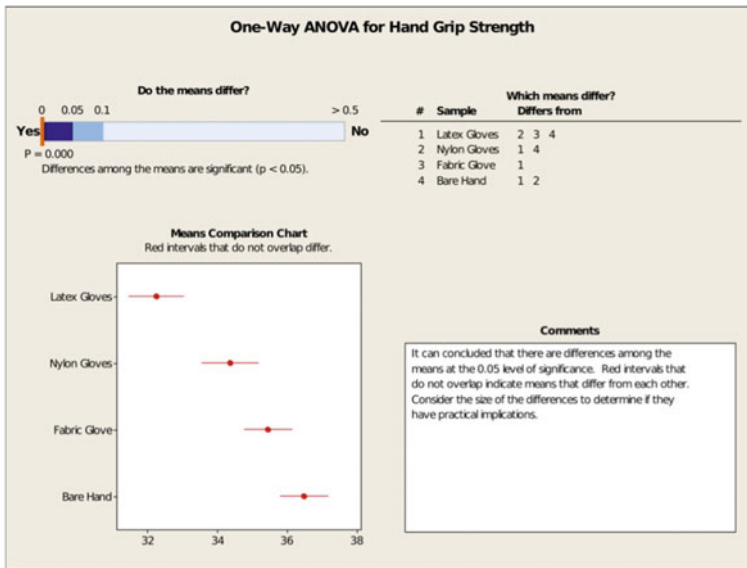


Fig. 2 Summary of one way ANOVA

## References

1. Meena ML, Dangayach GS, Bhardwaj A (2013) Measuring anthropometric data for designing hand tools in handicraft industries. *Int J Process Manage Benchmark* 3(3):334–351
2. Meena ML, Dangayach GS, Bhardwaj A (2016) A literature review of musculoskeletal disorders in handicraft sector. *Int J Appl Ind Eng* 3(2):36–46
3. Meena ML, Dangayach GS, Bhardwaj A (2014) Investigating ergonomic issues among workers in hand block textile printing industries. *Int J Bus Syst Res* 8(4):392–401
4. Jain R, Meena ML, Sain MK, Dangayach GS (2019) Impact of posture and upper-limb muscle activity on grip strength. *Int J Occup Saf Ergon* 25(4):614–620
5. Hamouda K, Rakheja S, Dewangan KN, Marcotte P (2018) Fingers' vibration transmission and grip strength preservation performance of vibration reducing gloves. *Appl Ergon* 66:121–138
6. Taylor NAS, Machado-Moreira C, Van Den Heuvel A, Caldwell J, Taylor EA, Tipton MJ (2009) The roles of hands and feet in temperature regulation in hot and cold environments. In: Thirteenth international conference on environmental ergonomics; University of Wollongong: Boston, MA, USA
7. Jaber R, Hewson DJ, Duchêne J (2012) Design and validation of the grip-ball for measurement of hand grip strength. *Med Eng Phys* 34:1356–1361
8. Chkeir A, Jaber R, Hewson DJ, Duchêne J (2013) Estimation of grip force using the grip-ball dynamometer. *Med Eng Phys* 35:1698–1702
9. Cheng CC, Shih YC, Tsai YJ, Chi CF (2014) The influence of cooling forearm/hand and gender on estimation of handgrip strength. *Ergonomics* 57(10):1499–1511
10. Toumi K, Joly L, Vlemminckx C, Schiffers B (2017) Risk assessment of florists exposed to pesticide residues through handling of flowers and preparing bouquets. *Int J Environ Res Public Health* 14:526
11. Garus-Pakowska A, Górajski M, Szatko F (2017) Awareness of the risk of exposure to infectious material and the behaviors of Polish paramedics with respect to the hazards from blood-borne pathogens—a nationwide study. *Int J Environ Res Public Health* 14:843
12. Sudhakar L, Schoenmarklin R, Lavender S, Marras W (1988) The effects of gloves on grip strength and muscle activity. In: Proceedings of the human factors society—annual meet, 1988
13. Fleming SL, Jansen CW, Hasson SM (1997) Effect of work glove and type of muscle action on grip fatigue. *Ergonomics* 40(6):601–612
14. Wimer B, McDowell TW, Xu XS, Welcome DE, Warren C, Dong RG (2010) Effects of gloves on the total grip strength applied to cylindrical handles. *Int J Ind Ergon* 40:574–583
15. Shyam K, Parmar V, Ahmed S, Kar S, Harper WM (2008) A study of grip endurance and strength in different elbow positions. *J Orthopaed Traumatol* 9:209–211
16. Liao KH (2016) Optimal handle grip span for maximum hand grip strength and accurate grip control strength exertion according to individual hand size. *J Osteopor Phys Act* 4:178
17. Eksioglu M (2016) Normative static grip strength of population of Turkey, effects of various factors and a comparison with international norms. *Appl Ergon* 52:8–17
18. Jais IS, Chan KL, Loke MK, Abdul Rahim S, Tay SC (2016) Normative data on functional grip strength of elderly in Singapore. *J Hand Therapy*:1–6
19. Abaroagu UO, Ezema CI, Ofodile UN, Igwe SE (2017) Association of grip strength with anthropometric measures: height, forearm diameter, and middle finger length in young adults. *Polish Ann Med*
20. Vikram M, Noor Shafiqah S, Muhammad J, Nor Y, Leonard JH, Ida O (2014) Forearm circumference and hand length predict maximal hand grip strength among Malaysian population. *Middle-East J Sci Res* 21(4):634–639
21. Fraser A, Vallow J, Preston A, Cooper RG (1999) Predicting 'normal' grip strength for rheumatoid arthritis patients. *Rheumatology* 38:521–528
22. Mohamed SS, Umama NS, Padmakumar S, Naajil M, Manjula S (2012) Correlation between grip strength and physical factors in men. *Int J Health Rehab Sci* 1:58–63
23. Incel NA, Ceceli E, Durukan PB, Erdem HR, Yorgancioglu ZR (2002) Grip strength: effect of hand dominance. *Singapore Med J* 43:234–237

24. Reikerås O (1983) Bilateral difference of normal hand strength. *Arch Orthop Trauma Surg* 101:223–224
25. Roberts HC, Denison HJ, Martin HJ, Patel HP, Syddall H, Cooper CA (2011) Review of grip strength in clinical and epidemiological studies: towards a standard approach. *Age Ageing* 40:423–429
26. Su C, Lin JH, Chein TH, Cheng KF, Sung YT (1994) Grip strength in different position of elbow and shoulder. *Arch Phys Med Rehabil* 75:812–815
27. Swanson S, Alfred B, Ivan BM, Groot D (1974) The strength of hand. *JACPOC* 13:1–8
28. Watson J, Ring D (2008) Influence of psychological factors on grip strength. *J Hand Surg Am* 33:1791–1795
29. Ramadan MZ (2017) The effects of industrial protective gloves and hand skin temperatures on hand grip strength and discomfort rating. *Int J Environ Res Public Health* 14:1506
30. Dianat I, Haslegrave CM, Stedmon AW (2012) Methodology for evaluating gloves in relation to the effects on hand performance capabilities: a literature review. *Ergonomics* 55(11):1429–1451
31. Kaiser J, Nimbarte AD, Davari D, Gopalakrishnan B, He X (2017) Study of skin conductance and perceived discomfort of the hand/finger system under controlled atmospheric conditions. *Theor Issues Ergon Sci*
32. Chi CF, Shih YC, Chen WL (2012) Effect of cold immersion on grip force, EMG, and thermal discomfort. *Int J Ind Ergon* 42:113–121
33. Goonetilleke RS, Hoffmann ER (2009) Hand-Skin temperature and tracking performance. *Int J Ind Ergon* 39:590–595
34. Dianat I, Haslegrave CM, Stedmon AW (2012) Using pliers in assembly work: short and long task duration effects of gloves on hand performance capabilities and subjective assessments of discomfort and ease of tool manipulation. *Appl Ergon* 43:413–423
35. Sormunen E, Oksa J, Pienimäki T, Rissanen S, Rintamäki H (2006) Muscular and cold strain of female workers in meatpacking work. *Int J Ind Ergon* 36:713–720
36. Eksioğlu M (2011) Endurance time of grip-force as a function of grip-span, posture and anthropometric variables. *Int J Ind Ergon* 41:401–409
37. Mylon P, Lewis R, Carré MJ, Martin N (2014) A critical review of glove and hand research with regard to medical glove design. *Ergonomics* 57:116–129
38. Dianat I, Haslegrave CM, Stedmon AW (2014) Design options for improving protective gloves for industrial assembly work. *Appl Ergon* 45:1208–1217



# A Comprehensive Study of Image Segmentation Techniques



Vivek Singh Sisodiya and Rohit Agrawal

**Abstract** One of the famous processes for processing of image is the division of images. The name given to this process was segmentation, which basically works on the principle of division. This technique is used to separate an image, which are called segments. For applications such as compression of an image or object recognition, it is most useful because it is expensive to process the entire image for these types of applications. For further processing, therefore, image segmentation is used to segment image components. Segmentation is used generally for the identification in digital images of objects, borders, and other related details. Segmentation such as thresholds, clustering, and transformation methods are different methods. The resulting separated image is a composite element collection of the complete image after these approaches have been taken. In this paper, a detailed description of various techniques are given which are used for division of images.

**Keywords** Segmentation · Edge discernment · Image processing · Object recognition

## 1 Introduction

Segmentation of images is the main topic in processing of image. This technique is used to isolate the image from the correct positions in critical regions. For this method, the first thing which we require are images of black and white color. The segmentation is accomplished by thresholds based on the distribution of pixel properties, such as gray values and color. There are [1] established techniques of image segmentation are the edge detection, threshold, region-based approaches, clustering, ANN, PDE, and watershed transformation which are still being used by the researchers. When pictures are color-based, they are divided into two types, i.e., gray and colored. The image segments for color pictures are entirely different from those of grayscale images, e.g., image restoration from the content [2]. The main purpose of this technique is to

---

V. S. Sisodiya · R. Agrawal (✉)

Department of Computer Engineering and Applications, GLA University, Mathura 281406, India  
e-mail: [rohit.agrwal@gla.ac.in](mailto:rohit.agrwal@gla.ac.in)

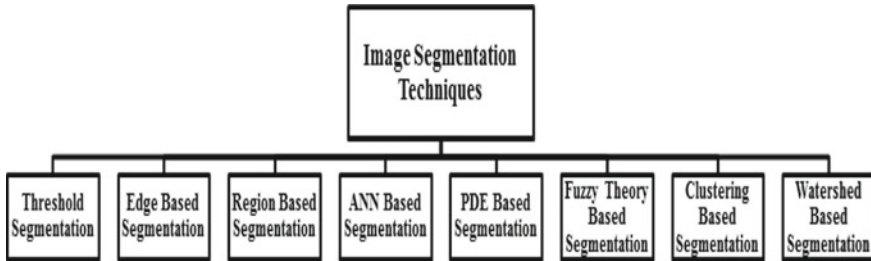


**Fig. 1** Techniques used for segmentation of images

divide the images further in terms of segment with same characteristics or patterns. It is noted that the image segmentation process is not ideal since each image has its distinct form. Finding a technique for segmenting a particular method of the image is also a very difficult task. Because an imaging approach cannot continue to be effective for certain types of images; it is, therefore, possible to separate segmentation methods into three groups: classic process-based segmentation techniques, AI techniques, and hybrid techniques. Image technology is describable by the three layers: first is the understanding of the image, then analysis of the image, and at last, the processing of the image [3] (Fig. 1).

## 2 Image Segmentation Techniques

### 2.1 *Threshold Segmentation*

The most commonly used image segmentation technique is the threshold method. It is used to distinguish the foreground. A gray image is transformed into a binary image in this process [4]. The binary picture provides the entire necessary information on the location and type of objects. The following are the threshold methods:

#### **Thresholding by Global Method**

A histogram of the input image intensity should disclose two peaks, corresponding respectively to the signals from the background and the object. It tells the degree to which two peaks are separated. These equations are describing it in mathematical form:

$$g(p, q) = \begin{cases} 1, & \text{if } f(p, q) > TH \\ 0, & \text{if } f(p, q) \leq TH \end{cases} \quad (1)$$

### Variable Thresholding

At the variable thresholding, the background and the front-end image objects are isolated depending upon the elements of image. A threshold of the variable if the image can be transformed by  $T$ .

- Regional or either local thresholds, if TH depends on a  $(p, q)$ .
- Threshold improvement if TH is a  $(p, q)$  functions.

### Multiple Thresholding

Multiple thresholds can be established by dividing the gray-level image into many different parts. It defines several thresholds and divides the image into some areas of glow and the background and several objects. It covers several areas of shine. Multiple thresholding:

$$g(p, q) = \begin{cases} a, & \text{if } f(p, q) > \text{TH}_2 \\ b, & \text{if } \text{TH}_1 < f(p, q) \leq \text{TH}_2 \\ c, & \text{if } f(p, q) \leq \text{TH} \end{cases} \quad (2)$$

The threshold values can be determined using the image histogram peaks. To estimate these, simple algorithms can also be built.

## 2.2 Edge-Based Segmentation

Side detection techniques are well-developed image processing techniques by itself. This works by a quick shift in the intensity value in an image since there are no good details about edges in a single intensity value. It helps to find those edges where threshold is lesser in comparison to first derivative of intensity.

One of the basic techniques for the detection of the edges can be used, such as the Sobel operator, Prewitt operator, and the Robert operator. Basically, a binary image is the output of such methods. These are the structural methods focused on recognition of discontinuity.

### Robert Edge Detection

For image processing for an edge, detection is used as the Roberts edge operator. Lawrence Roberts proposed it in 1963. This was the first edge detector. A 2-D spatial gradient measurement is performed by the Roberts operator on an image, easily and quickly. This focuses on areas with a high spatial gradient through which edges are fit. Operator inputs are usually gray; the values of element tells the spatial gradient magnitude [5] (Fig. 2).

**Fig. 2** Roberts cross convolution masks

<b>+1</b>	<b>0</b>
<b>0</b>	<b>-1</b>

$G_x$

<b>0</b>	<b>+1</b>
<b>-1</b>	<b>0</b>

$G_y$

**Fig. 3** Representing sobel method

a	b	c
d	e	f
g	h	i

**Fig. 4** Edge detection by Prewitt method

<b>+1</b>	<b>0</b>
<b>0</b>	<b>-1</b>

$G_x$

<b>0</b>	<b>+1</b>
<b>-1</b>	<b>0</b>

$G_y$

**Detection of Edges Through Sobel Method**

This technique was introduced by Irwin sobel and hence named as sobel method for detection of edges. This operator is used to detect two kinds of edges in an image one in vertical direction and other one in Horizontal direction. The most widely used masks are 3 \* 3 matrices. Here, orthogonal vectors pair are same as that of vector sum of operators of sobel. The sum of eight vector is in detailed is also described [6] (Fig. 3).

**Prewitt Edge Detection**

In this method, various algorithm based on edge detections are used for the processing of image. Here, image intensity function gradient is determined. It basically works on corners and has two filters, one is horizontal and other is vertical [7] (Fig. 4).

**2.3 Region-Based Method/Segmentation**

Regional segmentation can be described as creating different areas by dividing the same images; it directly identifies the region. Division takes place with gray image pixel values. Two simple regional segmentation techniques are used [8].

### Methods Based on Growing of Region

Here, the images are being divided on the basis of seed growth which reflects the initial elements. Depending on the previous data, such seeds are picked by a particular application. The seed output is then regulated by interconnections between pixels and can be stopped by a prior understanding of the problem. The basic algorithm for the region-building system (based on 8-connectivity) is:

If  $w(p, q)$  is the image segmented, that is, initial and  $r(p, q)$  represent the binary image same as the seed one. Here, 'TH' is any predicate for each  $(p, q)$  position to be evaluated.

- All the components of the 's' are destroyed first and foremost
- Calculate a PT image binary. Here,  $PT(x, y) = 1$ , and  $TH(x, y) = \text{True}$
- Measure a binary 'q' image where  $q(x, y) = 1$ , while the seed in the 's' is 8-connected with  $PT(x, y) = 1$  and  $(x, y)$ , respectively.

### Merging and Splitting Region Methods

In this technique, basically, two main features are there that are merging and splitting. Splitting is to separate an image in areas with similar features and merging helps to merge the neighboring related regions [9]. The fundamental algorithms for increasing and combining regions are:

The initial image should be 'p,' the basic predicate should be 'T.'

- The  $R_1$  is equal to  $p$  first.
- For each area,  $T(R_i) = \text{False}$  is divided into quadrants.
- If  $T(R_j) = \text{True}$  for each field, then merger  $R_i$  and  $R_j$  to  $T(R_i \cup R_j) = \text{True}$  to adjacent areas.
- Repeat step 3 to prevent merging.

## 2.4 Artificial Neural Networks (ANN)-Based Segmentation

Artificial neural network-based segmentation approaches model human brain learning techniques for decision-making purposes. It is nowadays primarily used for medical image segmentation. The appropriate image is separated from the background. It transforms the problem into a problem that is solved by neural networks [10].

This method has two basic steps: first, the capture of pictures and preprocessing, then extraction [11] of features, while the ANN classification [12] is used to classify texture. Clustering takes place to distinguish between sub-image backgrounds. ANN trained combines the input pixels into the results of two clusters. This allows the description of texture and image segmentation.

## 2.5 *Division by Partial Differential Equation (PDE)*

This process is quick segmentation methods. These are ideal for systems with critical time. The simple methods that exist in it are isotropic which are nonlinear (enhance the edges) filter based on diffusion and non-quadratic convex (noise removal) variation restore. The PDE method results are dull borders and boundaries which can be shifted with close operators. The fourth-order method is also being used [13].

Gloria Bueno introduced segmentation by anatomical structure [14].

Functional extraction systems for geometric complexity, change rate, and image orientation are capable of handling. A new segmentation system based on PDE is also presented which increases texture information contrast criteria. Using PDE models, the watershed approach is extended. The findings show that this method results in a high-quality image segmentation method. This proposed approach is contrasted with the watershed segmentation method.

## 2.6 *Fuzzy Theory Based Segmentation*

To evaluate and provide precise information from any pictures, fuzzy set theory is used. The fuzzy feature can also be used to minimize image noise [15]. By using a fuzzy function, various morphological operations with the fuzzy approach can be combined to achieve better results [16].

Pednekar and Kakadiaris [17] have suggested a new method based on fuzzy of dynamic weight relation. The author found that the issue of blurred medical images cannot be solved by conventional segmentation systems. The DyW algorithm is implemented to dynamically change the weights in fuzzy. The DyW algorithm in this many seeds were used to segment the image. It has also been found to offer 99% more accuracy than other techniques with DyW picture segmenting algorithm.

Yucheng and Yubin [18] proposed a new category for the segmentation of the morphological fusion image. In this, image is being smoothed and after this, operations related to gradient are carried out [11] Algorithm utilizes morphological opening and closing operations. It is found that fusion approach solve the problem of over-segmentation of watershed algorithm [19] and Prewitt methods.

The new fuzzy rule-based imaging technique was developed by Gour Chandra Karmakar [20] that is capable of integrating the complex relations of the pixel. Membership functions are mainly three which are being used to determine the area proximity and to detect the spatial relationship between pixels, i.e., membership function for the pixel distribution field. Parameters such as the FCM algorithm need not be specified in your technique. In the form of image segmentation, fuzzy rules use three membership features and IF-THEN fuzzy rule structure. In software named as MATLAB(5.3.1), on the image which is x-ray and the vocal tract image of human, FCM and proposed technique are implemented. Results showed that GFRIS exceeds FCM and precisely isolates the target from the context.

## 2.7 Clustering Based Segmentation

It is a method of pixel-wise segmentation. In this type of segmentation, make the cluster the pixels that are more similar to each other. Clustering of data is basically how data elements are grouped into clusters in such a manner that objects in the same cluster are more similar than others. The clustering methods are divided into two basic categories: partition and hierarchical. Hierarchy are depending on the tree structure. Tree root is the entire database and internal nodes are the clusters. Partition-based approaches on the other hand use techniques to refine the objective function to eliminate iteration. There are numerous cluster algorithms between these two approaches. Both forms of clustering are important [21].

### Hard Clustering

This method segment the images in form of a cluster such that only one image element in cluster's part is used. Some feature which have values 1 or 0, i.e., one pixel may or may not belong to the same cluster. An example is a technique used for clustering hard images and is known as HCM which is k-mean. Before the allocation of each element, centers are determined to the next in this process. It emphasizes optimizing the similarity of the intra-cluster and reducing equality.

### Soft Clustering

In this method, we can consider the example of noise which can cause accurate division in real life. Soft strategies for clustering images are most effective when the division is not rigid. The example is the fuzzy c-means clustering of these techniques. This degree of membership is represented by the values of membership. It can be part of multiple clusters. It is a more versatile approach than other techniques [22].

## 2.8 Watershed-Based Segmentation

The approaches focused on watersheds use a topological interpretation definition. This reflects the size of the tanks with a hole at the bottom from which the water spills. The adjacent basins are mixed as the water hits the boundary of the lake. To preserve the division between basin dams, the boundaries of the segmentation region are important. The dams are built with dilation. The methods of watersheds consider the picture gradient as a topographical surface. The more gradient pixels are defined as continuous boundaries [23]. The report is not yet published.

## 3 Conclusion

In this paper, the main image segmentation techniques used for image processing are addressed and evaluated. These techniques can be used to identify and detect objects. Its application are cancer discernment, road and bridge detection in satellite imagery.

Such methods apply in different areas, such as medical imaging, known artifacts, and patterns. The image segmentation outcome depends on a wide number of variables, i.e., color of the elements, surface, strength, and image quality. There are no perfect methods of image segmentation. Image separation is a critical and challenging task. In future image processing should be focused on the image separation and segmentation.

## References

1. Kang WX, Yang QQ, Liang RP (2009) The comparative research on image segmentation algorithms. In: 2009 First international workshop on education technology and computer science, vol 2. IEEE
2. Rehman M, Sharif M, Raza M (2016) Shape features extraction method for content based image retrieval. *Sindh Univ Res J-SURJ (Sci Ser)* 48(1)
3. Khan W (2014) Image segmentation techniques: A Survey. *J Image Graph* 1:166–170. <https://doi.org/10.12720/joig.1.4.166-170>
4. Singh P, Chadha RS (2013) A novel approach to image segmentation. *Int J Adv Res Comput Sci Softw Eng* 3(4)
5. Lakshmi S, Sankaranarayanan V Dr (2010) A study of edge detection techniques for segmentation computing approaches. In: *IJCA Special issue on “computer aided soft computing techniques for imaging and biomedical applications” CASCT*, pp 35–40
6. Sobel I (1990) An isotropic  $3 \times 3$  gradient operator, machine vision for three-dimensional scenes. Freeman, H., Academic Press, NY, pp 376–379
7. “Prewitt Edge,” <http://www.roborealm.com/help/Prewitt.php>
8. Angelina S, Padma Suresh L, Krishna Veni SH (2012) Image segmentation based on genetic algorithm for region growth and region merging. In: 2012 International conference on computing, electronics and electrical technologies (ICCEET). IEEE
9. Kaganami HG, Beiji Z (2009) Region-based segmentation versus edge detection. In: 2009 Fifth international conference on intelligent information hiding and multimedia signal processing. IEEE
10. Senthilkumaran N, Rajesh R (2009) Edge detection techniques for image segmentation—a survey of soft computing approaches. *Int J Recent Trends Eng* 1(2), May
11. Sharif M, Raza M, Mohsin S, Shah JH (2013) Microscopic feature extraction method. *Int J Adv Netw Appl* 4:1700–1703
12. Mohamed EI et al (2019) A novel morphological analysis of DXA-DICOM images by artificial neural networks for estimating bone mineral density in health and disease. *J Clin Densitometry* 22(3):382–390
13. Zhao F et al (2019) Segmentation of blood vessels using rule-based and machine-learning-based methods: a review. *Multimedia Syst* 25(2):109–118
14. Bueno S, Albala AM, Cosfas P (2004) Fuzziness and PDE based models for the segmentation of medical image. In: *Proceedings nuclear science symposium conference record*. IEEE, pp 3777–3780
15. Memon KH et al (2019) Kernel possibilistic fuzzy c-means clustering with local information for image segmentation. *Int J Fuzzy Syst* 21(1):321–332
16. Masood A, Shahid MA, Sharif M (2018) Content-based image retrieval features: a survey. *Int J Adv Netw Appl* 10(1):3741–3757
17. Pednekar AS, Kakadiaris IA (2006) Image segmentation based on fuzzy connectedness using dynamic weights. *IEEE Trans Image Process* 15:1555–1562
18. Yucheng L, Yubin L (2009) An algorithm of image segmentation based on fuzzy mathematical morphology. In: *International forum on information technology and applications, IFITA’09*, pp 517–520



19. Murali E, Meena K (2017) A phenomenological survey on various types of brain diseases using soft computing techniques. *Int J Civil Eng Technol* 8(9)
20. Karmakar GC, Dooley L (2000) A generic fuzzy rule based technique for image
21. Khan MJ et al (2018) Automated forgery detection in multispectral document images using fuzzy clustering. In: 2018 13th IAPR international workshop on document analysis systems (DAS). IEEE
22. Dhanachandra N, Chanu YJ, Singh KM (2020) A new hybrid image segmentation approach using clustering and black hole algorithm. *Computational Intelligence*
23. Jaglan P, Dass R, Duhan M (2019) A comparative analysis of various image segmentation techniques. In: *Proceedings of 2nd international conference on communication, computing and networking*. Springer, Singapore

# Autoencoder: Issues, Challenges and Future Prospect



Anega Maheshwari, Priyanka Mitra, and Bhavna Sharma

**Abstract** As of more recently, deep learning-based models have demonstrated considerable potential, as they have outperformed all traditional practices. When data becomes high dimensional, extraction of features and compression of data become progressively significant. In this paper, we describe the autoencoder deep learning algorithm. Autoencoder is primarily a neural network-based feature extraction methodology that accomplishes outstanding victory in producing highlights of high-dimensional data. Autoencoder assumes a principal job in unsupervised learning which targets to rework inputs into outputs with minimal reconstruction error.

**Keywords** Autoencoder · Convolutional autoencoder · Denoising autoencoder · Unsupervised learning

## 1 Introduction

While unaided learning of a mapping that generates “good” intermediary illustrations of the input appears to be the key, little is comprehended in regards to what comprises “good” illustrations for initializing deeper network architectures, or what unequivocal criteria may direct learning such intermediary illustrations. Gaining insights from an expansive sum of information could be a difficult job. Several dimensionality reduction strategies that are all around concentrated in the writing intend to acquire an understanding of an easier representation from the dataset.

Although numerous methods have been proposed to deal with dimensionality reduction, outcomes from models dependent on deep architectures are encouraging. Autoencoder has been taken to the forefront of generative modeling with the emergence of deep learning science. Autoencoders are basic learning systems that intend

---

A. Maheshwari · P. Mitra (✉) · B. Sharma  
Department of Computer Science, Jaipur Engineering College and Research Centre, Jaipur,  
Rajasthan, India  
e-mail: [priyankamitra.cse@jecrc.ac.in](mailto:priyankamitra.cse@jecrc.ac.in)

A. Maheshwari  
e-mail: [anegamaheshwari.cse20@jecrc.ac.in](mailto:anegamaheshwari.cse20@jecrc.ac.in)

to recast inputs into outputs with the slightest possible distortion. The notion of autoencoders has been widespread within the discipline of neural networks for a considerable length of time.

However, recently, the idea of autoencoders has been extensively utilized for mastering generative models of data. Autoencoders are commonly trained with a solo layer encoder and a solo layer decoder; however, utilizing deep autoencoders offers favorable points of interest.

In this paper, we proposed an approach to an autoencoder model which can extract features based on both data itself and the correlation among the data. Provided data relationships, reconstruction error can be diminished and, therefore, generate more powerful features. This paper presents a comprehensive survey on autoencoder architecture and its various variants. The various issues and challenges have been addressed for autoencoders.

We organize the paper as described. Section II describes the literature study of autoencoders. Section III begins with a simple autoencoder architecture and its basic components. Variants of autoencoder are explained in Section IV. Section V presents challenges and issues of autoencoders. Section VI presents conclusions and future work.

## 2 Literature Review

Autoencoders grasp a condensed representation of data by mapping the data into a smaller spatial dimension. The foremost precept of autoencoder follows from the name: “auto” favors that this technique is unsupervised and “encoder” signifies it learns encodings of data. Autoassociator or diabolito network are other names of autoencoder. In particular, encoded latent space features of data are learned by an autoencoder, which tries to limit the error between original data and output decoded from the encodings. The latent space representation carries fundamental characteristics of data.

In [1], autoencoder was developed as a neural network tool and that could be a successful solution for unsupervised learning using neural networks. This was presented as a strong replacement for the current approaches that were conducting a function close to that of principal component analysis (PCA) at the time. An analytical model [2] has been developed based on the minimal description duration (MDL) concept for the training of autoencoders. Their purpose was to lessen the knowledge needed to describe both the vector of code vector and the error in reconstruction.

In [3], the authors suggested the usage of deep autoencoder as a promising method for minimizing dimensionality. Experimentally, they demonstrated that the compression of deep autoencoders is significantly stronger than the equivalent shallow or linear autoencoders. In [4], the authors defined a novel algorithm for learning sparse representations and compared it with a related probabilistically trained machine, namely restricted Boltzmann machine (RBM), theoretically and experimentally. In [5], autoencoder is proposed as a means of directing supervised learning by the usage

of autoencoding in conjunction with supervised learning as a tuning denoising mechanism. The authors discussed a deep networking approach focused on piling layers of denoising autoencoders that were trained to denoise noisy forms of the inputs. This prompted them to address a conceptual flaw of conventional autoencoders, namely their failure to understand effective overcomplete code. The resulting algorithm of stacked denoising autoencoder for deep network training has proven capable of bridging the functional gap with deep belief networks, resulting in equal or finer classification results.

In [6], the authors demonstrated that a gradient of an autoencoder offers estimation to restricted Boltzmann machines' analogous divergence preparation. The authors in [7] proposed an innovative method to train deterministic autoencoders. They demonstrated that by applying a well-selected penalty term to the cost function of reconstruction, results can be obtained that equal or outclass those produced by denoising autoencoders and other regularized autoencoders on a number of datasets. In addition, they demonstrated that this penalty term has connection with both regularized and denoising autoencoders, and it can be interpreted as a bridge between deterministic and non-deterministic autoencoders.

In [8], a very efficient sparse coding system named k-sparse autoencoder was introduced by Makhzani and Frey, which attains good sparsity in the hidden representation. They also addressed how to use the k-sparse autoencoder for pretraining architectures that are shallow and deep. Bowman et al. [9] developed and analyzed a generative model focused on RNN variational autoencoder, which implements distributed latent space representations of complete sentences and can be utilized for natural language sentences. In [10], the authors described autoencoders and its variants and introduced a deep neural generative model that would merge variational autoencoders (VAEs) with comprehensive attribute discriminators to efficiently implement semantic structures.

In [11], the authors used deep autoencoders and feedforward networks for anomaly detection. NSL-KDD dataset has been considered for testing and comparing of the models.

In the literature, autoencoders have been utilized for information retrieval and dimensionality reduction. Backpropagation learning is employed for updating the weights within the network. Optimization algorithms such as stochastic gradient descent, root mean square prop, and Adam are employed for the learning of autoencoders.

The literature review recommends that autoencoders are acceptable candidates to find out spatial and temporal features and determine anomalies. There have also been numerous experiments undertaken on current state-of-the-art deep learning architectures present in the literature. Table 1 presents preliminary prominent contributions to the proposed architecture. To sum up the literature review concerning autoencoders, the accompanying table is offered for ease of access:

**Table 1** Literature review on autoencoders

Contribution	Papers
Autoencoders	Hinton and Zemel (1994)
Denosing autoencoders	Gallinari et al. (1987), Vincent and Larochelle (2008)
Convolutional autoencoders	Erhan et al. (2010), Masci et al. [7], Du et al. (2017)
Sparse autoencoders	Olshausen and Field (1997), Ranzato (2007), Mairal et al. (2009), Makhzani and Frey (2014)
Stacked autoencoders	Bengio et al. (2007), Vincent et al. (2010)
Contractive autoencoders	Rifai et al. (2011)

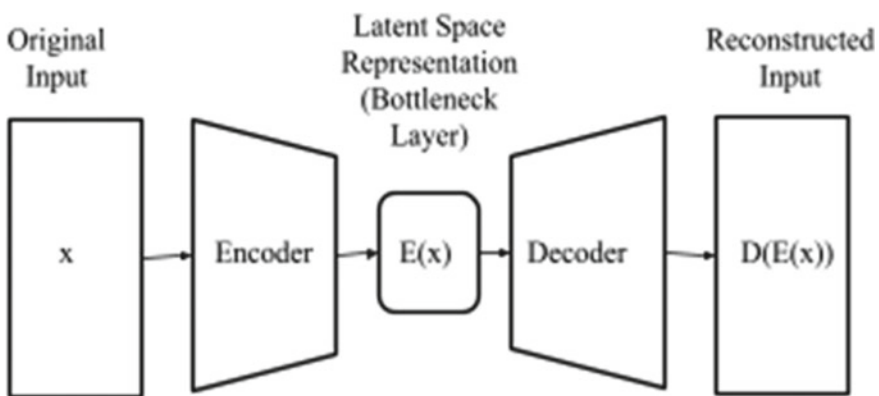
### 3 Architecture

This section begins with a description of the simple autoencoder architecture followed by its basic components.

**Basic Autoencoder and its Components.** An autoencoder is a class of neural networks that attempts to recreate the output relative to the input by estimating the identity function. To attenuate the reconstruction error which can be evaluated using loss functions, the model parameters are optimized.

Autoencoder [3] focuses on learning a compact and distributed representation for a collection of data. Using a fewer hidden units than inputs powers the autoencoder to memorize a condensed approximation.

Autoencoder comprises of three main components: an encoder network, a code and a decoder network. The encoder encodes the input image as a compressed representation in a reduced dimension; the code resembles the latent space encoding, i.e., the compressed input fed to the decoder; the decoder rebuilds input back to the initial dimension from the code (Fig. 1).

**Fig. 1** Basic components of an auto encoder

When the size of the hidden layer in a basic autoencoder is larger than the size of the input layer, this is considered an overcomplete autoencoder. When the size of the hidden layer in a basic auto encoder is less than the size of the input layer, it is considered an undercomplete autoencoder.

An autoencoder makes use of a series of “recognition weights” to transform a vector of input to a vector of code. It then makes use of a collection of “generative weights” to transform the vector of code into an estimated reconstruction of the vector of input.

The autoencoder calculation and its profound variant has been a remarkable accomplishment as of late. An autoencoder’s training procedure is based on cost-function optimization. The autoencoders are nonlinear by nature and can learn more intricate relations and more powerful features.

### 4 Variants of Autoencoder

**Denoising Autoencoder.** The basic principle behind denoising autoencoder (DAE) is to compel the autoencoders to no longer gain proficiency from the identity function, but more robust features, by reestablishing the input from a corrupted version of itself. An autoencoder can retrace a distorted input by capturing the statistical dependencies between the inputs.

Training denoising autoencoders requires learning to recover clean input from an adulterated sample, a task called denoising. Denoising autoencoders anticipate that well denoising can be accomplished if the model obtains highlights that seize valuable structure in the input distribution.

Denoising autoencoder’s key idea is to corrupt a portion of the input characteristics of a given dataset  $X$  before submitting it to an autoencoder model, train the network to rebuild a fair “restored” input from the adulterated input  $X'$  and then reduces the error between the reconstructed  $Y$  and original  $X$  (Fig. 2).

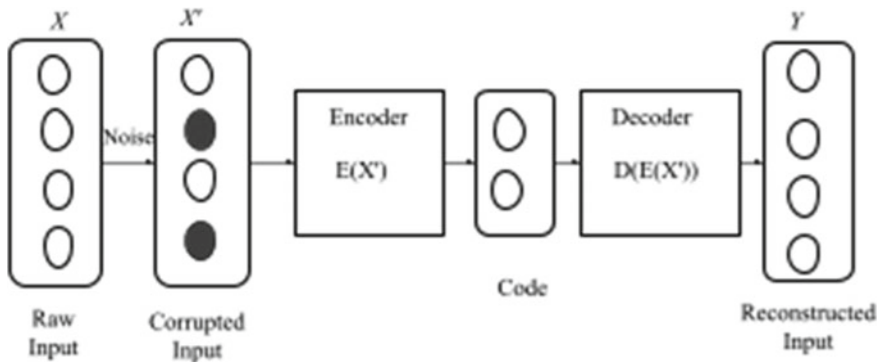


Fig. 2 Denoising autoencoder

The training operation of a denoising autoencoder works as follows:

- Stochastic mapping is brought into play to contaminate the initial input  $X$  into  $X'$ .
- The corrupted input  $X'$  is then mapped to a hidden encoding by using function  $E(X')$ .
- From the hidden encoding, the model reestablishes the input through mapping  $D(E(X'))$ .

The loss function minimizes error not from the original but the corrupted input and takes the following form:

$$L(X, D(E(X'))) \quad (1)$$

where  $D(E(X'))$  is the decoder output,  $E(X')$  is the encoder output encoded from the corrupted input  $X'$ .

**Convolutional Autoencoder.** Convolutional autoencoders (CAEs) are focused on convolutional neural networks (CNN). A CNN comprises of convolutional, pooling, and deconvolutional layers optionally accompanied by a fully connected layer. The convolutional operation is applied by extracting native receptive fields around the entire image to create an activity map from the inputs. Each ensuing layer increases the intricacy of the realized activity map. This activity map is also known as a feature map. The middle subsampling layer is connected to the decoder in unsupervised learning and then proceeds to restore the input image again with the convolutional process.

The convolution operator permits filtering an input signal to extract a considerable phase of its content. Convolutional autoencoders utilize the convolution operator to take advantage of the survey that a signal can be seen as an entirety of other signals. Convolutional autoencoders figure out how to encipher the contribution of inputs to a set of basic signals and afterward attempt to remake the contribution from those signals. We let the convolutional autoencoder model gain proficiency with optimal filters that lessen the error in the reconstruction. Once learned, these filters are applied to related input to retrieve information.

CAEs are a subset of CNNs: the key distinction between the frequent understanding of CNN and CAE is that the former are qualified end-to-end to master filters and integrate features to categorize their input. In addition, CNNs are generally classified as supervised learning algorithms [6]. CAEs are only equipped to comprehend optimal filters that can extract features and can be used for input recreation.

Convolutional autoencoder is a conventional autoencoder stacked with convolution layers. Convolutional autoencoder broadens the standard autoencoder's fundamental structure by altering the fully connected layers to convolution layers. The encoder network is modified to convolutional layers and the decoder network is modified to transpose convolutional layers in convolutional autoencoders. In the event that we use image data, the convolutional layer is smarter to catch the spatial statistics in the image (Fig. 3).

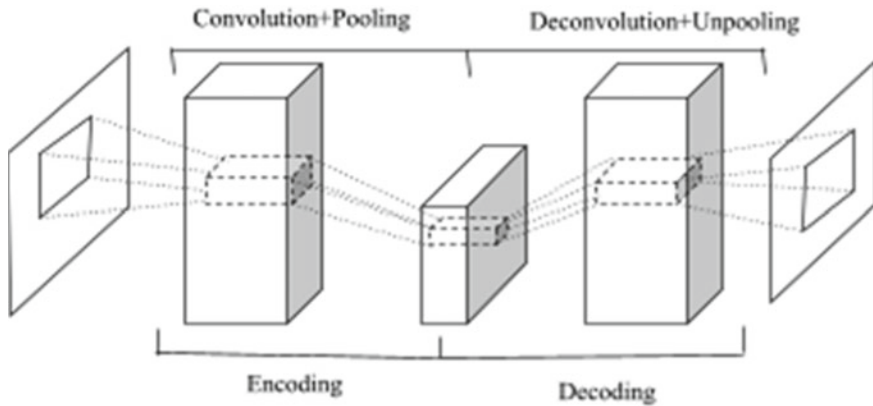


**Fig. 3** Convolutional autoencoder

As opposed to utilizing one hidden layer in a basic autoencoder, a convolutional autoencoder uses numerous layers to extract significantly high-level features appearing in the image. The quantity of unbound parameters in the fully connected layer is bigger than the quantity of unbound parameters in a multi-convolution layer, which makes the basic autoencoder arduous to train and time exorbitant.

Convolutional autoencoders can scale rigorously to realistic-sized high-dimensional images as a result of their convolutional character. Therefore, convolutional autoencoders are well acknowledged as “Feature Extractors” for general purpose functionality.

**Sparse Autoencoder.** A sparse autoencoder (SAE) incorporates additional hidden activation nodes than input nodes, but only a few nodes are dynamically active at once. The loss function penalizes the activation nodes present in the hidden layers, with the end goal that only a few nodes are actuated when the network is trained.

It is considered that if a sparsity penalty is upheld on the hidden layer activation nodes, at that point, the autoencoder would still discover captivating designs and statistical patterns within the data. The sparsity constraint permits the sparse autoencoder to figure out distinctive characteristics and features within the dataset. By enforcing constraint on a number of hidden layer activations, one can flatten the input to an optimally contracted latent space.

Sparse autoencoder is mathematically constrained, such limitations are added to the learning optimization handles using regularizers. Sparsity is extended to autoencoders as a mathematical constraint by means of several conceptualizations. It has been noted that sparse regularization prompts higher learning performance in many applications by improving the standard of encoding.

The network is driven to acquire representations in which only a minimal number of neurons are triggered. There are two different ways to impose sparsity constraint:



- L1 Regularization—It adds “absolute value of magnitude” of coefficients as a penalty term. A term can be added to the loss function that penalizes the absolute value of the vector of activations within the hidden layers.
- Kullback Leibler Divergence—It is the degree of contrast between two probability distributions. A sparsity parameter  $\rho$  is defined, which indicates the average activation of a node.

The  $k$ -sparse autoencoder [8] is an improvement over sparse autoencoder. Here,  $k$  nodes with the most elevated activation functions are picked.

## 5 Challenges and Issues

When addressing real-world data, existing algorithms dependent on autoencoders experience the ill effects of various issues which hinder their robustness and ease-to-use, such as

*Weights Initialization*—with huge introductory weights, autoencoders usually realize poor local minima; with tiny initial weights, the gradients within the early layers are little, creating it infeasible to train autoencoders with many hidden layers. Instantiating the weights with random values can add randomness to the obtained results.

*Model Architecture*—the model’s configuration, i.e., number of layers and their width, causes the network to seek a specific portrayal of the data while retaining the relevant details.

*Hyperparameters*—there are a few essential hyperparameters that are tough to be set; learning rate, weight-cost, dropout fraction, batch size, the number of epochs, the number of layers, the number of nodes in each of the encoding layers, kind of activation functions, number of nodes in each of the decoder layers, network weight initialization, optimization algorithms, and the number of nodes in the bottleneck layer.

Studying autoencoders in depth empowers one to achieve a general understanding of autoencoders, characterize key properties that are shared by different autoencoders and that should be checked consistently in any new form of autoencoder. The utilization of autoencoder encodings might offer a decent solution for errands that require more steady performance under the noise.

The key drawback of the autoencoders lies in the fact that they are data-driven or data-specific, and thus, their utility is restricted to the data that share similar properties with the training data.

Another principal constraint is that the compression by an autoencoder is lossy. Autoencoders do not flawlessly restore the original information. This essentially implies that compression and decompression operation degrades the output of the network, generating a less precise representation contrasted with its input. It should be noted that autoencoders do not perform noticeably better than the JPEG algorithm at encoding images.

## 6 Conclusion and Future Work

Autoencoders are broadly utilized for a diversity of tasks such as information retrieval, reverse image search, classification, anomaly detection, dimensionality reduction, image compression, image denoising, image blending, feature extraction, and plenty more. A smart idea for future work is to apply autoencoders in medical image analysis. Medical imaging including X-rays, MRI, CT, etc., are susceptible to noise. Reasons incorporate the use of different image acquisition techniques. Image denoising is a crucial preprocessing step in medical image analysis. Denoising autoencoders can be utilized here for efficient denoising of medical images.

Another potential future application is an encoder–decoder model capable of capturing temporal structure, such as long short-term memory (LSTM)-based autoencoders, which can fix machine translation issues. It can be used to determine a video's next frame. Besides the simple autoencoder, denoising autoencoder and convolutional autoencoder; variational autoencoder (VAE) is another autoencoder variant that is worth investigating. It would be fascinating to explore its potential in future work.

In short, autoencoders create a representation at the intermediate bottleneck layer to preserve only the components that are useful, and to reject not useful segments and noise. In the modern era, autoencoders are turning up to be a hot field of research and exploration in numerous aspects. This paper has successfully introduced autoencoders driven by the objective of learning intermediate representations of the input that are robust to small irrelevant changes in the input and much better suited for subsequent learning tasks.

## References

1. Hornik K, Baldi P (1989) Neural networks and principal component analysis: learning from examples without local minima. *Neural Netw* 1(2):54
2. Hinton G (1990) Connectionist learning procedures. In: *Machine learning*. Morgan Kaufmann, pp 555–610
3. Hinton GE, Osindero S, Teh YW (2006) A fast learning algorithm for deep belief nets. *Neural Comput* 18(7):1527–1554
4. Ranzato M, Boureau Y, LeCun Y (2007) Sparse feature learning for deep belief network. In: *Advances in neural information processing system*, vol 20 (NIPS 2007)
5. Vincent P, Larochelle H, Bengio Y, Manzagol P-A (2008) Extracting and composing robust features with denoising autoencoders (Technical report 1316). Université de Montréal, Department IRO
6. Bengio Y (2009) Learning deep architectures for AI. *Found Trends Mach Learn* 2(1):1–127
7. Masci J et al (2011) Stacked convolutional auto-encoders for hierarchical feature extraction. In: *Artificial neural networks and machine learning—ICANN 2011*, pp 52–59
8. Makhzani A, Frey B (2013) k-sparse autoencoders
9. Bowman SR, Vilnis L, Vinyals O et al (2016) Generating sentences from a continuous space. In: *CONLL*, pp 10–21

10. Zhai J, Zhang S, Chen J, He Q (2018) Autoencoder and its various variants. In: 2018 IEEE international conference on systems, man, and cybernetics (SMC), Miyazaki, Japan, 2018, pp 415–419. <https://doi.org/10.1109/SMC.2018.00080>
11. Albahar MA, Binsawad M (2020) Deep autoencoders and feedforward networks based on a new regularization for anomaly detection. Security Commun Netw